

Hydration and dimensional stability of calcium aluminate cement based systems

THÈSE N° 6336 (2014)

PRÉSENTÉE LE 8 OCTOBRE 2014

À LA FACULTÉ DES SCIENCES ET TECHNIQUES DE L'INGÉNIEUR
LABORATOIRE DES MATÉRIAUX DE CONSTRUCTION
PROGRAMME DOCTORAL EN SCIENCE ET GÉNIE DES MATÉRIAUX

ÉCOLE POLYTECHNIQUE FÉDÉRALE DE LAUSANNE

POUR L'OBTENTION DU GRADE DE DOCTEUR ÈS SCIENCES

PAR

Julien BIZZOZERO

acceptée sur proposition du jury:

Prof. D. Damjanovic, président du jury
Prof. K. Scrivener, directrice de thèse
Dr R. Barbarulo, rapporteur
Dr H. Fryda, rapporteur
Dr B. Lothenbach, rapporteuse



ÉCOLE POLYTECHNIQUE
FÉDÉRALE DE LAUSANNE

Suisse
2014

Fatti non foste a viver come bruti,
ma per seguir virtute e canoscenza.
— Dante Alighieri

À ma mère, a mio padre e a mia zia.

Acknowledgements

Special thanks to Prof. Karen Scrivener, director of the Laboratory of Construction Materials, for giving me the opportunity to work in an exceptional environment and to travel around the world. It was not in my “plans” to start PhD studies after my master but Karen convinced me to join her lab and I am now fully satisfied of this experience; thank you!

I would like to thank Kerneos France for the financial support for this research and particularly Dr. Hervé Fryda, Dr. Pascal Taquet and Dr. Séverine Lamberet.

I would like to thank the members of the jury for their helpful comments; Dr. Barbara Lothenbach, Dr. Hervé Fryda, Dr. Rémi Barbarulo and Prof. Dragan Damjanovic.

Thanks to the LMC colleagues for the great times in and out of the lab. Special thanks to my office mates, first Christophe and Hui and then Berta and Mohamad. It was a pleasure to work and to share an important fraction of my time with you. Thanks also to all the other colleagues (some of which become good friends) in a disordered order; Berta, Mohamad, Amélie, Ruben (thanks for teaching me “all” about Rietveld analysis), Cédric, Pierre, Cyrille (thanks for the help with the modelling and the reading of my thesis), Hui, Christophe, Cheng, Elise, Pawel, Aslam, Aditya, Alain, Antonino, Joao, Lionel (thanks for all the good running sessions and competitions), Sandra, Anne-Sandra, Maude, Marie-Alix, Ashley, Nico, Ted, Matt, Huang, Yoshi, Shigeyoshi, Boutaina, François, Lilian, Suhua, Mathieu, Théo, Aurélie, Hadi, Julien, Olga, Arnaud, John, Alexandra, Quang Huy, Emmanuelle... and the ones I forgot. Thanks also for the nice trips around the world with Mohamad, Pawel, Elise, Berta, Aslam, John and Cheng.

I have to thank also the bachelor and master students that contributed to this work; Selim, Alessio, Maxime and Claire.

I shared an important part of the years here in Lausanne with a special person that always supported and encouraged me; grazie Anna.

Finally, all my gratitude goes to my parents and to my aunt for their love and support. Merci, grazie di cuore, senza di voi non sarei mai arrivato fin qui.

Lausanne, September 3rd 2014

Julien Bizzozero

Abstract

Calcium aluminate cements (CAC) are often used in combination with calcium sulfate and Portland cement for special applications where rapid setting, rapid drying and shrinkage compensation are required. A growing fraction of the clinker, which has the highest CO₂ intensity, is being replaced by supplementary cementitious materials (SCM). These SCM are usually from industrial by-products such as slag, fly ashes or can simply be raw materials such as limestone. This project aims at replacing the Portland cement and fraction of the CAC in ternary binders with such SCM. Indeed, the understanding of their interactions, both physical and chemical, with calcium aluminate cements and calcium sulfate is fundamental for the development of innovative products.

This thesis focuses first on the hydration of systems with and without SCM, slag or limestone, from the first hours up to two years of hydration. Second, this study focuses on the expansion of these systems and on the mechanisms underlying the dimensional stability. The influence of the ratio between calcium sulfate and calcium aluminate on the hydration of the cement, on the reaction of SCM, and on the expansion is highlighted. This study indicated that the calcium sulfate reacts with CAC from the first hours of hydration and, only when sulfate is exhausted, does slag or limestone react with aluminate phases. Moreover, this research brings new insights on the main parameters influencing the dimensional stability of the studied systems and on the mechanisms governing expansion. Pore solution analyses showed that supersaturation with respect to ettringite increases with the calcium sulfate content, which results in an increase of the crystallization pressure. The supersaturation determines the minimum pore size in which crystals can grow. Therefore, with increasing supersaturation a larger pore volume can be accessed by ettringite crystals exerting pressure. This could explain the critical amount of calcium sulfate leading to high expansion. Both the confinement in nanometer size pores and the supersaturation of ettringite are necessary for expansion to occur.

Keywords: calcium aluminate cement, calcium sulfoaluminate cement, calcium sulfate, crystallization pressure, ettringite, expansion, limestone, nanoporosity, slag, supplementary cementitious materials, thermodynamic simulations.

Résumé

Les ciments alumineux (CAC) sont souvent utilisés en combinaison avec du sulfate de calcium et du ciment portland pour des applications particulières requérant une prise et un séchage rapide ainsi qu'une compensation du retrait. Une fraction croissante du clinker, responsable de la plupart des émissions de CO₂ liées à l'industrie cimentaire, est remplacée par des additions minérales. Ces additions sont généralement issues de déchets industriels tels que le laitier, les cendres volantes ou la fumée de silice ou peuvent être des additions minérales telles que la roche calcaire. Ce projet se focalise sur le remplacement du ciment portland et d'une fraction du CAC dans les systèmes ternaires par ces additions minérales. La compréhension des interactions physiques et chimiques entre les additions minérales, le sulfate de calcium et le ciment alumineux est fondamentale pour le développement de produits innovants.

Cette thèse se concentre, premièrement, sur l'hydratation de ces systèmes cimentaires avec ou sans additions minérales et, deuxièmement, sur l'étude des propriétés expansives et les mécanismes responsables de la stabilité dimensionnelle. Une attention particulière est apportée sur l'influence entre la quantité de sulfate de calcium par rapport à celle des aluminates de calcium sur l'hydratation du ciment, sur la réaction des additions minérales et sur l'expansion. Cette étude a montré que le sulfate de calcium réagit avec le CAC dès les premières heures et, une fois le sulfate de calcium consommé, les additions minérales telles que le laitier ou le calcaire réagissent avec les phases aluminates. Cette étude donne un nouvel aperçu des paramètres influençant la stabilité dimensionnelle et sur les mécanismes régissant l'expansion. Les analyses de la solution de pore ont montré que la sursaturation de l'ettringite augmente avec le taux de sulfate de calcium, ce qui se traduit par une augmentation des pressions de cristallisation. La sursaturation détermine la plus petite taille des pores où les cristaux peuvent croître. Par conséquent, l'augmentation de la sursaturation permet aux cristaux d'ettringite de croître et générer des pressions dans une plus grande fraction volumique de pores. Ceci peut expliquer la quantité critique de sulfate de calcium responsable d'une expansion importante. Le confinement des cristaux dans les pores nanométriques ainsi que la sursaturation de l'ettringite sont simultanément nécessaires pour l'expansion de ces systèmes.

Mots clefs : ciment alumineux, sulfate de calcium, pression de cristallisation, ettringite, expansion, calcaire, laitier, additions minérales, simulation thermodynamique.

Riassunto

I cementi alluminosi (CAC) sono spesso utilizzati in combinazione con il solfato di calcio e il cemento Portland per delle applicazioni specializzate richiedenti una presa ed essiccazione rapida così come una compensazione del ritiro. Una proporzione sempre maggiore di clinker, responsabile della gran parte delle emissioni di CO₂ legate all'industria del cemento, viene rimpiazzata da materiali cementizi supplementari. Questi materiali provengono normalmente da scarti industriali quali la loppa d'altoforno (o scoria d'altoforno), le ceneri o il fumo di silice oppure possono essere delle addizioni minerali quali la pietra calcarea. Questo progetto si focalizza sulla sostituzione del cemento Portland e di una frazione del CAC nei sistemi ternari con questi materiali cementizi supplementari. La comprensione delle interazioni fisiche e chimiche tra i materiali cementizi supplementari, il solfato di calcio e il cemento alluminoso è fondamentale per lo sviluppo di prodotti innovativi.

Questa tesi si concentra, primariamente, sull'idratazione di questi sistemi con o senza materiali cementizi supplementari e ,secondariamente, sullo studio delle proprietà espansive e del meccanismo responsabile della stabilità dimensionale. Una speciale attenzione è portata sull'influenza della quantità di solfato di calcio in rapporto a quella degli alluminati di calcio sull'idratazione del cemento, sulla reazione dei materiali cementizi supplementari e sull'espansione. Questo studio mostra che il solfato di calcio reagisce con il cemento alluminoso a partire dalle prime ore e, una volta consumato tutto il solfato di calcio, i materiali supplementari quali la loppa d'altoforno o il calcare reagiscono con gli alluminati di calcio. Questa ricerca fornisce una nuova visione dei parametri che influiscono sulla stabilità dimensionale e sui meccanismi responsabili dell'espansione. Le analisi della soluzione trovata nei pori del cemento hanno mostrato che la supersaturazione dell'ettringite aumenta con il tasso di solfato di calcio, ne consegue un aumento delle pressioni di cristallizzazione. La supersaturazione determina la taglia minima dei pori dove i cristalli possono precipitare. Dunque, l'aumento della supersaturazione permette ai cristalli di ettringite di crescere generando pressione in una frazione di pori più estesa. Questo può spiegare la quantità critica di solfato di calcio responsabile di un'espansione considerevole. La restrizione dei cristalli nei pori nanometrici così come la supersaturazione dell'ettringite sono simultaneamente necessarie per l'espansione di questi sistemi.

Parole chiave: cemento alluminoso, solfato di calcio, pressione di cristallizzazione, ettringite, espansione, loppa d'altoforno, calcare, materiali cementizi supplementari, simulazione termodinamica.

Contents

Acknowledgements	v
Abstract (English/Français/Italiano)	vii
Table of contents	xvi
List of figures	xx
List of tables	xxi
Glossary	xxiii
1 Introduction	1
2 Literature review	3
2.1 Calcium aluminate cement	3
2.1.1 Hydration of calcium aluminate cement	4
2.2 Calcium aluminate cement with calcium sulfate	6
2.2.1 Calcium sulfoaluminate cement with calcium sulfate	8
2.2.2 Tricalcium aluminate with calcium sulfate	8
2.3 Calcium aluminate cement with supplementary cementitious materials	11
2.3.1 Filler effect at early ages	11
2.3.2 Long term hydration of calcium aluminate cement with limestone	11
2.3.3 Long term hydration of calcium aluminate cement with slag	13
2.4 Dimensional stability and expansion mechanisms	16
2.4.1 Expansion associated with ettringite formation	16
2.4.2 Crystallization in restrained conditions	17
2.4.3 Crystallization in porous media	19
2.4.4 Salt supersaturation: the case of ettringite	22
2.4.5 Factors affecting the expansion	24
2.5 Characterization of the confinement	25
3 Materials and methods	27
3.1 Materials	27
3.2 Methods	30

Contents

3.2.1	Experimental conditions	30
3.2.2	Compressive strength tests	31
3.2.3	Expansion tests	31
3.2.4	Isothermal calorimetry	31
3.2.5	Sample preparation for microstructural characterization	31
3.2.6	X-ray diffraction	32
3.2.7	Thermogravimetric analysis	34
3.2.8	Scanning electron microscopy	34
3.2.9	Porous structure characterization	36
3.2.10	Pore solution analysis	40
3.2.11	Thermodynamic simulations	41
3.2.12	Finite element modelling of the expansion	41
4	Early age hydration	43
4.1	Introduction	43
4.2	Formulations	44
4.3	Overview of hydration kinetics	45
4.4	Effect of calcium sulfate	45
4.4.1	Low calcium sulfate system	45
4.4.2	High calcium sulfate system	51
4.4.3	Comparison between low and high calcium sulfate	54
4.4.4	Characterization of microstructure and phase assemblage	55
4.5	Effect of supplementary cementitious materials	61
4.5.1	Effects on the kinetics	61
4.5.2	Effects on the pore solution	63
4.6	Summary on the early age hydration	65
4.6.1	Effect of sulfate	65
4.6.2	Filler effect	66
5	Long term hydration with SCM	67
5.1	Introduction	67
5.2	Formulations	68
5.3	Systems containing limestone	69
5.3.1	Compressive strength	69
5.3.2	Hydration kinetics	71
5.3.3	Experimental and thermodynamic prediction of phase assemblages	72
5.3.4	Porosity evaluation and links to compressive strength	79
5.3.5	Microstructure characterization	82
5.3.6	Summary on systems containing limestone	84
5.4	Systems containing slag	85
5.4.1	Compressive strength	85
5.4.2	Hydration kinetics	85
5.4.3	Experimental phase assemblage	86

5.4.4	Microstructure and degree of reaction of slag by SEM-IA	91
5.4.5	Thermodynamic simulation	95
5.4.6	Summary on systems containing slag	98
6	Mechanisms leading to expansion	99
6.1	Introduction	99
6.2	Materials and formulations	100
6.3	Expansion characterization: effect of calcium sulfate	101
6.3.1	Experimental study	101
6.3.2	Pore solution analyses and supersaturation	106
6.4	Understanding expansion: effect of calcium sulfate	109
6.4.1	Pore stresses	109
6.4.2	Summary on the effect of calcium sulfate	118
6.5	Modelling of expansion: an elastic approach	120
6.5.1	Introduction of the model	120
6.5.2	Sensitivity analysis	122
6.5.3	Comparison between the model and the experiments	125
6.6	Other factors influencing the expansion	126
6.6.1	Effect of porosity: water to binder ratio	126
6.6.2	Effect of porosity: substitution effect	129
6.6.3	Summary on the effect of porosity: insights from the modelling	132
6.6.4	Effect of ettringite solubility and kinetics: temperature effect	133
6.6.5	Effect of alkalis	135
6.7	Long term expansion	136
7	Conclusions	139
7.1	Conclusions	139
7.1.1	Hydration with and without SCM: effect of calcium sulfate	139
7.1.2	Mechanisms leading to expansion	141
7.2	Perspectives	144
A	Appendix	145
A.1	Properties of the main hydrates	145
A.1.1	AFt phases: Ettringite	145
A.1.2	AFm phases	148
A.1.3	Hydrogarnet	151
A.1.4	Aluminium hydroxide	151
A.2	Calculation of enthalpies	152
A.2.1	Enthalpies of dissolution	152
A.2.2	Calculation of the enthalpy of reaction of calcite	153
A.3	How does Na ₂ SO ₄ lead to alkaline solution?	154
A.4	Study on ternary systems based on PC-CAC-C _s	155
A.5	Code used for the measurement of the degree of reaction of slag by SEM-IA	167

Contents

A.6 Code used for the modelling of the expansion	170
Bibliography	185
List of publications	187
Curriculum Vitae	189

List of Figures

2.1	Solubility curves of the CaO-Al ₂ O ₃ -H ₂ O system calculated at 5, 20 and 40 °C . . .	5
2.2	Areas composition for various applications in the CAC-C ₅ -PC system	6
2.3	Solubility diagrams of the CaO-Al ₂ O ₃ -SO ₃ -H ₂ O system at 50 °C	7
2.4	Hydration kinetics of ye'elimite with gypsum	9
2.5	Hydration kinetics of C ₃ A with gypsum	10
2.6	Hydration kinetics and slope values of quartz-Portland cement pastes with increasing replacement level of quartz	12
2.7	Thermodynamic simulation of a hydrated mixture of C ₃ A, portlandite, sulfate and carbonate	12
2.8	Crystallization experiments done by Taber	17
2.9	Pore model 1: Crystal growing in a cylindrical pore	20
2.10	Pore model 2: Crystal growing in a spherical pore with small pore entries	20
2.11	Pore model 3: Crystal growing in a cylindrical pore with small pore entries	21
3.1	Particle size distribution of the anhydrous powders	29
3.2	Secondary electron images of anhydrous powders	29
3.3	Backscattered electron images of anhydrous CAC	30
3.4	Algorithm used to quantify the degree of reaction of slag by SEM-IA	35
3.5	Pore diameters classification and terminology used in concrete science	38
3.6	Methods used to characterize the pore structure	39
3.7	Example of MIP cumulative and derivative curves.	40
4.1	Ternary diagram showing the studied compositions	44
4.2	Hydration kinetics of the systems with variable calcium sulfate content and variable substitution levels	46
4.3	Hydration kinetics of the systems with variable calcium sulfate content without any substitution	47
4.4	X-Ray diffractograms of the low calcium sulfate system at early ages	47
4.5	In-situ XRD analyses of the low calcium sulfate system	49
4.6	Pore solution analyses of the low calcium sulfate system	50
4.7	In-situ XRD of the low calcium sulfate system with 40 wt.% of slag	52
4.8	In-situ XRD and pore solution analyses of the high calcium sulfate system	53
4.9	Concentration of the pore solution as a function of calcium sulfate	54

List of Figures

4.10	Labelling of the main calorimetric peaks	55
4.11	TGA and DTG analyses of the low and high calcium sulfate system at early ages	56
4.12	Microstructure of the low and high calcium sulfate systems during the first 4 hours of hydration	57
4.13	Microstructure of the low and high calcium sulfate systems between 9 to 12 hours of hydration	58
4.14	Adsorption of sulfate on aluminium hydroxide gel	59
4.15	EDS analyses at early ages	60
4.16	Speed of reaction and cumulative heat as a function of the substitution level . .	62
4.17	Hydration kinetics with variable water to binder ratio and substitution	62
4.18	Concentration of the pore solution as a function of the substitution level	63
4.19	Saturation index of the main phases as a function of the substitution level . . .	64
4.20	Illustration of the hydration kinetics of CAC with hemihydrate	65
5.1	Ternary diagram showing the studied compositions	68
5.2	Compressive strength of low and high calcium sulfate mortars blended with quartz or limestone	70
5.3	Compressive strength as a function of limestone substitution for variable calcium sulfate amounts	70
5.4	Heat flow and cumulative heat measurements of the low and high sulfate systems blended with limestone	71
5.5	TGA and DTG curves at various ages for the low calcium sulfate system	72
5.6	XRD Rietveld analyses of limestone systems	74
5.7	XRD Rietveld analyses of limestone systems	75
5.8	Degree of hydration of CAC for the different systems	76
5.9	Thermodynamic simulation of stable phase volumes of CA-HH-C \bar{c} systems . .	77
5.10	Degree of reaction of limestone as a function of calcium sulfate	78
5.11	Thermodynamic simulation of stable phase assemblages as a function of the fraction of reacted limestone	79
5.12	Comparison between XRD and thermodynamic simulation	80
5.13	Porosity as a function of calcium sulfate of systems with and without limestone	81
5.14	Compressive strength as a function of the total porosity	81
5.15	Microstructures of limestone samples at 28 days	82
5.16	SEM-EDS analyses of limestone samples at 28 days	83
5.17	Compressive strength of low and of high calcium sulfate mortars blended with quartz or slag	85
5.18	Heat flow and cumulative heat measurements of the low and high sulfate systems blended with slag	86
5.19	TGA and DTG curves at various ages for slag systems	87
5.20	XRD diffractograms of the low calcium sulfate system without and with slag . .	88
5.21	XRD diffractograms of the medium calcium sulfate system without and with slag	89
5.22	XRD diffractograms of the high calcium sulfate system without and with slag .	90

5.23	Phase assemblage of slag systems after 2 years of hydration	91
5.24	Microstructures of slag samples at 2 years of hydration	93
5.25	SEM-EDS analyses of slag samples after 2 years of hydration	94
5.26	Degree of reaction of slag quantified with SEM-BSE-IA coupled with EDS analyses	94
5.27	Thermodynamic simulation of stable phase volumes of CA-HH-S systems . . .	95
5.28	Thermodynamic simulation of stable phase assemblages as a function of the degree of reaction of slag	96
5.29	Comparison between XRD and thermodynamic simulation	97
5.30	pH evolution of the curing water for 28 days	98
6.1	Expansion of CAC systems	103
6.2	Expansion of CSA systems	104
6.3	Deterioration of CAC and CSA systems cured under water	104
6.4	Expansion as a function of gypsum content at 28 days	105
6.5	Hydration kinetics of CAC and CSA systems	106
6.6	XRD of CAC and CSA systems	107
6.7	DTG curves at 1 and 14 days of low and high expansion systems	108
6.8	Microstructures of low and high expansion systems	109
6.9	Cumulative porosity from MIP	110
6.10	Ion concentration as a function of gypsum content	111
6.11	Thermodynamic simulation of stable aqueous solution	112
6.12	Thermodynamic simulation of stable hydrates	113
6.13	Ettringite saturation index as a function of gypsum content	114
6.14	Crystallization pressure as a function of the pore radius	115
6.15	Volume of measured percolated porosity and confined ettringite range needed to cause cracking	117
6.16	Effect of supersaturation on the pore size access	119
6.17	Crystallization pressure as a function of the pore entry radius	120
6.18	Model microstructure generated from MIP measurement with stress fields . . .	121
6.19	Modelling of expansion as a function of ettringite SI: effect of thin layer of solu- tion around the crystal	122
6.20	Modelling of expansion as a function of ettringite SI: effect of the pore size . . .	123
6.21	Modelling of expansion as a function of ettringite SI: effect of the porosity and pore model	124
6.22	Modelling of expansion as a function of ettringite SI: comparison between ex- periments and modelling	125
6.23	Expansion, MIP and ettringite SI of different calcium sulfate systems with vari- able water to binder ratios	127
6.24	XRD quantification of the main phases for high expansive systems with variable water to binder ratios	128
6.25	Modelling of expansion as a function of ettringite SI: effect of the water to binder ratio	129

List of Figures

6.26	Expansion, MIP and ettringite SI of different calcium sulfate systems without and with substitution	130
6.27	XRD quantification of the main phases for high expansive systems without and with limestone	131
6.28	Modelling of expansion as a function of ettringite SI: effect of the substitution .	132
6.29	Comparison between MIP and H NMR measurements	133
6.30	Expansion of variable calcium sulfate systems at 20 and 38°C	134
6.31	Effect of the temperature on the solubility of ettringite and on the crystallization pressure	134
6.32	Hydration kinetics and expansion of the high calcium sulfate systems with variable NaOH concentrations	135
6.33	Comparison between the phase assemblage predicted by thermodynamic simulation and measures with XRD	136
6.34	Comparison between the expansion and the phase evolution of variable calcium sulfate systems without and with limestone substitution	137
7.1	Comparison between the hydration kinetics of low and high calcium sulfate systems	140
7.2	Phase content for variable water to binder ratios	140
7.3	Expansion as a function of calcium sulfate: comparison of different compositions	141
7.4	Effect of supersaturation on the pore size access	142
A.1	Influence of the temperature and of the pH on ettringite solubility	146
A.2	Crystal structure of ettringite	147
A.3	Example of synthesized ettringite crystals	147
A.4	Effect of relative humidity and temperature on the dehydration of ettringite . .	148
A.5	Example of AFm hexagonal platelets: monosulfoaluminate and monocarboaluminate	149
A.7	Monosulfoaluminate and hydroxy-AFm solid solution	149
A.6	Structure of a single principal layer representing an AFm phase	150
A.8	Thermodynamic stabilities of selected AFm phases at 25 °C	150
A.9	Volume changes of monosulfoaluminate with respect to changes in RH at 25 °C.	150
A.10	Solubility of gibbsite as a function of pH	151

List of Tables

2.1	Oxide composition of the CAC-C \bar{s} -Slag systems compared to SSC	15
3.1	XRF oxides composition of the components used for the study of the hydration	28
3.2	XRD Rietveld analyses of the components used for the study of the hydration .	28
3.3	Phases and references used for quantitative Rietveld analyses	33
3.4	DTG main dehydration peaks positions	34
4.1	Studied compositions for the early age reactions	44
4.2	Enthalpies of dissolution reactions	48
5.1	Studied compositions for the limestone reaction	69
5.2	Studied compositions for the slag reaction	69
6.1	Oxides composition of CAC and CSA cements used for the study of the expansion	101
6.2	Mineralogical composition of the cements used for the study of the expansion	101
6.3	CAC and CSA systems for the expansion study	102
6.4	Phase content by XRD Rietveld and by TGA at 14 days	103
6.5	Pore size and total porosity measured by MIP on 1 day samples	106
6.6	Pore radii, fraction of percolated porosity, tensile strength and averaged crystallization pressure	115
A.1	Main hydrates chemical formula, density and phase structure	145

Glossary

Cement shorthand notation for oxides compounds:

C: CaO A: Al₂O₃ \bar{s} : SO₃ \bar{c} : CO₂ S: SiO₂ F: Fe₂O₃ T: TiO₂ M: MgO H: H₂O

Abbreviations for the main anhydrous and hydrated phases:

CA	CaO.Al ₂ O ₃	Monocalcium aluminate
C \bar{s} H _{0.5}	CaSO ₄ .0.5H ₂ O	Hemihydrate
C \bar{s} H ₂	CaSO ₄ .2H ₂ O	Gypsum
C \bar{c}	CaCO ₃	Calcite
C ₃ A.3C \bar{s} .H ₃₂	[Ca ₃ (Al)(OH) ₆ · 12H ₂ O] ₂ · (SO ₄) ₃ · 2H ₂ O	Ettringite (Ett)
C ₃ A.C \bar{s} .H ₁₂	[Ca ₂ (Al)(OH) ₆] ₂ · SO ₄ · 6H ₂ O	Monosulfoaluminate (Ms)
C ₃ A.C \bar{c} _{0.5} .H ₁₂	4CaO.Al ₂ O ₃ .0.5CO ₂ .12H ₂ O	Hemicarboaluminate (Hc)
C ₃ A.C \bar{c} .H ₁₁	4CaO.Al ₂ O ₃ .CO ₂ .11H ₂ O	Monocarboaluminate (Mc)
C ₂ ASH ₈	2CaO.Al ₂ O ₃ .SiO ₂ .8H ₂ O	Strätlingite
AH ₃	2Al(OH) ₃	Microcrystalline aluminium hydroxide
C ₃ AH ₆	3CaO.Al ₂ O ₃ .6H ₂ O	Hydrogarnet

Materials:

CAC	Calcium aluminate cement
CSA	Calcium sulfoaluminate cement
HH	Hemihydrate
G	Gypsum
SCM	Supplementary Cementitious Materials
S	Slag
C \bar{c}	Limestone
PC	Portland cement

Glossary

Techniques:

XRD	X-Ray Diffraction
XRF	X-Ray Fluorescence
TGA	Thermogravimetric Analysis
SEM	Scanning Electron Microscopy
BSE	BackScattered Electron
EDS	Energy Dispersive x-ray Spectroscopy
MIP	Mercury Intrusion Porosimetry
NMR	Nuclear Magnetic Resonance
PSA	Pore Solution Analyses
TS	Thermodynamic Simulation

Other abbreviations:

w/b	Water to binder ratio
wt.%	Weight percent
mol.%	Molar percent

1 Introduction

Since the 1990s, trends in the Portland cement industry changed under the pressure of environmental considerations. Concrete based on Portland cement is the most widely used material in the world and its massive production* is responsible for approximately 5 to 8% of the global manmade CO₂ emissions [3]. These emissions are due to energy consumption during the manufacturing process, but mostly to the decarbonation of limestone occurring in the burning of the raw materials. Reducing the clinker in cement by substituting supplementary cementitious materials (SCM) has environmental and economic benefits. SCM can be inorganic minerals coming from industrial waste such as slag, fly ash and silica fume, or raw materials such as limestone.

The same considerations are valid for calcium aluminate cements (CAC) despite the smaller scale of production compared to Portland. CAC are used for refractory concrete, sewage protection lining and mainly in dry mix mortars for the building chemistry industry. The main applications of building chemistry products are: specialist mortars for fixing, tile adhesives, fast repairs, and self levelling compounds. These alternative cements also have useful properties when developing formulated binders with tailored behaviour, for example with fast setting and hardening, or shrinkage compensation. These binders are usually composed of CAC, calcium sulfate and Portland cement. Portland cements with high substitutions are increasingly common in these ternary binders, and the reaction of these SCM with calcium aluminate and calcium sulfate need to be further investigated.

This thesis focuses on the study of such products dominated by CAC and calcium sulfate where plain Portland is wholly substituted by SCM, namely limestone and slag. These products with SCM are new and little research has been done on this. The study of the hydration and of the dimensional stability of these systems is crucial for their development in the market.

* Between 2000 to 2013 the annual cement production rose from $1.5 \cdot 10^9$ tons to $4 \cdot 10^9$ tons in the world [1], which corresponds approximately to an increase of concrete production from $9 \cdot 10^9$ tons to $24 \cdot 10^9$ tons. To give an idea, the annual steel production in 2013 was about $1.6 \cdot 10^9$ tons [2].

Chapter 1. Introduction

There are studies on ternary systems composed of calcium aluminate cement with calcium sulfate and Portland cement [4, 5, 6], on binary systems composed of calcium aluminate cement with slag or limestone [7, 8, 9, 10] and calcium aluminate cement with calcium sulfate [11, 12]. These studies give a baseline for the understanding of the hydration reaction and properties development of ternary systems with SCM. The mechanisms of expansion related to ettringite formation are not well defined and are unclear in the literature. A systematic study of the factors influencing the expansion is presented in this thesis and a simplified model is suggested to describe the main parameters controlling the expansion.

The main objectives of the thesis are:

Study of the early hydration (<24 hours) of the rapid CAC-calcium sulfate binder without and with SCM (Chapter 4). The early age reactions were followed by isothermal calorimetry, in-situ XRD quantitative analyses and pore solution analyses. The kinetics, the phase assemblage and pore solutions combined with thermodynamic modelling were used to understand the effects of calcium sulfate and of SCM on the calcium aluminate hydration.

Study of the long term hydration Understanding the effects of the CAC-calcium sulfate composition on the reaction of limestone and slag (chemical effect of SCM, Chapter 5). Mechanical tests on mortars combined with XRD analyses were used to identify the chemical interactions between the binder and SCM. Thermodynamic simulation was compared to experimental results to understand the effect of calcium sulfate on the reaction of SCM. The degree of reaction of limestone was measured by XRD quantitative analyses while the degree of reaction of slag was measured by SEM image analyses. Experimental observations were in good agreement with the thermodynamic prediction. Finally, the microstructure and porosity were linked to compressive strengths.

Study the dimensional stability Understanding the mechanisms and the factors affecting the expansion which is generated to compensate the shrinkage (Chapter 6). Expansion measurements on paste samples cured under water were used to identify low and high expansive systems. Then, the hydration kinetics, the phase assemblage and the microstructure of low and high expansive systems were compared. As no clear difference was observed, pore solution analyses were used to find the main difference between these two systems having different expansive properties. Pore solution analyses compared to thermodynamic modelling and combined with porosity characterization by MIP showed the links between expansion, porosity and chemical composition of the system. Finally, a finite element code was used to model the expansion in such systems.

2 Literature review

Contents

2.1 Calcium aluminate cement	3
2.1.1 Hydration of calcium aluminate cement	4
2.2 Calcium aluminate cement with calcium sulfate	6
2.2.1 Calcium sulfoaluminate cement with calcium sulfate	8
2.2.2 Tricalcium aluminate with calcium sulfate	8
2.3 Calcium aluminate cement with supplementary cementitious materials . .	11
2.3.1 Filler effect at early ages	11
2.3.2 Long term hydration of calcium aluminate cement with limestone . .	11
2.3.3 Long term hydration of calcium aluminate cement with slag	13
2.4 Dimensional stability and expansion mechanisms	16
2.4.1 Expansion associated with ettringite formation	16
2.4.2 Crystallization in restrained conditions	17
2.4.3 Crystallization in porous media	19
2.4.4 Salt supersaturation: the case of ettringite	22
2.4.5 Factors affecting the expansion	24
2.5 Characterization of the confinement	25

2.1 Calcium aluminate cement

Calcium aluminate cements were born in 1888 with the first patent for a limestone-bauxite cement. The industrial development of these cements is mainly due to the work of Bied in the Lafarge laboratories. In 1908, another patent was created on a manufacturing process in which bauxite, or other aluminous and ferruginous materials having a low silica content, were fused with limestone. It took several years to bring this manufacturing process to an industrial scale and Lafarge put CAC on the market in 1918 under the name of *Ciment Fondu Lafarge*.

Chapter 2. Literature review

The first uses of this cement were during the World War I for constructions requiring a rapid hardening of the material and good sulfate resistance [12].

The two raw materials (limestone and bauxite or alumina) are ground and/or homogenised, then they are fused or sintered (depending on the Al_2O_3 content) at temperatures above 1450°C . The clinker obtained is ground into a fine powder. The annual production of calcium aluminate cements is very small, approximately 2 million tons per year, compared to Portland cement, 4 giga tons per year [1]. It is also more expensive than Portland cement (6-8 times more expensive) due to the high alumina content ($> 40 \text{ wt}\%$) and application in niche markets. The main properties are good refractory performance, high early strength (compressive strength of $\sim 50 \text{ MPa}$ at 24 hours), good chemical resistance to sulfates and acids, resistance to abrasion and mechanical shock. The properties of calcium aluminate cements and their higher cost compared to Portland cements make them suitable for specialist applications such as: refractory concretes, concretes for aggressive environments, rapid repair concretes and dry mix mortars. A big part of the CAC market worldwide is dedicated to dry mix mortars used for building chemistry applications. These products are used in rapid repair mortars, tile adhesives and flooring applications with self levelling compounds.

2.1.1 Hydration of calcium aluminate cement

The hydration of calcium aluminate cement is driven by a dissolution and precipitation process. Anhydrous phases in contact with water dissolve to give ions in solution. For example, the main phase of calcium aluminate cement, monocalcium aluminate (CA), in water leads to the formation of Ca^{2+} and $\text{Al}(\text{OH})_4^-$ ions. The precipitation and growth of the hydrates takes place through solution. When supersaturation is reached, calcium and aluminium ions can combine in variable ratios to precipitate different hydrates as a function of the time and temperature. The main hydrates in calcium aluminate cements are CAH_{10} , C_2AH_8 , C_3AH_6 and AH_3 . The latter phase is called aluminium hydroxide, it may be amorphous or microcrystalline, or crystallise as gibbsite, bayerite or nordstrandite. The rate of reaction only slows down when one of the reactants (cement or water) is consumed or when there is a lack of free space allowing the precipitation of the hydrates. This phenomenon causes the setting of cement paste, mortar or concrete.

The first phase forming is linked to the evolution of the concentrations in solution as described by the solubility curves of the $\text{CaO-Al}_2\text{O}_3\text{-H}_2\text{O}$ system at different temperatures (figure 2.1). The solubility of CAH_{10} (1) increases with the temperature. Therefore, as the anhydrous monocalcium aluminate dissolves in water, the concentration of Ca^{2+} and $\text{Al}(\text{OH})_4^-$ in the solution increase and CAH_{10} becomes highly supersaturated at 5°C . When the temperature increases to 40°C , the solution becomes rapidly supersaturated with respect to C_3AH_6 . This shows the effect of the temperature on the type of hydrate forming. Complete reaction can be assumed on the long term and the most stable phases should precipitate. The precipitation of the different phases occurs in order to minimize the energy in the system, thus thermody-

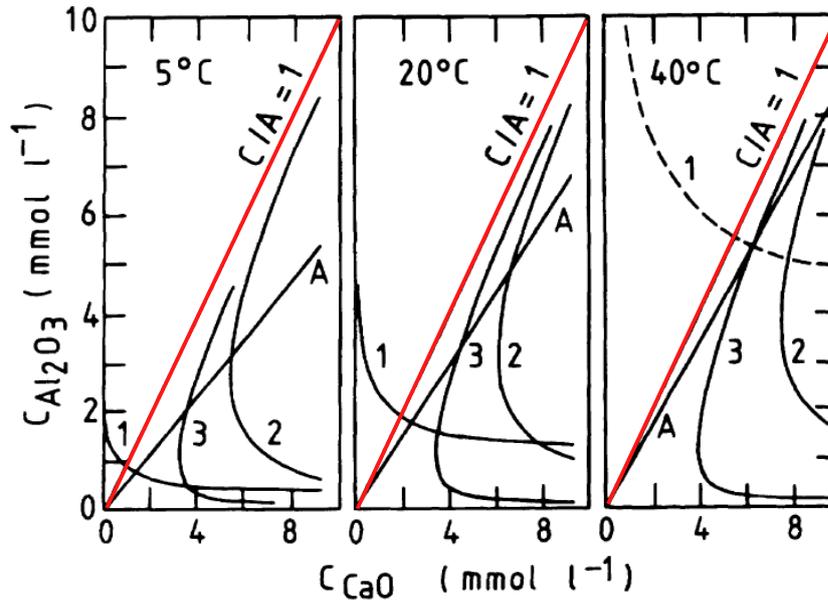


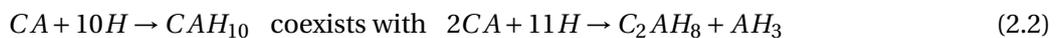
Figure 2.1: Solubility curves of the CaO-Al₂O₃-H₂O system calculated at 5, 20 and 40 °C. (A) poorly crystalline AH₃, (1) CAH₁₀, (2) C₂AH₈ and (3) C₃AH₆. Adapted from Capmas and [13].

namic calculations can be used to predict phase assemblages at equilibrium conditions (see section 3.2.11).

In real conditions there are nucleation barriers and kinetics effects, therefore it is possible that CAH₁₀ forms even at 20°C, because of the presence of some impurities (acting as nucleation sites) allowing the growth. This metastable phase is of higher energy than the stable one, so the driving forces for formation of the stable phase can generate a conversion of the metastable phases depending on the time and the temperature [14]. The hydration of monocalcium aluminate below 15°C leads to the formation of metastable CAH₁₀



whereas at temperatures between 15 to 27°C, the two metastable hydrates CAH₁₀ and C₂AH₈ coexist



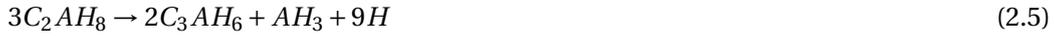
Between 27 to 50°C there is only formation of metastable C₂AH₈ and above 50°C there is formation of stable hydrogarnet C₃AH₆



The conversion reactions describing the two steps that occur with time are



from metastable to metastable hydrates and after



from metastable to stable hydrogarnet. When reactions 2.4 and 2.5 occur, usually under warm and wet conditions, there is conversion of hexagonal metastable hydrates into stable cubic hydrogarnet hydrate. The stable cubic hydrate has a higher density than CAH_{10} and C_2AH_8 which leads to an increase of the porosity [9]. The increase in porosity and its impact on the properties (strength and durability) has to be taken into account for the material design. A misunderstanding of the conversion reaction and a non anticipation of its impact led to some damage in the past [12, 15]. This conversion reaction can be accelerated by curing at high temperatures ($>50^\circ C$). Its impact can also be reduced with the addition of supplementary cementitious materials such as slag or limestone which modify the hydrates assemblage.

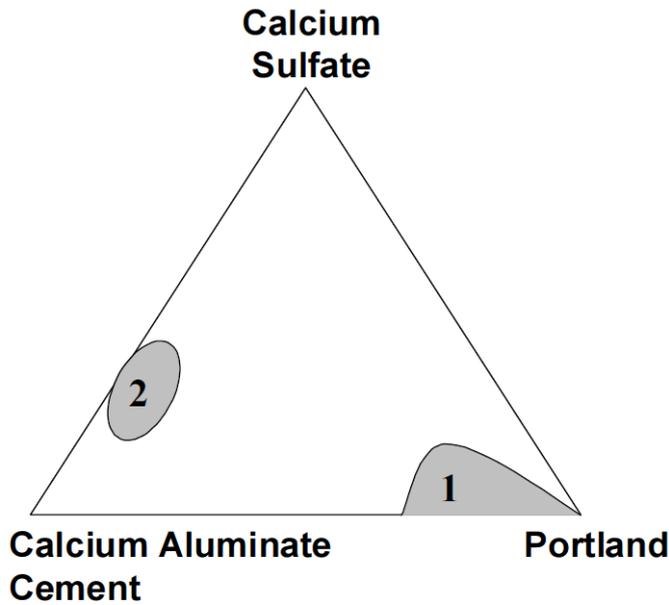


Figure 2.2: Areas composition for various applications in the CAC-Cs-PC system. From [4].

2.2 Calcium aluminate cement with calcium sulfate

One of the main markets of calcium aluminate cements is the building chemistry market as discussed in the previous section. Calcium aluminate cements are usually blended with Portland cement, calcium sulfate and special additives as shown in the zone 1 of figure 2.2 and are used to produce specialist mortars for fixing, tile adhesives and fast repairs. This thesis focuses on CAC rich systems as shown in zone 2; these formulated binders with tailored

2.2. Calcium aluminate cement with calcium sulfate

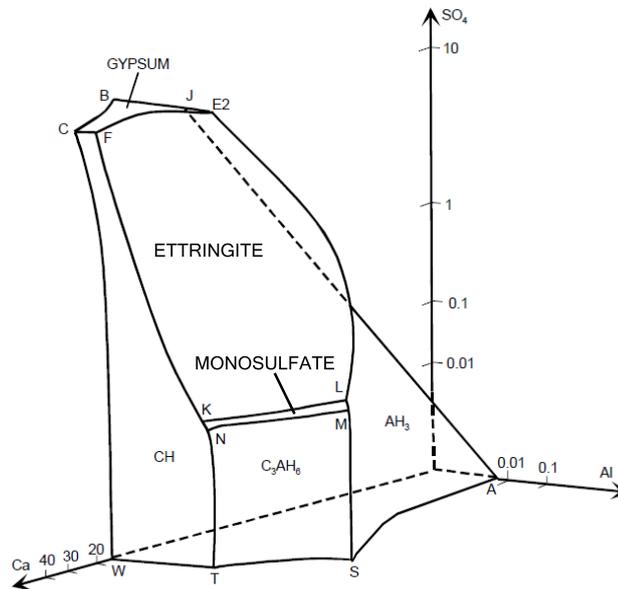
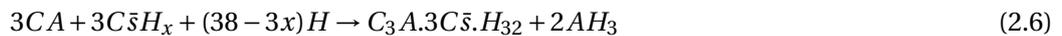


Figure 2.3: Solubility diagrams of the CaO-Al₂O₃-SO₃-H₂O system at 50 °C showing crystallization surfaces. The concentrations are given in mmol/L. From [16].

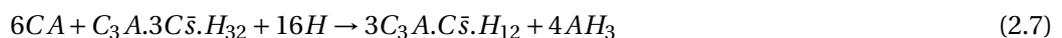
behaviour require special properties such as very fast setting and hardening, self drying capacity, and size variation control. These kind of products are used for floor levelling, tile adhesives and rapid repair mortars. The minor component Portland cement can be replaced by supplementary cementitious materials such as slag, limestone, fly ash, metakaolin and silica fume. In the following sections are presented the hydration of calcium aluminate with calcium sulfate and the reactions with the selected supplementary cementitious materials; limestone and slag.

When calcium sulfate is added to the CaO-Al₂O₃-H₂O system, new hydrates appear as in figure 2.3 and the hydrates susceptible to conversion are not formed anymore. The reactions leading to the formation of the main hydrates presented in this diagram are described here below and the characteristic properties of these hydrates are presented in appendix A.1.

The reaction of monocalcium aluminate and calcium sulfate leads to the formation of ettringite and amorphous aluminium hydroxide



where $x=0$ for anhydrite, $x=0.5$ for hemihydrate and $x=2$ for gypsum. If the amount of calcium sulfate is less than that needed for all the CA to react according to reaction 2.6, calcium monosulfoaluminate will form after the depletion of calcium sulfate [17]

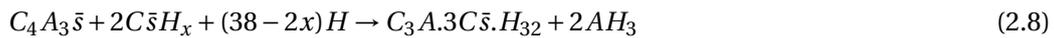


2.2.1 Calcium sulfoaluminate cement with calcium sulfate

Systems composed of CAC with calcium sulfate are chemically comparable to calcium sulfoaluminate cement (CSA) blended with calcium sulfate. The two systems are compared in chapter 6 dedicated to the study of the dimensional stability.

The modern development of the calcium sulfoaluminate cement (CSA) started in the 1970's in China. This cement is made of limestone, bauxite and calcium sulfate. The raw materials are ground, homogenized and after burned at 1350°C in a rotary kiln, like for Portland cement. The clinker is then ground with addition of calcium sulfate. The first addition of calcium sulfate allows the formation of the main phase ye'elinite ($C_4A_3\bar{s}$) with the reaction between the three raw materials and the second addition introduces gypsum and/or anhydrite into the final grinding process. This cement is commonly used for similar applications than CAC-calcium sulfate based binders.

The hydration of ye'elinite with calcium sulfate leads to the formation of ettringite and aluminium hydroxide



and when calcium sulfate is depleted there is formation of calcium monosulfoaluminate



These reactions clearly show that CAC or CSA blended with calcium sulfate lead to the formation of the same hydrates, nevertheless the kinetics can differ.

The effect of calcium sulfate on systems composed of ye'elinite was studied by Winnefeld and Barlag [18]. The kinetics are influenced by the amount of sulfate, the first peak is accelerated compared to pure ye'elinite and the second peak is related to the amount of gypsum as shown in figure 2.4. The intensity of the second peak decreases with the amount of gypsum. The origin of this peak and on the effect of sulfate on dissolution of the aluminate phase are discussed in the following section with analogies to another system based on C_3A and calcium sulfate.

2.2.2 Tricalcium aluminate with calcium sulfate

The literature on the first hours of hydration of monocalcium aluminate, the main phase of calcium aluminate cement, with calcium sulfate is quite scarce. Nevertheless, it is useful to consider similar systems composed of tricalcium aluminate (C_3A , phase being important in Portland cement) and calcium sulfate.

The hydration of tricalcium aluminate with calcium sulfate leads to the following reaction



2.2. Calcium aluminate cement with calcium sulfate

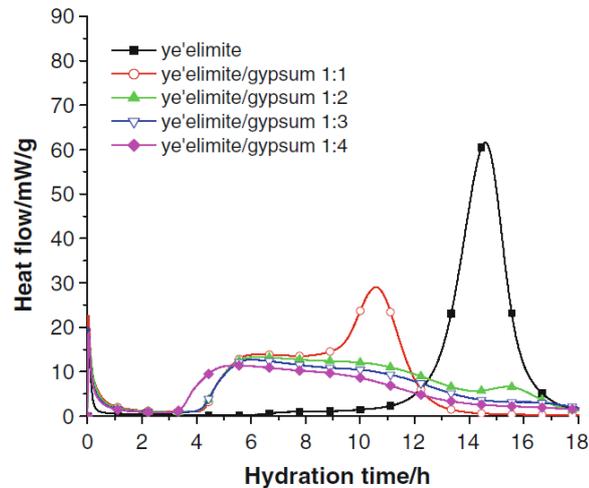


Figure 2.4: Isothermal calorimetry curves of ye'elimite with different molar amounts of gypsum. From [18].

where $x=0$ for anhydrite, $x=0.5$ for hemihydrate and $x=2$ for gypsum.

This reaction differs from reaction 2.6 as no aluminium hydroxide forms.

The hydration of tricalcium aluminate with gypsum can be divided in two main stages as shown by figure 2.5 [19]:

1. The first hours of hydration are characterized by the hydration of C_3A with gypsum leading to the formation of ettringite. The C_3A reaction is slowed down as long as there is solid gypsum. The mechanisms controlling C_3A dissolution are discussed below. During this stage, the reaction rate is controlled by tricalcium aluminate dissolution [20, 21, 22] and is not influenced by the amount of gypsum.
2. After gypsum depletion, extra C_3A reacts with ettringite leading to monosulfoaluminate formation. The acceleration period of this second peak is linked to the nucleation of AFm phases and the kinetics are controlled by the exposed surface area of C_3A particles. The deceleration period where AFm phases grow is controlled by space filling.

The amount of calcium sulfate does not influence the first stage of the hydration of C_3A but has an important role in the second stage of the hydration as shown in figure 2.5. The peak is delayed as the amount of calcium sulfate increases because the slow reaction between C_3A and gypsum takes more time to consume all the sulfate. After this peak follows a slow process where monosulfoaluminate forms [22]. The broadening of the calorimetric peak is observed also with the increase of gypsum content in cement pastes but it was not observed in diluted suspensions [22]. This suggests that the deceleration period of the peak is controlled by space filling [19] and therefore the water to binder ratio has an influence on it [23]. The peak intensity is related to the exposed surface area as it influences strongly the nucleation [19].

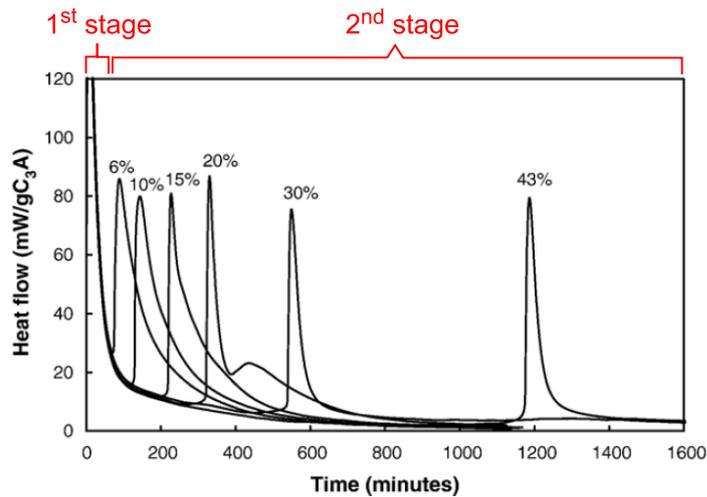


Figure 2.5: Isothermal calorimetry curves showing the stages of C₃A hydration in saturated lime solutions with increasing amounts of gypsum. Adapted from [22].

The mechanisms controlling C₃A dissolution have been widely discussed in the literature and two main hypotheses are proposed:

- During the first steps of the reaction, hydration products form around anhydrous C₃A grains forming a more or less permeable layer that reduces the anhydrous phase dissolution. The hydrates could be either ettringite [20], AFm platelets together with ettringite [24], amorphous aluminium hydroxide [25] or a mixture of more hydrates.
- The adsorption of sulfates on the active sites of C₃A are responsible for its low dissolution rate [26].

The first hypothesis seems not to be the cause of low C₃A dissolution as the dissolution rate would be linked to the amount of hydrates formed, which is not the case. Moreover, the dissolution rate would not increase abruptly after sulfate depletion if there was a semi-permeable membrane on C₃A grains [22]. It was also mentioned that the morphology of the hydrates formed around C₃A is unlikely to act as a barrier against ion transport [27]. Therefore, the most plausible mechanism slowing down the reaction of C₃A is the adsorption of sulfate ions on the anhydrous grains [26]. However, it was reported that other sources of sulfates such as Na₂SO₄ do not influence C₃A hydration [20]. Other studies [28, 22] showed that both calcium and sulfate ions of gypsum are responsible for the slowing down of C₃A hydration. Calcium ions are chemisorbed on C₃A grains leading to positively charged surfaces that are able to adsorb negatively charged sulfates. The dissolution of C₃A is then reduced due to ion adsorption on active dissolution sites. Other sources of positively charged ions such as CaCl₂ or NaCl solutions are not affecting C₃A dissolution.

2.3 Calcium aluminate cement with supplementary cementitious materials

The replacement of a certain fraction of cement with supplementary cementitious materials (SCM) has two important advantages; the reduction of a material which is CO₂ intensive [3] and the reduction of the costs of the product due to the use of limestone, which is a low cost and a low environmental impact material, or due to the use of industrial by-products such as slag which is usually considered as waste.

2.3.1 Filler effect at early ages

Calcium aluminate cement with calcium sulfate systems need to develop rapid strength but SCM are known to have low hydraulic properties and to have negligible reaction during the first days. They act as inert fillers and have mainly a physical effect called filler effect which was extensively studied in Portland cement systems. This leads to an increase of the reactivity of the clinker and higher degree of hydration at early ages because of [29, 30, 31, 32]:

- More available space or water for hydrate growth. When adding 20% of filler at constant water to solid ratio, the water to reactive binder ratio increases from 0.4 to 0.5.
- Enhanced nucleation, specially for fine powders. The additional surfaces act as nucleation sites for hydrates.

The amount of filler has an effect on the kinetics as shown in figure 2.6a where the slope of the first peak (acceleration period) increases with the substitution and the deceleration period is extended. The fineness of the SCM has also a direct effect on the kinetics of the cement hydration as shown in figure 2.6b, the slope of the acceleration period increases with the fineness and amount of filler. The filler should have finer particles than the clinker or cement to accelerate the kinetics of the reaction [33]. The nature of the filler can modify the kinetics as they are related to the affinity between the SCM and the hydrates. Recent studies showed that the accelerated kinetics and reaction rates are linked to the reduced inter-particle distance obtained when filler particles, finer than PC, are in the system. The shear rate increases as the inter-particle distance decreases, thus more nuclei are created [34]. The late reaction and the chemical contribution of limestone or slag are very important for the final properties of the material.

2.3.2 Long term hydration of calcium aluminate cement with limestone

The literature on the topic is scarce for blends of CAC-C_s and limestone. Studies were done on CAC cements blended with limestone to reduce and/or avoid the conversion reaction. The addition of calcium carbonate to the aluminous cement leads to the formation of stable monocarboaluminate [35, 36] instead of metastable phases. More recent studies done by

Chapter 2. Literature review

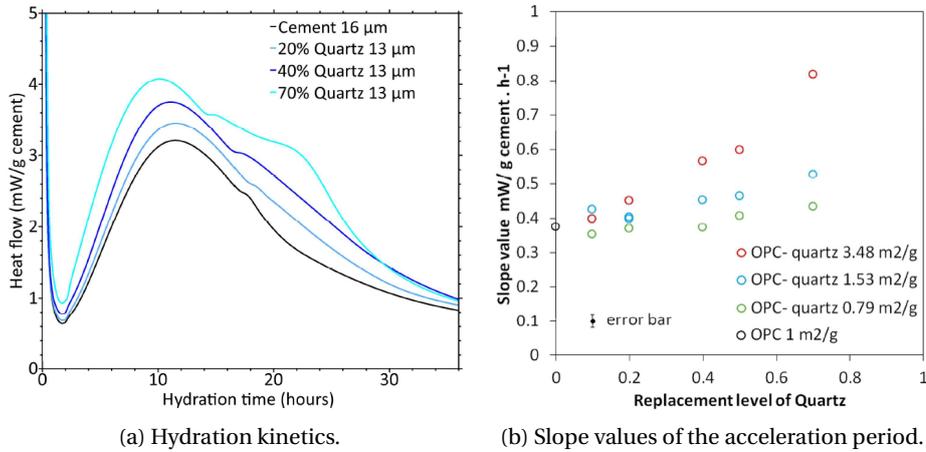


Figure 2.6: Hydration kinetics and slope values of quartz-Portland cement pastes with increasing replacement level of quartz. From [34].

Pelletier-Chaignat et al. [37] on systems containing calcium sulfate, CSA and limestone or quartz filler indicate that limestone gives higher strengths compared to quartz. Hemicarboaluminate and monocarboaluminate are formed and there is less monosulfoaluminate. The impact of calcium sulfate on the limestone reaction was not discussed. Ohba et al. [38] indicated that the amount of reacted limestone decreases with the calcium sulfate content in mixtures of calcium aluminate, anhydrite and limestone.

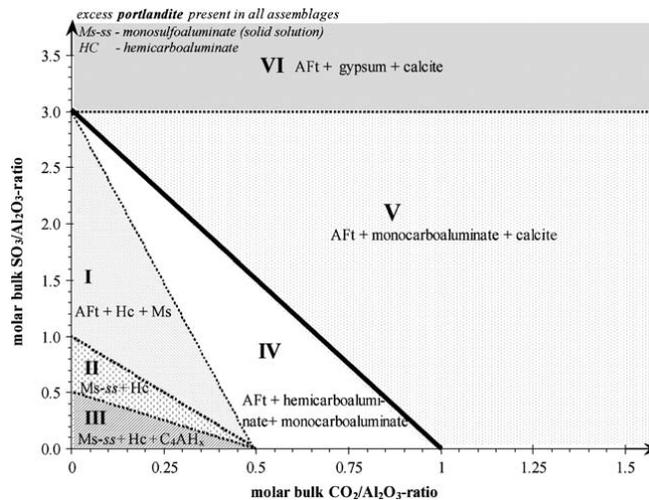


Figure 2.7: Phase assemblage from thermodynamic simulation of a hydrated mixture of C₃A, portlandite and varying initial sulfate and carbonate amounts. From [39].

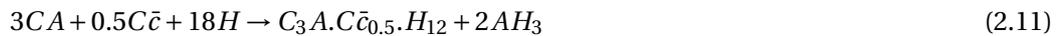
2.3. Calcium aluminate cement with supplementary cementitious materials

Limestone addition in cement has been widely studied in PC based systems [34, 39, 40, 41, 42]. These studies indicate that:

- At early ages of hydration, limestone has a larger accelerating effect compared to other SCM. The increased C-S-H nucleation on limestone surfaces accelerates the kinetics [34].
- Calcite reacts with aluminate phases forming the AFm phases monocarboaluminate and hemicarboaluminate. Consequently, the addition of calcite reduces ettringite consumption due to monosulfoaluminate formation when sulfate is depleted.
- The formation of carboaluminate can increase the volume of hydrates, decrease the porosity and, as a consequence, can increase the strength at modest levels of addition.
- The amount of calcite which can react is limited by the aluminate content in the system. Above this amount, calcite acts as inert filler.

Figure 2.7 shows the phase assemblage of a hydrated mixture of C_3A and portlandite with various sulfate and carbonate amounts. This scenario describes what should form in a PC based system containing portlandite and C_3A being the source of aluminate. The figure clearly shows that above a sulfate to aluminate ratio of 3, calcite does not react (is a filler) and that for low sulfate and carbonate levels there is formation of monosulfoaluminate. The main difference between PC and CAC-C \bar{s} based systems is that the latter clearly contains much higher quantities of aluminate so there is the potential for much higher amounts of calcite to react and contribute to strength development.

When limestone is added to the CAC-C \bar{s} system, the formation of hemicarboaluminate (reaction 2.11) and/or monocarboaluminate (reaction 2.12) is thermodynamically more favourable compared to the formation of monosulfoaluminate (reaction 2.7), which is not stable anymore. This results in an increase of the amount of ettringite and a decrease of the porosity [43].



2.3.3 Long term hydration of calcium aluminate cement with slag

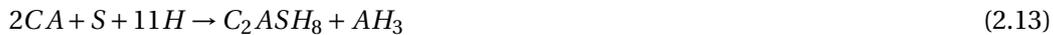
Slag is an industrial by-product coming from the steel manufacture. It is produced from the fusion of fluxing stone (limestone or dolomite) with gangue (siliceous and aluminous materials), which are residues from the iron ore. The oxides present in slag are mainly lime, silica and alumina with small amounts of magnesia, sulfur, iron and other minor elements. The green colour of the blended cements with slag comes from the sulfur. There are two

Chapter 2. Literature review

main types of slag resulting from different cooling regimes which confers varying properties depending on the solidification method. Air-cooled slag solidifies slowly and is almost all crystalline. The other one is granulated slag and is amorphous because of the rapid quenching; this product is used in cement industry and exhibits latent hydraulic properties[44].

Most of the studies done on CAC with slag do not contain calcium sulfate. These blends have been developed by the Building Research Establishment under the name of BRECEM in the 1990s to reduce or avoid the conversion reaction [9, 45]. CAC-slag hydration leads to the formation of stable strätlingite C_2ASH_8 instead of metastable CAH_{10} and C_2AH_8 , avoiding the conversion reaction.

Slag is a source of silica, therefore its addition modifies the phase assemblage of CAC-C \bar{s} systems. The silica contained in the slag leads to the following reaction



and when CA is not available anymore, the calcium from other minor phases or from slag dissolution consumes AH_3



Slag activation

The knowledge on slag reaction in PC and CAC systems is well known but scarce literature is available on CAC-C \bar{s} systems with slag. The late reaction of slag is strongly influenced by the pore solution of the cementitious matrix as the solubility of amorphous silica present in slags increases with pH between 12 and 14 [31, 46]. At high pH, dissolution of Si and Al ions is promoted because the silanol Si-O and aluminol Al-O bonds in the network structure of the glassy slag are broken [47]. High pH are obtained with $Ca(OH)_2$ or alkaline activators such as KOH, NaOH and $Na_2SO_4^*$. Other ionic species coming from the clinker dissolution influence strongly the dissolution of slag; $Al(OH)_4^-$ incorporation on the silica surface at high pH reduces or inhibits slag dissolution [46, 48] and an increase of Ca^{2+} concentration is followed by a reduction of silica dissolution at pH 13 [49]. Additions of calcium sulfate lead to a reduction of the ionic concentration of Ca^{2+} and $Al(OH)_4^-$ because they are consumed for the formation of ettringite [50].

In calcium aluminate cement, slag activation is enhanced by minor phases present in the CAC like the alkali metal hydroxides (Na^+ , K^+)[†] [8].

* Appendix A.3 explains how Na_2SO_4 leads to high pH.

† CAC has usually 0.1 to 0.2 wt.% of Na_2O and K_2O , in PC the values are between 1 to 2 wt.%

2.3. Calcium aluminate cement with supplementary cementitious materials

Analogies with other sulfate containing blends

The hydration of similar systems containing CAC, calcium sulfate and fly ash (FA, Class-F) is reported in [51]. As slag, siliceous fly ash should be activated with alkalis to break down the glassy phase in order to hydrate. The formed hydrates are ettringite, monosulfoaluminate, AH_3 , C_3AH_6 , C_2ASH_8 , C_4AH_x . The ettringite formation depends on the ratio between sulfate and aluminate. At early ages the silicate seem not to have relevant impact on the development of the hydrates.

There are other systems called supersulfated slag cements (SSC) which have calcium sulfate amounts comparable to CAC-C \bar{s} -slag systems. SSC are composed of 80-85% slag, 10-15% calcium sulfate and 5% PC. The main hydrates are ettringite, monosulfoaluminate and C-S-H [52]. Table 2.1 shows the oxide composition of the CAC-C \bar{s} -slag systems compared to the SSC. The main difference being the silica over alumina ratio, which is much higher for SCC. High contents of aluminium reduce slag dissolution as mentioned above and could explain potential differences between these two systems. Experiments on CAC-C \bar{s} -slag systems are therefore needed to understand the effect of the balance between sulfate and aluminate on slag reaction.

Table 2.1: Oxide composition of the CAC-C \bar{s} -Slag systems compared to SSC.

[wt%]	CAC-C \bar{s} -Slag	SSC
CaO	38-39	45
SiO ₂	15-16	27
Al ₂ O ₃	21-25	12
SO ₃	7-12	7
S/A	0.6-0.8	2.2
\bar{s} /A	0.3-0.6	0.6

2.4 Dimensional stability and expansion mechanisms

Cementitious materials undergo volumetric changes during their hydration. The porosity is initially saturated with water but when the hydration proceeds, self-desiccation occurs in conjunction with external evaporation. This leads to capillary stresses causing macroscopic shrinkage and possibly cracking [53, 54]. To overcome this, expansive cements which can compensate shrinkage are used. This section presents a brief review of the theories of expansion associated with ettringite formation followed by a review of the basics of crystallization of salts in porous materials. The last section presents the equations that are used in chapter 6 to relate the expansion to experimental data such as the measured saturation index of ettringite and the analysed porous media.

2.4.1 Expansion associated with ettringite formation

The expansive behaviour associated with ettringite formation in cement systems has been widely studied [55, 56, 57, 58, 59, 60] but the mechanisms of expansion are still not fully understood. Various mechanisms implicated in external sulfate attack of cementitious materials were reviewed by Brown and Taylor [61]. Most of their arguments have a general validity to systems in which expansion is related to ettringite formation: the main points are summarised here.

- A simple way to explain expansion is that the precipitation of ettringite leads to **an increase of solid volume** [62]. However, there is a lack of evidence to link expansion directly to the amount of ettringite [63, 64]. Furthermore, the formation of other hydrates, such as CAH_{10} , also gives an increase in solid volume, but their formation is not generally considered to be expansive.
- Mehta [57] linked expansion to **the adsorption of water by colloidal sized ettringite crystals**. However, he gave little theoretical support for this hypothesis. It is unlikely that crystalline ettringite would show gel-like swelling behaviour and such behaviour has never been reported for synthetic preparations of this phase. A crystalline structure cannot adsorb water molecules within the crystal lattice and therefore it cannot swell by water adsorption. Furthermore, he suggested that the “colloidal” ettringite formed only in the presence of lime or calcium hydroxide, whereas expansion also occurs when lime is absent, as in the present study. Other studies confirm that swelling is not the main cause of expansion [65, 66]
- Several authors [61, 67] have proposed that expansion is due to the **solid state formation of ettringite around the cement grains**. However, the totally different crystal structure of ettringite from any of its pre-cursors make such theories invalid.

These arguments leave the **theory of crystallization pressure** as the most plausible mechanism of expansion, which is presented in the next section.

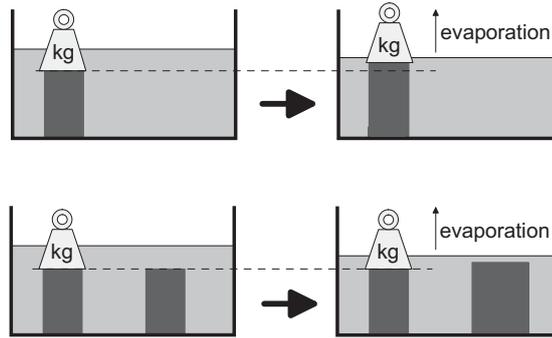


Figure 2.8: Crystallization experiments done by Taber. Upper experiment: one crystal in contact with a supersaturated solution grows under pressure. Lower experiment: when two crystals are in contact with a supersaturated solution, the crystal under pressure does not grow and the unloaded crystal grows to consume the supersaturation. From [71].

2.4.2 Crystallization in restrained conditions

The first experiments showing that crystal growth can exert pressure were done more than a century ago when Lavalley [68] observed that crystals growing from their solutions were able to lift a certain mass. In 1916, Taber [69] showed that a crystal in a saturated solution is not always able to lift a weight. When two crystals, one loaded and one unloaded, are in contact with a saturated solution and water evaporates, the solution becomes supersaturated and therefore the unloaded crystal will grow to consume the supersaturation (Figure 2.8). If the solution cannot evaporate, the loaded crystal will dissolve while the unloaded crystal will grow. This shows that pressure tends to increase the solubility of the salt [70] (in the case of solidification process, the pressure tends to lower the melting point). These experiments were done under equilibrium conditions where the kinetics and transport of ions are negligible.

Correns and Steinborn in 1949 [72, 73] developed the first equation relating the pressure ΔP and the solubility of the salt as

$$\Delta P v_m = RT \ln \left(\frac{c}{c_s} \right) \quad (2.15)$$

where $R=8.314 \text{ J/K/mol}$ is the universal gas constant, T the absolute temperature and v_m the molar volume of the crystal. The supersaturation is presented here as the ratio between the actual concentration c and the concentration when saturated c_s .

In 1961 Everett [74] published a paper on “The thermodynamics of frost damage to porous solids” where he used a thermodynamic approach to link the chemical potential μ of a small crystal immersed in a liquid subjected to hydrostatic pressure P_l . This is shown in the following equation

$$\mu = \mu(P_l) + v_m \gamma_{cl} \left(\frac{dA}{dV} \right) \quad (2.16)$$

Chapter 2. Literature review

where $\mu(P_l)$ is the chemical potential of the bulk solid at pressure P_l and γ_{cl} is the interfacial free energy between the crystal and the liquid[‡]. The area and the volume of the crystal are represented by A and V , respectively, and dA/dV is the curvature of the crystal.

For a spherical crystal of radius r_c , equation 2.16 reduces

$$\mu = \mu(P_l) + v_m \gamma_{cl} \left(\frac{2}{r_c} \right) \quad (2.17)$$

From this equation it is shown that the chemical potential of the crystal is higher for smaller crystals or higher curvatures. For $r_c \rightarrow \infty$, the chemical potential is equal to the bulk chemical potential of a non-curved crystal. When $r_c \approx \text{nm}$, the chemical potential of the highly curved crystal becomes higher than the bulk crystal. Therefore, when the crystal is placed under an hydrostatic pressure P_l , the increase of chemical potential due to the curvature can be related by equation 2.18 to an increase of pressure in the crystal given by $\Delta P = P_c - P_l$.

$$\mu - \mu(P_l) = \mu(P_c) - \mu(P_l) = v_m \gamma_{cl} \left(\frac{dA}{dV} \right) = v_m \Delta P \quad (2.18)$$

After removal of the term v_m , the following equation is obtained

$$\Delta P = \gamma_{cl} \left(\frac{dA}{dV} \right) \quad (2.19)$$

This equation can easily be obtained by using another approach. The work that the pressure ΔP has to provide to increase the volume of a crystal of a given shape should be equal to the increase of surface energy as shown by equation 2.20. This equation is identical to equation 2.19.

$$\Delta P dV = \gamma_{cl} dA \quad (2.20)$$

For a sphere, the increase in volume is expressed as $dV/dr = 4\pi r^2$ and the increase in surface as $dA/dr = 8\pi r$. By introducing these terms in equation 2.20, equation 2.17 for a spherical crystal can be easily demonstrated. The curvature of the sphere is $2/r$. In the case of a cylindrical crystal of height h , the increase in volume is expressed as $dV/dr = 2\pi r h$ and the increase in surface as $dA/dr = 2\pi(2r + h)$. Assuming that $h \gg r$ the curvature of the cylinder is $1/r$.

The Freundlich equation 2.21 is obtained by combining equation 2.15 and equation 2.19 [75].

$$\frac{RT}{v_m} \ln \left(\frac{c}{c_s} \right) = \gamma_{cl} \frac{dA}{dV} \quad (2.21)$$

This equation shows that for a given supersaturation there is a corresponding crystal curvature dA/dV where equilibrium conditions are met.

[‡]Assumed to be independent of V and isotropic on all the crystal faces. It can be taken as the average interfacial free energy of all the faces of the crystal.

2.4. Dimensional stability and expansion mechanisms

An equation linking the increase of solubility due to the increase in pressure generated in small spherical crystals is obtained from the Freundlich equation.

$$c = c_s \exp \frac{2v_m \gamma_{cl}}{RT r_c} \quad (2.22)$$

This confirms mathematically what was observed by Thomson [70].

2.4.3 Crystallization in porous media

In this section, the crystallization of crystals in porous media is described. When crystals grow in pores there is an energy mismatch between the surface of the growing crystal and the pore walls [58]. This is due to electrostatic and Van der Waals forces. No direct contact is possible and there is a thin film of solution of thickness δ between the crystal and the pore wall that brings ions for the crystal growth [76]. This film of solution δ is estimated to be 1-2 nm [59][§]. The pore radius r_p is linked to the crystal radius r_c by $r_c = r_p - \delta$. The energy mismatch and the supersaturation are at the origin of crystallization damage [76].

In building materials, the porous matrix is formed by various pores sizes, coarse pores often being connected through smaller pores [74] and pore shapes are complex. Different simplified pore shapes are used to describe three main pore models. The equations resulting from these analyses are used for further calculations in the thesis in chapter 6.

Pore model 1: Crystal growing in a cylindrical pore [58, 76, 77]

If a spherical crystal is placed in a cylindrical pore containing a supersaturated solution, the crystal grows on its free surfaces as shown in figure 2.9 and becomes cylindrical with hemispherical sides. The crystal growth consumes the supersaturation until reaching an equilibrium saturation determined by the curvature of the hemispherical side of the crystal. There is a liquid film of thickness δ and of uniform concentration surrounding the crystal. The curvature of the crystal at the hemispherical end is $2/r_c$ and the curvature of the cylindrical part is $1/r_c$. Therefore, the solubility at the tips of the crystal is higher than at the cylindrical part as described by equation 2.22. This results in a supersaturated cylindrical part with respect to the spherical part (which is in equilibrium with the solution). Equilibrium is attained when both parts have the same chemical potential. Consequently, the cylindrical part will grow and generate pressure, which causes an increase of chemical potential, until equilibrium is reached. The pressure difference in the anisotropically stressed crystal is expressed by

$$\Delta P = \gamma_{cl} \left(\frac{2}{r_c} - \frac{1}{r_c} \right) = \gamma_{cl} \frac{1}{r_c} = \gamma_{cl} \frac{1}{r_p - \delta} \quad (2.23)$$

In this case, higher pressures are generated in the smaller pores.

[§]To give an idea, the size of a water molecule is $2.8\text{\AA}=0.28\text{ nm}$. The size of sulfate anions is similar. This motivates the minimum value of 1 nm for δ which should be a few molecules thicker.

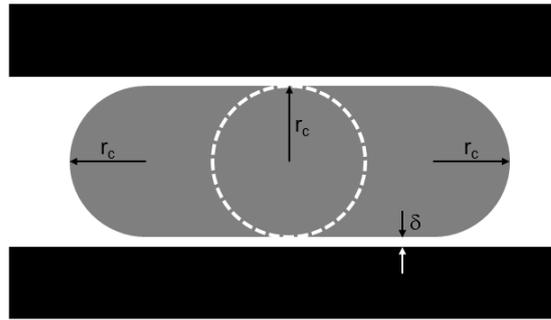


Figure 2.9: Pore model 1: Crystal (grey) growing in a cylindrical pore (black). Initially the crystal is spherical (white dotted line) and grows to become cylindrical. There is a liquid film of thickness δ between the crystal and the pore wall. The concentration is uniform throughout the liquid (white). The radius of the hemispherical and the cylindrical part of the crystal is r_c . Adapted from [77].

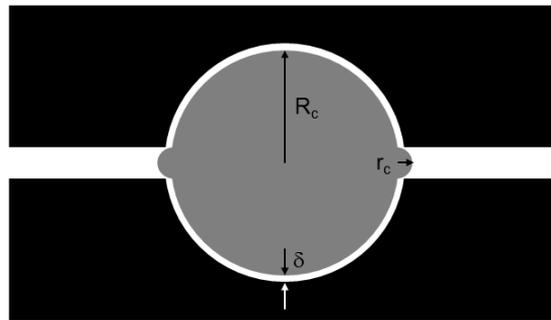


Figure 2.10: Pore model 2: Crystal (grey) growing in a spherical pore (black) with small pore entries. There is a liquid film of thickness δ between the crystal and the pore wall. The concentration is uniform throughout the liquid (white). The radius of the small portion of the crystal at the pore entry is r_c and the radius of the crystal in the spherical pore is R_c . Adapted from [77].

Pore model 2: Crystal growing in a spherical pore with small pore entries [58, 76, 77]

Consider now a spherical pore with smaller cylindrical pore entrances in which a crystal is growing. The surrounding solution around the larger (low curved) portion of the crystal has the same concentration as the solubility of the small (highly curved) portion of the crystal growing in the pore entrance (figure 2.10). Therefore, the pore entrance determines the equilibrium solubility of the small and highly curved portion of the crystal that can just penetrate the pore as described by equation 2.22. The difference between the curvature at the entrance ($2/r_c$) and in the larger interior of the pore ($2/R_c$) determines the supersaturation of the larger portion of the crystal. The large spherical crystal will grow to increase its pressure until its chemical potential equals that of the highly curved pore entry crystal. This situation can be described by

$$\Delta P = \gamma_{cl} \left(\frac{2}{r_c} - \frac{2}{R_c} \right) \quad (2.24)$$

To simplify this equation and as $R_c \gg r_c$ the second term in the brackets can be neglected. This assumption is done in section 6.4 and is called second assumption. It gives an upper bound of pressure generation and the simplified relation becomes

$$\Delta P = \gamma_{cl} \frac{2}{r_c} = \gamma_{cl} \frac{2}{r_p - \delta} \quad (2.25)$$

This shows that the pressure that builds up in a pore is determined by the size of the pore entry.

Pore model 3: Crystal growing in a cylindrical pore with small pore entries [77]

This pore model (figure 2.11) differs from the pore model 2 as the large portion of the pore is cylindrical and can be described with

$$\Delta P = \gamma_{cl} \left(\frac{2}{r_c} - \frac{1}{R_c} \right) \approx \gamma_{cl} \frac{2}{r_c} = \gamma_{cl} \frac{2}{r_p - \delta} \quad (2.26)$$

This equation is the same as equation 2.25.

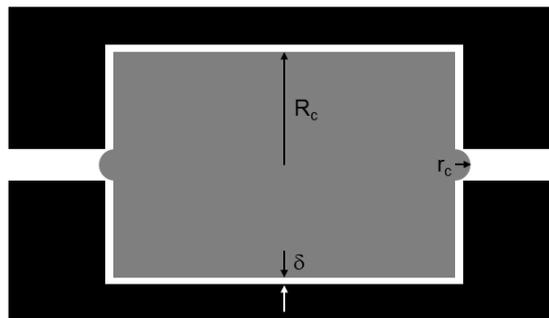


Figure 2.11: Pore model 3: Crystal (grey) growing in a cylindrical pore (black) with small pore entries. There is a liquid film of thickness δ between the crystal and the pore wall. The concentration is uniform throughout the liquid (white). The radius of the small portion of the crystal at the pore entry is r_c and the radius of the crystal in the cylindrical pore is R_c . Adapted from [77].

Concluding remarks

These three pore models (equations 2.23, 2.25 and 2.26) try to describe the different pore shapes that can be found in a porous material in a simplified way. It is shown that there are two distinct cases describing a lower and higher pressure generation. These are the cylindrical pores and the spherical or cylindrical pores with small pore entries, respectively. The pressure varies up to a factor of 2. The spherical model is taken for further calculations. The most important findings from what described above is that **the maximum pressure that can be generated is determined by the size of the pore entry** [58, 77].

This observation was also done by Everett [74] on ice crystallization using glass cylinders connected by a capillary tube. He found that the ice crystals form in the glass cylinders (coarse pores) while the small capillary tubes (small pores r_p) supply the water and determine the difference in chemical potential and consequently the pressure. The large crystals grow at the expense of the small crystals but this is controlled by kinetic factors determined by the permeability of the porous media. In the case of salt crystallization, the kinetics are also controlled by diffusion of ions to the crystals.

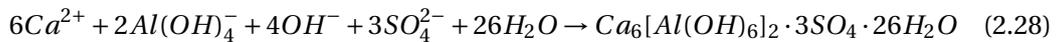
2.4.4 Salt supersaturation: the case of ettringite

Supersaturation provides the driving force for the development of crystallization pressure ΔP and expansion [58, 59]. Thus, a crystal cannot grow without supersaturation. The saturation index SI is defined as

$$SI = \log_{10} \left(\frac{K}{K_{sp}} \right) \quad (2.27)$$

where K is the ion activity product and K_{sp} is the solubility product of a given phase. If $SI = 0$ the solution is at equilibrium, if $SI < 0$ the solution is undersaturated and if $SI > 0$ the solution is supersaturated with respect to a given crystal.

The species forming ettringite are



The resulting ion activity product K for this phase is

$$K = (a_{Ca^{2+}})^6 \cdot (a_{Al(OH)_4^-})^2 \cdot (a_{OH^-})^4 \cdot (a_{SO_4^{2-}})^3 \cdot (a_{H_2O})^{26} \quad (2.29)$$

and the solubility product of ettringite at 20 °C is $K_{sp} = 10^{-45.52}$ [78]. Thermodynamic simulations are used to calculate the activities of the different species found in the pore solution as described in section 3.2.11.

In the previous section 2.4.2 the equation 2.15 relates the saturation to the crystallization pressure. The Correns equation was originally developed using the salt concentration. For

2.4. Dimensional stability and expansion mechanisms

complex salts containing a various number of species, the ion activity product is used [58, 59] and this leads to

$$\Delta P = \frac{RT}{v_m} \ln \left(\frac{K}{K_{sp}} \right) \quad (2.30)$$

where $R=8.314 \text{ J/K/mol}$ is the universal gas constant, T the absolute temperature and v_m the molar volume of the crystal (for ettringite $v_m=705.8 \text{ cm}^3/\text{mol}$ using a density of 1.78 g/cm^3 [79] and a molar mass of 1255 g/mol). The maximum pressure that can be achieved for a given supersaturation is ΔP .

Equation 2.31 is obtained by substituting the concentrations with the ion activity product in the Freundlich equation 2.21 and using the curvature of the sphere $2/r$. This equation represents the equilibrium condition and allows the minimum pore radius r_{min} to be calculated from the supersaturation of ettringite.

$$\frac{RT}{v_m} \ln \left(\frac{K}{K_{sp}} \right) = \gamma_{cl} \frac{2}{r_{min} - \delta} \quad (2.31)$$

The interfacial free energy of salts present in cementitious materials is expected to be highly anisotropic and there are no reliable data for these values. The value used in this study ($\gamma_{cl}=0.1 \text{ J/m}^2$) is an estimate previously used by other authors [60, 77].

For a given supersaturation, there is a corresponding pore radius r_{min} where equilibrium conditions are met. Crystallization pressure develops only when crystals grow in pores with radii r_p larger than r_{min} according to equation 2.25. Large stresses are localized in nanometers size pores and the phase generating crystallization pressures has to be confined [60].

To summarize, crystals will always grow preferentially in free space (large pores) at equilibrium conditions, without exerting expansive forces. In practice, the crystal growth depends also on the kinetics of diffusion of the ions to the crystal (transport properties). Therefore, pressure can build up in pores with small pore entrances if the kinetics of crystal growth are faster than the diffusion of ions into larger pores. The size of the pore entrance determines the maximum pressure that can be generated. The bigger the difference between the curvature at the entrance and the curvature in the larger interior of the pore, the bigger the crystallization pressure. In general, the small pores generate the largest pressures [76]. Consequently, the upper bound of the crystallization pressure is determined by the supersaturation while the lower bound is related to the interfacial free energy between the crystal and the liquid, the pore size and the shape of the crystal [58].

2.4.5 Factors affecting the expansion

The main factors affecting the expansion related to ettringite formation are summarized here:

1. The relative amount of aluminate and sulfate (CA or $C_4A_3\bar{s}$ vs $C\bar{s}$) [80, 81]
2. The kinetics or the time of ettringite formation [67, 82, 83]
3. The fineness of the anhydrous powders [82, 83]
4. The porous structure, *i.e.* the water to binder ratio [84]
5. The temperature [85]
6. The alkali content or the calcium hydroxide content [67, 86, 87]

In this thesis the main studied factor is the balance between $C\bar{s}$ and CA or $C\bar{s}$ and $C_4A_3\bar{s}$. A mechanism of expansion is proposed based on the results obtained by changing the relative amounts of aluminate and sulfate (section 6.4). It is known that an increase of calcium sulfate content relative to calcium aluminate leads to higher expansions (Point 1).

The kinetics of ettringite formation (Point 2) are directly linked to the fineness of the anhydrous powders (Point 3); the expansion increases as the fineness of the anhydrous particles decreases. Coarse particles lead to slower kinetics of hydration, therefore ettringite formation is extended to longer periods of time generating expansion if this phase grows when a solid hydrated matrix has formed. When finer powders are used, the kinetics are faster and most of the ettringite precipitates before a solid skeleton has formed.

The porous structure (Point 4) can be modified by changing the water to binder ratio or by adding fillers. Higher water to binder ratios lead to a decrease of the expansion as the porosity or the confinement are modified. This is also linked to the higher consumption of anhydrous before the formation of a solid hydrated matrix.

The temperature (Point 5) has two main effects on ettringite; it increases its solubility as described in appendix A.1.1 and accelerates the reactions. Previous studies observed an increase of the amount of ettringite formation and of expansion with higher temperatures [85, 88].

The effect of alkalis or of pH on expansion is not clear in the literature (Point 4). Some authors observed an increase of the expansion with the amount of alkalis [86], while other authors noticed the opposite [67, 87]. According to Ogawa and Roy [67], the kinetics are accelerated with NaOH. Therefore, more ettringite forms during the first hours of hydration, before a proper structural development of the solid matrix, leading to lower expansions. This is the opposite that what it is observed with higher temperatures where the kinetics are accelerated but the expansion is amplified. Some authors observed the effect of calcium hydroxide on ettringite morphology [57, 67]. In saturated calcium hydroxide solutions, ettringite causes

expansion whereas without calcium hydroxide no expansion was observed. This is controversial as in the present study we observe expansion in systems without calcium hydroxide. Nevertheless, it was observed that the pH of the solution has an impact on the morphology of ettringite, fine and colloidal crystals form in saturated calcium hydroxide solutions whereas in undersaturated solutions large needles form [57]. It is claimed that the specific surface of fine and colloidal ettringite crystals adsorbs water molecules and causes expansion as described in section 2.4.1.

At the end of the study of the expansion, the effect of the water to binder ratio, substitution, alkalis and temperature are studied and discussed. The main discrepancies are found on the effect of the alkalinity of the solution and on the effect of the temperature.

2.5 Characterization of the confinement

Expansion caused by crystal growth in porous materials is strongly linked to the porous structure or confinement. The main technique used in this thesis is mercury intrusion porosimetry (MIP). The advantages and drawbacks of using this technique are discussed. More details about MIP are found in the next chapter in section 3.2.9.

Diamond [89] criticizes this technique because of the ink-pore effect and because two assumptions are done to calculate the pore radius from the intrusion pressure:

- A cylindrical pore model is used to calculate the pore radii as a function of the pressure (this is described by the Washburn equation).
- The pores are entirely and equally accessible from the outer surface of the sample.

But in reality the pores are not cylindrical and are irregularly shaped. He also claims that most pores being reported by this method are one or two order of magnitude smaller than they really are.

Vočka [90] showed that pore radii measured with this technique depend on the pore size distribution and also on the connectivity of the pore space. As connectivity decreases, the position of the peak of the derivative shifts toward smaller pore radii for larger pores. This influence becomes less important for smaller pores.

A comparative study of the porosity in CSA systems was done with nitrogen adsorption/desorption at 77 K (NAD) and thermoporometry (TPM) [91]. It shows that in these systems, which are similar to the CSA and also to the CAC with gypsum systems used for the study of the expansion (chapter 6), the pore size ranges from 2 to 100 nm. The most important population of pores is found between 10-30 nm in TPM measures and 2-50 nm in NAD isotherms for 1 day samples. MIP measurements show that similar systems have most of the pores between 2-10 nm. MIP is used here mainly to characterize the pore volume and the pore entry radius which are important parameters related to the expansion.

Chapter 2. Literature review

Sun and Scherer [92] report that neither TPM nor NAD are accurate for measuring pores above 25 nm. One method that could be used to quantify the porosity of μm size is SEM image analysis of backscattered electrons. The main problem of this technique is related to ettringite loosing water in high vacuum conditions. This causes shrinkage of this phase and cracking, therefore it is not possible to distinguish real porosity from porosity created in ettringite cracks. For this reason it is preferable to proscribe this method when studying ettringite rich systems.

3 Materials and methods

Contents

3.1 Materials	27
3.2 Methods	30
3.2.1 Experimental conditions	30
3.2.2 Compressive strength tests	31
3.2.3 Expansion tests	31
3.2.4 Isothermal calorimetry	31
3.2.5 Sample preparation for microstructural characterization	31
3.2.6 X-ray diffraction	32
3.2.7 Thermogravimetric analysis	34
3.2.8 Scanning electron microscopy	34
3.2.9 Porous structure characterization	36
3.2.10 Pore solution analysis	40
3.2.11 Thermodynamic simulations	41
3.2.12 Finite element modelling of the expansion	41

3.1 Materials

The materials used in this work were:

- Calcium aluminate cement (CAC, Ternal RG from Kerneos)
- Calcium sulfate β -hemihydrate (HH, Prestia Selecta from Lafarge)
- Limestone (C \bar{c} , Durcal 15 from Omya)
- Slag (S, from Ecocem)
- Inert quartz (K10 and K13)

Chapter 3. Materials and methods

Table 3.1: XRF oxides composition of the components used for the study of the hydration and mass attenuation coefficients (MAC).

[wt.%]	CaO	SiO ₂	Al ₂ O ₃	Fe ₂ O ₃	MgO	Na ₂ O	K ₂ O	SO ₃	TiO ₂	CO ₂	MAC
CAC TRG	36.6	4.1	40.3	16.3	0.1	0.04	0.04	0.3	1.8	-	97.4
HH	38.5	0.9	0.0	0.0	0.2	0.0	0.0	52.8	0.0	0.0	73.3
Cc	57.3	0.1	0.1	0	0.4	0.1	0.2	0	0	40.9	76.1
Q K13	0	97.9	1	0	-	-	0.8	-	0	-	-
Slag	42.7	34.2	12.6	0.4	5.3	0.3	0.6	2.7	0.6	-	74.9
Q K10	0	97.7	0.9	0	-	-	0.8	-	0	0	-
MAC [cm ² /g] [93]	124	36	31.7	214.9	28.6	25	122.3	44.5	124.6	9.4	-

The oxide composition of the different materials obtained with X-ray fluorescence (XRF) spectrometry is given in table 3.1. The mineralogical compositions of the CAC cement, hemihydrate and limestone were obtained with XRD Rietveld analysis and are presented in table 3.2. Note that hemihydrate contains 3.5 wt.% of calcite and limestone is composed of 99.8% of calcite. The XRD analyses are not shown for slag as it is completely X-ray amorphous. The particle size distributions (PSD) of the main materials shown in figure 3.1 were measured with a laser diffraction particle size analyzer Malvern Mastersizer S, the dry powders were dispersed into isopropanol using an ultrasonic bath.

Table 3.2: XRD Rietveld analyses of the components used for the study of the hydration (Error of the measurement $\pm 2\%$).

[wt.%]	CA	C ₂ S	C ₄ AF	C ₂ AS	CFT Perovskite	C \bar{s} H _{0.5}	C \bar{s}	C \bar{c}	SiO ₂	Fe ₃ O ₄	Minor phases
CAC	50.7	4.6	10.9	12.3	10.0	-	-	-	-	6.3	5.2
HH	-	-	-	-	-	89.7	5	3.5	1.8	-	-
Cc	-	-	-	-	-	-	-	99.8	0.2	-	-

The secondary electron images of the main anhydrous materials are shown in figure 3.2. Calcium aluminate cement particles are characterized by sharp edges. The main particle shown in figure 3.2a is of 10 μm size but there are a lot of smaller particles on it. Hemihydrate has an hexagonal crystal structure where the water molecules are in the channels parallel to the c-axis and its β form is less crystalline than the α form [13]. Therefore its particles have a rounded elongated structure as shown in figure 3.2b. Limestone particles have a layered structure with parallel planes. Smaller particles are found on bigger particles as in figure 3.2c. Slag particles are similar than CAC particles as they have smooth surfaces (Figure 3.2d).

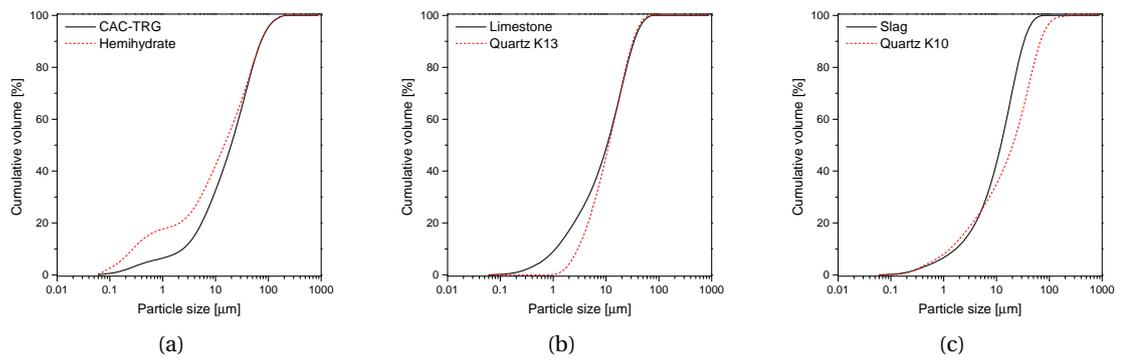


Figure 3.1: Particle size distribution of the components used for the study on the hydration. CAC and hemihydrate (a), limestone and quartz (b), slag and quartz (c).

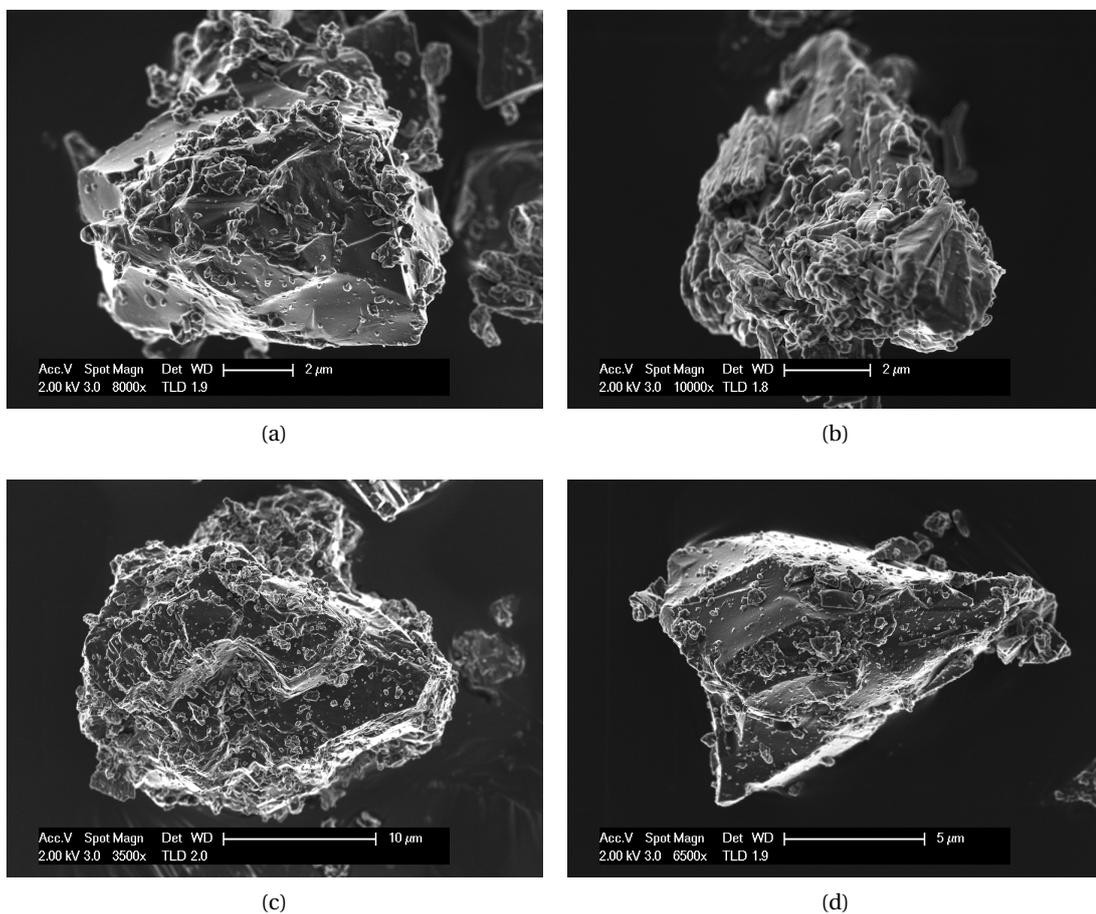


Figure 3.2: Secondary electron images of anhydrous powders. CAC TRG (a), hemihydrate (b), limestone (c) and slag (d). Note that the scale differs for each figure.

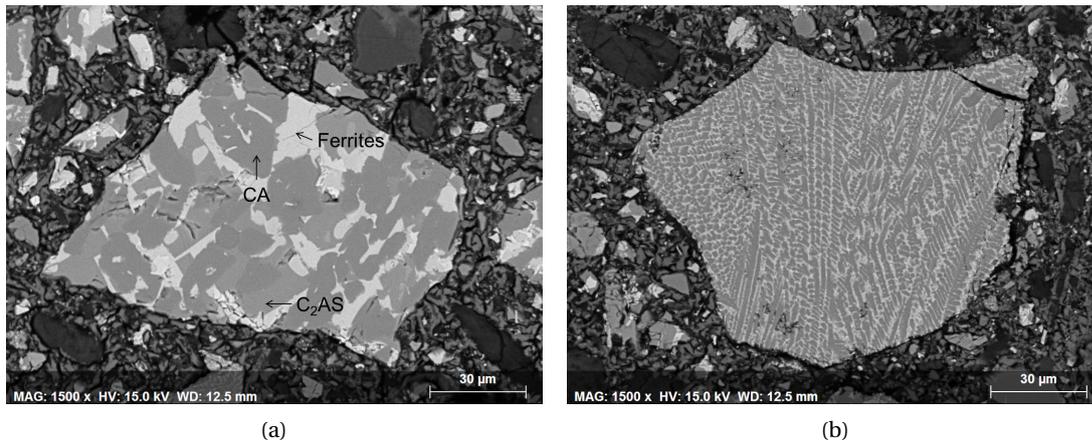


Figure 3.3: Backscattered electron images of anhydrous CAC grains, polyphased and dendritic growth.

Backscattered electron images on polished sections of CAC grains are shown in figure 3.3. The grey level is proportional to the molar mass of the phase, the brightest phase being the heaviest. Two types of crystalline grains are shown here, an equiaxed grain with the indication of the main phases (figure 3.3a) and a dendritic grain (figure 3.3b). The clinker of this cement was produced in a reverberatory furnace where the raw materials are fused and the liquid is cast in metallic molds. According to the cooling conditions, the solidification process leads to the formation of different crystalline structures. There can be formation of equiaxed grains or formation of dendritic grains which are typical of a quenched liquid. Generally, in a solidification process heterogeneous nucleation occurs as there are impurities (nuclei) in the molten material. The number of initial nuclei is proportional to the final size of the grains. Heterogeneous nucleation is energetically more favourable than homogeneous nucleation, therefore low undercooling is needed to solidify the material [94].

3.2 Methods

3.2.1 Experimental conditions

All the experiments were carried out at 20°C. Paste samples were cast with a water to binder ratio (w/b, binder includes CAC, C₃S and SCM if present) of 0.4 and were used for all the experiments except compressive strength tests which were done on mortars with a water to binder ratio of 0.5. Because of the interfacial transition zone a w/b of 0.5 in mortar is comparable to 0.4 in paste. The dry powders were weighted in a recipient of 250 ml and dry mixed for 30 seconds before mixing all the powders with water for 2 minutes using a paddle mixer at 1600 rpm. The sample names are composed of the molar percentage of CA relative to

HH and the wt.% of substitution if there is any. Molar amounts of calcium sulfate are used to indicate how far the systems are from stoichiometric conditions described by reaction 2.6 which is at 50 mol.% (indicated as 50HH on the diagram). One batch of materials was used for each chapter, therefore there may be some small differences, especially in the kinetics at early age, between the same composition in the different chapters. The materials, XRF and XRD analyses of the components used for the expansion study are presented in chapter 6 as they differ from the ones used for all the other chapters.

3.2.2 Compressive strength tests

Mortars were cast according to the norm EN 196-1 with a water to binder ratio of 0.5. Three mortar bars of $40 \times 40 \times 160 \text{ mm}^3$ were cast from a blend of 1350 g of normalized sand with 450 g of binder and 225 g of water. The mixing protocol was: 30 seconds at low speed to blend the dry powders, water is added and mixed for 30 seconds at low speed, the sand is then added and mixed for 30 seconds at low speed followed by a break of 15 seconds and 60 seconds at high speed. The mixing duration was reduced from that specified in the norm because of the rapid setting of the systems. After one day the bars were unmoulded and cured in a high humidity environment (96% R.H.). The results at each time are an average of four compression tests.

3.2.3 Expansion tests

For the expansion tests, the cement paste was cast in steel molds of $10 \times 10 \times 40 \text{ mm}^3$ with end pieces for the measurement of the length evolution. The samples were then cured for one day in the molds in a high humidity environment (96% R.H.) and unmoulded after 24 hours to start the measurements. The samples (6 prisms) were then submerged into 60-70 g of deionised water. The length of the samples (~40 mm) was measured regularly with an extensometer having a precision of $\pm 1 \mu\text{m}$. The expansion values result from the average of 3 measures.

3.2.4 Isothermal calorimetry

Hydration kinetics were followed by isothermal calorimetry (TAM Air from TA Instruments) at 20°C . 10 g of cement paste (mixed outside the calorimeter) were introduced in a glass ampoule which was then sealed with a cap and placed in the calorimeter .

3.2.5 Sample preparation for microstructural characterization

For SEM, XRD, TGA and MIP the samples were cast in polystyrene cylinders ($35 \text{ mm}\varnothing \times 50 \text{ mm}$). These cylinders were introduced in a water bath at 20°C to maintain a constant temperature for the first 24 hours. Then they were unmoulded and placed in cylindrical recipients of 37 mm of diameter containing around 8 g of demineralized water per 95 g of sample mass to ensure a

continuous supply of water while minimizing leaching. At each age, three slices of 2-3 mm thickness were cut from the cylinders and then immersed in isopropanol to stop the hydration. After 7 days in the solvent, they were stored in a desiccator under vacuum and over silica gel for 2 days to remove the alcohol, prevent carbonation and remove possible moisture. Stopping the hydration with isopropanol and storing the samples under vacuum has a detrimental effect on the crystallinity and water content of the hydrates, particularly ettringite [95, 96]. It was reported that stopping the hydration with isopropanol causes a partial conversion of hemicarboaluminate into monocarboaluminate [97]. Stopping the hydration has also detrimental effects on the pore structure of the sample, the worst being oven-drying at 60°C or more and the less damaging being solvent replacement [98]. Despite these problems, the results should be comparable if the same preparation protocol is followed. The slices were then used for SEM and MIP analyses and were crushed into fine powder (<100 μm) for XRD and TGA analyses.

For the early hydration (<24 hours) characterization, the freeze-drying or lyophilisation technique is used. The fresh samples were immersed into liquid nitrogen at -196°C for 5 minutes and were then placed in the lyophilizer (Telstar Cryodos 50) under vacuum and at -50°C for 24 hours to sublimate the ice present in the sample. This method is efficient for rapidly stopping the hydration but has detrimental effects on the crystalline structure and of the water content of the hydrates. It was used only for the preparation of TGA and SEM samples.

3.2.6 X-ray diffraction

X-ray diffraction (XRD) analyses were done with a Philips X'Pert Pro PANalytical (CuKα, λ=1.54 Å) working in Bragg-Brentano geometry. The 2θ-range goes from 5° to 65° with a step size of 0.017°, a time per step of 30 s and a scan speed of 0.07°/s. This leads to a total scan of 15 minutes. The X-ray source was operated at 45 kV and 40 mA. The analyses were done on dry powders using the back loading technique to minimize preferred orientation. In-situ XRD measurements were done on a freshly mixed paste that was placed on a special sample support and was covered with a Kapton foil (polyamide film with a thickness of about 7 μm) to prevent or reduce water evaporation. The all set was then placed on a peltier junction cooled by water to maintain a constant temperature of 20°. The quantitative in-situ results are then smoothed with a windows function (Hamming). The method is comparable to the one previously used in PC systems and described in [99].

Quantitative Rietveld analyses were done with the HighScore Plus software using the external standard method (with rutile Kronos 2300, TiO₂) for absolute quantification of the crystalline phases [100]. The weight fraction of phase *k* is given by the following equation

$$w_k = \frac{S_k \rho_k V_k^2 MAC_{sample}}{S_s \rho_s V_s^2 MAC_s} c_s \quad (3.1)$$

Table 3.3: Phases and references used for quantitative Rietveld analyses.

Phase	ICSD code	Ref	Phase	ICSD code	Ref
CA	260	[101]	Hemihydrate	92947	[102]
C ₄ AF	2842	[103]	Ettringite	155395	[104]
C ₂ S	81096	[105]	Kuzelite	100138	[106]
CFT	79353	[107]	Gibbsite	6162	[108]
C ₂ AS	67689	[109]	Monocarboaluminate	59327	[110]
Magnetite	158745	[111]	Hemicarboaluminate	-	[112]
Calcite	73446	[113]	C ₃ AH ₆	34227	[114]
Gypsum	151692	[115]	C ₂ ASH ₈	69413	[116]

where w_k is the weight fraction of the crystalline phase k , S_k and S_s are the scale factors of phase k or of the external standard s , ρ is the density, V is the unit-cell volume and c_s is the crystallinity of the standard. The mass attenuation coefficient (MAC) of the bulk sample is MAC_{sample} and of the standard is MAC_s . The mass attenuation coefficient of each oxide is given in table 3.1 and is used to calculate the mass attenuation coefficient of the analysed samples. The bound water content in the sample is taken as the mass loss between 20 and 600 °C from TGA, this value is needed for the MAC calculation (MAC of H₂O is 10.1 cm²/g). The weight fraction of amorphous or unrefined phases is given by

$$w_{amorphous} = 1 - \sum_k w_k \quad (3.2)$$

w_k is the percentage of the phase k in the sample. Usually, the amount of hydrates m_k is normalized to 100 g of solid with equation 3.3. The bound water content $w_{H_2O, TGA}$ is needed for that and is defined as the water mass loss measured with TGA from 30 to 600 °C.

$$m_k = \frac{w_k}{1 - w_{H_2O, TGA}} \quad (3.3)$$

Table 3.3 lists the crystal structures of the different phases used to simulate the experimental diffractograms.

The degree of hydration α of the cement is calculated according to the following equation

$$\alpha(t) = 1 - \frac{w_{anhydrous}(t)}{w_{anhydrous}(t=0)(1 - w_{H_2O, TGA})} \quad (3.4)$$

where $w_{anhydrous}(t)$ is the weight fraction of the main anhydrous CAC phases at time t measured with XRD.

3.2.7 Thermogravimetric analysis

Thermogravimetric analysis (TGA) was carried out using a Mettler Toledo TGA/SDTA851e. Around 50 mg of ground cement paste were placed in alumina crucibles covered by aluminium lids to reduce carbonation before analysis. The temperature ranged from 30 to 1000 °C with a heating rate of 10 °C/min under N₂ atmosphere to prevent carbonation. The mass loss as a function of the temperature is obtained. After derivation the DTG curve is obtained and shows various peak that correspond to the dehydration or dehydroxylation of the phases. Above 600°C the peaks correspond to the decarbonation of the phases. Each phases losses mass at a given temperature range. The list of the main phases is shown in table 3.4. This table show the peak overlap between many phases. The peak position varies with the heating rate and the amount of one phase, but the sequence remains unchanged. Usually TGA is coupled with XRD analyses to detect all the hydrates.

Table 3.4: DTG main dehydration peaks positions. The temperatures above 600°C are related to decarbonation.

Phase	Dehydration temperature [°C]
Ettringite	100-150
Gypsum	140-160
Hemicarboaluminate and monocarboaluminate	150-180
Monosulfoaluminate and C ₂ ASH ₈	180-200
AH ₃ , hemicarboaluminate and monocarboaluminate	250-280
C ₃ AH ₆	290-310
Calcite, hemicarboaluminate and monocarboaluminate	700-800

The water loss of a single phase dm_k is related to the amount of that phase with the following equation

$$w_k = \frac{dm_k M_k}{n_{H_2O} M_{H_2O}} \quad (3.5)$$

where w_k is the weight fraction of phase k , M_k is the molar mass of phase k , n_{H_2O} is the number of water molecules in phase k and M_{H_2O} is the molar mass of water.

3.2.8 Scanning electron microscopy

The slices were impregnated under vacuum with an epoxy resin (EPOTEK 301) and polished with diamond spray ranging from 9 to 1/4 μm. The polished samples were examined by backscattered electrons (BSE) and energy dispersive X-ray analyses (EDS, Bruker AXS XFlash Detector 4030) in a scanning electron microscope (SEM, FEI Quanta 200) with an accelerating voltage of 15 kV.

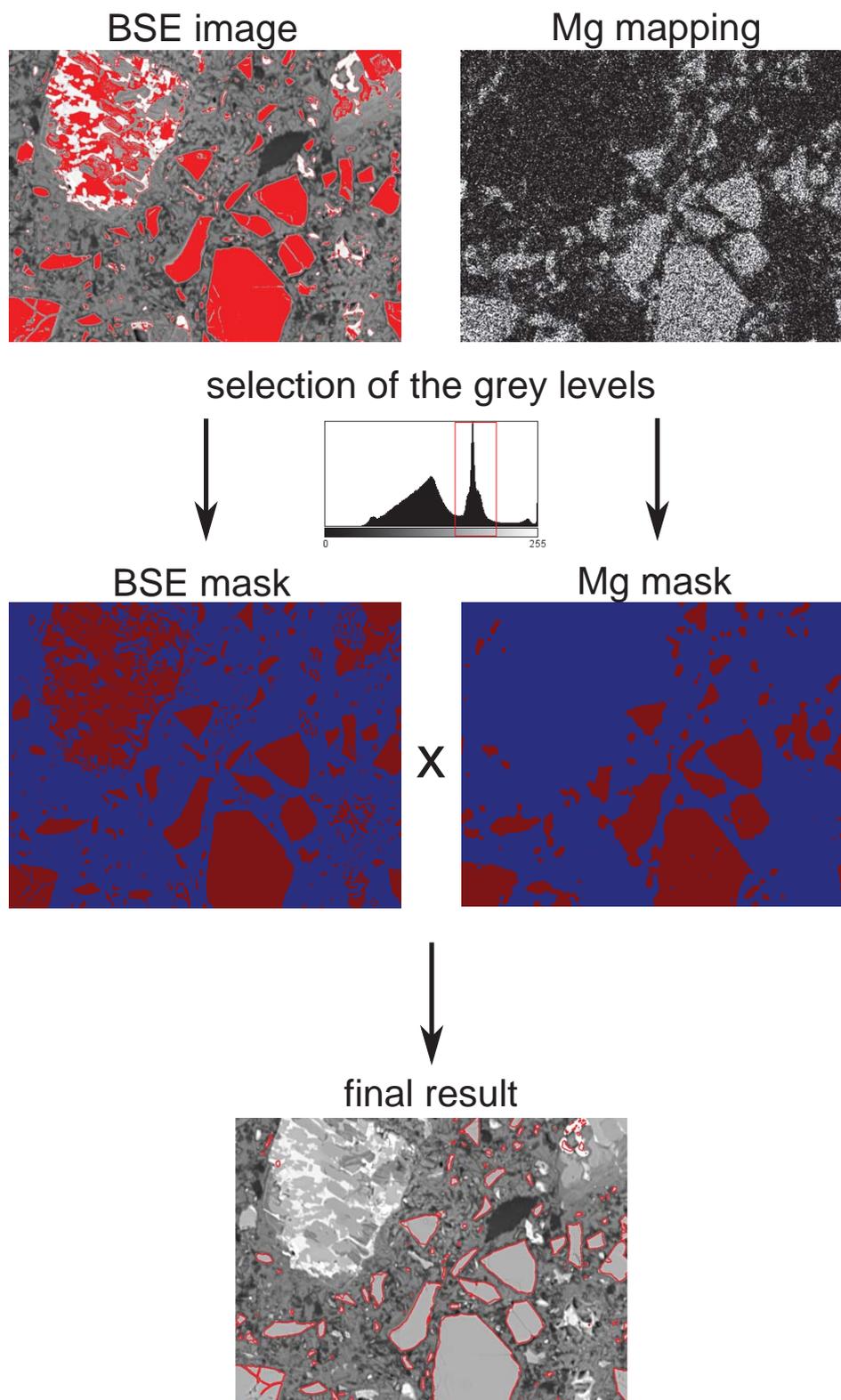


Figure 3.4: Algorithm used to quantify the degree of reaction of slag (white) by SEM-IA.

Measure of the degree of reaction of slag with image analysis

The degree of reaction of slag was measured with coupled image analysis (IA) of BSE and EDS Mg mappings. The method used is similar to the one described by Kocaba et al. [117] but a new algorithm was written by P. Durdzinski and J. Bizzozero using MATLAB (the code is presented in appendix A.5). The algorithm is described in figure 3.4. BSE images are characterized by a range of grey levels. Each grey level is related to the backscattering coefficient of a given phase, which is proportional to the weight atomic averaged density. Therefore, the grey level of BSE images gives useful information about the different phases, the heaviest elements being bright and the lightest elements being dark. The main problem is that the grey level of slag corresponds to the anhydrous CAC phase C_2AS [118]. For this reason, coupled analyses with Mg mappings are required to select only slag grains. Initially, each Mg mapping is averaged using an Hamming window and is then segmented to have the Mg mask where the pixel in the slag grain position have a value of 1 and the pixels outside slag have a value of 0. The Mg mask is used to detect the position of each slag grain; this position is then used in the BSE image to find the grey level corresponding to slag. The image is then segmented according to the grey level of slag and averaged with an Hamming windows, this is the BSE mask. The Mg mask and the BSE mask are multiplied and as a result only the slag grains are found. An operation to close the holes is then used. Finally, the slag surfaces in each of the 225 images are averaged. According to the principle of Delesse (1843), in an isotropic material the area fraction equals the volume fraction. The degree of reaction is calculated with the following equation

$$DR_{slag} = 1 - \frac{V_{slag}(t)}{V_{slag}(t=0)} \quad (3.6)$$

where $V_{slag}(t)$ is the volume fraction of slag at time t and $V_{slag}(t=0)$ is the initial volume fraction of slag. The deviation of the degree of reaction is given by

$$\Delta DR_{slag} = DR_{slag} \frac{SE_{slag}(t)}{V_{slag}(t=0) - V_{slag}(t)} \quad (3.7)$$

Where $SE_{slag}(t)$ is the standard error of the mean and is defined as the standard deviation s divided by the square root of the number of images $N=225$

$$SE_{slag}(t) = \frac{s}{\sqrt{N}} \quad (3.8)$$

The main limit of this technique is that the smallest particles ($<1\mu m$) are missed, i.e. around 7% of slag particles according to particle size distribution shown in figure 3.1.

3.2.9 Porous structure characterization

Cementitious materials and, in general, building materials have empty spaces into their volume. These can be pores, cracks or cavities. The volume fraction of these empty spaces is defined as porosity. It has strong influence on the mechanical properties, durability, thermal

properties, permeability and adsorption properties. The characterization of the pore distribution and of the porosity of a material is thus important. There is open and connected porosity and closed and inaccessible porosity. Pore sizes can be classified according to different conventions. The International Union of Pure and Applied Chemistry (IUPAC) classifies the pores size (internal pore radius) as:

- Micropores (<1 nm)
- Mesopores (1-25 nm)
- Macropores (>25 nm)

Other authors call capillary pores the pores between 2 to 10'000 nm [98]. In this study the pore size is indicated.

The porous structure of cementitious materials is tortuous and complex, therefore different methods have been developed and are used to characterize porosity according to the specific needs. In the case of dimensional stability of porous materials, the surface energy between the pore solution and the solids is relevant. The magnitude of the influence of the surface energy is related to the surface area and the pore size. Figure 3.5 indicates which pore sizes are affecting the different paste properties. The pore sizes affecting dimensional stability like shrinkage, creep and expansion are between 0.2 to 25 nm radius according to [119]. Therefore the most suitable methods that could be used to characterize this range of porosity are mercury intrusion porosimetry, thermoporometry, nuclear magnetic resonance and small-angle scattering as shown in figure 3.6. For the pores smaller than 10 nm also gas adsorption and helium pycnometry can be used. In this thesis mercury intrusion porosimetry and nuclear magnetic resonance are used and are described in the following sections.

Mercury intrusion porosimetry MIP

A big advantage of MIP is that it characterizes a broad range of pore sizes, from the mm down to 2 nm. Mercury intrusion porosimetry (MIP) is used to characterize the connected pore space and the pore entry radius. Mercury intrusion porosimetry (MIP) was carried out on Thermo Scientific Pascal 140 and 440 machines with a pressure capacity of 400 MPa. Five pieces of samples of about $4 \times 5 \times 5 \text{ mm}^3$ were used for the analysis, which corresponds to 1-1.5 g.

Mercury has a non-wetting liquid in contact to cement paste. Therefore a pressure is applied to intrude the porous matrix and the pore radius is calculated according to some assumptions and using the Washburn equation 3.9 [120]. The main limit of this technique is that it measures the volume of connected porosity that can be accessed from a given pore entry and not the real pore size [121, 89]. The pore entry radius corresponding to the pressure when most of the pore volume starts to be intruded by mercury is called threshold pore radius [98]. This marks the

Chapter 3. Materials and methods

According to IUPAC [1.35]		According to P. Mehta, 1986 [1.40]		According to S. Mindess <i>et al.</i> , 2002 [1.4]			
Name	Diameter	Pore type	Size range	Name	Diameter	Role of water	Paste properties affected
Micropores	Up to 2 nm	Interparticle space between C-S-H sheets	1 nm to 3 nm	Micropores "inter layer"	Up to 0.5 nm	Structural water involved in bonding	Shrinkage, creep at all RH
				Micropores		0.5 nm to 2.5 nm	Strongly adsorbed water; no menisci form
Mesopores	2 nm to 50 nm			Capillary pores (low w/c)		10 nm to 50 nm	Small (gel) capillaries
Macropores	>50 nm	Capillary pores (high w/c)	3 μm to 5 μm	Medium capillaries	10 nm to 50 nm	Moderate surface tension forces generated	Strength, permeability, shrinkage at high RH, >80%
				Large capillaries	50 nm to 10 μm	Behaves as bulk water	Strength, permeability
		Entrained voids	50 μm to 1 mm	Entrained air	0.1 mm to 1 mm		Strength

Figure 3.5: Pore diameters classification according to the general classification by IUPAC and to terminology used in concrete science. From [98].

onset of percolation and can be determined mathematically by the tangent intersection of the two slopes as shown in figure 3.7. The critical pore radius is determined by the inflection point of the cumulative curve and is referred to as the maximum continuous pore radius through which mercury penetrates the bulk of the sample. It is the most frequently occurring pore size in the connected pores that allows maximum percolation [122]. The threshold pore radius seems to be more representative of the size of the radius when mercury starts to intrude the sample and is used in this study.

$$P(r) = \frac{2\sigma \cos(\theta)}{r} \quad (3.9)$$

The above equation relates the applied pressure to the pore radius r . The parameters related to the mercury and the analysed material are the surface tension of the mercury $\sigma=0.48$ N/m and the contact angle between mercury and cement paste θ . The contact angle was measured by Cook [123] on hardened cement paste and the value varies between 139° to 150° . A value of $\theta=140^\circ$ is generally used. In the literature some discrepancies are found whether or not MIP characterizes well the pore size distribution. Some authors [89, 124] state that most of the mercury intrudes the porous media only when the critical pore radius is attained. The size related to smaller pores can then include both smaller and larger interconnected pores, the so called ink-bottle pores. Combined volumes of the larger and smaller pores are mistakenly allocated to the size of the small pores. Nevertheless, the critical pore radius is a good indicator of the size of the pores entries [125]. It is strongly related to the diffusion and permeability of the cement paste, which are an indicator of the material durability [126, 127]. Another way to measure porosity filled by water is ^1H NMR and the next section describes this technique.

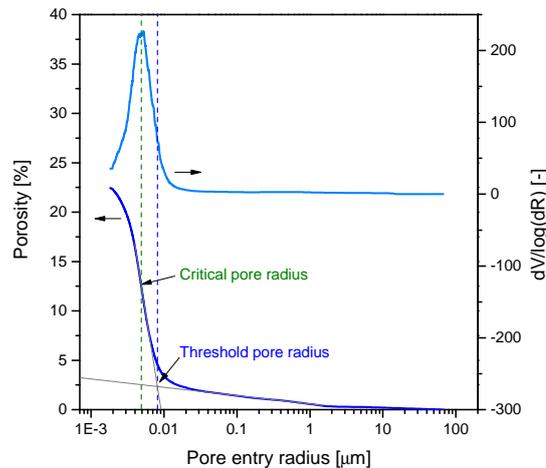


Figure 3.7: Example of MIP cumulative and derivative curves. Definition of critical pore radius.

using μs units for the measured relaxation time gives the pore radius in nm. NMR and MIP give comparable pore sizes distributions, especially for pores in the range between 10 to 100 nm [98].

3.2.10 Pore solution analysis

Pore solutions were extracted from cylindrical cement paste specimens 50 mm diameter and 100 mm high. 350 g of cement paste were cast in plastic bottles and stored for 24 hours in sealed conditions. Then the samples were tested or cured for the desired time under a small amount of water (40 g of water for 350 g of cement paste). These storage conditions limit leaching, but ensure that pores are filled with pore solution. They also best represent the conditions under which the other samples are cured and expansion takes place.

The pore solution was extracted at pressures of 50 MPa for less than 5 hours old samples and 560 MPa for samples above 9 hours, applied for 3-7 minutes to extract 5-10 ml of pore solution. The method has been adapted from the one used by [129, 130]. The extracted pore solution was then filtered with a $0.45 \mu m$ filter and diluted 3 times in an acid solution containing 0.2 ml HNO_3 8M for 10 ml of total solution. Acidification prevents precipitation of stable phases at high pH. Then the solution was stored in a plastic vial at $5^\circ C$ to slow down any kinetic effect before analysis. The ionic composition of the solutions was measured with a Dionex ICS-3000 ion chromatograph for sulfate ion analysis and a Shimadzu ICPE 9000 spectrometer for cation analysis. The standard error of measurement is about 10%.

The applied pressure is known to have an influence on the concentrations in the pore solution [131]. For pressures up to 560 MPa the values are comparable and the main effect is measured on sulfate. The increase of the concentrations could be due to the increase of the solubility of solids under high pressure [132].

3.2.11 Thermodynamic simulations

Thermodynamic simulations were carried out using the GEMS-PSI [133, 134] software with thermodynamic data for aqueous species and other solids from the GEMS-PSI thermodynamic database [135] and the CEMDATA14 database from EMPA [78, 136] for the cementitious phases. The inputs are the anhydrous phases, the water content, the temperature and the pressure. The results are obtained from the minimization of the Gibbs free energy in the system and no kinetics are taken into account.

The ion activity product K of each phase is needed for the calculation of the Gibbs free energy ΔG_T as described by the following equation

$$\Delta G_T = -RT \ln K \quad (3.12)$$

where $R=8.314 \text{ J/K/mol}$ is the universal gas constant and T the absolute temperature.

The ion activity product of a given phase is defined as the product of the activities forming this phase to the power of the stoichiometric coefficient (an example for ettringite is presented in section 2.4.4, equation 2.29). The activity of an ion i is given as the product between its concentration $[i]$ and its activity coefficient γ_i . The activity coefficients depend on various factors such as the ionic strength of the solution, the other ionic species and the temperature. The extended Debye-Hückel equation is used to calculate the activity coefficients

$$\log \gamma_i = \frac{-Az_i^2 \sqrt{I}}{1 + B\alpha_i \sqrt{I}} + bI \quad (3.13)$$

where A and B are Debye-Hückel solvent parameters dependent on the dielectric constant of water and temperature, z_i is the ionic charge, α_i is a parameter dependent on the size of the ion, b is a semi-empirical parameter and I is the ionic strength. The activities are calculated with GEMS.

3.2.12 Finite element modelling of the expansion

The modelling of the expansion was done with extended finite element modelling (XFEM) using the modelling platform AMIE developed by Cyrille Dunant [137], the code is presented in the appendix A.6. This platform was developed to model the alkali silica reaction (ASR) occurring in concrete, and one of the main challenges was to mesh a microstructure with the aggregates a few orders of magnitude bigger than the gel pockets where expansion takes place. AMIE stands for “Automated meshing for integrated experiments”. This platform delivers the characteristics needed for the modelling of expansion as in the current thesis, where the modelled cement paste is formed of pores ranging from 1 nm to 150 nm. The automated meshing is necessary for this application. Isostatic pressure according to the laws described in the literature on the expansion mechanisms (Section 2.4.1) is applied to each pore in the

Chapter 3. Materials and methods

generated microstructure. The deformations caused by the pressure are purely elastic and no creep nor damage are considered in the modelling.

4 Early age hydration

Contents

4.1 Introduction	43
4.2 Formulations	44
4.3 Overview of hydration kinetics	45
4.4 Effect of calcium sulfate	45
4.4.1 Low calcium sulfate system	45
4.4.2 High calcium sulfate system	51
4.4.3 Comparison between low and high calcium sulfate	54
4.4.4 Characterization of microstructure and phase assemblage	55
4.5 Effect of supplementary cementitious materials	61
4.5.1 Effects on the kinetics	61
4.5.2 Effects on the pore solution	63
4.6 Summary on the early age hydration	65
4.6.1 Effect of sulfate	65
4.6.2 Filler effect	66

4.1 Introduction

This chapter focuses on the study of the early age hydration (<24 hours) of CAC-calcium sulfate systems with and without substitutions. It is essential to understand the first steps of the hydration as one of the most important properties of these products is rapid setting. During this period of time, supplementary cementitious materials usually contribute physically to the hydration and they do not have any chemical influence. It is the so-called filler effect. Isothermal calorimetry linked to in-situ XRD and pore solution analyses were done to study the effects of calcium sulfate on calcium aluminate hydration and the effects of fillers on early hydration. Microstructural studies on early age samples contributed to the understanding of the effect of calcium sulfate. This study confirms what has been observed in comparable systems but it is the first time that quantitative in-situ XRD combined with pore solution analyses have been applied to the early hydration of CAC-calcium sulfate systems.

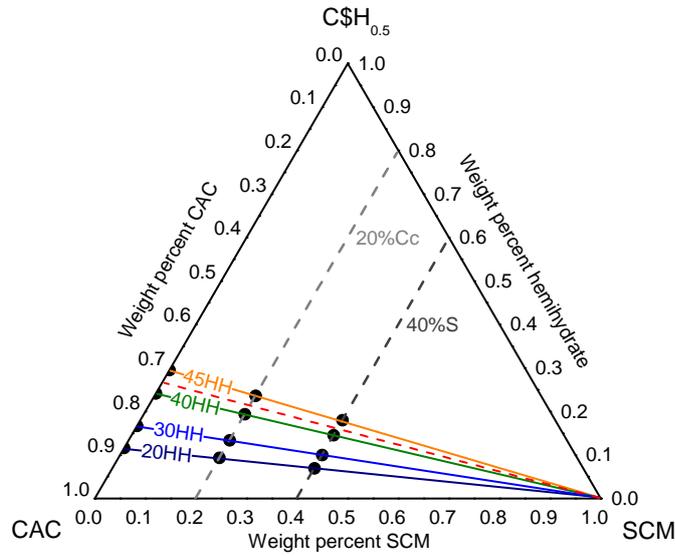


Figure 4.1: Ternary diagram showing the studied compositions. The weight percentages are shown on the diagram and the molar amount of calcium sulfate (HH) is indicated by straight lines. The substitution are 20 wt.% limestone or 40 wt.% slag. The dotted red line between 40 to 45 mol.% of hemihydrate indicates the threshold between low and high calcium sulfate systems.

4.2 Formulations

Table 4.1: Studied compositions. The sample names are composed of the molar percentage of CA relative to HH and the wt.% of limestone substitution (C \bar{c} or Cc) or slag substitution (S).

Sample name	CA	HH	CAC	HH	C \bar{c} or S
	[mol.%]	[mol.%]		[wt.%]	
80CA-20HH	80%	20%	88.4	11.6	0.0
70CA-30HH	70%	30%	83.3	16.7	0.0
60CA-40HH	60%	40%	75.8	24.2	0.0
55CA-45HH	55%	45%	70.5	29.5	0.0
80CA-20HH-20Cc	80%	20%	70.7	9.3	20.0
70CA-30HH-20Cc	70%	30%	66.7	13.3	20.0
60CA-40HH-20Cc	60%	40%	60.6	19.4	20.0
55CA-45HH-20Cc	55%	45%	56.4	23.6	20.0
80CA-20HH-40S	80%	20%	53.1	6.9	40.0
70CA-30HH-40S	70%	30%	50.0	10.0	40.0
60CA-40HH-40S	60%	40%	45.5	14.5	40.0
55CA-45HH-40S	55%	45%	42.0	18.0	40.0

Calcium aluminate cement was blended with calcium sulfate β -hemihydrate (HH). The level of substitution is of 20 wt.% for limestone and 40 wt.% for slag systems. The compositions of the systems studied are presented on a ternary diagram in figure 4.1 and are listed in details in table 4.1.

4.3 Overview of hydration kinetics

The kinetics of hydration during the first 18 hours are shown in figure 4.2 for different levels of calcium sulfate and additions of slag and limestone. Figure 4.2a shows the heat flow of the lowest calcium sulfate system (80CA-20HH) without any substitution, with 20 wt.% limestone and with 40 wt.% slag. The amount of calcium sulfate increases by moving towards figure 4.2d, where are presented the heat flows of the systems with the highest calcium sulfate content (55CA-45HH). The height of the first peak is proportional to the amount of hemihydrate in the system (figure 4.3), while the second peak is slightly influenced by the amount of hemihydrate and strongly modified by the substitution level. Moreover, the time of occurrence of the first two peaks seems to be affected by the amount of substitution, no or little effect related to the amount of calcium sulfate. The third peak, if present, is highly influenced by the calcium sulfate amount and the substitution level. Therefore, both the calcium sulfate amount and the substitution level affect the kinetics of hydration.

The study characterizing the phase evolution during the early age of hydration is required to understand the origin of each peak and the factors affecting the kinetics. This study is divided in two main parts:

- Study of the effects of calcium sulfate.
- Study of the effects of substitution. Filler or “reactive filler” effect.

4.4 Effect of calcium sulfate

Figure 4.3 shows the kinetics of hydration of the four systems with variable calcium sulfate content without any substitution. The system with the more pronounced third peak (80CA-20HH) is considered first as there should be more evidence of the nature of this peak. Then, the system with the higher amount of hemihydrate (55CA-45HH) is studied.

4.4.1 Low calcium sulfate system

Figure 4.4 shows the diffractograms of the 80CA-20HH system during the first 16 hours of hydration. Hemihydrate is rapidly consumed during the first hours while gypsum forms. Ettringite appears already after 30 minutes of hydration and its amount increases with time. Traces of monosulfoaluminate are detected at 16 hours. In-situ XRD coupled with Rietveld

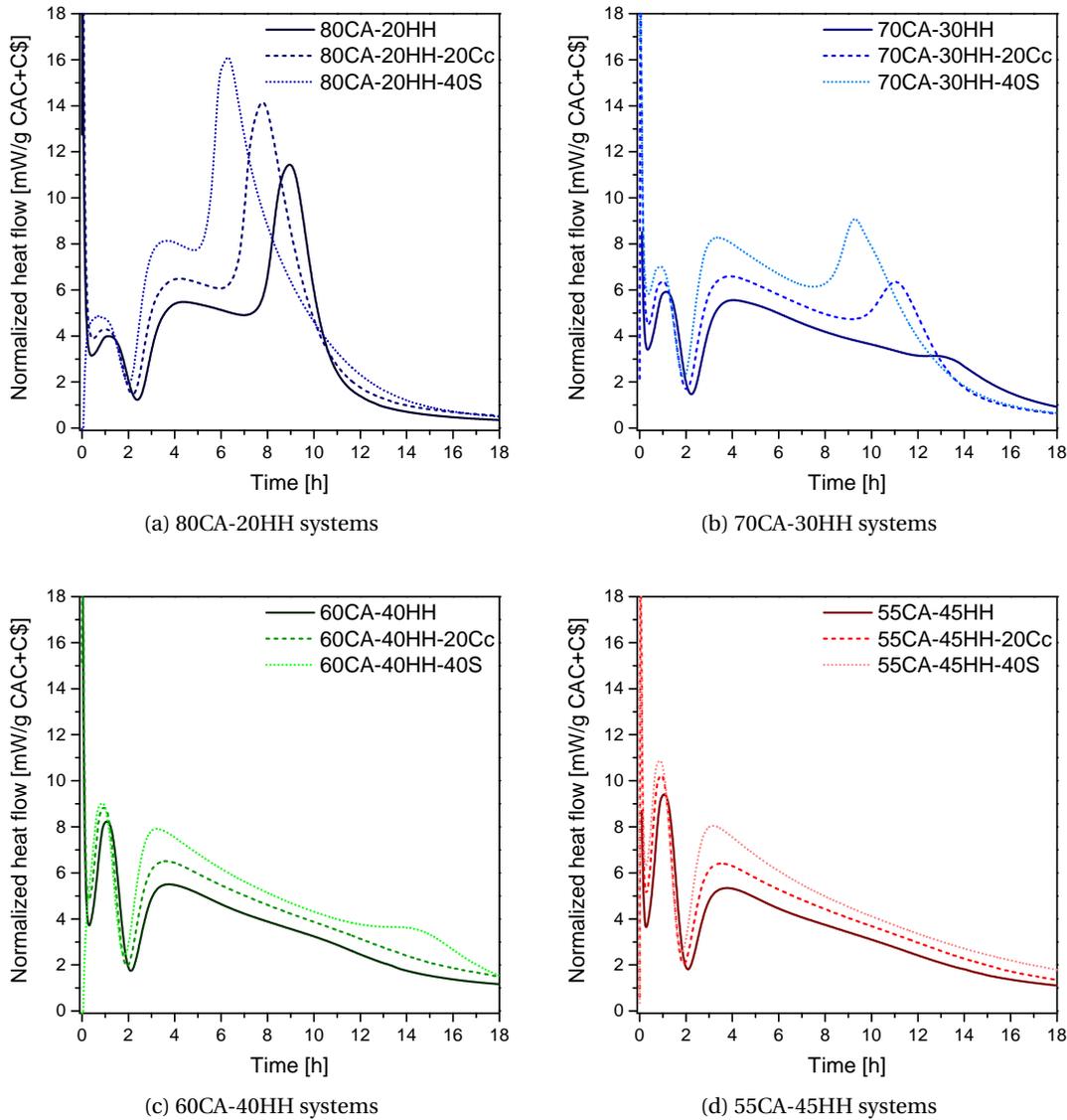


Figure 4.2: Hydration kinetics of the systems with variable calcium sulfate content and variable substitution levels.

analysis shows the crystalline phase evolution as in figure 4.5a, expressed in g per 100 g of anhydrous solid. The open symbols indicate the ex-situ XRD quantitative measurements. During the first peak, hemihydrate dissolves rapidly and gypsum precipitates. CA and C_4AF also dissolve during this period of time and some ettringite precipitates. The second peak is characterized by CA and gypsum dissolution and precipitation of the main phases - ettringite and probably amorphous aluminium hydroxide as described by reaction 2.6. The third peak coincides with gypsum depletion followed by rapid CA dissolution. The amount of ettringite is quite stable and monosulfoaluminate forms (detected only with ex-situ XRD, probably because of its poor crystallinity).

4.4. Effect of calcium sulfate

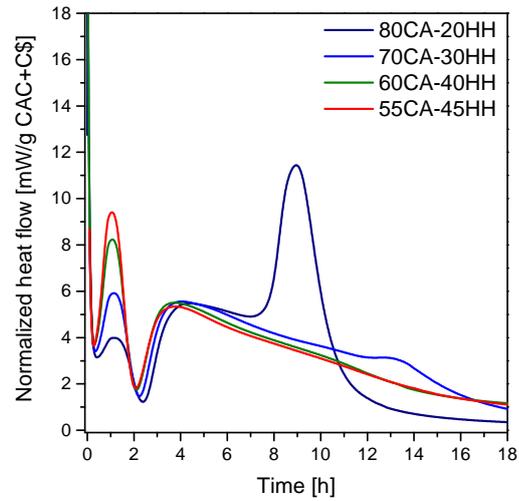


Figure 4.3: Hydration kinetics of the systems with variable calcium sulfate content without any substitution.

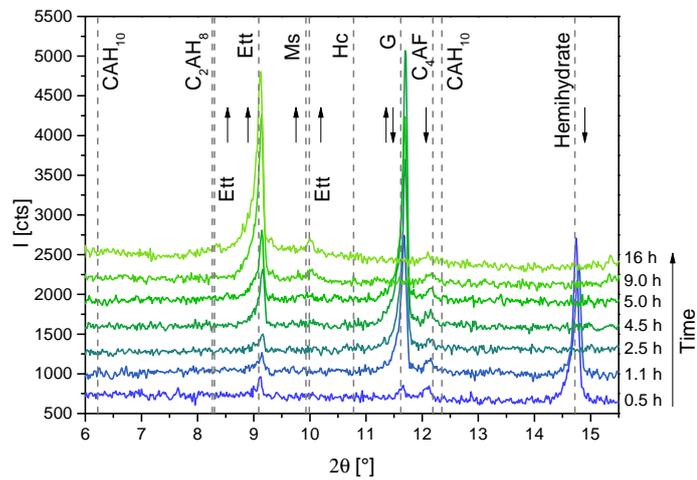


Figure 4.4: X-Ray diffractograms of the low calcium sulfate system 80CA-20HH during the first 16 hours of hydration.

Chapter 4. Early age hydration

Table 4.2: Enthalpies of dissolution reactions at 20°C. The detailed calculations are presented in appendix A.2.1.

Phase	Enthalpy of dissolution ΔH_d [J/g]
CA	-416.4
C ₄ AF	-1061.8
C \bar{S} H _{0.5}	-126.1
C \bar{S} H ₂	6.4
Ettringite	172.0
Monosulfoaluminate	75.5
AH ₃ microcrystalline	-29.5

The derivative of the phase content with respect to time is shown in figure 4.5c for CA and gypsum. The reaction rate of CA, defined as $r(t) = dm/dt$, is always negative indicating its dissolution while the reaction rate of gypsum is firstly positive indicating its precipitation followed by a negative period when it is dissolving (note that the left-y axis is inverted). The peaks appearing in the derivative curves coincide with the peaks of the heat flow measurements. The reaction rates of the main phases are used to calculate the heat produced or consumed by each phase during its dissolution (negative dm/dt) or precipitation (positive dm/dt) with the following equation

$$\text{Cumulative heat} = \frac{m(t) - m(t=0)}{100} \Delta H_d \quad (4.1)$$

where the enthalpies ΔH_d describing the dissolution reactions are listed in table 4.2 and detailed in appendix A.2.1. They are calculated from the enthalpies of formation found in the CEMDATA14 database [78]. Figure 4.5b shows the comparison between the measured heat and the calculated heat from in-situ XRD measurements. The comparison between these two different measurements is useful to emphasize the influence of each phase on the heat generation. The dissolution of the main phase of the cement, CA, has the highest influence on the heat generated by exothermic reactions. Minor phases such as C₄AF have minor influence. The dissolution of hemihydrate produces a low amount of heat and the precipitation-dissolution of gypsum is negligible. Massive amounts of ettringite formation lead to an important heat release due to exothermic reactions. Amorphous aluminium hydroxide formation is estimated by mass balance according to reaction 2.6 and its formation occurs in an endothermic reaction. When calcium sulfate is depleted, there is formation of monosulfoaluminate which produces negligible heat. The measured and the calculated heat differ slightly but show the same trends. The experimental error due to in-situ XRD measurements and probably the variation of stoichiometric coefficients assumed in the reactions to calculate the enthalpies are responsible for the small differences. The fast dissolution of CA during the first 2 hours of hydration is not clearly understood and leads to the main discrepancy between the calculated and measured heat flow. The in-situ measurements of the other systems do not show such rapid CA dissolution at the beginning.

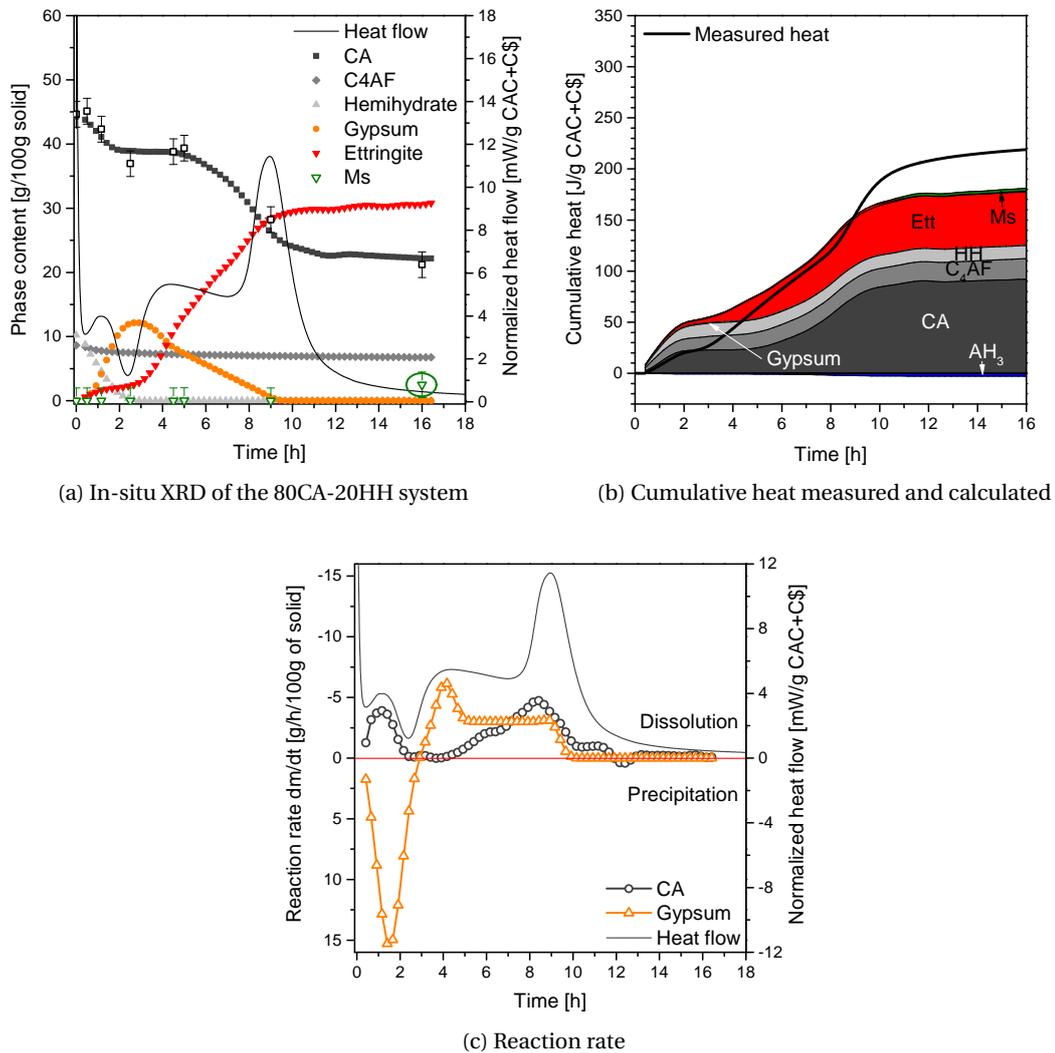


Figure 4.5: In-situ XRD analyses of the low calcium sulfate system 80CA-20HH.

The concentrations resulting from the pore solution analyses at selected intervals of hydration are shown in figure 4.6a. The initial rapid dissolution of hemihydrate leads to high Ca^{2+} and SO_4^{2-} concentrations as the solubility of hemihydrate is 125.1 mmol/L [78]. When hemihydrate is exhausted, the concentrations of calcium and sulfate ions are below the solubility of gypsum which is 16.2 mmol/L and decrease to negligible values when gypsum is depleted. The concentration of aluminium hydroxyl ions is stable during the first 5 hours and increases when sulfate ions are exhausted at 9 hours.

The saturation index of the main anhydrous phase and of the main hydrates are calculated from the concentration of the solution. Figure 4.6b shows the saturation index as a function of time. A saturation index of 0 indicates equilibrium conditions while a positive saturation index indicates that the phase should precipitate and a negative saturation index indicates

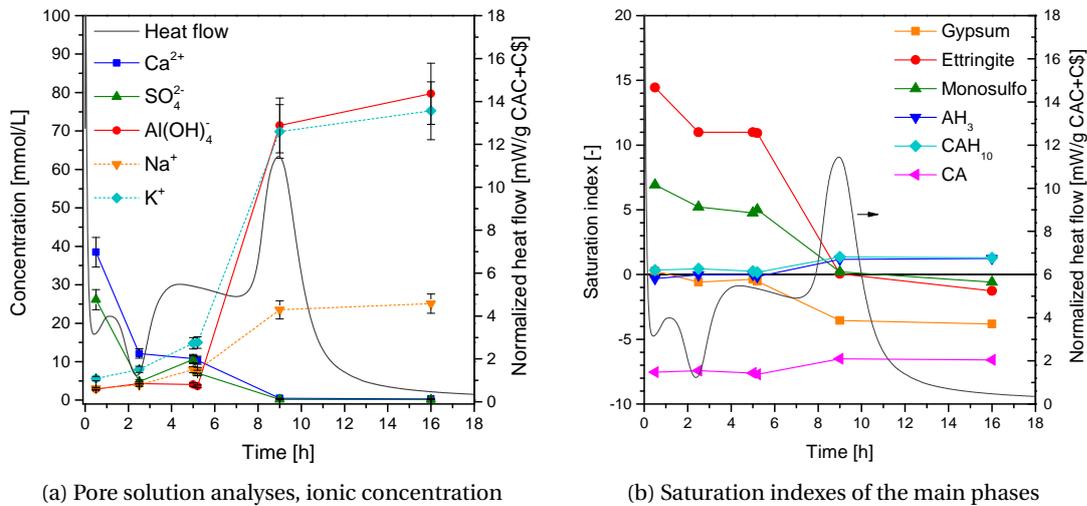


Figure 4.6: Pore solution analyses of the low calcium sulfate system 80CA-20HH.

that the phase should dissolve or not precipitate at all. Monocalcium aluminate is highly undersaturated during the first 5 hours of hydration and after it becomes less undersaturated as its reaction rate increases*. Consequently, the undersaturation is not the cause of the faster CA dissolution when calcium sulfate is depleted. It is not possible with the actual experimental results to draw clear conclusions on the reason why CA dissolution is slowed down in presence of calcium sulfate, nevertheless the adsorption of sulfate ions on active dissolution sites of CA could explain the experimental observations.

Moving back to figure 4.6b, gypsum is close to equilibrium during the first 5 hours and becomes undersaturated when is depleted. Ettringite and monosulfoaluminate are supersaturated when calcium sulfate is in excess and become close to equilibrium when gypsum is depleted. Aluminium hydroxide and CAH₁₀ are close to equilibrium before gypsum depletion and after become supersaturated. The amorphous or poorly crystalline aluminium hydroxide is not detected with XRD but is detected with TGA analyses and SEM-EDS analyses as shown below in section 4.4.4. The same consideration can be done for CAH₁₀ as it is not detected with XRD and may be poorly crystalline.

*The theoretical solubility of CA is high as in the thermodynamic database (1087 mmol/L for Ca²⁺ and 2Al(OH)₄ ions [78]). The solubility decreases to 20.5 mmol/L for Ca²⁺ and 18.2 mmol/L for 2Al(OH)₄ ions if we consider the solubility measured by dissolution experiments [138]. The lower solubility is due apparently to the hydroxylated surface layer of Ca[Al(OH)₄]₂ on CA particles. In both cases CA is always undersaturated.

Low calcium sulfate system with 40 wt.% of slag

From figure 4.2a it can be noticed that the system with 40 wt.% of slag substitution has a more pronounced third peak than the system without substitution, indicating a stronger effect of sulfate depletion on the heat evolution. Therefore, in-situ XRD analyses of this system are presented in figure 4.7a to confirm and better describe what has been said previously.

The CA consumption during the first hours of hydration is smaller in this system compared to the previous system without substitution. The main difference between this system and the one without substitution is the consumption of ettringite after the exhaustion of calcium sulfate, indicating that reaction 2.7 occurs. Here again, monosulfoaluminate is detected only by ex-situ XRD.

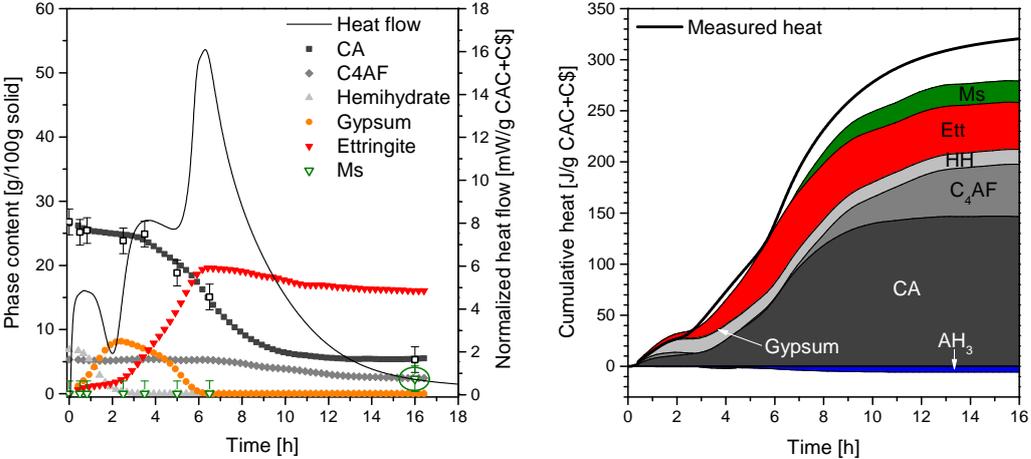
The reaction rate of monocalcium aluminate is shown in figure 4.7c. It clearly follows the isothermal calorimetry curve and highlights the rapid dissolution of CA after sulfate depletion. The cumulative heat is calculated from the reaction rate of the main phases as shown in figure 4.7b. The calculated heat is closer to the measured heat for this system than for the one without substitution. As the effect of sulfate is more pronounced here, the relative errors are probably smaller and a better agreement is obtained between the calculation and the measurement.

4.4.2 High calcium sulfate system

Figure 4.8a shows the in-situ XRD results for the 55CA-45HH system. Hemihydrate is rapidly consumed during the first hours of hydration while gypsum forms. Ettringite forms from the beginning from the reaction between CA and the sulfates in solution. The reaction of CA is slower than in the previous systems as there is always an excess of calcium sulfate. Ettringite content increases during the whole period of the measurement. No third peak is observed here.

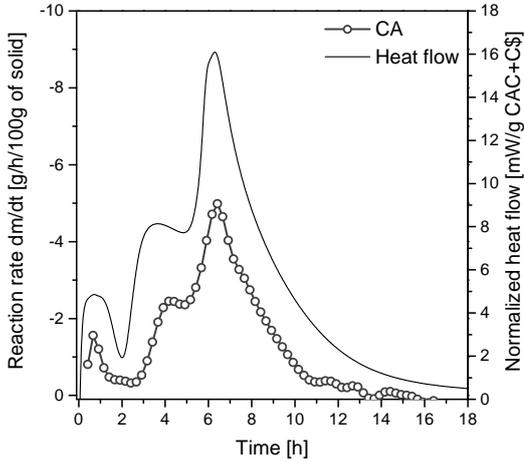
The calculated heat is close to the measured cumulative heat as shown in figure 4.8b. Here, the main phases participating in the exothermic reaction are CA, hemihydrate and ettringite.

The pore solution of this system was analysed only at 5 and 16 hours as the characterization of the first peak was done in the low calcium sulfate system. Figure 4.8c shows that the calcium, aluminium and sulfate concentrations are stable over time as there are always anhydrous phases in excess. The alkali concentration increases as the CA dissolution proceeds. The saturation index is stable for all the phases; ettringite and monosulfoaluminate are always supersaturated as shown in figure 4.8d. The undersaturation of CA is stable.



(a) In-situ XRD of the 80CA-20HH-40S system

(b) Cumulative heat measured and calculated



(c) Reaction rate

Figure 4.7: In-situ XRD of the low calcium sulfate system 80CA-20HH with 40 wt.% of slag.

4.4. Effect of calcium sulfate

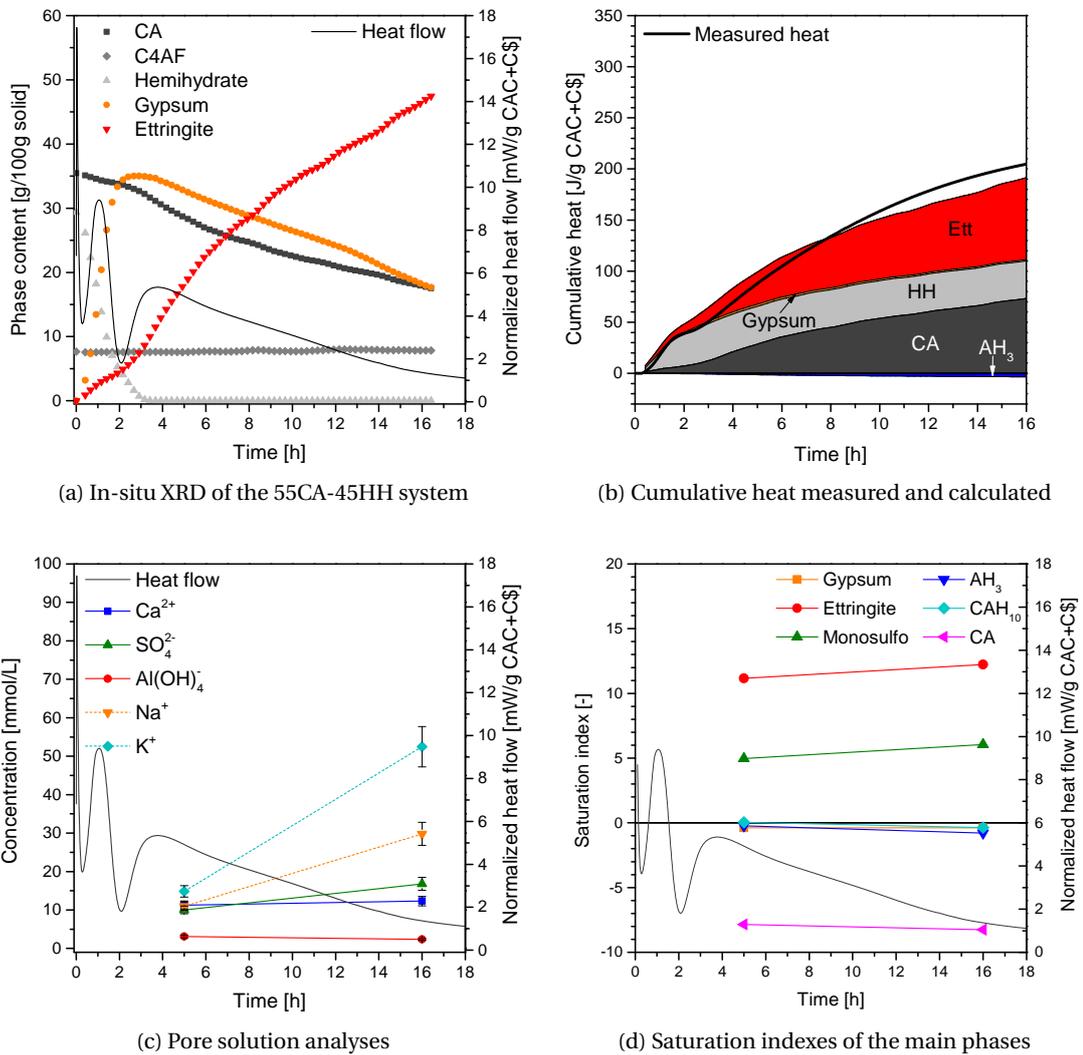


Figure 4.8: In-situ XRD characterization and pore solution analyses of the high calcium sulfate system 55CA-45HH.

4.4.3 Comparison between low and high calcium sulfate

Figure 4.9 shows the concentration of calcium, sulfate and aluminium ions in solution at 16 hours as a function of calcium sulfate. As expected, calcium and sulfate ions increase with hemihydrate content and there is a clear increase between 30 to 45 mol% of calcium sulfate. The concentration of aluminium hydroxyl ions decreases as calcium sulfate increases. The systems below 40 mol% of calcium sulfate are referred to as low calcium sulfate systems whereas the systems above this value are called high calcium sulfate systems in this manuscript.

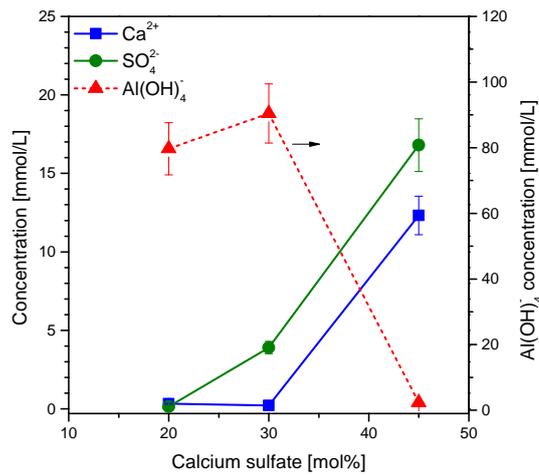


Figure 4.9: Concentration of the pore solution as a function of calcium sulfate at 16 hours.

4.4.4 Characterization of microstructure and phase assemblage

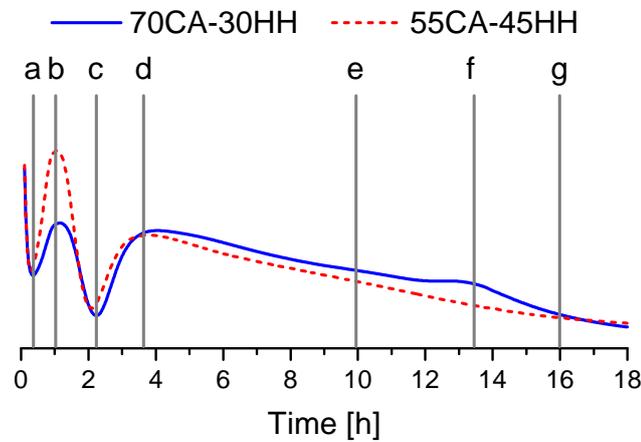
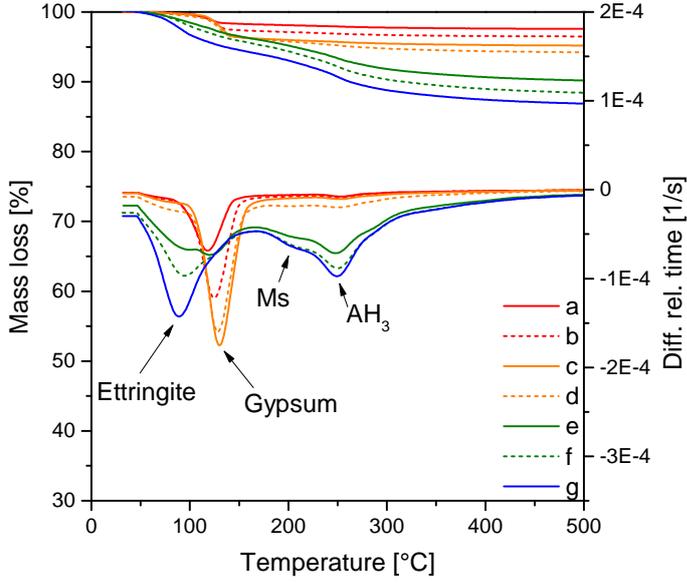


Figure 4.10: Labelling of the main calorimetric peaks for each time of analysis.

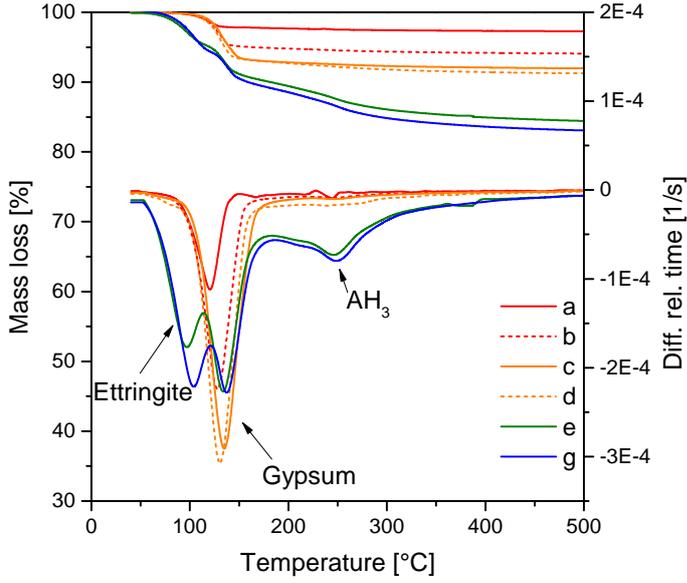
In this section the development of the phases assemblage and microstructures of low calcium sulfate and high calcium sulfate systems are compared. These analyses were done on similar compositions to the ones presented in the previous section but using a different batch of materials, therefore there can be some small differences in the kinetics. The low calcium sulfate system analysed here is the 70CA-30HH, rather than 80CA-20HH, while the high calcium sulfate system is the same as before 55CA-45HH. Figure 4.10 shows the calorimetric curve of these two systems with the labels indicating each time of analysis.

Figure 4.11 shows the TGA analyses of these systems. The gypsum peak of the low calcium sulfate system (figure 4.11a) increases during the first hours until reaching the maximum at time step *c*, followed by its consumption and formation of ettringite. Amorphous aluminium hydroxide starts to form from the second peak. Some traces of monosulfoaluminate are detected at the third peak. Other AFm phases or CAH_{10} which were predicted from the saturation index calculated from the pore solution analyses would not be easy to identify as their dehydration peaks overlap with the ettringite and gypsum peaks. The TGA analyses of the high calcium sulfate system (figure 4.11b) confirm the formation of ettringite and aluminium hydroxide. The amount of aluminium hydroxide increases slightly between time *e* to *g*.

Figures 4.12 and 4.13 show the microstructure evolution of low (left) and high (right) calcium sulfate systems. At the first peak there is still some hemihydrate dissolving and there are the calcium aluminate cement grains (figure 4.12.b). Gypsum forms between CAC grains as the hydration proceeds to time *c* (figure 4.12.c). During the second peak (figure 4.12.d) there are still gypsum grains and the first aluminate containing hydrates start to form but they are not clearly visible. After the second peak, (figure 4.13.e) the hydrated matrix is clearly visible with ettringite characterized by bright grey levels and amorphous aluminium hydroxide by dark grey. From time *e* to *g*, only a densification of the hydrated matrix is observed, other hydrates such as monosulfoaluminate are hardly visible as they are intermixed.



(a) 70CA-30HH



(b) 55CA-45HH

Figure 4.11: TGA and DTG analyses of the low (left) and high (right) calcium sulfate system at early ages.

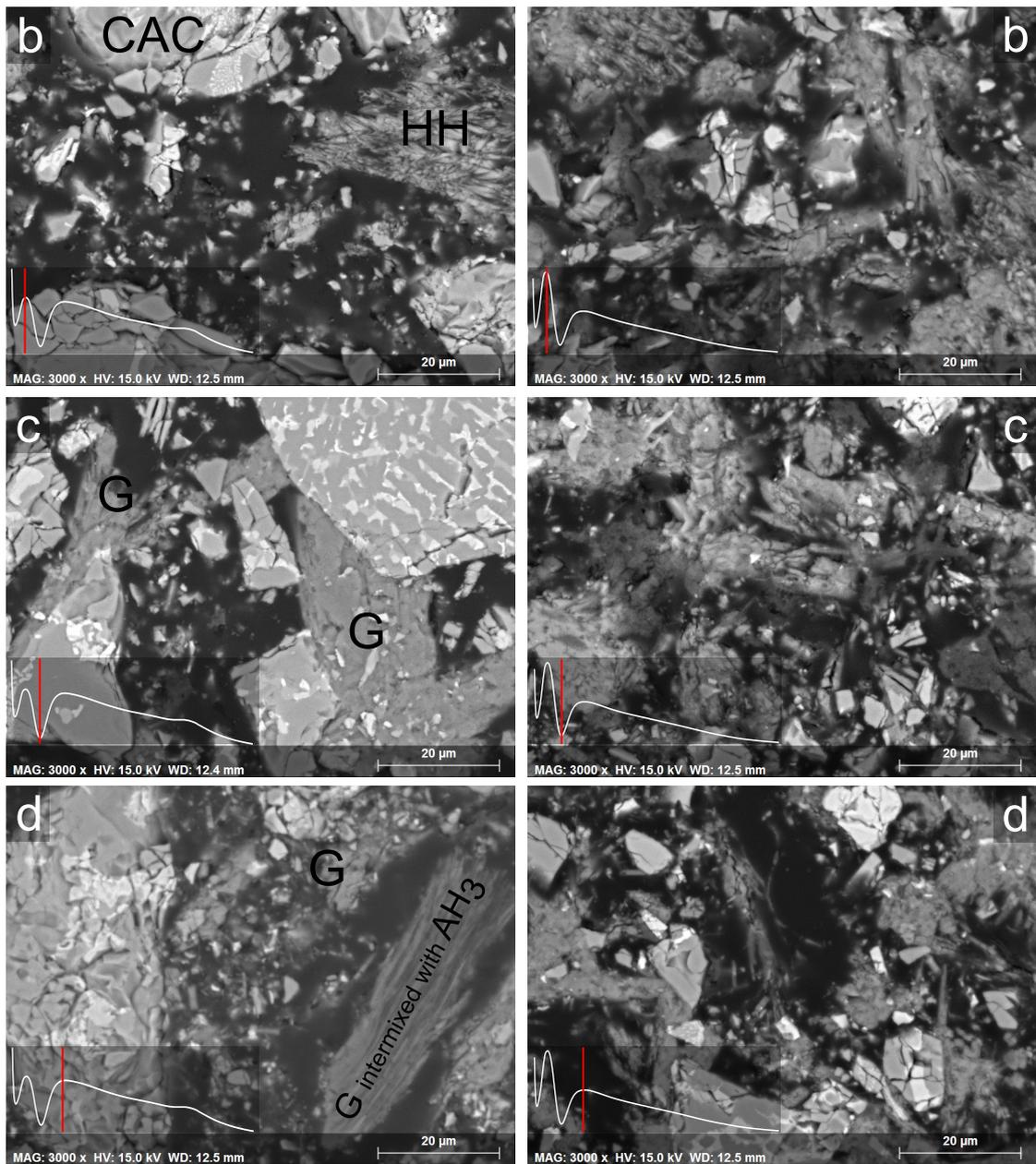


Figure 4.12: Microstructure of the low (70CA-30HH, left) and high (55CA-45HH, right) calcium sulfate systems during the first 4 hours of hydration.

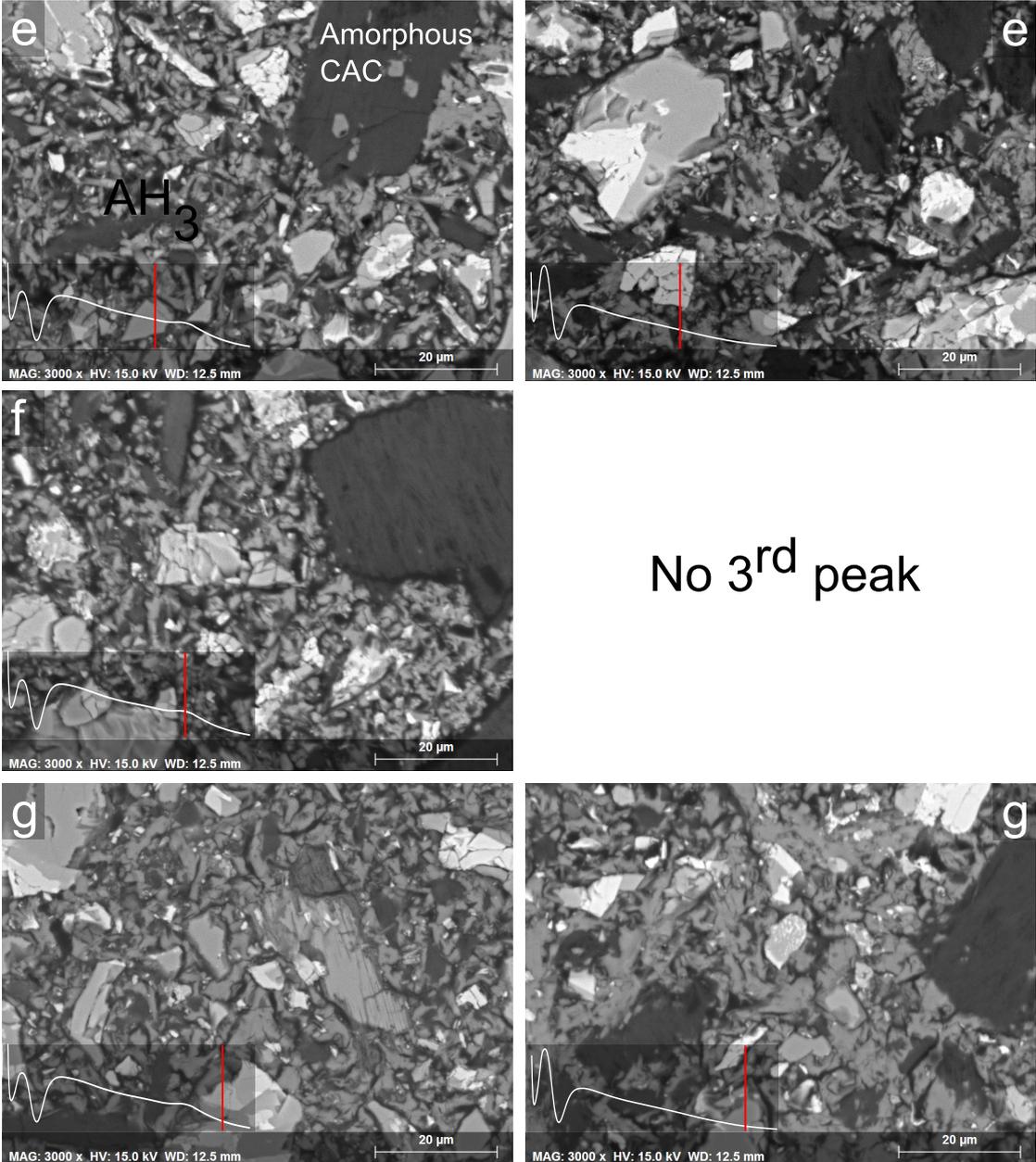


Figure 4.13: Microstructure of the low (70CA-30HH, left) and high (55CA-45HH, right) calcium sulfate systems between 10 to 16 hours of hydration.

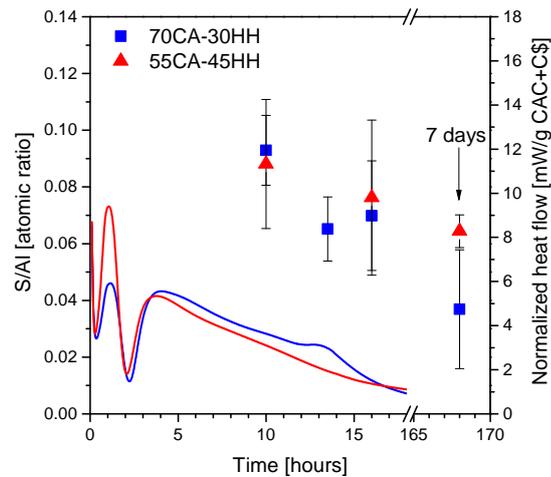
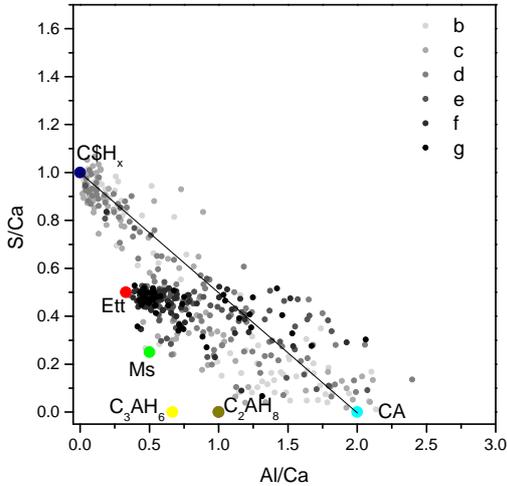


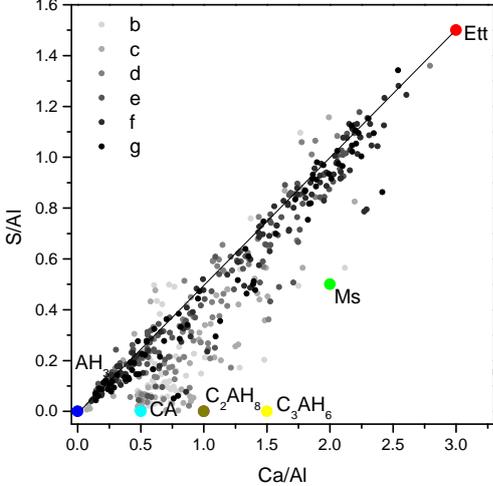
Figure 4.14: Adsorption of sulfate on aluminium hydroxide gel measured with SEM-EDS analyses.

The first in-situ XRD measurement shown in figure 4.5a shows that ettringite remains as the main hydrate phase even after gypsum depletion. This could be due to sulfate adsorption on amorphous aluminium hydroxide or on ettringite which is then released after gypsum depletion. As aluminium hydroxide is negatively charged, there should be cations (such as Ca^{2+}) adsorbed on the surface and then the sulfates adsorbed on the cations. The measure of sulfate adsorbed on ettringite is hardly feasible as the phase itself is rich in sulfate. Nevertheless, the elemental ratio of sulfate to aluminates of aluminium hydroxide is shown in figure 4.14. The measures start from 10 hours of hydration (time e) as no aluminium hydroxide was detected before. The analysis at 7 days is presented just to better show the trend. The S/Al ratio decreases with time and the first points are comparable between low and high calcium sulfate systems. As the time increases, the low calcium sulfate system has lower S/Al values indicating a potential desorption of sulfate ions from AH_3 in the solution. Probably, the slow consumption of ettringite after gypsum depletion is due to a kinetic effect and to the desorption of sulfate ions from amorphous aluminium hydroxide. Studies on pure systems composed of C_3A -gypsum without AH_3 report a direct consumption of ettringite when calcium sulfate is depleted followed by rapid precipitation of monosulfoaluminate [19].

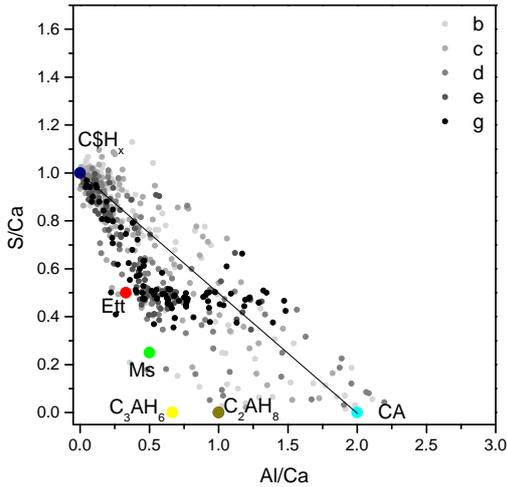
Chemical analyses on polished sections with SEM-EDS analyses show the main phases forming in these systems on elemental ratio plots. The analyses of the low calcium sulfate system during the first hours of hydration show, in figures 4.15a and 4.15b, points around gypsum and CA composition (bright dots). As the hydration proceeds, the cloud of points (from bright to dark dots) moves towards ettringite, aluminium hydroxide and monosulfoaluminate compositions highly intermixed. The analyses of the high calcium sulfate system are shown in figures 4.15c and 4.15d. Initially, the bright dots confirm the presence of gypsum and CA and, as the hydration evolves, the cloud of points moves towards ettringite, aluminium hydroxide and gypsum composition as it is in excess.



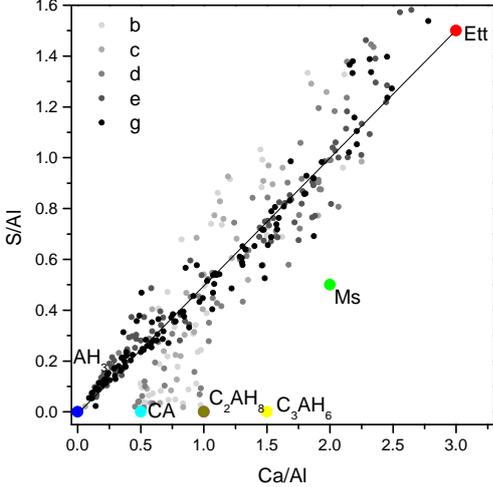
(a) EDS analyses of the 70CA-30HH system



(b) EDS analyses of the 70CA-30HH system



(c) EDS analyses of the 55CA-45HH system



(d) EDS analyses of the 55CA-45HH system

Figure 4.15: EDS analyses at early ages.

4.5 Effect of supplementary cementitious materials

4.5.1 Effects on the kinetics

The substitution clearly has an effect on the kinetics of hydration as previously shown in figure 4.2. Two distinct effects are identified:

- The calorimetric peaks occur earlier and their slopes are steeper, especially for the third peak.
- The intensity of the peaks increases with the substitution level.

From the comparison of the in-situ XRD results of the low calcium sulfate system presented in the previous section in figures 4.5a and 4.7a, a faster nucleation of gypsum and ettringite is observed with 40% substitution. There is also a faster consumption followed by exhaustion of calcium sulfate resulting to the occurrence of the third peak. More space due to inert substitution during the first hours of hydration also leads to an apparent increase of the water to reactive binder ratio[†]. The space effect leads to a more intense third peak; this is mainly due to a higher degree of hydration of CA, which is around 80% for the system with 40 wt.% substitution against 50% for the system without any substitution, and results in higher heat flow generated by the faster dissolution of the anhydrous phase. More details about the filler effect are given in section 2.3.1.

The slope of the acceleration period of the first peak seem not to be affected but the slopes of the second and third peaks are highly affected by the substitution as shown in figure 4.16a. The second peak is slightly affected by the calcium sulfate amount and its slope increases with the substitution level. The third peak is highly affected by the calcium sulfate amount as shown in the previous section. The values close to or below zero indicate that there is no peak. Moreover, the slope of the third peak of the low calcium sulfate system increases strongly with the substitution level. Higher slopes indicate faster reaction rates of the anhydrous cement. This indicates that the acceleration period of the calorimetric peaks is highly influenced by the substitution level due to nucleation effects. The extra surface of the substitution provides sites for nucleation of hydrates and this effect can vary according to the affinity between SCM and the hydrates.

The cumulative heat at 16 hours of hydration increases with the substitution level and decreases with the calcium sulfate amount as shown in figure 4.16b. The increase in space for hydration products due to inert substitution can be compared to an increase in the water to binder ratios. Previous studies on plain CAC showed that [23] the water to binder ratio affects mainly the deceleration period of the calorimetric peaks and the cumulative heat. More space for the growth of the hydrates is followed by higher cumulative heat. The hydration kinetics

[†]20 wt.% and 40 wt.% inert substitution correspond to a water to reactive binder (CAC+C₅) ratio of 0.5 and 0.67, respectively.

Chapter 4. Early age hydration

for different water to binder ratios of the low calcium sulfate system (70CA-30HH) are shown in figure 4.17. These measurements were done on another batch of materials, therefore the kinetics are slightly different from the ones presented in figure 4.16. As the water to binder ratio increases, there is more space between the anhydrous grains and more space for hydrate growth. This affects the deceleration period of the second peak and the intensity of the third peak. When 40 wt.% of slag is added, which corresponds to a w/b of 0.67, the peaks intensity increase and the peaks occur before. These differences are due to nucleation effects.

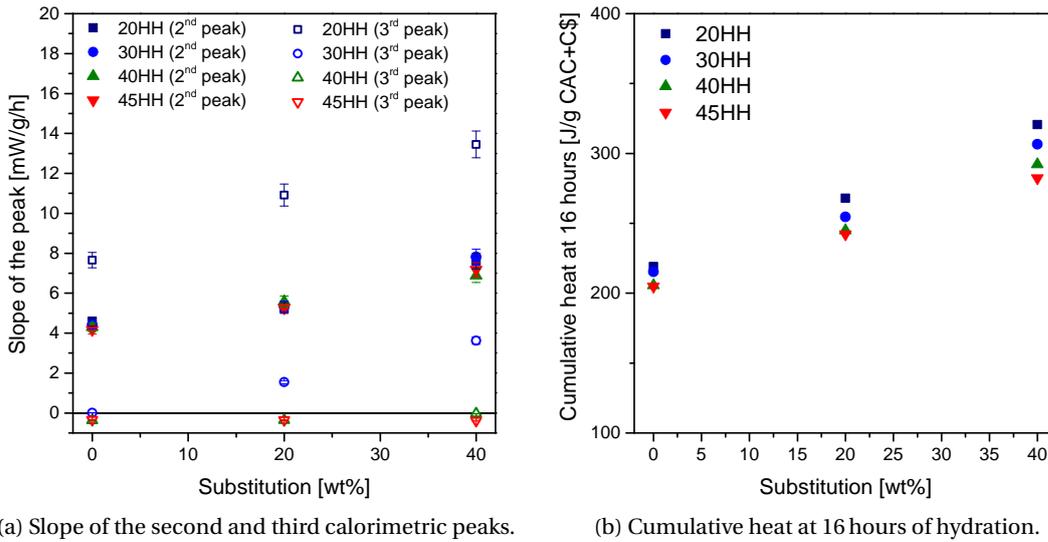


Figure 4.16: Slope of the acceleration period of the second and third calorimetric peaks and cumulative heat for different calcium sulfate amounts as a function of the substitution level.

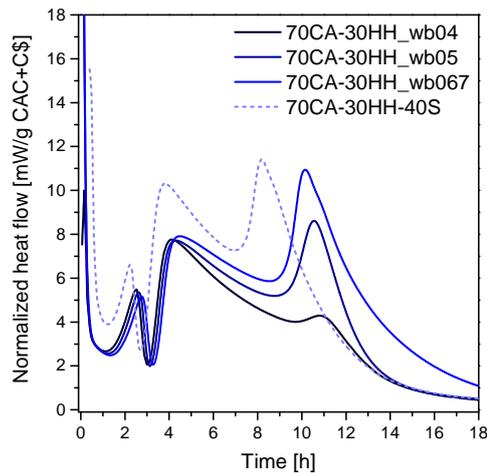


Figure 4.17: Hydration kinetics of the low calcium sulfate systems (70CA-30HH) with variable water to binder ratio and substitution.

4.5.2 Effects on the pore solution

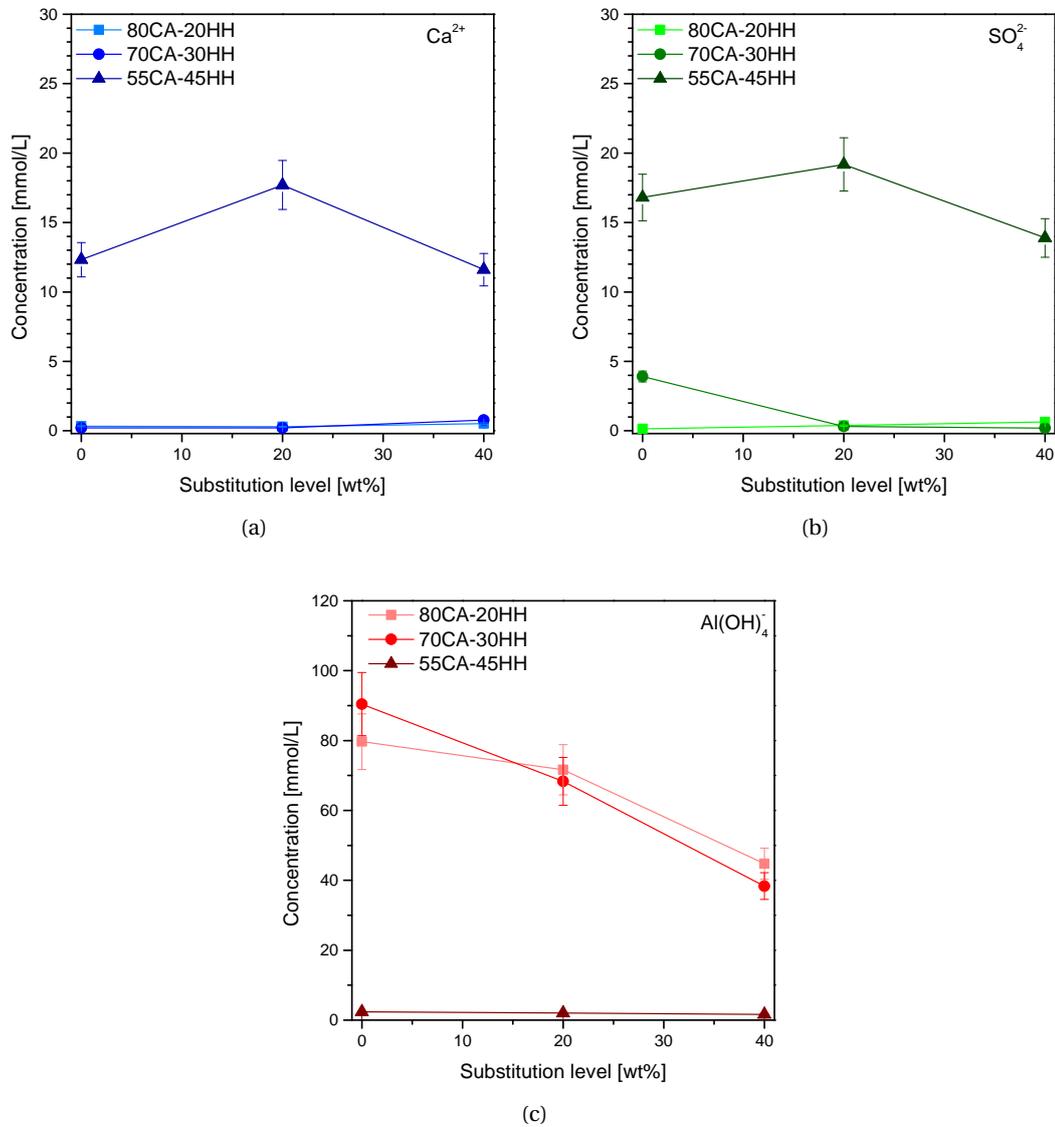


Figure 4.18: Concentration of calcium, sulfate and aluminate ions of the pore solution at 16 hours of hydration as a function of the substitution level.

Figure 4.18 shows the concentrations of calcium, sulfate and aluminate ions at 16 hours of hydration. The calcium concentration is quite stable with the substitution level and is negligible for low calcium sulfate systems, both 80CA-20HH and 70CA-30HH. Calcite dissolution experiments in alkaline solutions showed that calcium concentration goes up to 0.4 mmol/L [42]. Therefore, in the system with 20 wt.% C \bar{c} this would not be noticeable. The sulfate concentration is stable with the substitution level and is higher for the high calcium sulfate system. There is an earlier exhaustion of sulfates in the undersulfated systems because of the accelerated kinetics caused by the filler effect. The aluminate ions decrease with the substitution level and

Chapter 4. Early age hydration

are always close to zero for the 55CA-45HH system. This is likely to be due to the dilution effect of the substitution, probably the aluminate concentration is controlled by CA dissolution and not by the hydrate growth as it happens for the other species. The silica concentrations are not presented as the values are below 0.01 mmol/L which is close to the detection limit of the measurement. No or little silica in solution and the absence of silicate hydrates suggest that slag acts as filler during the first day of hydration.

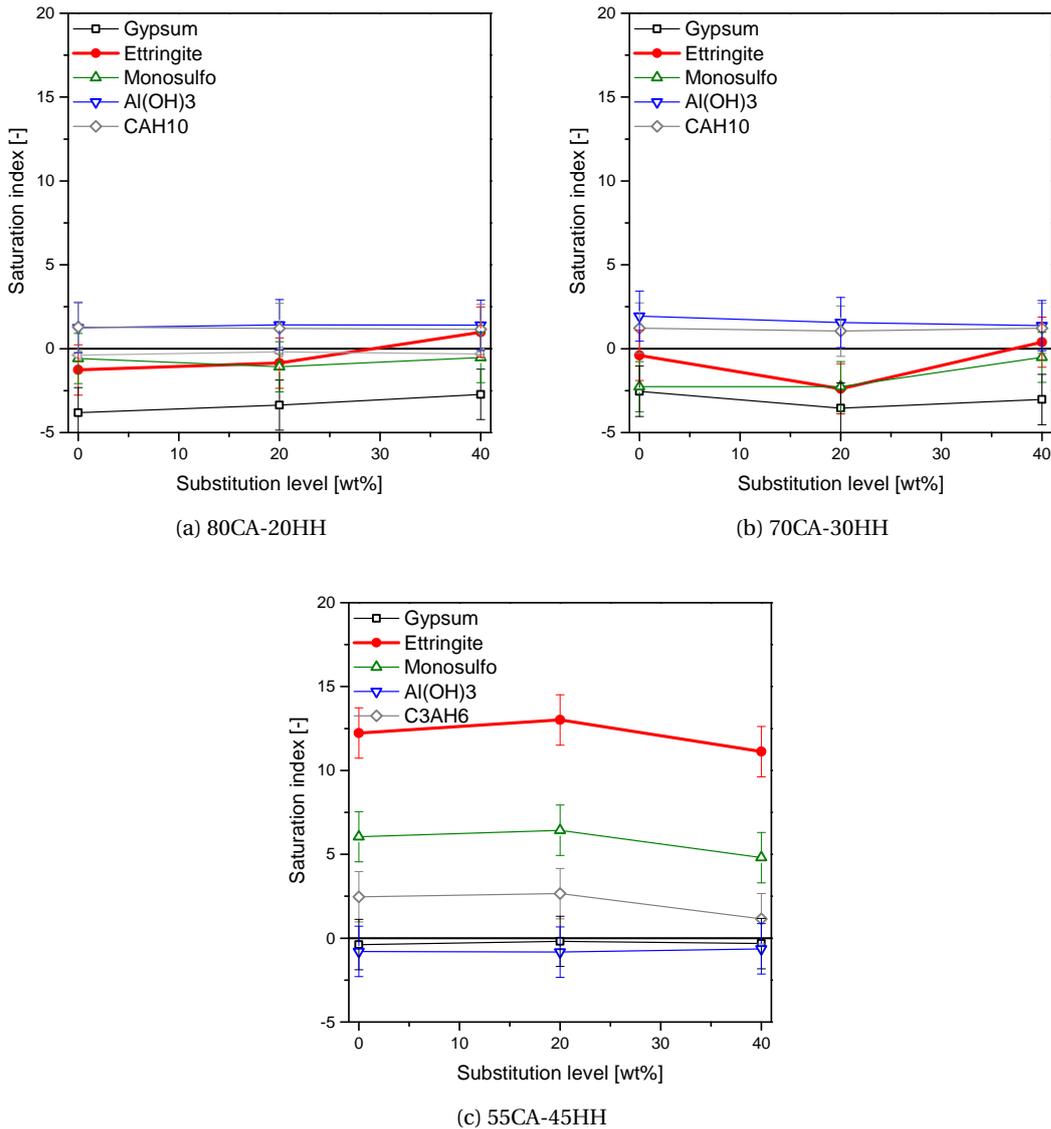


Figure 4.19: Saturation index of the main phases at 16 hours of hydration as a function of the substitution level.

The saturation index of the main hydrates is shown as a function of the substitution level in figure 4.19. Here again the substitution level does not have a clear impact on the saturation. The saturation index of ettringite increases slightly with the substitution but the values are within the error of the measures. The only and clear difference is due to the amount of calcium sulfate; where the saturation index of ettringite increases considerably, from negative values to 12 ± 2 .

4.6 Summary on the early age hydration

4.6.1 Effect of sulfate

The study of the kinetics and on the effect of calcium sulfate shows that there are three calorimetric peaks when calcium sulfate is exhausted and the origin of these peaks, shown in figure 4.20, are summarised here:

- First peak: rapid dissolution of hemihydrate followed by the precipitation of gypsum.
- Second peak: dissolution of CA and gypsum followed by ettringite and amorphous aluminium hydroxide precipitation (reaction 2.6).
- Third peak: accelerated reaction of CA and gypsum depletion, followed by ettringite consumption and monosulfoaluminate formation (reaction 2.7). It is difficult to observe monosulfoaluminate with XRD as it may be poorly crystalline at this stage of hydration [18]. The presence of both monosulfoaluminate and amorphous aluminium hydroxide is confirmed by TGA and EDS analyses.

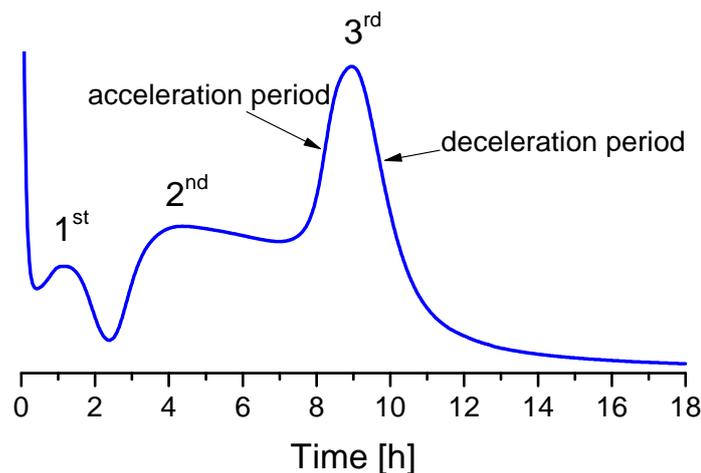


Figure 4.20: Illustration of the main peaks of isothermal calorimetry curves.

This study confirms that CA dissolution is slowed down as long as there are calcium and/or sulfate ions in solution. The peaks measured by calorimetry are mainly due to CA dissolution. In the literature it is usually attributed to the depletion of gypsum and formation of monosulfaluminate [139, 18], but this is the consequence and is not the cause of the peak. The retarded CA hydration and the origin of the third peak could be due to sulfate adsorption on CA active dissolution sites as described in other studies on C₃A-gypsum hydration [26, 28, 20, 22, 19].

4.6.2 Filler effect

Supplementary cementitious materials such as limestone or slag act as inert fillers at early age in blends of calcium aluminate cement and hemihydrate. The substitution has a clear physical filler effect that influences strongly the kinetics and is distinguished by nucleation and space effect:

- There are more nucleation sites with inert substitution leading to more surfaces for the heterogeneous nucleation of the hydrates and growth, therefore the reaction of cement is accelerated. This is valid when the particle size of the substitution are smaller than the ones of the cement. The acceleration period of the calorimetric peaks are steeper and the intensities are higher.
- There is more space available for hydrate growth due to dilution effect. The concentration of the pore solution and the saturation index of the main hydrates is almost not affected by the substitution at 16 hours, except the aluminium hydroxyl ions. This affects the deceleration period of the second calorimetric peak, and the intensity and deceleration period of the third peak.

This chapter shows that supplementary cementitious materials act as fillers at early age, they have a physical effect. The study of long term hydration up to one or two years is needed to understand their chemical effect and quantify their reaction in calcium aluminate cement blended with variable amounts of calcium sulfate. The effect of calcium sulfate on the pore solution and the apparently inert effect of SCM is linked to the expansion mechanisms in chapter 6.

5 Long term hydration with SCM

Contents

5.1 Introduction	67
5.2 Formulations	68
5.3 Systems containing limestone	69
5.3.1 Compressive strength	69
5.3.2 Hydration kinetics	71
5.3.3 Experimental and thermodynamic prediction of phase assemblages	72
5.3.4 Porosity evaluation and links to compressive strength	79
5.3.5 Microstructure characterization	82
5.3.6 Summary on systems containing limestone	84
5.4 Systems containing slag	85
5.4.1 Compressive strength	85
5.4.2 Hydration kinetics	85
5.4.3 Experimental phase assemblage	86
5.4.4 Microstructure and degree of reaction of slag by SEM-IA	91
5.4.5 Thermodynamic simulation	95
5.4.6 Summary on systems containing slag	98

5.1 Introduction

The study of hydration over longer periods of time looks at the impact of limestone and slag on the CAC-C \bar{s} systems. The effect of the relative amounts of calcium sulfate and calcium aluminate on the reaction of SCM from the first day of hydration to one or two years is investigated. Strength development is linked to the degree of hydration, phase formation and the reaction of SCM. Thermodynamic simulations are used to understand the impact of calcium sulfate content on the phase assemblage of these systems and to estimate the maximum amount of SCM which can react. The part of this chapter concerning limestone has

been submitted for publication as “Limestone reaction in calcium aluminate cement-calcium sulfate systems” [140].

5.2 Formulations

Calcium aluminate cement was blended with variable amounts of calcium sulfate β -hemihydrate ranging from 10 to 30 wt.%. The level of substitution is of 20 wt.% for limestone and 40 wt.% for slag systems. Systems substituted with inert quartz (Q) instead of the reactive filler were also prepared for compressive strength tests and isothermal calorimetry measurements. This was done to separate the physical and the chemical effects of the substitution discussed in the previous chapter. To have comparable physical effects it is important to have similar particle size distributions (PSD) for quartz and reactive fillers as shown in section 3.1, figure 3.1. Despite the fact that limestone and quartz K13 or slag and quartz K10 have slightly different PSD, isothermal calorimetry was done to find the quartz that gave the closest heat flow evolution compared to limestone or slag systems. Moreover, substitution should be at constant volume when studying the filler effect but in this work constant mass was chosen and calorimetry confirmed that both filler and SCM had comparable heat flows*.

The compositions of the systems studied are presented on a ternary diagram in figure 5.1 and are listed in details in table 5.1 for limestone systems and in table 5.2 for slag systems.

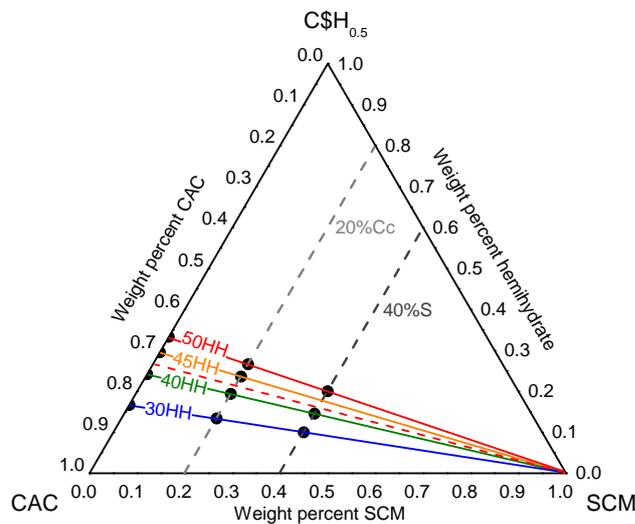


Figure 5.1: Ternary diagram showing the studied compositions. The molar amount of calcium sulfate (HH) is indicated by straight lines. The substitution are 20 wt.% limestone or 40 wt.% slag. The dotted red line between 40 to 45 mol.% of hemihydrate indicates the threshold between low and high calcium sulfate systems.

*As densities are very similar between limestone (2.71 [g/cm³]) and quartz (2.65 [g/cm³]), there is not much difference in volume when adding 20 wt.% of powder. For slag there is more difference as its density (2.97 [g/cm³]) is higher than the one of quartz and the replacement is of 40 wt.%.

5.3. Systems containing limestone

Table 5.1: Studied compositions. The sample names are composed of the molar percentage of CA relative to HH and the wt.% of limestone substitution (C \bar{c}) or quartz substitution (Q). The 50CA-50HH-20C \bar{c} composition is only for compressive strength tests.

Sample name	CA	HH	CAC	HH	C \bar{c} or Q
	[mol.%]		[wt.%]		
70CA-30HH	70%	30%	83.3	16.7	0.0
60CA-40HH	60%	40%	75.8	24.2	0.0
55CA-45HH	55%	45%	70.5	29.5	0.0
70CA-30HH-20Cc	70%	30%	66.7	13.3	20.0
60CA-40HH-20Cc	60%	40%	60.6	19.4	20.0
55CA-45HH-20Cc	55%	45%	56.4	23.6	20.0
50CA-50HH-20Cc	50%	50%	53.4	26.6	20.0

Table 5.2: Studied compositions. The sample names are composed of the molar percentage of CA relative to HH and the wt.% of slag substitution (S) or quartz substitution (Q).

Sample name	CA	HH	CAC	HH	S or Q
	[mol.%]		[wt.%]		
70CA-30HH	70%	30%	83.3	16.7	0.0
60CA-40HH	60%	40%	75.8	24.2	0.0
50CA-50HH	50%	50%	66.7	33.3	0.0
70CA-30HH-40S	70%	30%	50.0	10.0	40.0
60CA-40HH-40S	60%	40%	45.5	14.5	40.0
50CA-50HH-40S	50%	50%	40.0	20.0	40.0

5.3 Systems containing limestone

5.3.1 Compressive strength

Figure 5.2a shows the compressive strength of the low calcium sulfate system mortars (70CA-30HH) without substitution, with 20 wt.% of quartz and with 20 wt.% of limestone. The compressive strength of all the systems increases with time. The quartz systems have the lowest compressive strength. In contrast, the limestone systems show compressive strengths similar or higher than the reference system without substitution from seven days.

The high calcium sulfate systems 50CA-50HH show higher compressive strength compared to the low calcium sulfate systems as shown in figure 5.2b. In these systems there is no significant difference between limestone and quartz additions, suggesting that limestone acts purely as filler in high sulfate environments.

Figure 5.3 shows the compressive strength as a function of limestone substitution (0, 10, 20 and 40 wt.%) of mortars with 30, 40, 45 and 50 mol.% calcium sulfate at 28 days of hydration. The compressive strength increases with the calcium sulfate content whereas it decreases with

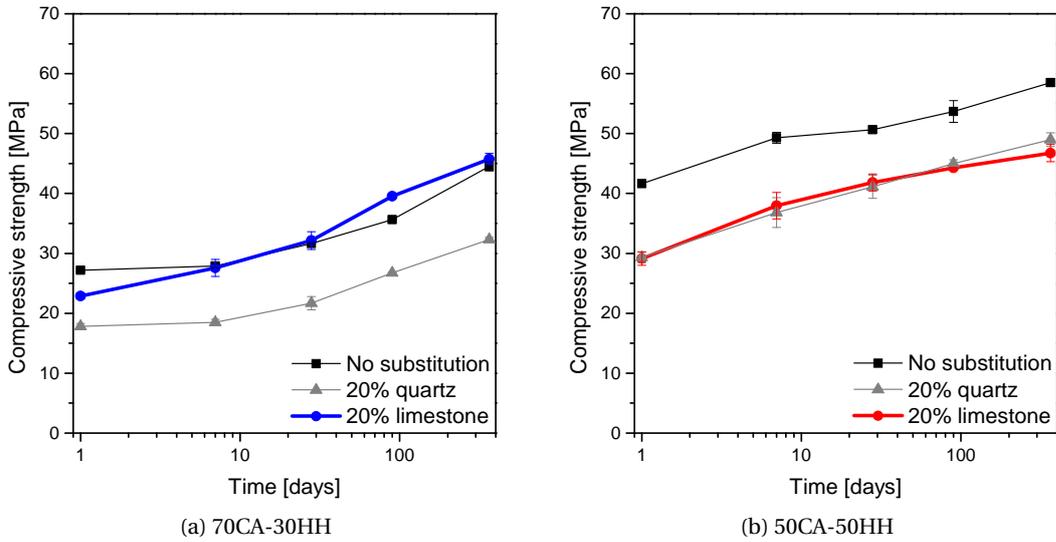


Figure 5.2: Compressive strength of low (a) and high (b) calcium sulfate mortars blended with inert quartz or limestone.

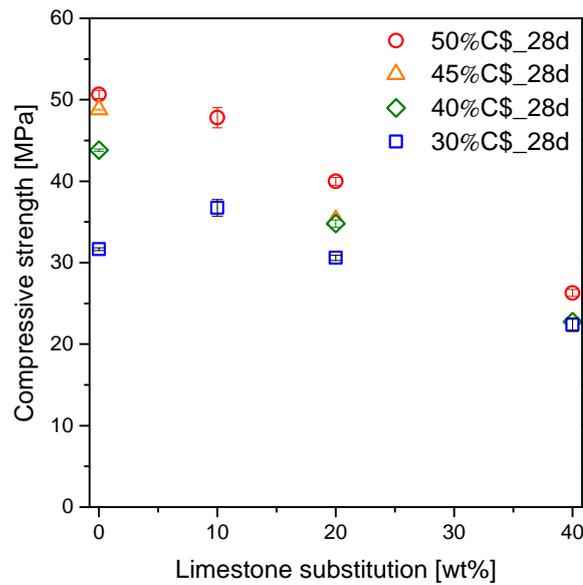


Figure 5.3: Compressive strength as a function of limestone substitution for variable calcium sulfate amounts.

the substitution level, except for the 30 mol.% calcium sulfate system where the maximum is reached at 10 wt% limestone replacement. For the low calcium sulfate system, similar strengths are maintained up to 20 wt.% of limestone.

As described previously, one of the properties of these binders is shrinkage compensation or dimensional stability. This property is highly influenced by the calcium sulfate content in the system, i.e. the expansion compensating the shrinkage increases with the calcium sulfate content. Chapter 6 is dedicated to the mechanisms of expansion and it shows that above 40 mol.% of calcium sulfate the systems are highly expansive. So the higher strength seen with high sulfate content can not be exploited in practice.

5.3.2 Hydration kinetics

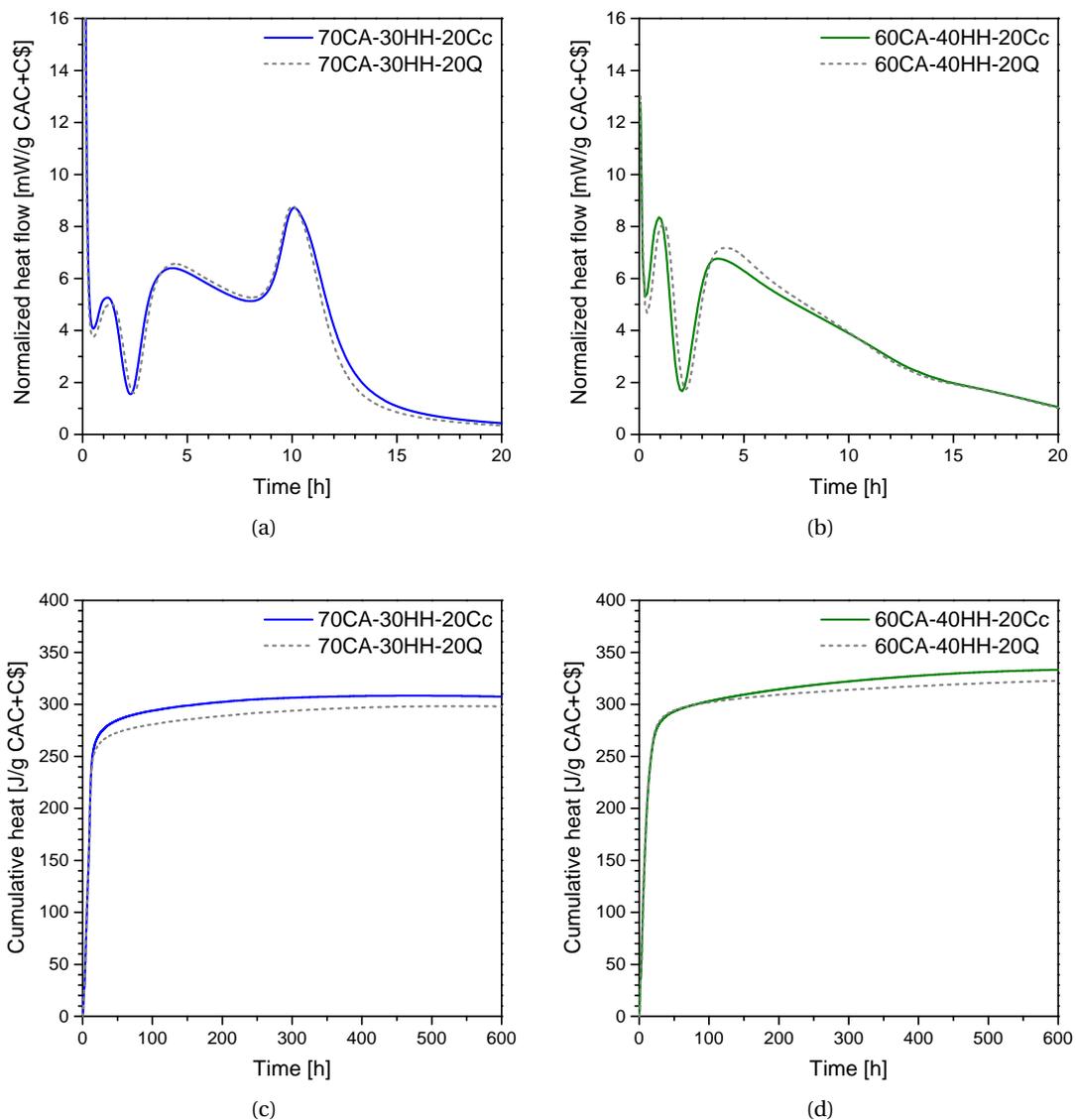


Figure 5.4: Heat flow (a and b) and cumulative heat (c and d) measurements of the low and high sulfate systems blended with limestone.

For both systems with low and high calcium sulfate content the hydration kinetics are comparable for limestone and inert quartz during the first hours of hydration as shown in figures 5.4a and 5.4b indicating that they both act as fillers. The cumulative heat of hydration is also similar for limestone and inert quartz during the first 28 days as shown in figures 5.4c and 5.4d. From these figures it is difficult to determine if the limestone is reacting as it seems to act as filler like quartz during the first 28 days of hydration. Nevertheless, the compressive strength tests confirm that limestone reacts from the first day in the low calcium sulfate system. The heat generated in reactions 2.11 and 2.12 (section 2.3.2) describing the formation of mono-carboaluminate and hemicarboaluminate varies from 26 to 60 J/g CAC+C₃S (appendix A.2.2), respectively. These values were calculated from the enthalpies of the reactions using the values from the CEMDATA14 database [78]. In the low sulfate systems there is a difference of around 20 ± 10 J/g CAC+C₃S, which is in the range of the heat that should be generated by the reactions described above. The experimental error is relatively high compared to the small differences due to limestone reaction; therefore calorimetry measurements cannot be used to detect the reaction of limestone in sealed conditions. Comparable tests with water on top of the sample were done but the high calcium sulfate system expanded breaking the glass capsule. Therefore these measurements are not presented.

5.3.3 Experimental and thermodynamic prediction of phase assemblages

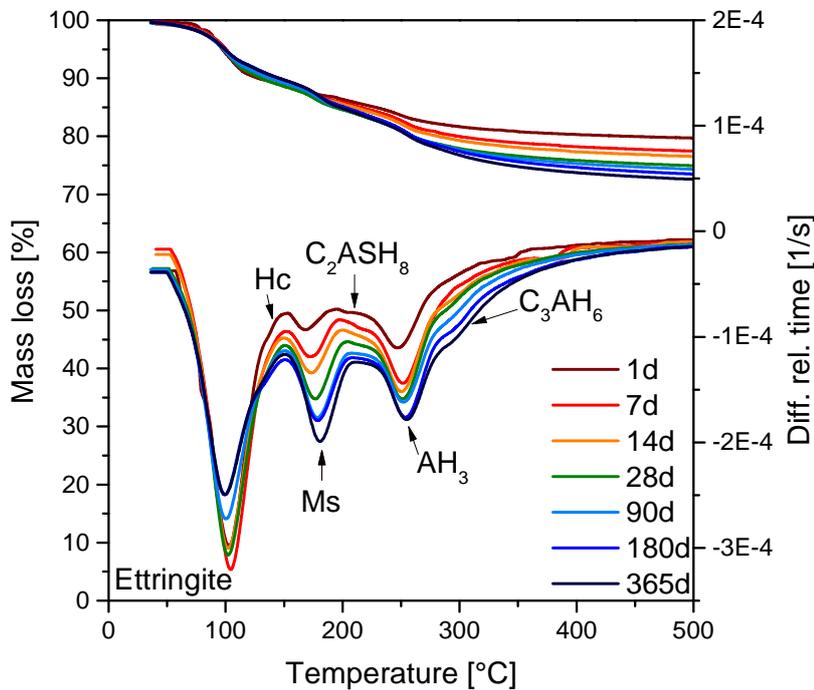


Figure 5.5: TGA and DTG curves at various ages for the low calcium sulfate system without limestone (70CA-30HH). Phase abbreviations: monosulfoaluminate (Ms) and hemicarboaluminate (Hc).

The phase assemblages of the 3 calcium sulfate compositions studied with and without limestone substitution are presented in this section. The samples analysed with XRD, TGA and SEM were cured under water whereas the calorimetry samples were in sealed conditions. TGA was used to quantify the amount of bound water and this value is needed for Rietveld analyses. TGA is also useful to identify the presence of amorphous aluminium hydroxide (found in all systems), which cannot be obtained from the quantitative XRD. The TGA results of the 70CA-30HH system are shown as an example in figure 5.5, the AH_3 peak is at $\sim 260^\circ\text{C}$.

Figures 5.6 and 5.7 show the evolution of the anhydrous and hydrated phases for the different systems without (left) and with (right) limestone. The analyses were done at 1, 7, 14, 28, 90, 180 and 365 days of hydration and the results show the phase masses expressed in g per 100 g of anhydrous solid. The data points are joined by straight lines as a guide only. Hemihydrate reacts rapidly and completely to form gypsum both of which are indicated as $\text{C}\bar{\text{S}}\text{H}_x$ in the figure.

In all the systems there is a rapid consumption of calcium sulfate and CA in the first day to form ettringite and AH_3 (identifiable by TGA but part of amorphous in figures 5.6 and 5.7), according to reaction 2.6. Limestone addition enhances slightly the degree of hydration of CAC cement at 1 day as observed in figure 5.8. This is due to the so-called filler effect; it is related to more available space or water for hydrate growth and to more nucleation sites as discussed in chapter 4.

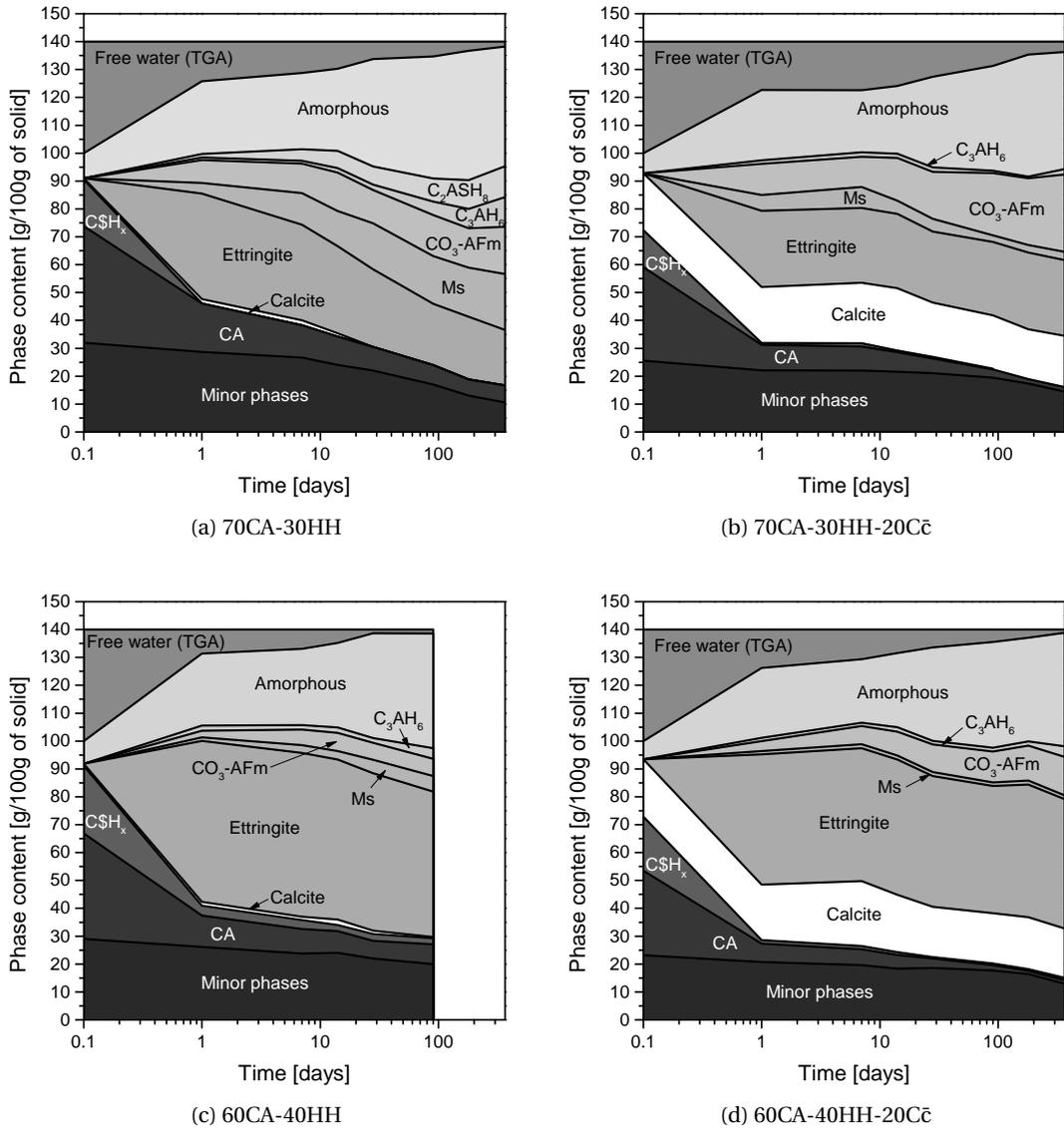


Figure 5.6: XRD Rietveld analyses of the low calcium sulfate system without (a) and with (b) limestone, and the medium calcium sulfate system (c and d). Error of the measurement ± 2 g/100g of solid. Values at 0.1 day correspond to the anhydrous composition. Minor phases label includes C_4AF , C_2S , CFT, C_2AS and magnetite. $C\bar{S}H_x$ includes hemihydrate and gypsum. Ms is monosulfoaluminate. CO_3 -AFm includes hemicarboaluminate and monocarboaluminate. Amorphous includes AH_3 and unrefined phases.

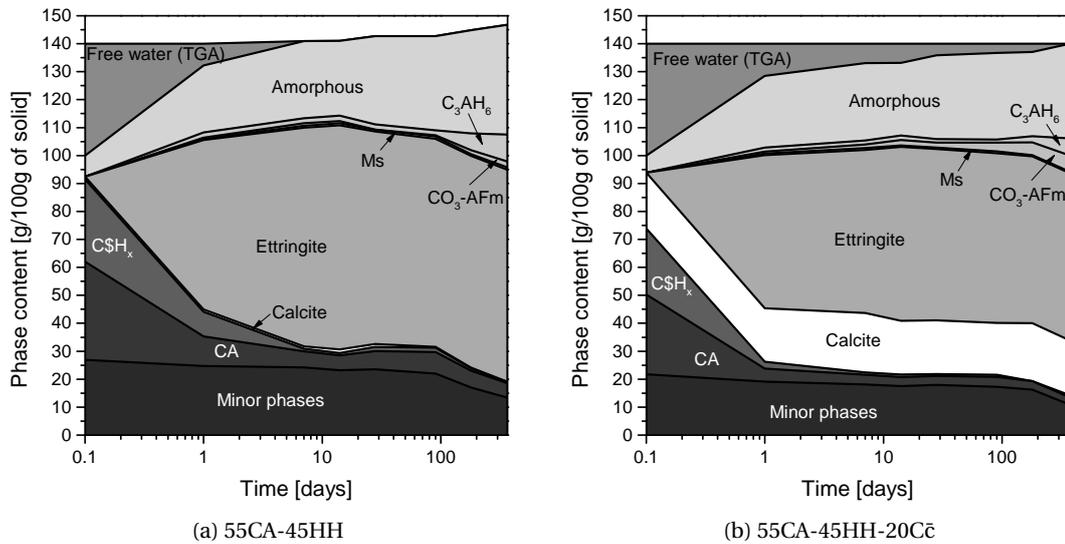


Figure 5.7: XRD Rietveld analyses of the high calcium sulfate system (a and b). Error of the measurement ± 2 g/100g of solid. Values at 0.1 day correspond to the anhydrous composition. Minor phases label includes C_4AF , C_2S , CFT, C_2AS and magnetite. $C\bar{S}H_x$ includes hemihydrate and gypsum. Ms is monosulfoaluminate. CO_3 -AFm includes hemicarboaluminate and monocarboaluminate. Amorphous includes AH_3 and unrefined phases.

In the low sulfate systems (70CA-30HH) the amount of ettringite after one day decreases due to the lack of sulfate and monosulfoaluminate precipitates (reaction 2.7). In the system with limestone only a small amount of monosulfoaluminate is formed and there is no significant decrease in the amount of ettringite. This is due to the formation of hemicarboaluminate and monocarboaluminate (indicated as CO_3 -AFm) when $CaCO_3$ is added to the system which consumes the excess aluminate from CA, instead of reacting with ettringite to form monosulfoaluminate as described by reactions 2.11 and 2.12. This is similar to the reaction of limestone in Portland cement systems [39]. There is also a small amount of CO_3 -AFm phases formed in the system without limestone addition due to the calcite impurity in the calcium sulfate hemihydrate.

Moving from the low sulfate system to the intermediate (60CA-40HH-20C̄) and then to the high sulfate (55CA-45HH-20C̄), the amount of carboaluminate formed in the systems with limestone decreases, indicating less and less reaction on the limestone component. Calcium sulfate is in excess in the high sulfate systems, this could result in high expansion as described in chapter 6.

Figure 5.8 shows the degree of hydration of cement for the different systems as a function of time calculated from XRD analyses. The degree of hydration of the systems 70CA-30HH and 60CA-40HH follows a logarithmic trend during the analysed period of time. The high calcium sulfate system (55CA-45HH) has a rapid increase of degree of hydration during the first 7 days,

followed by a plateau and an increase between 100 and 365 days. This last part is characterized by the consumption of minor anhydrous phases for the formation of hydrogarnet.

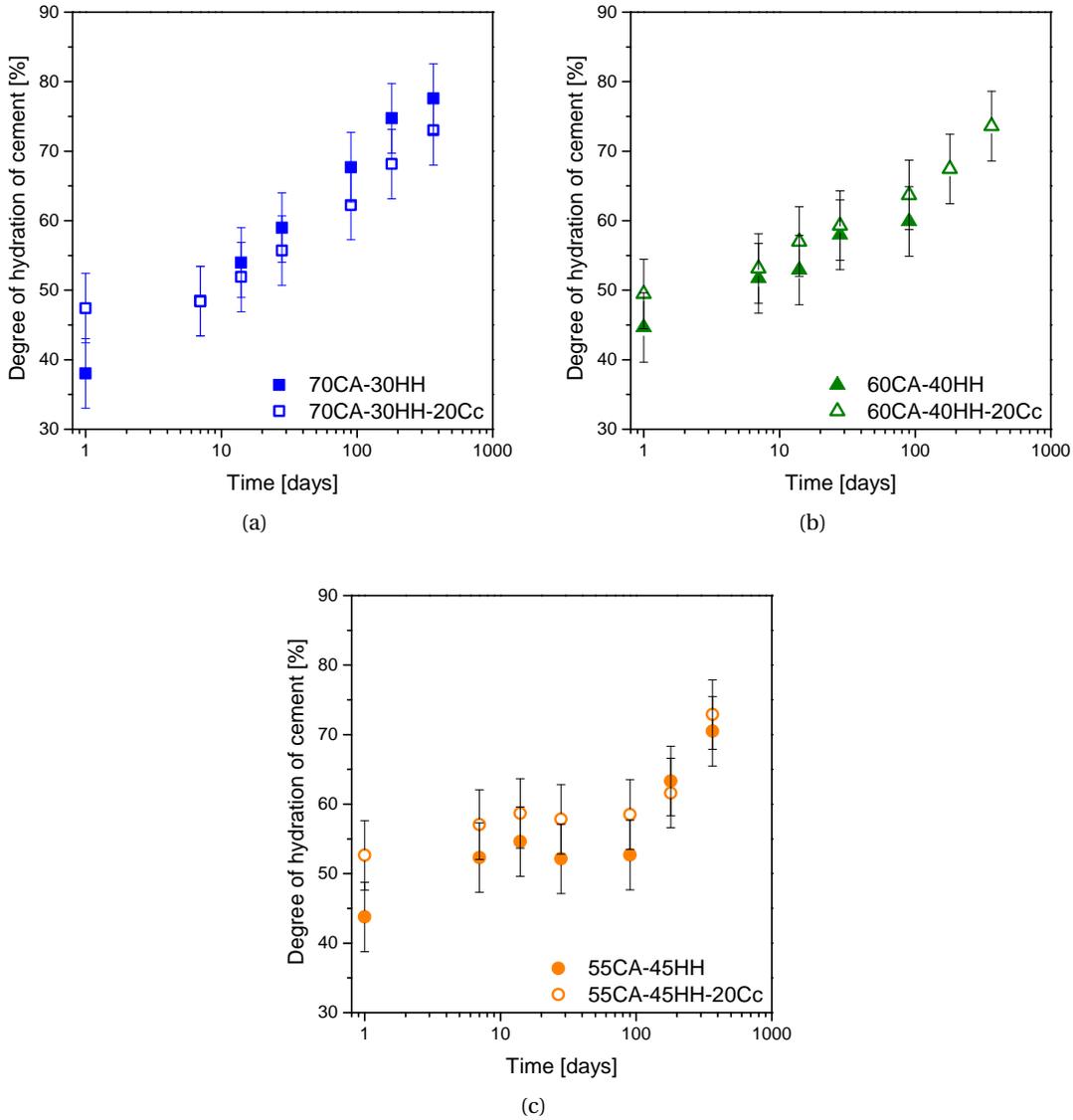


Figure 5.8: Degree of hydration α of CAC for the different systems calculated from XRD Rietveld analyses.

The experimental phase assemblage can be compared with the thermodynamic prediction of the stable phases that can be formed. Figure 5.9 shows the systems with variable proportions of hemihydrate relative to CA with 20 wt.% limestone and a w/b ratio of 0.4. The degree of hydration of CA and hemihydrate is set to 100% and limestone is free to react. The 3 dashed vertical lines indicate the 3 studied compositions. The amount of reacted limestone decreases with the calcium sulfate content. Above 50 mol.% of calcium sulfate, when there is excess of calcium sulfate, the limestone does not react anymore. The sulfate reacts with all the aluminat

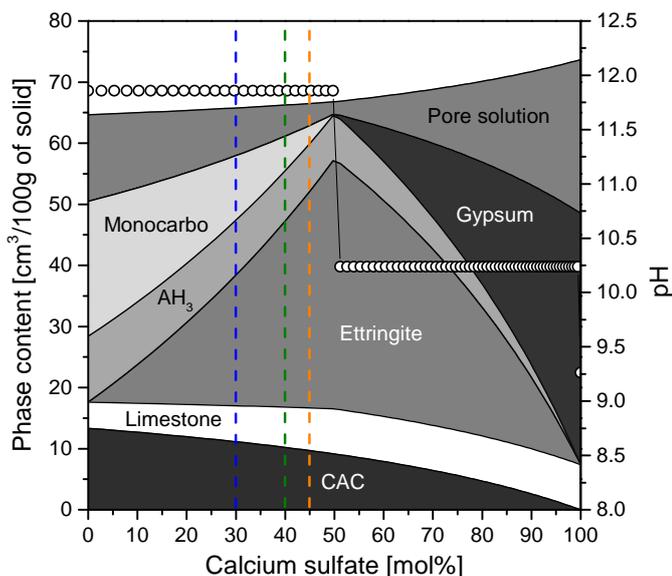


Figure 5.9: Thermodynamic simulation of stable phase volumes at 20 °C for CA-HH-Cc systems with variable calcium sulfate.

forming ettringite and aluminium hydroxide. Therefore no calcium aluminosulfate phases can form. This is the reason why in the compressive strength tests there is little or no limestone contribution in high sulfate systems. The maximum amount of ettringite is attained at 50 mol.% according to the stoichiometry of reaction 2.6 (but such a system would be expansive). By reducing the degree of hydration of CA, the maximum solid volume attained at 50 mol.% decreases and shifts to lower calcium sulfate amounts. The pH (Figure 5.9, right axis) drops when there is excess of gypsum, i.e. when limestone cannot react. The same simulation was done using the full composition of CAC cement with the degree of hydration according to the experimental measurements at 1 year of hydration. The phase assemblage did not differ much from the simpler CA-HH-Cc systems; the main difference being the formation of C_2ASH_8 from C_2AS present in the CAC. As this phase was not detected with XRD analyses of limestone systems, the simulation of the simpler system is presented here.

Figure 5.10 shows the maximum amount of reacted limestone as a function of calcium sulfate. The values on both the y-axes are valid for a system where CA is 50 wt.% of CAC and the degree of hydration of CA is 100%. The relative amount of reacted limestone is indicated on the left y-axis, while the relative mass of reacting limestone with respect to CAC-HH content is indicated on the right y-axis. It can be observed how fast the amount of reacted limestone decreases when the amount of calcium sulfate increases. Above 50 mol.% of calcium sulfate, i.e. when there is an excess of sulfate with respect to aluminates, the ettringite is more stable than carbonate AFm therefore limestone is not consumed. Experimental values are also presented for the 3 studied compositions; the amount of reacted limestone is calculated from the amount of hemicarboaluminate and monocarboaluminate formed measured by XRD

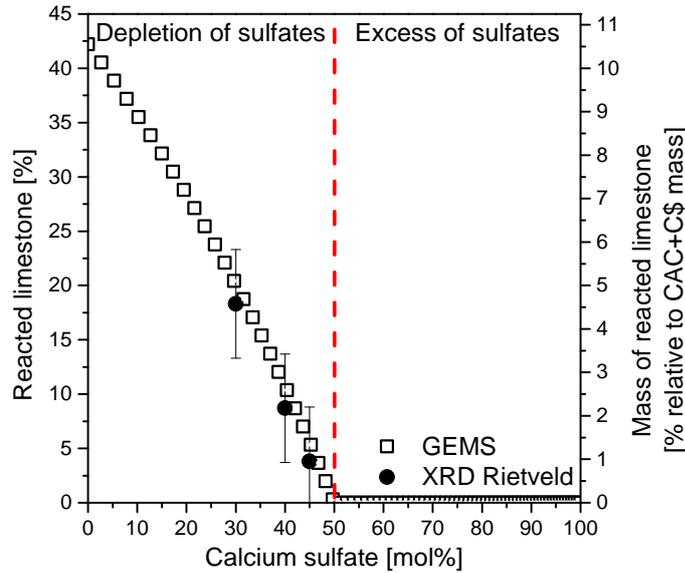


Figure 5.10: Maximum amount of reacted limestone as a function of calcium sulfate content relative to CA. On the right axis is presented the relative mass of reacting limestone with respect to CAC+HH content (for systems where CA is 50 wt.% of CAC). The closed circles show experimental values calculated from the amount of hemicarboaluminate and monocarboaluminate measured with XRD Rietveld analyses at 1 year.

Rietveld analyses. The measured values are in reasonable agreement with the simulation. It is shown that only a small amount of limestone can react in these systems, less than one fifth of it for a substitution level of 20 wt.%. Limestone or calcium carbonate is consumed only when the SO_3^{2-} ions are depleted in the pore solution, i.e. below 50 mol.% of calcium sulfate. In this case the remaining Ca^{2+} and $\text{Al}(\text{OH})_4^-$ ions will react with carbonates to form hemicarboaluminate and/or monocarboaluminate.

Figure 5.11 shows the phase assemblage for the 3 different studied compositions as a function of the fraction of reacted limestone. These simulations are indicated with TS2 (Thermodynamic Simulation 2) in the following figure and are done with the correct degree of hydration for CA according to XRD analyses at 1 year. TS1 are the simulations presented in figure 5.9. As the amount of reacted limestone increases, the total solid volume increases and therefore the porosity decreases. Here the main effect of limestone on the hydration is clear; as the reaction proceeds the amount of monosulfoaluminate decreases and the amount of monocarboaluminate and ettringite increase. The pH drops from 12.1 to 10.2 where there is excess of gypsum like in the 55CA-45HH-20C \bar{c} system (this system has a low amount of gypsum of 0.04 g/100g of solid).

Comparison between the masses of the phases measured experimentally and the ones obtained by thermodynamic simulation at 1 year of hydration are presented in figure 5.12. The results indicated with TS2 are from the simulation shown in figure 5.11 while TS1 are from

the first simulation with 100% degree of hydration for CA and hemihydrate (Figure 5.9). The TS2 simulation is more representative of the real samples. The simulation shows only the stable phases. Therefore, hemicarboaluminate is not formed and only monocarboaluminate forms. Hemicarboaluminate is a metastable phase which occurs in real systems due to kinetic limitations. The portion marked CO₃-AFm includes both monocarboaluminate and hemicarboaluminate from the XRD results. The amount of ettringite predicted thermodynamically is always above the experimental values which may be attributed to the sample preparation technique as discussed in section 3.2.5. Hydrogarnet does not appear as a stable phase in the thermodynamic simulation even though small amounts are detected experimentally. The amount of amorphous aluminium hydroxide is calculated from TGA results (with equation 3.5 in section 3.2.7 taking the mass loss in the interval of temperatures between 220 to 300°C) as it is microcrystalline and mainly XRD amorphous. Despite these differences, the agreement between the experimental and simulated phase assemblages is quite reasonable.

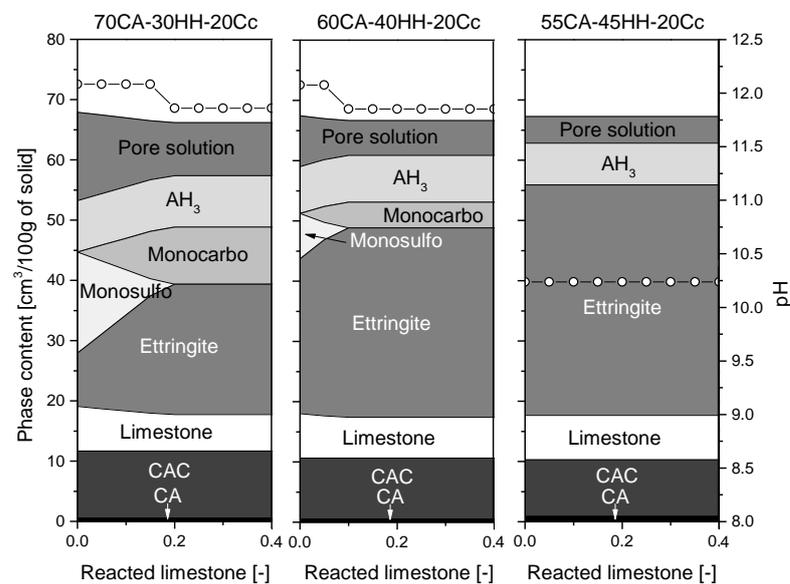


Figure 5.11: Thermodynamic simulation (TS2) of stable phase assemblages at 20°C for the three studied compositions as a function of the fraction of reacted limestone.

5.3.4 Porosity evaluation and links to compressive strength

The porosity can be calculated from the thermodynamic simulation presented in figure 5.9 by assuming that the volume of pores corresponds to the difference between the initial total volume (anhydrous solid + water) and the final solid volume (anhydrous solid + hydrates). Figure 5.13a and 5.13b show the calculated porosity as a function of calcium sulfate content for the simulated systems without and with limestone substitution, respectively. The degree of hydration of CA varies from 80% to 100% for non-substituted systems and 85% to 100% for substituted systems. The values of 80% and 85% correspond roughly to the degree of hydration

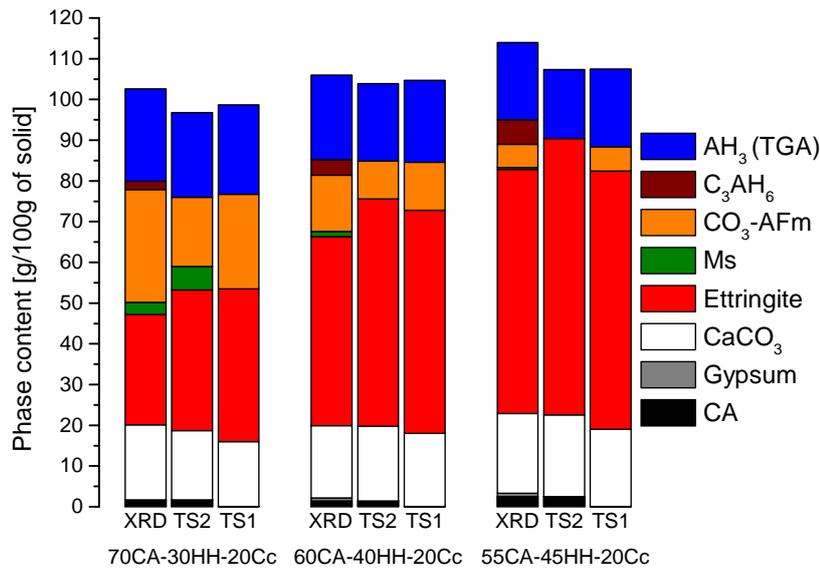


Figure 5.12: Comparison between the phase quantification with XRD at 1 year and GEMS. TS1 are the values from the simulation presented in figure 5.9 and TS2 from the simulation with corrected CA degree of hydration as in figure 5.11. CO₃-AFm from XRD includes Mc and Hc.

of CA at 28 days of hydration, which is the age at which the MIP measurements were made. In the systems without substitution, the water is totally consumed between 40 to 70 mol.% of calcium sulfate if considering 100% degree of hydration of CA (Figure 5.13a), this limits the reactions of anhydrous phases and the porosity stays above 10% over this range of calcium sulfate. There is very good agreement between the experimental and calculated values despite the differences in the phases assemblages discussed above and the likelihood that the sample preparation technique (solvent exchange and vacuum) may dehydrate some phases (such as ettringite) and so increase the porosity.

The mechanical properties of a material are strongly related to its porosity. The compressive strength decreases when the porosity increases [141, 142]. This is observed in figure 5.13. The compressive strength of the mortars hydrated for 28 days increases as the porosity decreases with the calcium sulfate content.

Figure 5.14 shows the compressive strength as a function of the total porosity for the systems without and with limestone substitution at 28 days. The 70CA-30HH systems have comparable compressive strength even though the porosity increases with the limestone substitution. The two other systems with higher calcium sulfate content show a reduction of the compressive strength and an increase of the total porosity when limestone is added. The differences in compressive strengths decrease as the amount of reacted limestone increases. This highlights the fact that two chemically different systems (with or without limestone) can have similar compressive strength even if the total porosities are different. The nature of the hydrates (presence of CO₃-AFm) can affect strongly the strength of the material. Consequently, there is not a unique relation between porosity and strength when the chemical composition changes.

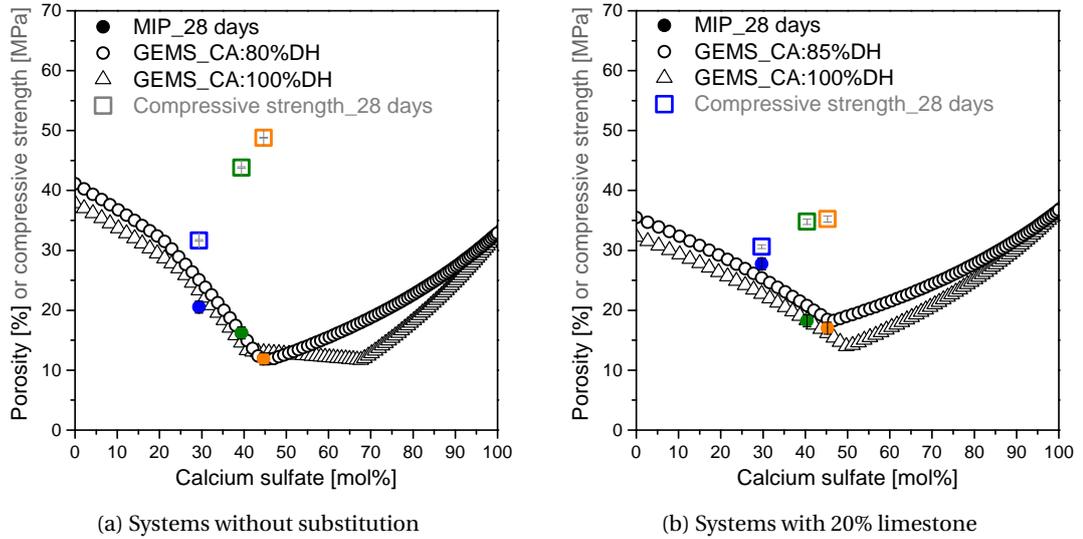


Figure 5.13: Porosity as a function of calcium sulfate for non-substituted (a) and substituted systems with 20 wt.% of limestone (b). Comparison between MIP and simulation. The compressive strength is also presented.

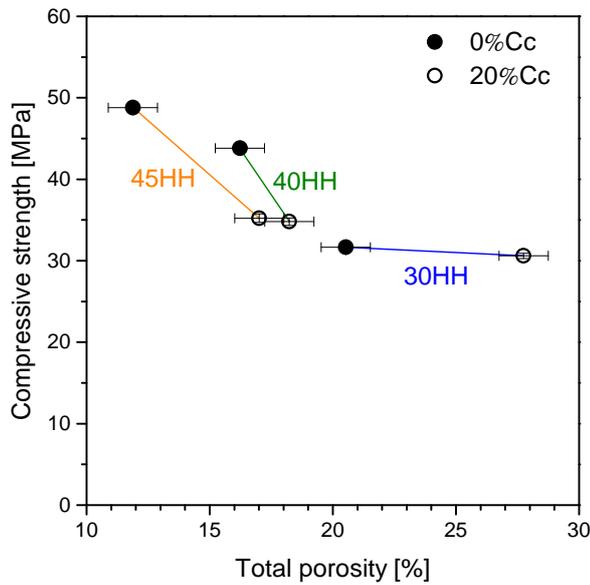
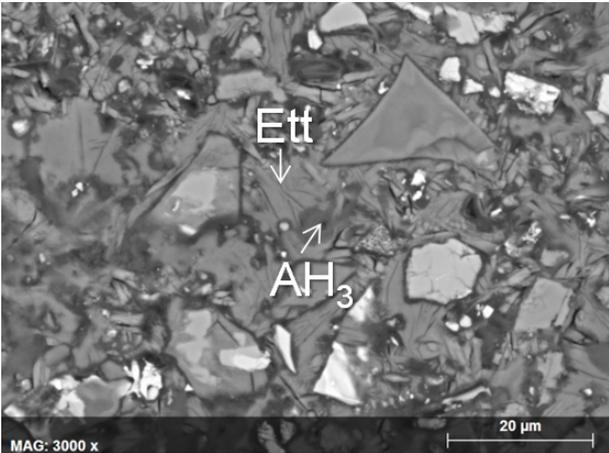
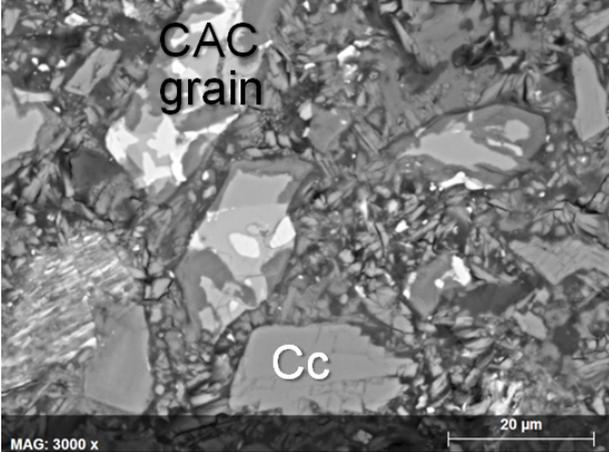


Figure 5.14: Compressive strength as a function of the total porosity at 28 days measured with MIP. The 2 points corresponding to each hemihydrate amount (30, 40 and 45HH) are connected by lines.

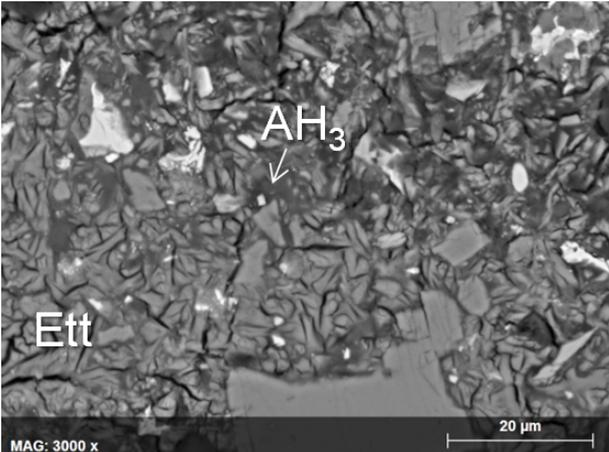
5.3.5 Microstructure characterization



(a) 70CA-30HH-20C \bar{c}



(b) 60CA-40HH-20C \bar{c}



(c) 55CA-45HH-20C \bar{c}

Figure 5.15: SEM-BSE images of limestone samples at 28 days.

5.3. Systems containing limestone

The microstructures of the different systems with 20 wt.% limestone substitution are shown in figure 5.15. There are partially hydrated CAC grains, limestone grains and hydrates. Ettringite is characterized by a lot of small cracks. This is due to the exposure to vacuum during sample preparation and in the microscope chamber which removes water from this phase and causes shrinkage and cracking. There is a higher amount of ettringite in the high calcium sulfate system (Figure 5.15c). The dark grey hydrates correspond to amorphous aluminium hydroxide and the light grey hydrates are highly intermixed phases. Plots of the element ratios (S/Al vs Ca/Al) for EDS analyses done on 200 points in the hydrated matrix at 28 days are shown in figure 5.16. The high level of intermixing of the phases is clearly visible in these plots as there is a cloud of points between the composition of AH₃, ettringite, monosulfoaluminate, hemicarboaluminate and monocarboaluminate. As the calcium sulfate content increases (from figure 5.16a to 5.16b), the cloud of points moves towards the binary composition of AH₃ and ettringite highly intermixed.

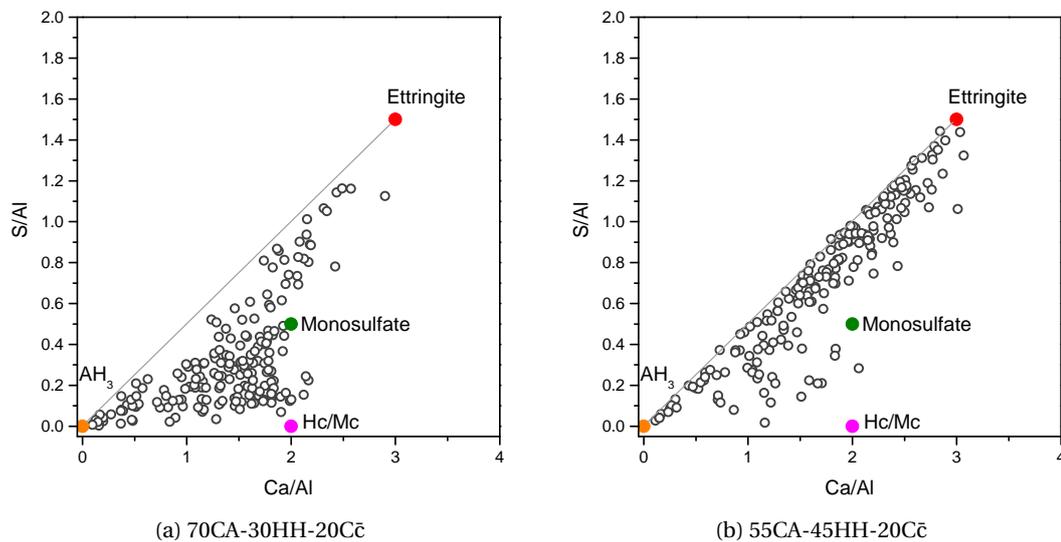


Figure 5.16: SEM-EDS analyses of limestone samples at 28 days for low (a) and high (b) sulfate levels.

5.3.6 Summary on systems containing limestone

Experiments and thermodynamic simulation show that the reaction of limestone is very dependent of the relative amounts of aluminates and sulfate. Two scenarios for the role of limestone in the CAC-calcium sulfate system are observed:

- Calcium sulfate reacts completely (<40 mol.% calcium sulfate): calcium aluminate reacts with carbonate ions from the limestone to form hemicarboaluminate and monocarboaluminate. The ettringite formed is conserved instead of reacting with CA to form calcium aluminate monosulfoaluminate.
- Excess of calcium sulfate (>40 mol.% calcium sulfate): all the calcium aluminate reacts with sulfate ions to form ettringite and aluminium hydroxide. In this case, limestone acts as filler.

Even in the system with the lowest content of calcium sulfate (30 mol% HH) the amount of limestone which reacts is only 4 g for 100 g of total solid binder (one fifth of the 20 wt.% added). Nevertheless, these systems have comparable or higher strengths than the systems without limestone from 7 days, despite their higher porosity.

The systems with higher sulfate content form more ettringite and have generally higher compressive strengths. The main drawback at these high levels of calcium sulfate is that the samples can expand uncontrollably, which may lead to the destruction of the material as discussed in chapter 6.

5.4 Systems containing slag

5.4.1 Compressive strength

Compressive strength tests of the low sulfate mortars (70CA-30HH) without substitution, with 40 wt.% quartz and 40 wt.% slag substitution are shown in figure 5.17a. The systems without substitution have the highest compressive strength while the systems with quartz substitution have the lowest compressive strength. However, the systems with slag show improved strengths with respect to quartz. Slag makes an important contribution to the compressive strength after 7 days.

High sulfate systems (50CA-50HH) show globally higher compressive strength than low sulfate systems as in figure 5.17b. The same trends are observed, as in the low calcium sulfate system but the slag contribution is reduced and becomes relevant after 1 year of hydration.

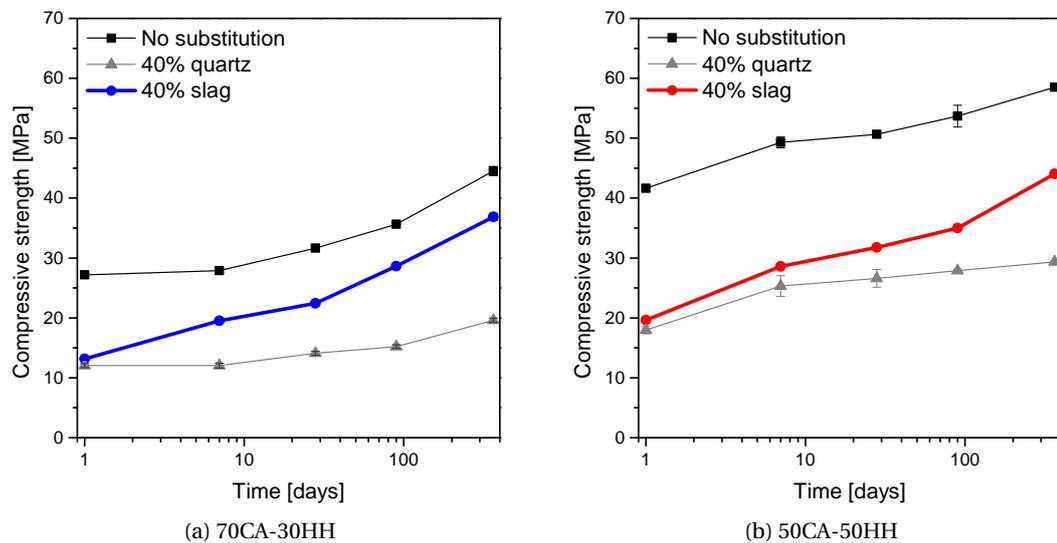


Figure 5.17: Compressive strength of low (a) and of high (b) calcium sulfate mortars blended with inert quartz or slag.

5.4.2 Hydration kinetics

Figure 5.18 shows the heat flow (a and b) and the cumulative heat (c and d) of low and high calcium sulfate systems with 40% slag or quartz substitution. In all the systems slag and quartz have comparable filler effect during the first 20 hours of hydration. Cumulative heat up to 28 days shows that slag contributes to the hydration after approximately 4 days in low sulfate systems (Figure 5.18c). For higher calcium sulfate content, slag seems to be completely inert during 28 days as shown in figure 5.18d. It is not possible to estimate the amount of reacted slag from these measurements as the enthalpy of formation of slag is not known.

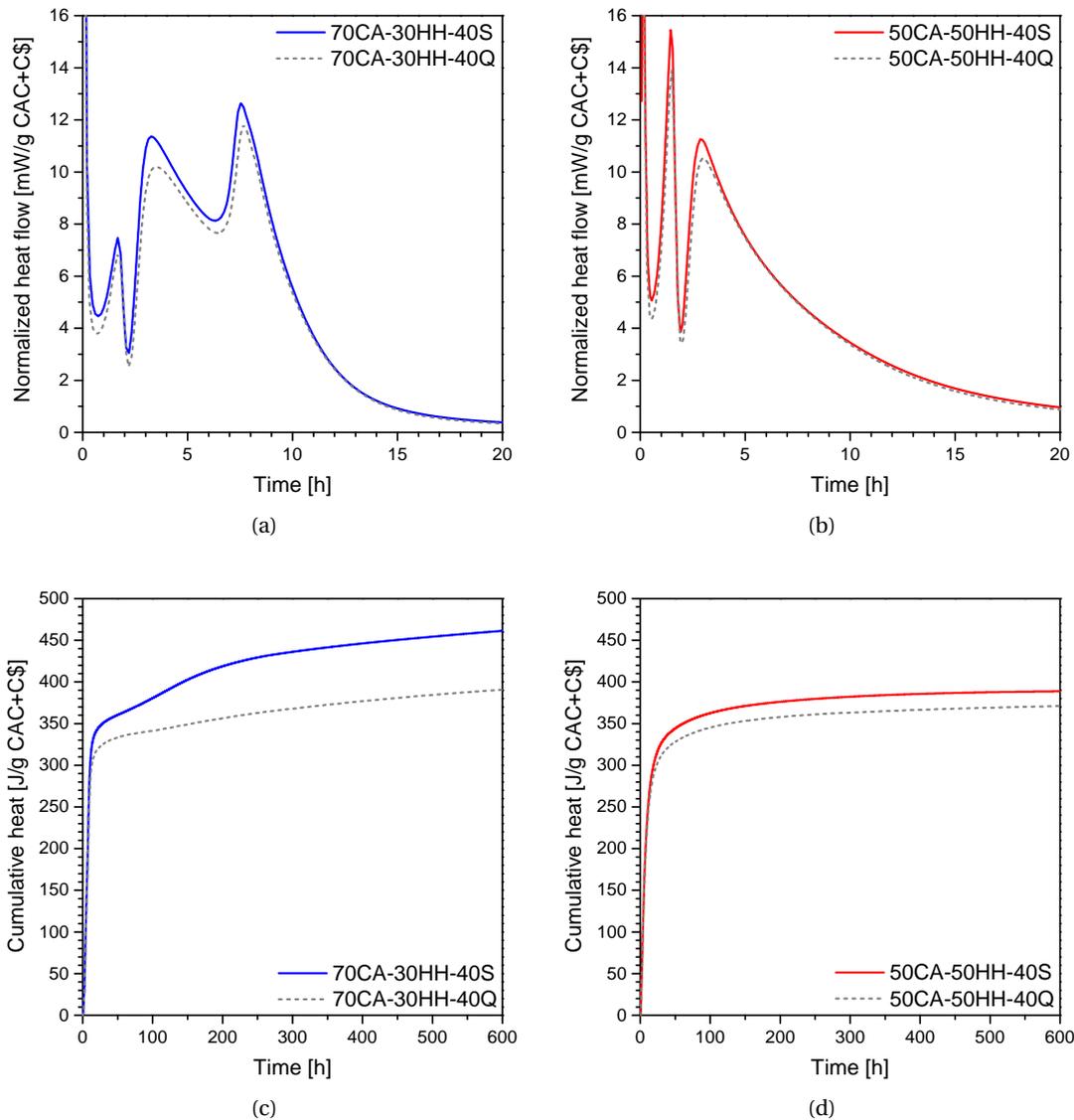
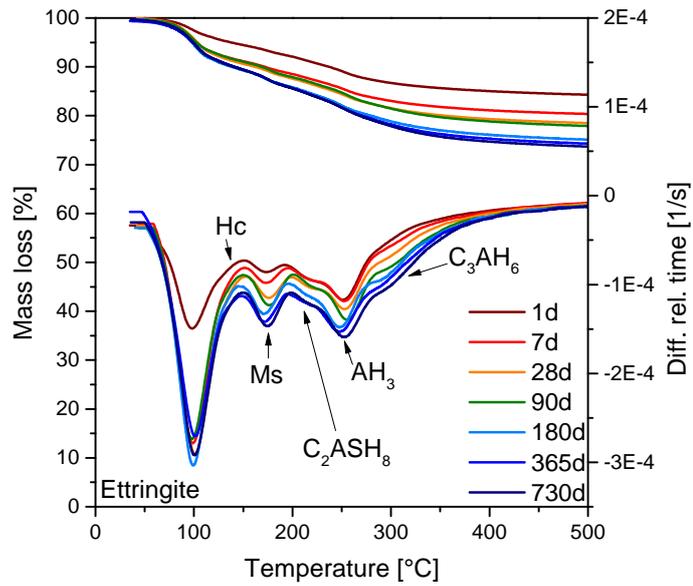


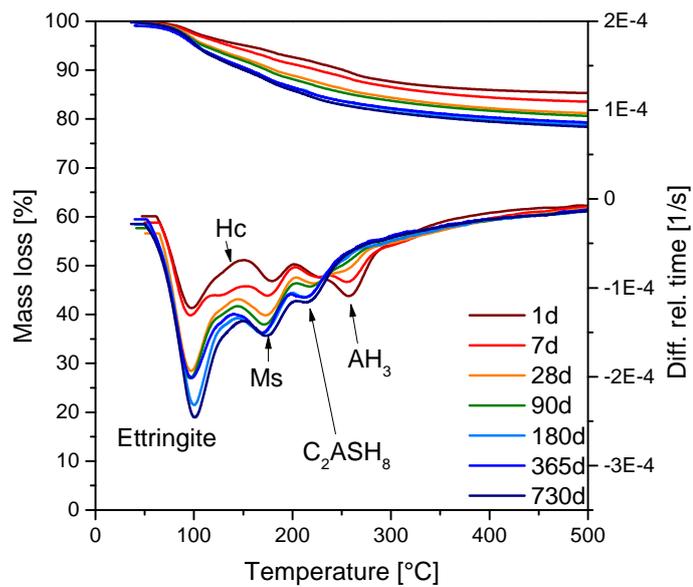
Figure 5.18: Heat flow (a and b) and cumulative heat (c and d) measurements of the low and high sulfate systems blended with slag.

5.4.3 Experimental phase assemblage

TGA and XRD analyses were used to follow the phase assemblage evolution over time. TGA results are presented only for the low calcium sulfate systems to show the presence of X-ray amorphous aluminium hydroxide (Figure 5.19). XRD diffractograms are shown for 1, 7 and 28 days (Figures 5.20, 5.21 and 5.22) and quantitative Rietveld analyses were done only for 2 year samples (Figure 5.23).



(a) 70CA-30HH



(b) 70CA-30HH-40S

Figure 5.19: TGA and DTG curves at various ages for the low calcium sulfate systems without (a) and with (b) slag. Phase abbreviations: monosulfoaluminate (Ms) and hemicarboaluminate (Hc).

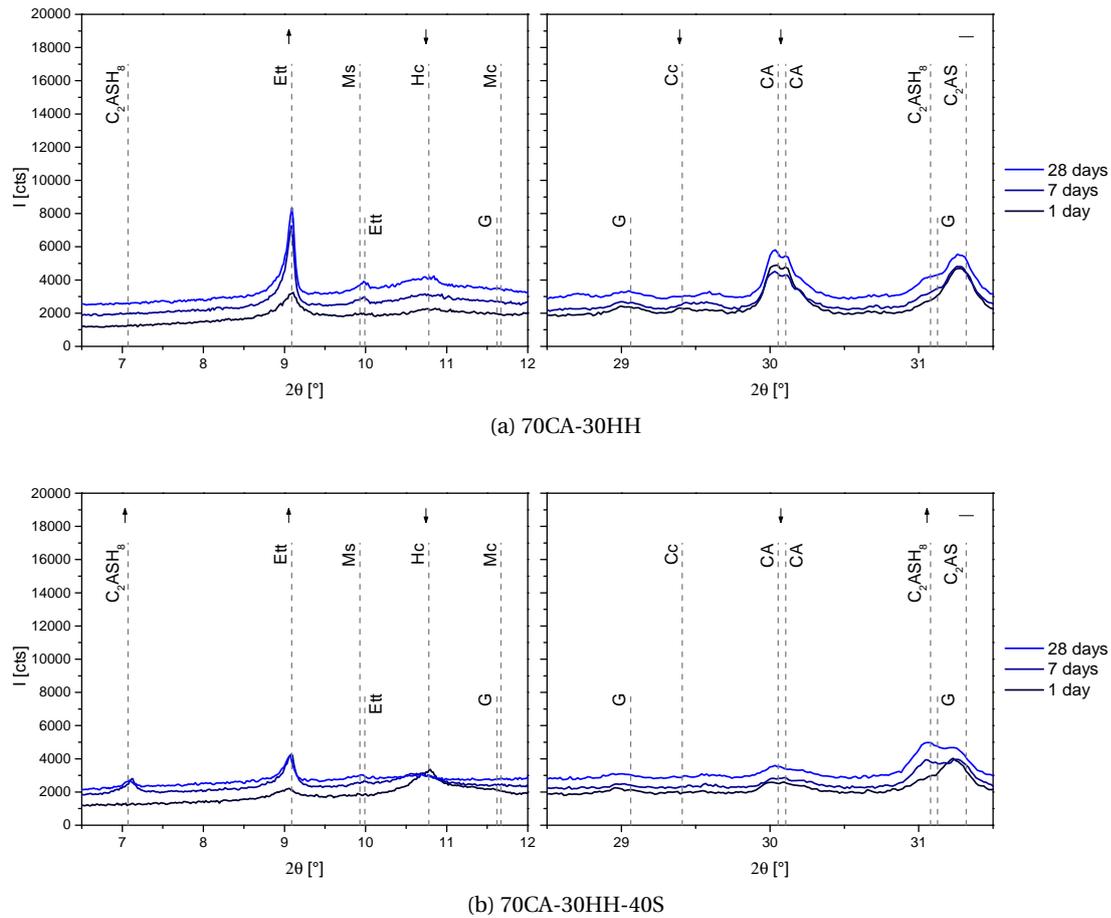


Figure 5.20: XRD diffractograms of the low calcium sulfate system without (a) and with (b) slag.

Figure 5.20a shows the phase evolution of the low calcium sulfate system (70CA-30HH) without substitution. Ettringite and amorphous aluminium hydroxide (observed with TGA in figure 5.19a) form from reaction 2.6 between CA and calcium sulfate. Hemihydrate reacts with water and forms gypsum during the first hours of hydration and is completely consumed during the first day. A small amount of hemicarboaluminate forms from the traces of calcite present in hemihydrate. TGA confirms the formation of monosulfoaluminate and C_3AH_6 after 28 days of hydration. After 2 years the main phases are ettringite, AH_3 , monosulfoaluminate, hemicarboaluminate, traces of monocarboaluminate and C_3AH_6 (Figure 5.23).

Additions of slag to the low calcium sulfate system result in less ettringite and amorphous aluminium hydroxide as shown in figure 5.20b. This is simply due to the dilution of the CAC-C \bar{s} with slag. Strätlingite (C_2ASH_8) forms while AH_3 is consumed as shown from TGA in figure 5.19b. Gehlenite (C_2AS) from CAC is not consumed, therefore it can be assumed that strätlingite formation is due to slag dissolution and is an indicator of the amount of reacted slag. Monosulfoaluminate is observed with TGA. After 2 years traces of hemicarboaluminate and monocarboaluminate are detected (Figure 5.23). Mg from the slag could result in the formation of hydrotalcite [143] but this phase was not detected in these systems.

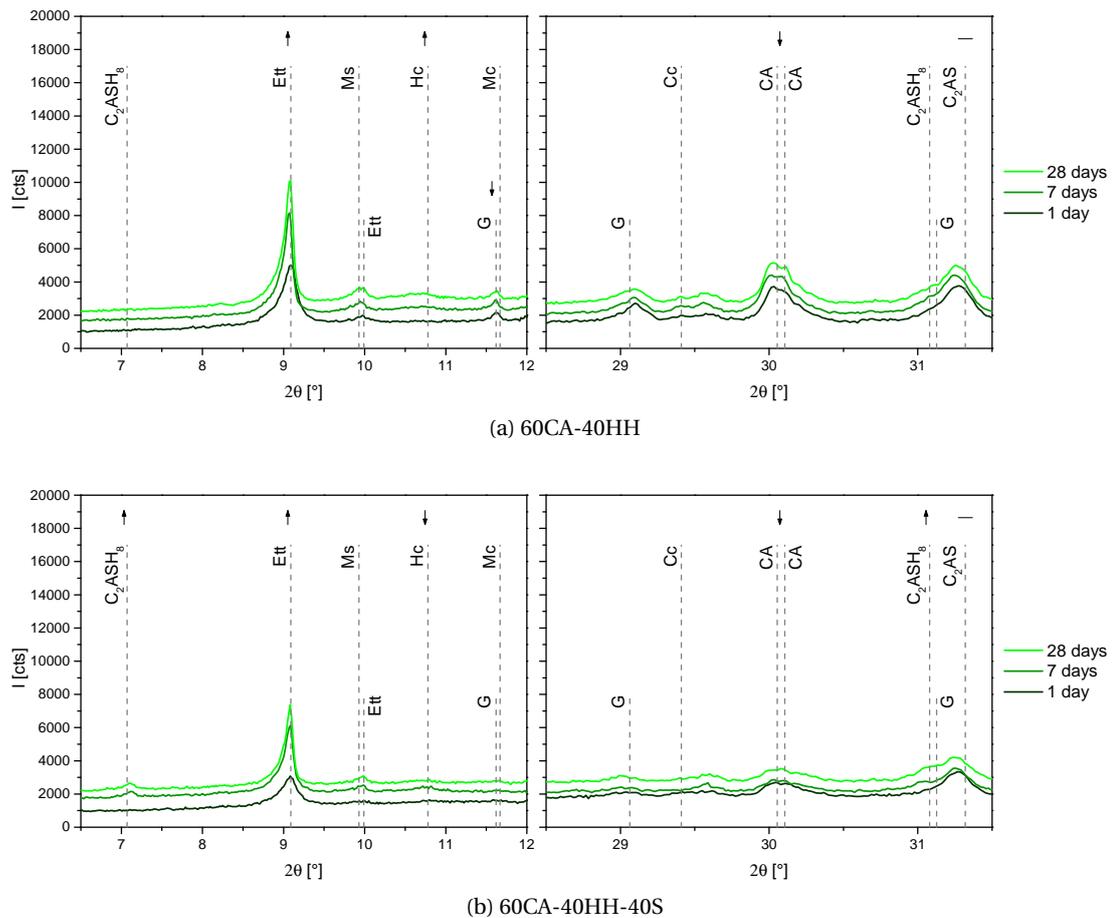


Figure 5.21: XRD diffractograms of the medium calcium sulfate system without (a) and with (b) slag.

As the amount of calcium sulfate increases to 40 mol.% and then to 50 mol.% in the systems without substitution, the intensities of the ettringite and gypsum peaks increase (Figures 5.21a and 5.22a). Monosulfoaluminate does not form until gypsum is depleted and is detected after 2 years in the medium calcium sulfate system. After 2 years there is C_3AH_6 in all these systems.

Increasing the level of calcium sulfate in systems with slag results in a decrease of the strätlingite peak indicating that slag reaction is reduced (Figures 5.21b and 5.22b). There is an excess of gypsum during the first day in the medium calcium sulfate systems and throughout 2 years in the high calcium sulfate systems with slag. When sulfate is in excess, only ettringite and amorphous aluminium hydroxide are formed. After 2 years there is some C_3AH_6 and there is no crystalline strätlingite in the high sulfate system but TGA (not presented here) indicates some traces of it, probably microcrystalline or in too low amounts to be detected with XRD.

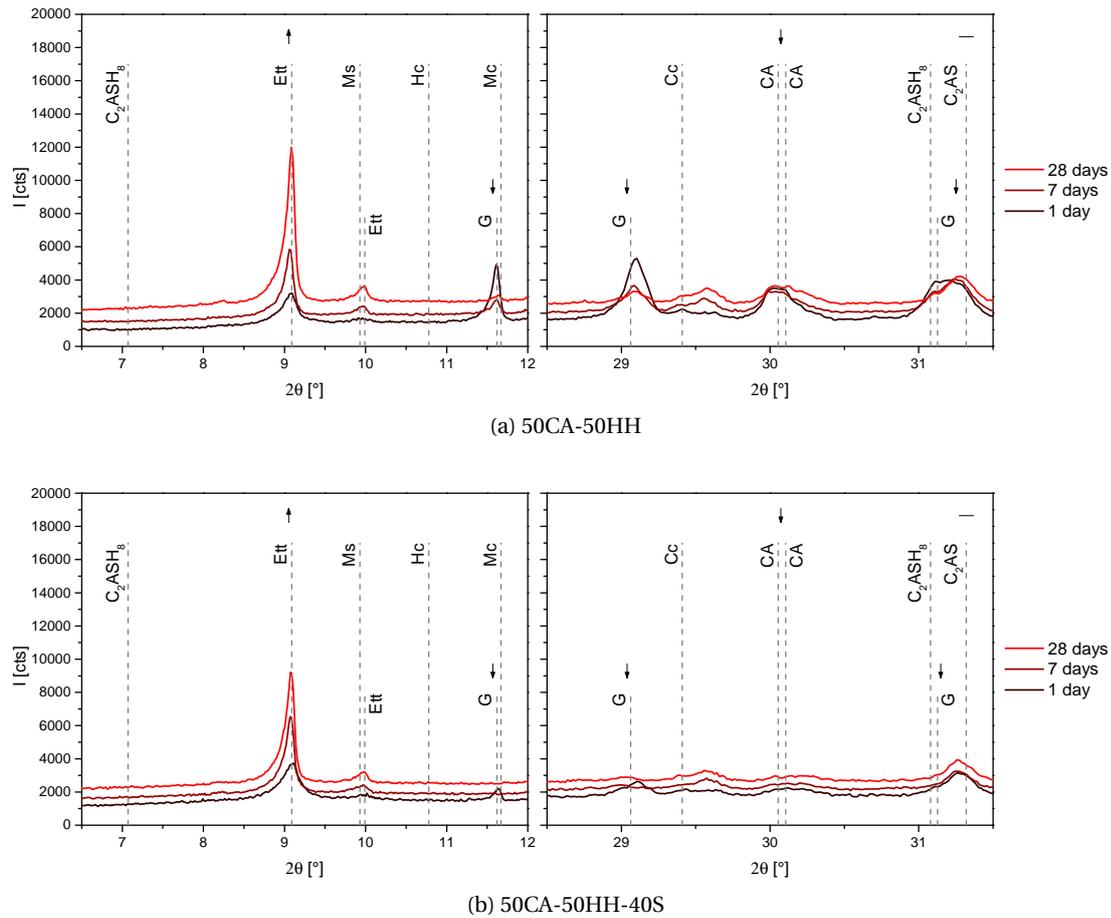


Figure 5.22: XRD diffractograms of the high calcium sulfate system without (a) and with (b) slag.

Reduced amounts or no traces of aluminium hydroxide and C_3AH_6 are detected when strätlingite forms. AH_3 is consumed by the formation of strätlingite as in reaction 2.14. The general trend is that the reaction of slag is reduced when calcium sulfate levels are higher.

Slag dissolves congruently above pH of 9-10 according to [144], therefore it can be assumed that the amount of silica in the reaction products is proportional to the slag reaction and all of it is present in strätlingite. This allows the degree of reaction of slag to be estimated, the values are presented in figure 5.26.

The slag reaction is observed qualitatively with isothermal calorimetry and strätlingite formation from XRD suggests that it is reacting. Another way of measuring the degree of reaction of slag is image analysis on SEM micrographies coupled with EDS mappings. The experimental phase assemblage at 2 years of hydration is compared to thermodynamic simulation showing the stable phases assemblage.

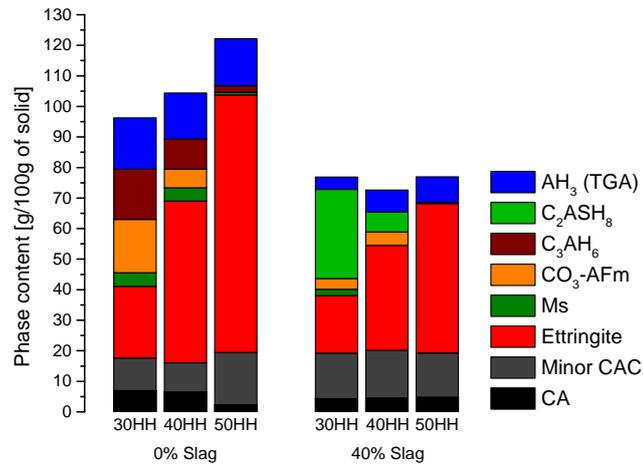


Figure 5.23: Phase assemblage of not substituted and 40 wt.% slag substituted systems after 2 years of hydration.

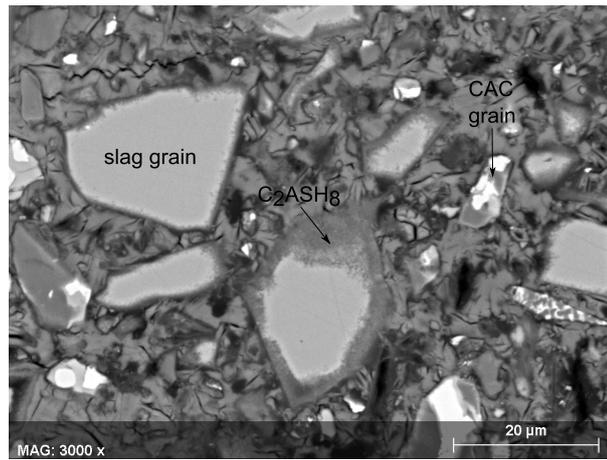
5.4.4 Microstructure and degree of reaction of slag by SEM-IA

The microstructure of the low calcium sulfate system at 2 years of hydration is shown in figure 5.24a. There are light grey slag grains that are partially reacted and are surrounded by a rim of C_2ASH_8 . The main phases in the CAC grain are reacted except the bright phases that contain iron and titanium. The hydrated matrix contains all the phases that were identified by XRD, highly intermixed. The slag in the medium calcium sulfate system (Figure 5.24b) seems to react less than in the previous sample. The high calcium sulfate system shows almost no slag reaction (Figure 5.24c). The high ettringite content is easily noticed by the cracks in the hydrated matrix, which are due to the drying of ettringite under vacuum. Dark grey phase represents amorphous aluminium hydroxide. EDS analyses done on 200 points in the hydrated matrix at 2 years of hydration (Figure 5.25a) show a clear evolution from strätlingite-ettringite dominating phases in the low sulfate system and aluminium hydroxide-ettringite in the high sulfate system.

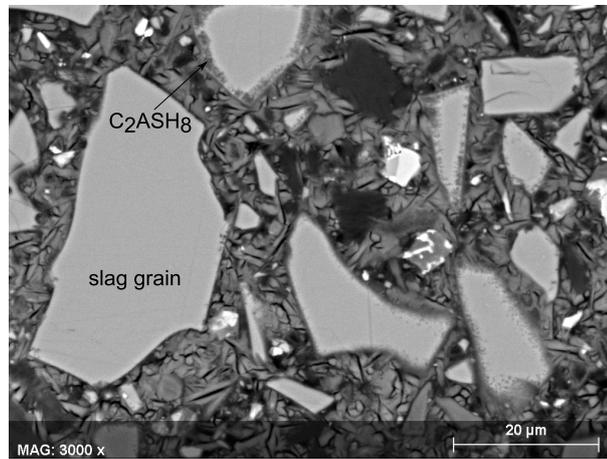
The trends observed in slag reaction from these images are confirmed by measurement of the degree of reaction of slag by SEM image analysis as described in section 3.2.8. The results calculated using the equation 3.6 are shown in figure 5.26. The volume of slag measured at 1 day is assumed to correspond to a degree of reaction of 0% as the smallest particles below $1\mu m$ are missed. The degree of reaction of slag decreases with the calcium sulfate amount and reaches a maximum of 35% after 2 years of hydration in the low calcium sulfate system. These values are quite low compared to PC systems, where slag reacts up to 80-90% in 2 years. The degree of reaction calculated from the amount of strätlingite quantified after 2 years of hydration is also presented on the figure. There is good agreement for the low calcium sulfate system but a difference of 10% for the higher sulfate systems, this could be due to the smallest particles (approximately 7 vol.% of slag) that are missed with this method.

Chapter 5. Long term hydration with SCM

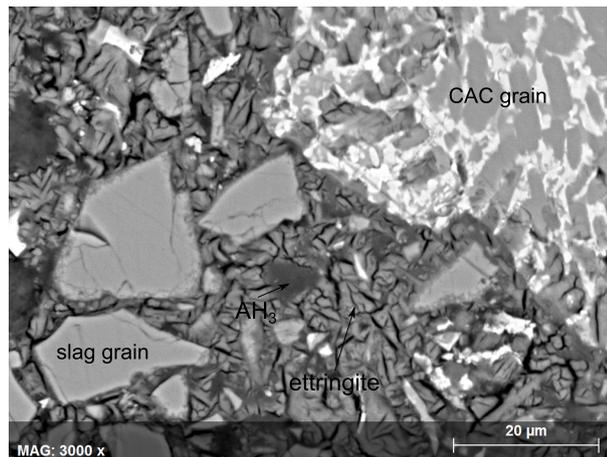
The degree of reaction of slag measured on pastes in high sulfate systems is between 0 to 5%, whereas compressive strength tests on mortars indicate that slag reacts considerably as there is an increase of strength of about 20 MPa compared to inert quartz substituted systems as observed in figure 5.17b. This shows that the links between the volume of the hydrates formed and the strength are not straightforward. The way hydrates form has a direct influence on the strength and more investigations are needed to understand this.



(a) 70CA-30HH-40S



(b) 60CA-40HH-40S



(c) 50CA-50HH-40S

Figure 5.24: SEM-BSE images of slag samples at 2 years of hydration.

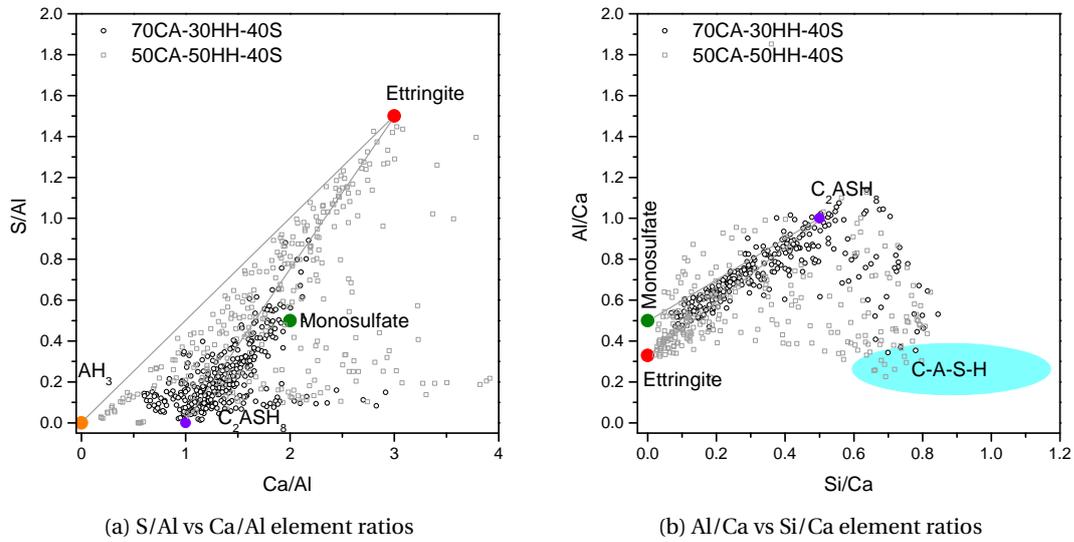


Figure 5.25: SEM-EDS analyses of slag samples after 2 years of hydration.

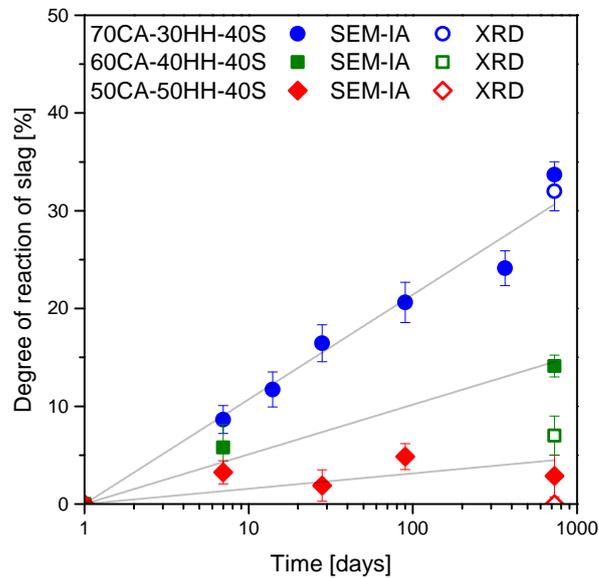


Figure 5.26: Degree of reaction of slag quantified with SEM-BSE-IA coupled with EDS analyses (closed symbols) and comparison with XRD results at 2 years (open symbols).

5.4.5 Thermodynamic simulation

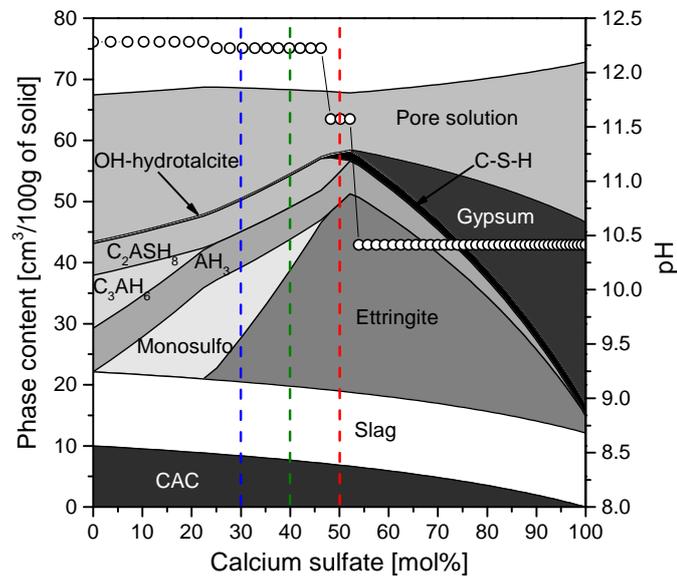


Figure 5.27: Thermodynamic simulation of stable phase volumes at 20°C for CA-HH-S system with variable calcium sulfate.

Figure 5.27 shows the thermodynamic simulation of the stable phases assemblage for systems with variable proportions of hemihydrate relative to CA, with 40 wt.% of slag and a w/b ratio of 0.4. The degree of hydration of CA and hemihydrate was assumed to be 100% and the degree of reaction of slag is set arbitrarily to 10%. The oxides forming the slag phase are forced to react and phases containing silica (strätlingite or C-S-H) and magnesium (hydratalcite) form. The sulfur from slag is not taken into account as it is not a sulfate but it is mainly a sulfide frozen in calcium polyhedra [145]. The three dashed vertical lines indicate the three studied compositions. The maximum amount of ettringite should be at 50 mol.% of calcium sulfate according to reaction 2.6, nevertheless in the figure the maximum is reached above this value as aluminium is also coming from the slag. Below 50 mol.% of calcium sulfate there is formation of monosulfoaluminate and strätlingite. Above 50 mol.% gypsum is in excess and strätlingite does not form. All the silicates go in the C-S-H phase. The pH (Figure 5.27, right axis) drops at this point.

The experimental phase assemblage at 2 years of hydration is compared with the thermodynamic simulation showing the stable phases that form. In the thermodynamic simulations the reaction of slag is imposed; therefore the three studied compositions are modelled with different degrees of reaction of slag, from 0 to 100%. For each simulation the amount of hemihydrate is fixed (with a degree of hydration of 100%) and the degree of hydration of CA is adjusted according to XRD Rietveld analyses. The w/b ratio was adjusted to 0.45 to have always an excess of water.

Chapter 5. Long term hydration with SCM

The phase evolution of the low calcium sulfate system is shown in figure 5.28a. As the degree of reaction of slag increases, the amount of monosulfoaluminate decreases and is replaced by strätlingite. Above 40% the extra silicates precipitate in the C-(A)-S-H phase (Al incorporation in C-S-H). At this point the pH drops from 12.2 to 11.6. The phase assemblage corresponding to the degree of reaction of slag measured by XRD and SEM-IA (30-35%) is shown by the colored area (vertical bar). Figure 5.29 shows the comparison between the experimental phase assemblage measured with XRD and the thermodynamic prediction of the stable phases, the values are in reasonable agreement. The medium calcium sulfate system (Figure 5.28b) shows similar trends. The degree of reaction of slag in the thermodynamic simulation corresponding to the point where monosulfoaluminate is depleted and the pH drops is of 10%. The estimated degree of reaction of slag with XRD and SEM-IA is between 5 to 15%.

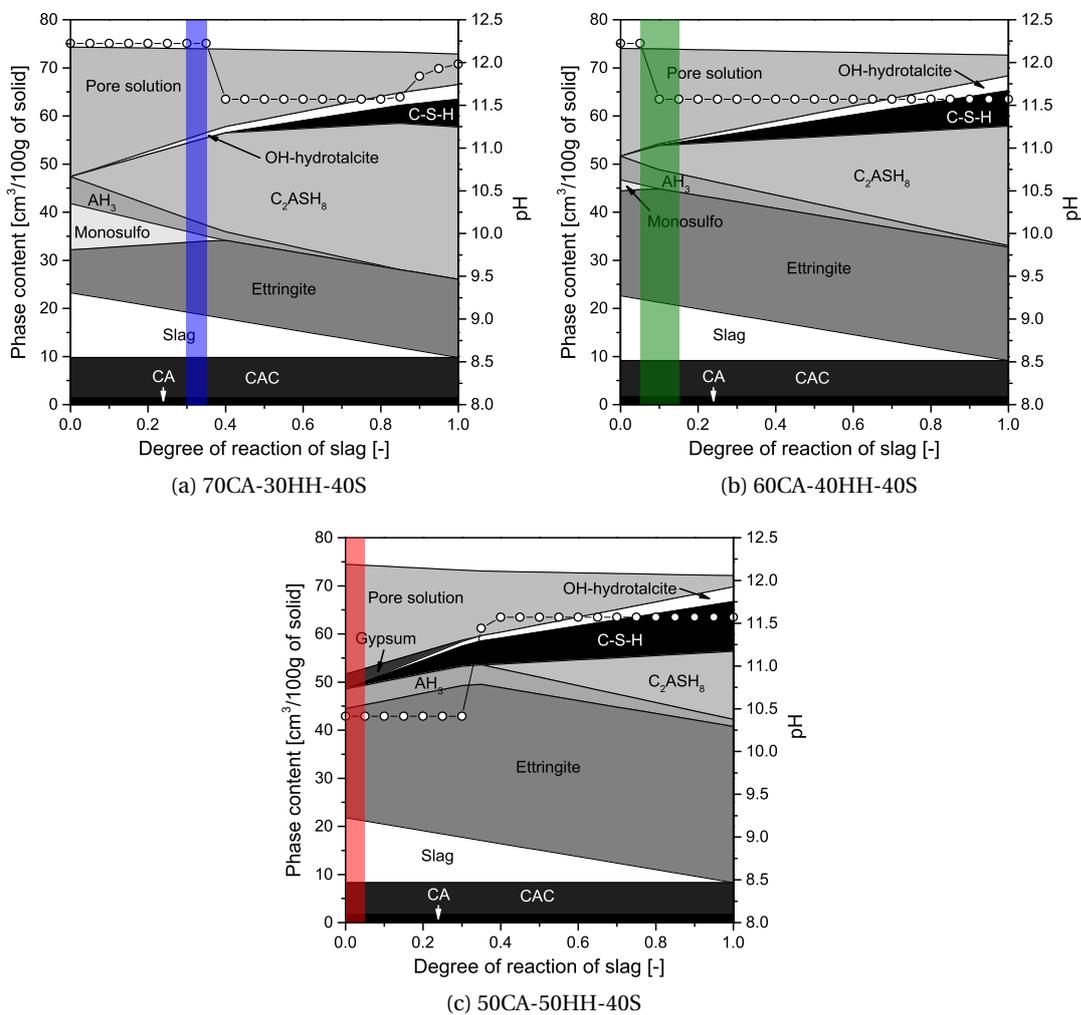


Figure 5.28: Thermodynamic simulation of stable phase assemblages at 20°C for the low (a), medium (b) and high (c) calcium sulfate systems as a function of the degree of reaction of slag. The colored area shows the range corresponding to the degree of reaction of slag in the samples after 2 years of hydration.

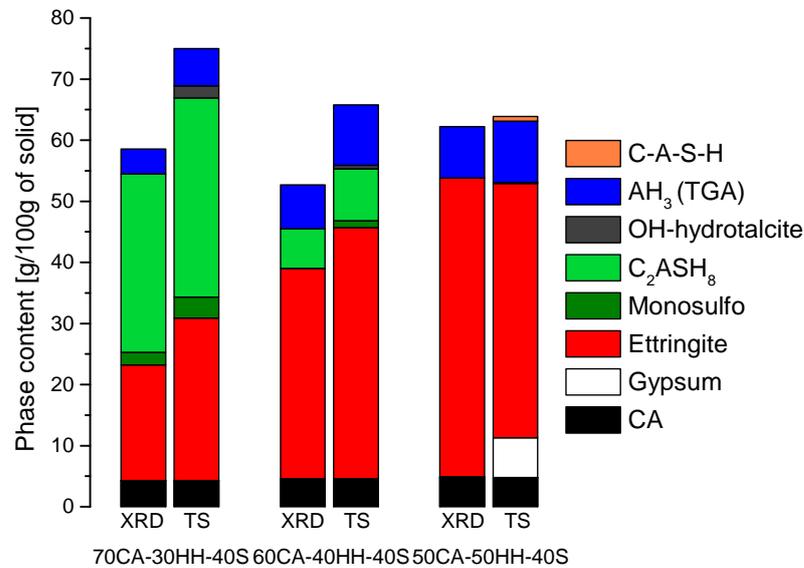


Figure 5.29: Comparison between the phase assemblages measured with XRD at 2 years and calculated with thermodynamic simulation (TS).

The high calcium sulfate system (figure 5.28c) shows a different behaviour; as the degree of reaction of slag increases, the excess of gypsum decreases and the amount of C-S-H increases. When gypsum is depleted ($DR_{slag}=35\%$) the pH increases from 10.4 to 11.6 and strätlingite forms. As the calculated degree of reaction of slag is between 0 to 5%, C-S-H formation is expected in this system and no strätlingite should form. EDS point analyses confirmed that no C-(A)-S-H forms in this system after 2 years of hydration as shown in figure 5.25b. The simulation predicts up to 1.6 g of C-S-H formation which is probably below the detection limit of EDS analyses. Some poorly crystalline strätlingite may be formed but it is not detected with XRD.

The degree of reaction of slag of the low and medium calcium sulfate levels corresponds with the drop of pH. Probably, in the high sulfate system the pH is too low because the excess sulfates in the pore solution maintain a pH around 10.4. As described in the introduction, the solubility of amorphous silica present in slag increases with pH between 12 and 14. Therefore, excess calcium sulfate should reduce slag dissolution. Experiments and thermodynamic simulation agree.

The pH of the curing water of the prisms used to measure the expansion (see section 3.2.3) was measured during the first 28 days of hydration and the values are shown in figure 5.30. The pH increases during 7 days and after decreases slowly, probably because of the reaction of atmospheric CO₂ with water. The increase of hemihydrate content reduces the pH and the addition of slag increases it (dotted lines). The pH of the high calcium sulfate system without slag is around 10 and with slag substitution it goes to a maximum of 11.5. This is due to the faster depletion of gypsum in the substituted systems as shown in figure 5.22. This shows that

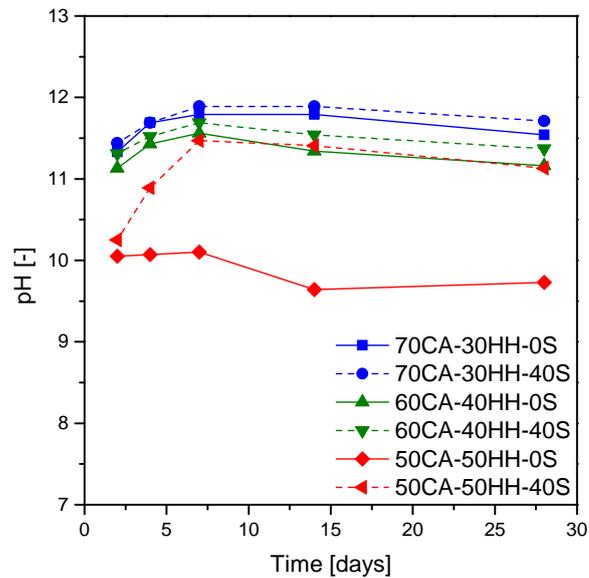


Figure 5.30: pH evolution of the curing water for 28 days.

the pH of this system is very close to the pH needed to enable slag dissolution. The addition of extra alkali may activate the reaction of slag in this system and result in higher degree of reaction of slag above 40% as shown in figure 5.28c .

5.4.6 Summary on systems containing slag

Slag acts as filler during the first 4 days in low calcium sulfate systems. Later it reacts and strätlingite formation is observed below 40 mol.% of calcium sulfate. Two discrete conditions are described:

- Depletion of sulfates (<40 mol.% calcium sulfate): the pH increases and is above 11.5. This helps the dissolution of the slag releasing silica. Silica can then react with calcium and aluminate ions promoting the formation of strätlingite (C_2ASH_8).
- Excess of sulfates (>40 mol.% calcium sulfate): the pH stays below 11.5 as long as there are sulfate ions in the solution, therefore slag dissolution is slowed down. Moreover, sulfate reacts with calcium and aluminate ions to form the most stable phases in these conditions such as ettringite.

Thermodynamic simulation gives satisfactory prediction of the phase assemblage and helps to understand the effect of the relative amounts of aluminate and sulfate.

6 Mechanisms leading to expansion

Contents

6.1 Introduction	99
6.2 Materials and formulations	100
6.3 Expansion characterization: effect of calcium sulfate	101
6.3.1 Experimental study	101
6.3.2 Pore solution analyses and supersaturation	106
6.4 Understanding expansion: effect of calcium sulfate	109
6.4.1 Pore stresses	109
6.4.2 Summary on the effect of calcium sulfate	118
6.5 Modelling of expansion: an elastic approach	120
6.5.1 Introduction of the model	120
6.5.2 Sensitivity analysis	122
6.5.3 Comparison between the model and the experiments	125
6.6 Other factors influencing the expansion	126
6.6.1 Effect of porosity: water to binder ratio	126
6.6.2 Effect of porosity: substitution effect	129
6.6.3 Summary on the effect of porosity: insights from the modelling	132
6.6.4 Effect of ettringite solubility and kinetics: temperature effect	133
6.6.5 Effect of alkalis	135
6.7 Long term expansion	136

6.1 Introduction

Cementitious materials undergo volumetric changes during their hydration and special binders based on CAC-calcium sulfate or CSA-calcium sulfate can be deliberately formulated to expand and to compensate the shrinkage. Part of this chapter was already published

Chapter 6. Mechanisms leading to expansion

as “Expansion mechanisms in calcium aluminate and sulfoaluminate systems with calcium sulfate” [81].

CAC and CSA blended with calcium sulfate are chemically similar. It can be considered that the reactive phase in CSA, $C_4A_3\bar{s}$, is chemically equivalent to $C\bar{s} + 3CA$ (which is the reactive phase in CAC). Therefore, the hydration of CAC blended with calcium sulfate and CSA is similar as shown in section 2.2. Both cements can be used in expansive or shrinkage compensating formulations [17, 11]. The kinetics of hydration and development of mechanical properties depend on the CAC/ $C\bar{s}$ or CSA/ $C\bar{s}$ ratio and the type of calcium sulfate (anhydrite, hemihydrate or gypsum) [12, 11]. The effect of gypsum content in CAC [4] and CSA [83, 146, 147] has already been reported, showing that the expansion increases with the gypsum content. Expansion is generally attributed to the formation of ettringite. However, there is a lack of understanding of the exact link between ettringite formation and expansion. Rapid strength development is related to the fast hydration of monocalcium aluminate and ye’elimite. The complete reaction of ye’elimite, gypsum and water to form ettringite and aluminium hydroxide requires a high water/binder ratio (about 0.6 for 30 wt% of calcium sulfate) [146]. In the present study the water/binder ratio of 0.4 is insufficient for complete hydration.

In this chapter we looked first at the progressive addition of gypsum to both CAC and CSA, linking the expansive behaviour to microstructural changes and pore solution evolution, in order to better understand the underlying mechanisms of expansion. At the end of the chapter other factors affecting the expansion are studied and discussed.

6.2 Materials and formulations

Two commercial cements were used, a calcium aluminate cement (CAC, Secar 51) from Kerneos and a calcium sulfoaluminate cement (CSA, this was a commercial product whose source cannot be disclosed).

Table 6.1 shows the oxide composition of the cements (by XRF) and table 6.2 the main anhydrous phases (by XRD and Rietveld refinement). These cements were blended with gypsum (Acros Organics, 98+% purity) in different proportions, from zero to around 50 wt%. Table 6.3 indicates the composition of the systems studied. To compare the molar calcium sulfate relative to CA content between the two cements, the molar quantity of ye’elimite in the CSA systems is expressed as the molar quantity of equivalent CA: $C_4A_3\bar{s} \rightarrow 3CA + C\bar{s}$.

The calcium sulfate part of $C_4A_3\bar{s}$ is taken into account for the molar percentage of gypsum. The notation adopted for the presentation of the results for CAC systems is %CA - %G and for CSA systems is %eqCA - %G, see table 6.3. In the figures of this chapter the %G of CAC or CSA systems is indicated as “Calcium sulfate [mol%]”.

6.3. Expansion characterization: effect of calcium sulfate

Table 6.1: Oxides composition of CAC and CSA cements (wt%).

	CaO	Al ₂ O ₃	SiO ₂	Fe ₂ O ₃	K ₂ O	Na ₂ O	TiO ₂	MgO	SO ₃
CAC	37.5	52.4	5.1	1.1	0.2	0.11	2.5	0.5	<0.05
CSA	42.5	26.5	6.5	2	<0.5	<0.5	1.0	1.5	19.5

Table 6.2: Mineralogical composition of the cements.

Anhydrous phase	Cement notation	[wt%]
CAC		
Calcium aluminate	CA	70
Gehlenite	C2AS	20
Belite	C2S	2
Ferrite	C3FT	3
Perovskite	CT	2
Spinel	MgAl ₂ O ₄	3
CSA		
Ye'elimite	C4A3\$	50
Belite	C2S	20
Anhydrite + Gypsum	C\$ + C\$H ₂	22
Calcite	Cc	< 3
Aluminates	C3A	< 8
Brownmillerite	C4AF	< 3
Periclase	M	< 1

6.3 Expansion characterization: effect of calcium sulfate

6.3.1 Experimental study

As this work was focused on long term dimensional stability, the expansion was measured from 24 hours. Of course dimensional changes will occur before this time [148, 149].

Figure 6.1 shows the expansion profiles as a function of time for the different CAC systems. Expansion increases with the gypsum content. Macro-cracks appear after 2-2.5 % of expansion (Figure 6.3a). There is a qualitative change in the expansion behaviour between the systems with a gypsum content lower than 40 mol% and those with a content above 45 mol%. The low expansion systems (solid curves) show an increase in expansion at the beginning (swelling when the samples are introduced into water) followed by a plateau. For the high expansion systems (dotted curves), there is rapid initial expansion, which slows to a much lower rate after a few days.

Figure 6.2 shows the expansion as a function of time for CSA systems. CSA systems are more sensitive to expansion than the CAC systems. In CSA systems, the macro-cracks appear after

Chapter 6. Mechanisms leading to expansion

Table 6.3: CAC and CSA systems.

mol% CA or eqCA	mol% C \bar{S} H $_2$	Sample name	wt% CAC	wt% Added C \bar{S} H $_2$	wt% CSA	wt% Added C \bar{S} H $_2$
100	0	100%CA-0%G_ref	100.0	0.0		
80	20	80%CA-20%G	84.0	16.0		
70	30	70%CA-30%G	75.4	24.6		
65	35	65%CA-35%G	70.9	29.1		
60	40	60%CA-40%G	66.3	33.7		
55	45	55%CA-45%G	61.6	38.4		
54	46	54%CA-46%G	60.6	39.4		
		<i>54%eqCA-46%G_ref</i>			<i>100.0</i>	<i>0.0</i>
53.5	46.5	<i>53.5%eqCA-46.5%G</i>			<i>99.3</i>	<i>0.7</i>
53	47	<i>53%eqCA-47%G</i>			<i>98.6</i>	<i>1.4</i>
52	48	52%CA-48%G	58.7	41.3		
50	50	50%CA-50%G	56.7	43.3		
		<i>50%eqCA-50%G</i>			<i>93.1</i>	<i>6.9</i>
48	52	48%CA-52%G	54.8	45.2		
		<i>48%eqCA-52%G</i>			<i>91.4</i>	<i>8.6</i>
46	54	46%CA-54%G	52.8	47.2		
		<i>46%eqCA-54%G</i>			<i>88.9</i>	<i>11.1</i>
44	56	<i>44%eqCA-56%G</i>			<i>85.3</i>	<i>14.7</i>
43.8	56.2	<i>43.8%eqCA-56.2%G</i>			<i>84.6</i>	<i>15.4</i>
43	57	<i>43%eqCA-57%G</i>			<i>83.1</i>	<i>16.9</i>

~0.5% of expansion, leading to fracture of the samples (Figure 6.3b). The systems are very sensitive to small additions of gypsum; at 56.2 mol% of gypsum and below there is a small expansion followed by a plateau, while for 57 mol% gypsum there is destructive expansion.

Figure 6.4 compares the expansion at 28 days as a function of gypsum content for the two systems. The expansion increases slowly and linearly up to around 45 mol% gypsum for CAC and 56 mol% gypsum for CSA systems (the gypsum relative to eqCA is always considered for comparison with CAC), and then expands much more steeply. The sudden change in expansion behaviour observed suggests some kind of threshold effect.

Below this threshold the expansion at 28 days increases gradually. Initial swelling is observed within a few days of immersion of the samples in water; after this the sample dimensions remain stable and the samples stay intact over a long period of time (at least 65 days). Above this threshold the samples continue to expand gradually after the first swelling and eventually fail.

6.3. Expansion characterization: effect of calcium sulfate

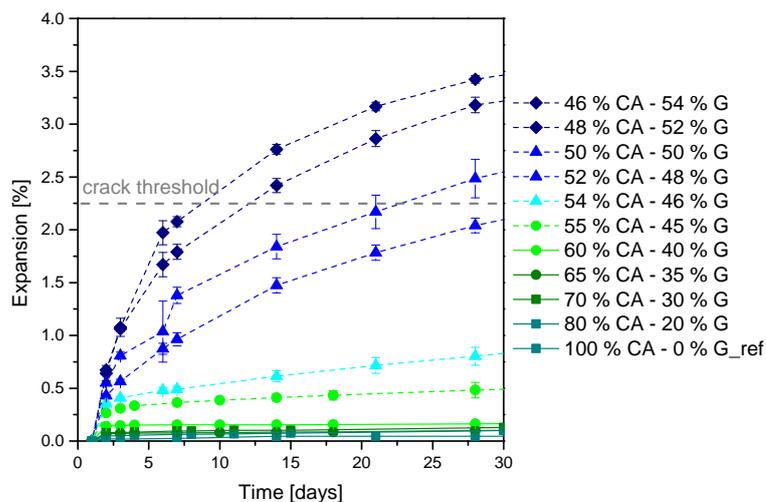


Figure 6.1: Expansion of CAC systems.

Table 6.4: Phase content by XRD Rietveld (Error of measurement $\pm 2\%$) and by TGA (Error of measurement $\pm 5\%$) at 14 days.

[wt%]	CAC systems		CSA systems	
	LE	HE	LE	HE
Ettringite, XRD	40.1	42.8	48.9	50.4
Ettringite, TGA	45	45	49	50
AH ₃ , TGA	20	21	17	19

Study of low expansion and high expansion systems

From the expansion measurements presented in section 6.3.1, low expansion and high expansion blends were identified for both CAC and CSA systems.

Low expansion (LE) - CAC: 60%CA-40%G; CSA: 44%eqCA-56%G

High expansion (HE) - CAC: 55%CA-45%G; CSA: 43%eqCA-57%G

The rate of heat evolution is shown in figure 6.5a for CAC systems and in figure 6.5b for CSA systems. There is no difference in kinetics between low expansion and high expansion systems for both CAC and CSA. The CSA systems hydrate faster than the CAC systems, but the cumulative heat is comparable after 100 hours of hydration (not shown in the figure).

Figure 6.6 shows the quantitative evolution of the phase assemblage from the XRD Rietveld analyses of slices of cement paste cured in water for the four systems. In none of these systems are the anhydrous phases (CA or ye'elite and gypsum) completely consumed. Table 6.4 shows the values of ettringite determined by XRD and by TGA at 14 days. It is noted that:

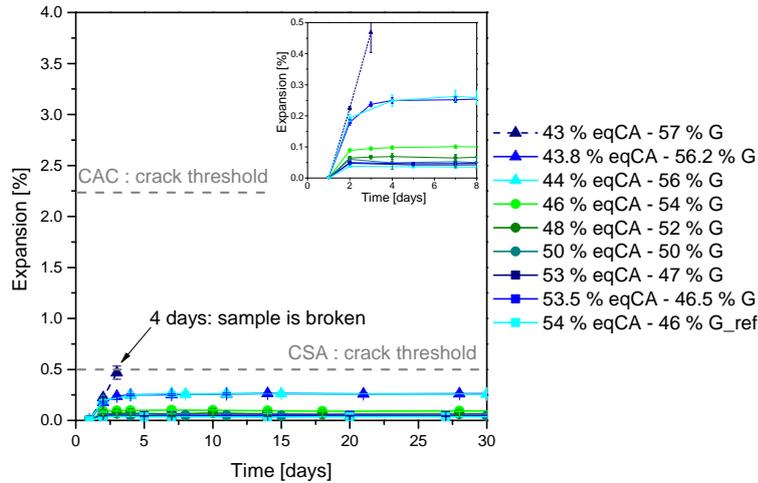
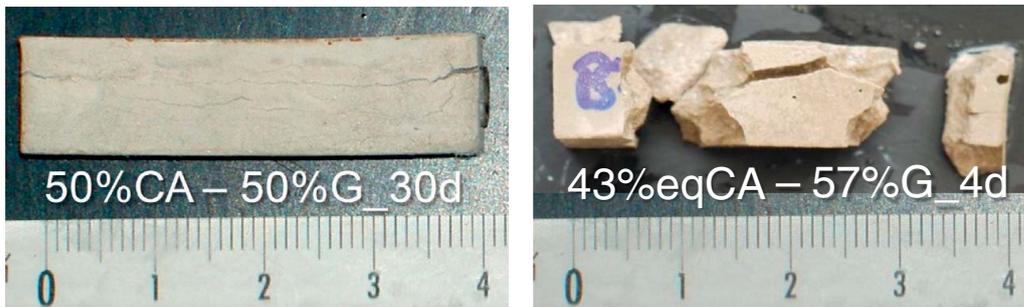


Figure 6.2: Expansion of CSA systems.



(a) CAC: Cracks after 30 days.

(b) CSA: Deterioration after 4 days.

Figure 6.3: Deterioration of CAC and CSA systems cured under water.

- For the low expansion systems, the expansion is stable after 3 days and the ettringite content increases slightly thereafter.
- For the high expansion systems ettringite precipitation continues over 10 days but expansion still increases afterwards. The expansion occurs while there is no measurable increase in the amount of crystalline hydrates.
- The absolute amount of ettringite is very similar in the two systems; slightly higher for the high expansive case in both the CAC and CSA systems. However, these small differences are within the error of measurement.

Figure 6.7a and 6.7b show the derivative thermogravimetric (DTG) curves of the four studied systems at 1 and 14 days. The main peak position corresponding to the water loss of ettringite is around 140°C, the peak of gypsum is around 150°C and AH₃ is observed at 270°C. There is more aluminium hydroxide in CAC systems (Figure 6.7a) and slightly higher ettringite content in the CSA systems (Figure 6.7b). The amount of ettringite increases slightly between 1 and

6.3. Expansion characterization: effect of calcium sulfate

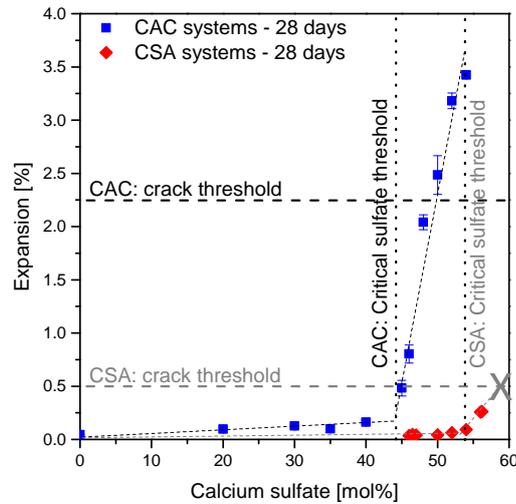


Figure 6.4: Expansion as a function of gypsum content at 28 days.

14 days in both CAC and CSA systems. The amorphous AH_3 increases between 1 and 14 days for CAC systems but seems to be stable in the CSA systems. At 1 day there is more ettringite in high expansion systems. At 14 days no substantial difference between low expansion and high expansion systems is observed in CAC systems, however in CSA systems a slightly less ettringite content is observed in high expansion system compared to the low expansion one. A rough estimation (Table 6.4) of the ettringite content was made by taking twice the integral of the left half of the peak (from 30 to 140 °C), as gypsum overlaps the ettringite peak in the range 140-170 °C. The AH_3 content is calculated by integrating from 200 to 350 °C (crystalline gibbsite, AH_3 , has 3 moles of water per mole of phase, but the water content may be somewhat different for the poorly crystalline or amorphous aluminium hydroxide formed here). XRD and TGA results show similar trends, TGA overestimates slightly the ettringite content.

Figure 6.8 shows SEM-BSE images of the low expansion and high expansion CAC and CSA systems after 14 days of hydration. The observations are done on the basis of the analysis of several images per sample but here only one image per sample is shown. The cracks cannot be attributed only to the expansion, they are also a result of the drying during sample preparation. Ettringite is characterised by the small parallel cracks which form on drying. There is a clear difference in the distribution and morphology of the hydrates between CAC and CSA systems. AH_3 (dark grey) and ettringite (denoted Aft, light grey) are more closely intermixed and finer in the CSA systems than in the CAC systems, this is probably a result of the faster hydration of the CSA systems. However, within each system there is no obvious difference between the low expansion and high expansion systems. It can be noticed (Figure 6.8b) that around the gypsum grains there is more AH_3 than in the rest of the hydrated matrix.

Figure 6.9 shows the cumulative porosity curves as a function of the pore entry radius at 1, 3 and 14 days. The threshold pore radii at 1 day are considered as characteristic of the systems in the ensuing discussion, because this is the age of the samples when immersed in water

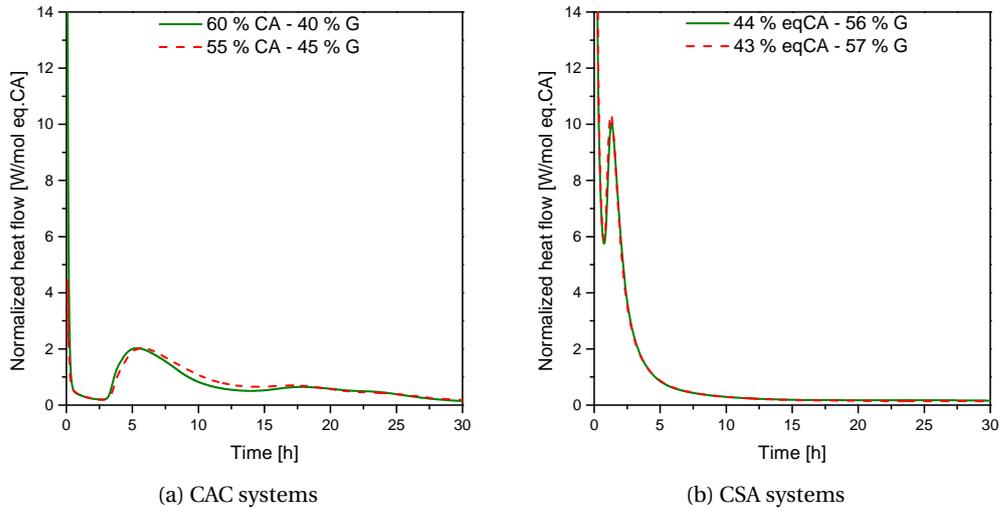


Figure 6.5: Hydration kinetics of CAC and CSA systems.

Table 6.5: Pore size and total porosity measured by MIP on 1 day samples.

	CAC systems		CSA systems	
	LE	HE	LE	HE
Total porosity [% $\pm 2\%$]	22.4	20.1	14.5	17.2
Pore size at inflection point [nm $\pm 0.5\%$]	5.2	5.5	4.1	4.1
Threshold pore size (tangent intersection) [nm $\pm 0.5\%$]	8	9	6	6

for the expansion. The threshold pore radius is taken at the intersection of the 2 tangents as shown in figure 6.9, i.e. where the mercury starts to intrude the porous matrix. We could also consider the value at the inflection point as a characteristic value. Both values are given in table 6.5. CAC systems have a slightly larger threshold pore radius and a greater total porosity than CSA systems. Again there is no noticeable difference between the low expansion and high expansion systems. The small differences between the samples in the same system (CSA-C \bar{s} or CAC-C \bar{s}) are typical of the inter sample variation obtained on MIP.

6.3.2 Pore solution analyses and supersaturation

Figure 6.10 shows the ionic concentration of the pore solutions as a function of the gypsum content after 7 days of hydration for both CAC and CSA systems. The extracted pore solution gives an average composition throughout the sample. Both systems show similar trends; the Ca^{2+} and SO_4^{2-} concentrations increase with the gypsum content and the $\text{Al}(\text{OH})_4^-$, Na^+ , K^+ and consequently pH decrease. The pH is calculated by charge balance from experimental values of the ionic concentrations. The same trends are observed in the early hydration study in figure 4.9.

6.3. Expansion characterization: effect of calcium sulfate

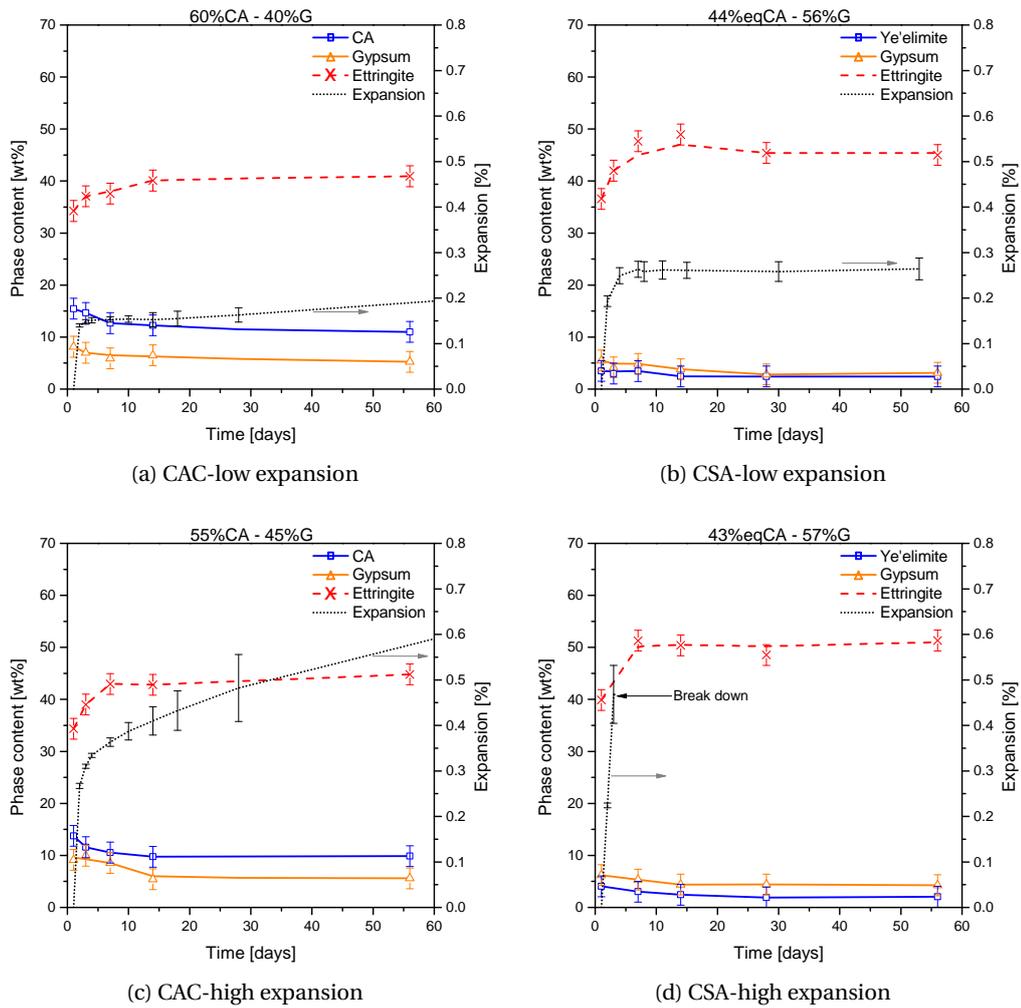


Figure 6.6: XRD on slices cured in water for CAC and CSA systems (lines for eye guide only).

For the CAC system, the relative concentrations of the different ions changes abruptly between the low expansive and the high expansive system (40 and 45 mol% of gypsum respectively). The concentration of calcium ions increases by almost an order of magnitude and the concentration of aluminate ions drops to very low values. It is difficult to understand the reason for this sudden change. Normally, pore solutions in cementitious systems are in quasi equilibrium with the hydrate phases present [132] and there is no change in the assemblage of solid phases present around the threshold of unstable expansion: solid CA or $C_4A_3\bar{s}$ and gypsum are present in both cases. Even though some gypsum remains in the low expansive samples and it seems to be no longer in thermodynamic equilibrium with the solution. This may be because the few remaining grains become isolated from the solution by hydrates, for example AH_3 as in figure 6.8b, and hence cannot dissolve.

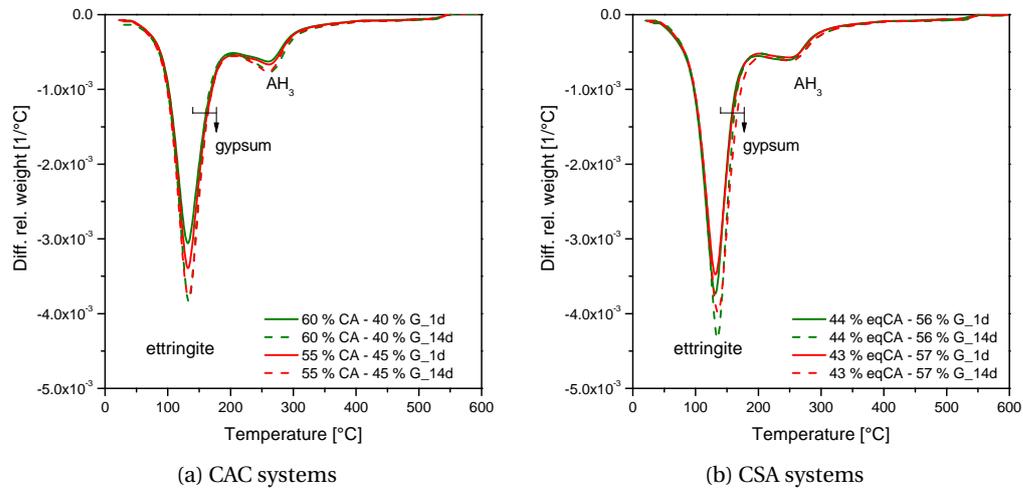


Figure 6.7: DTG curves at 1 and 14 days of low (solid lines) and high (dashed lines) expansion systems.

The equilibrium pore solution compositions (figure 6.11) and stable phase assemblage (figure 6.12) of the CA-C \bar{s} H $_2$ and the C $_4$ A $_3\bar{s}$ -C \bar{s} H $_2$ systems were also calculated by minimisation of the Gibbs free energy with the GEMS-PSI software [133]. The thermodynamic data for aqueous species and other solids is from the GEMS-PSI thermodynamic database [150] and the CEMDATA database for the solubility products of cementitious phases [151]. A degree of hydration of 100% was assumed (i.e. all the CA or C $_4$ A $_3\bar{s}$ and gypsum are free to react completely) and a w/b ratio of 0.65 used to have an excess of water allowing full hydration.

Figure 6.11a and 6.11b show the dissolved ions in the CA-C \bar{s} H $_2$ and C $_4$ A $_3\bar{s}$ -C \bar{s} H $_2$ systems, respectively. For CA-gypsum systems there is a small decrease of Ca $^{2+}$ and Al(OH) $_4^-$ at 25 mol% of calcium sulfate corresponding to the point where C $_3$ AH $_6$ is depleted and ettringite starts to be thermodynamically stable (figure 6.12a). But more importantly there is a threshold at 50 mol% of calcium sulfate, corresponding to the point at which solid gypsum starts to remain in excess, where the Ca $^{2+}$ and SO $_4^{2-}$ ions increase suddenly and Al(OH) $_4^-$ and pH decrease. The same observations are done for the ye'elimite-gypsum systems. The absolute amounts are different from those observed experimentally in figure 6.10 due to the absence of alkalis in the thermodynamic model, but the same trends between experimental measurements and modelling are observed and the change is similar to that seen in the experimental measurements of the pore solution between 40 and 45 mol% of calcium sulfate. Although this threshold value is somewhat different to that seen experimentally, we know the hydration is not complete in the experimental systems. Figure 6.12b shows the similar phase assemblage for ye'elimite-gypsum systems. The plain CSA without gypsum addition (CSA_ref) is indicated by a vertical line at 46 mol% of calcium sulfate. In this system there is a similar point at which solid gypsum remains in excess and a corresponding change in the pore solution composition.

6.4. Understanding expansion: effect of calcium sulfate

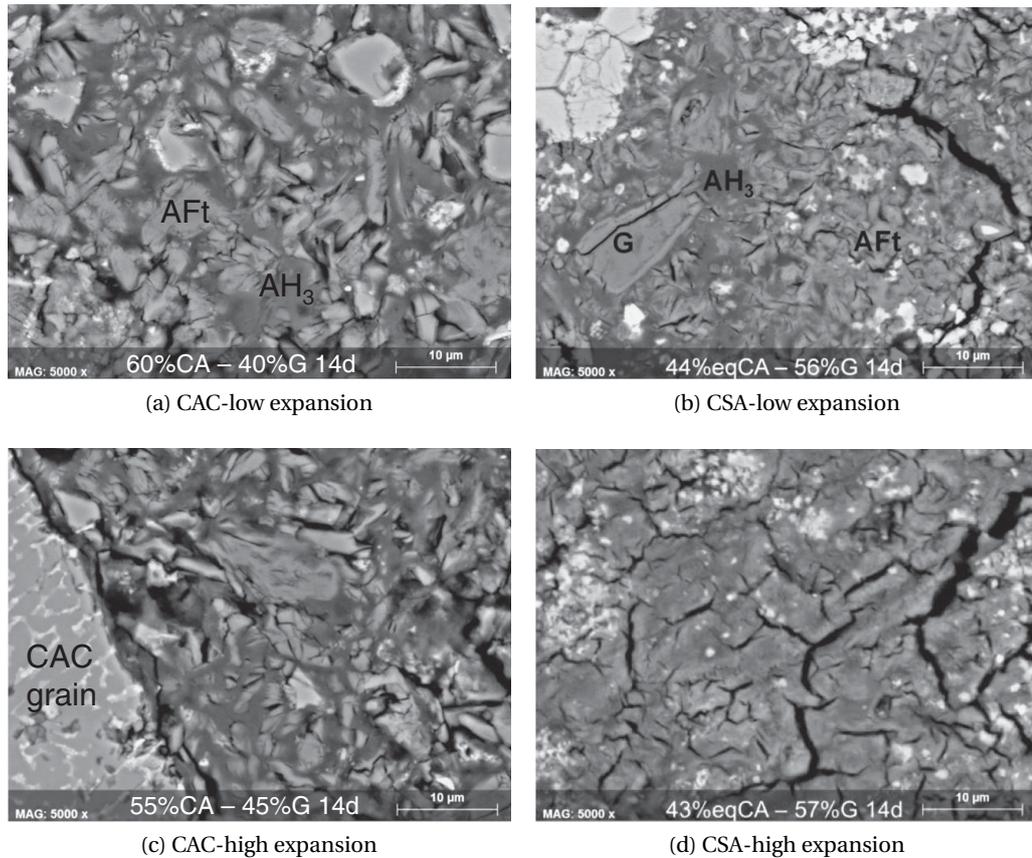


Figure 6.8: Microstructures of low and high expansion systems (AFt: ettringite, AH₃: amorphous aluminium hydroxide, G: gypsum).

6.4 Understanding expansion: effect of calcium sulfate

6.4.1 Pore stresses

From previous results it is shown that there is a difference in the microstructure of hydrated CAC-gypsum and CSA-gypsum. In the latter, ettringite and amorphous aluminium hydroxide are more intimately intermixed. These differences could explain the greater sensitivity to expansion of the CSA system. However within each system the calorimetry, XRD, SEM, TGA and MIP results do not indicate any clear difference between low expansive and high expansive systems.

If we consider that the underlying cause of expansion lies in the crystallization pressure of ettringite, we need to consider:

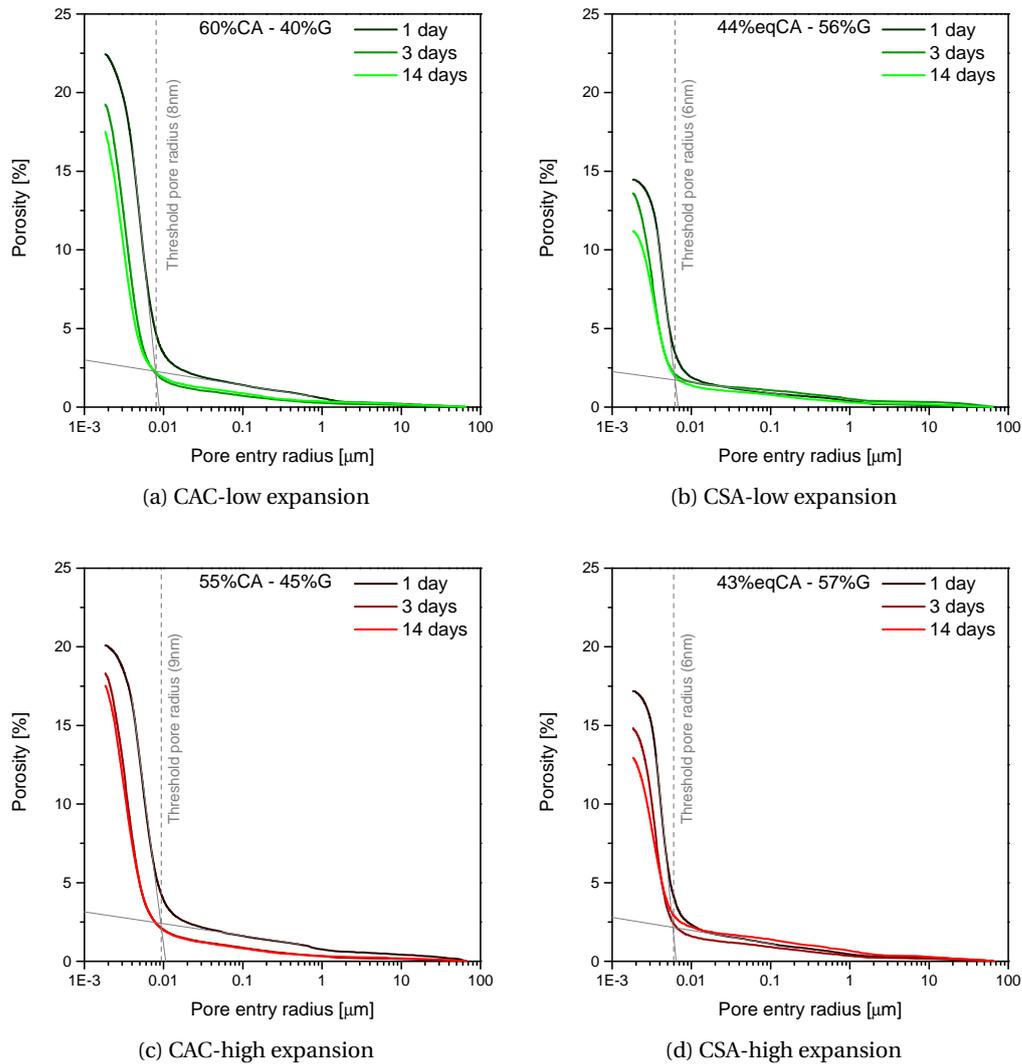


Figure 6.9: MIP cumulative porosity at 1, 3 and 14 days of hydration.

- The supersaturation with respect to ettringite.
- The confinement of ettringite, the size of pores in which it is growing.
- The mechanical links between the local effects of the growing ettringite and the macroscopic level of the prisms.

Supersaturation with respect to ettringite

The ettringite saturation index was calculated from the activities of the different species, this is plotted as a function of the gypsum content in figure 6.13. Activities were calculated from the experimentally determined concentrations with the extended Debye-Huckel equation

6.4. Understanding expansion: effect of calcium sulfate

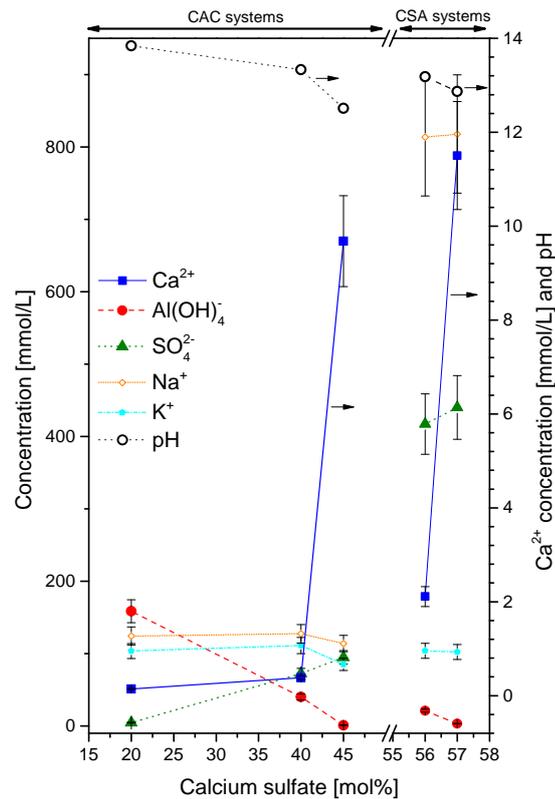


Figure 6.10: Ion concentration as a function of gypsum content at 7 days. Right y-axis: Ca^{2+} concentration and pH, left y-axis: all other ions concentrations.

implemented in GEMS [133]. On the right axis of figure 6.13 the crystallization pressure (ΔP) is shown calculated from equation 2.30. Although the supersaturations (and maximum crystallization pressures) corresponding to the high expansion systems are higher than those for the low expansive systems, there is no obvious threshold and the values for the low expansive CSA-gypsum system are very similar to the values for the high expansive CAC-gypsum system.

Confinement of ettringite crystals

In Portland cement systems undergoing external sulfate attack [152] or internal sulfate attack due to high temperature curing (so-called delayed ettringite formation) [60, 63], it has been shown that expansion occurs only when ettringite forms within C-S-H gel. Regions of C-S-H gel contain only small pores of ten nanometres or less, in which growing ettringite crystals exert expansive pressure. In contrast there are no clearly distinguishable microstructural environments identifiable in the case of the systems investigated here, where the hydrated matrix is composed of both ettringite and amorphous aluminium hydroxide. There should be an interfacial difference between the porous matrix and ettringite crystals generating pressure. Moreover, a film of solution is assumed between the crystal and the porous matrix.

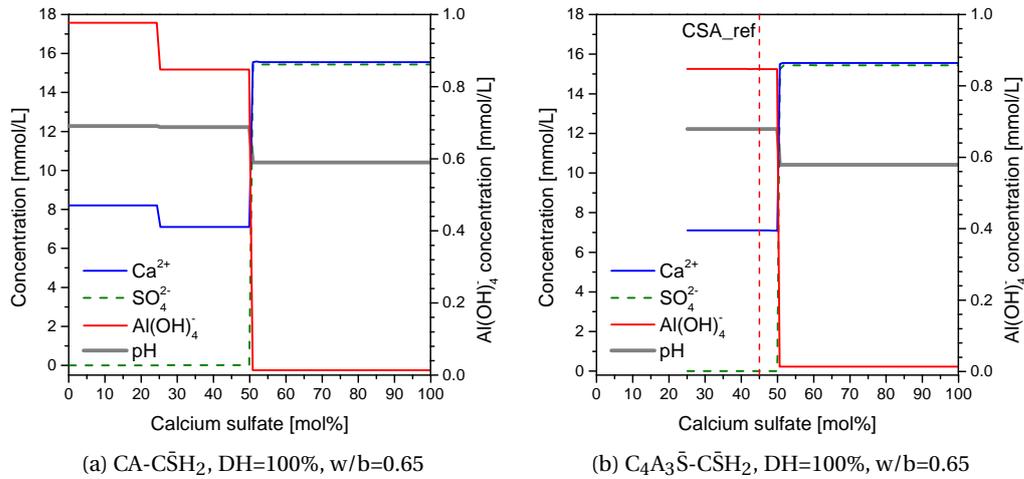


Figure 6.11: Thermodynamic simulation of stable aqueous solution at 20 °C (for b. the calcium sulfate amount is relative to eq. CA). The right y-axis shows the Al(OH)₄⁻ concentrations.

Questions remain as to why this film of solution can exist between two crystals of the same phase (ettringite). Probably, the high anisotropy of ettringite crystals and the different surface energies of each crystallographic direction could explain this.

The calculation of the stresses generated in pores can be done following two different assumptions which give similar conclusions and are based on the spherical pore shape described in the pore model 2, section 2.4.3:

1. The pressure generated in the pores is given by equation 2.24. The supersaturation defines the minimum pore entry size ($r_{min} - \delta = r_c$) through equation 2.31 and the pore size R_c where crystals grow is measured with MIP. Here it is assumed that MIP gives the pore size distribution.
2. The pressure generated in the pores is described by equation 2.24 where R_c is assumed to be much higher than r_c and the simplified equation 2.25 is obtained. The supersaturation defines again the minimum pore entry size above which crystals can grow, as in the previous assumption, and the pore entry size r_c is measured with MIP. This leads probably to a more accurate interpretation of MIP results.

First assumption, spherical pores with pressure $\Delta P = \gamma_{cl} \left(\frac{2}{r_c} - \frac{2}{R_c} \right)$

Figure 6.14a shows the crystallization pressure ΔP as a function of the pore radius for the different systems calculated according to equation 2.24 (assuming spherical pores, an interfacial free energy $\gamma_{cl}=0.1 \text{ J/m}^2$ [60] and the thickness of the film of solution between the crystal and the pore $\delta=1.5 \text{ nm}$). This shows there is a minimum pore radius where $\Delta P=0$, which corresponds to the size of pore for which the supersaturated solution is at equilibrium.

6.4. Understanding expansion: effect of calcium sulfate

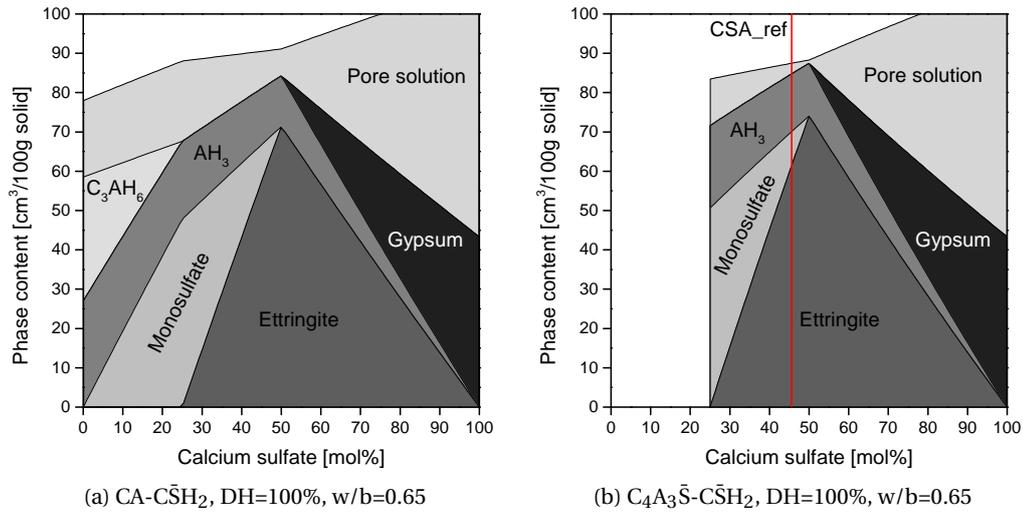


Figure 6.12: Thermodynamic simulation of stable hydrates at 20 °C (for b. the calcium sulfate amount is relative to eq. CA).

Consequently, ettringite crystals cannot grow into pores of smaller size. Vertical lines indicate the threshold pore radius of CAC and CSA systems measured by MIP on 1 day samples. The range of pores between the minimum pore radius and the threshold pore radius is assumed to be the amount of percolated porosity in which ettringite can exert crystallization pressure. Both low expansive and high expansive systems have a minimum pore radius smaller than the threshold pore radius, which means ettringite can grow through the pore network percolating the microstructure. Only the CAC system with 20 mol% of gypsum has a minimum pore radius above the threshold pore radius, indicating that ettringite can grow in a few large isolated pores.

The main difference between low and high expansive systems is that in the later cases there is a larger amount of percolated porosity where ettringite grows exerting crystallization pressure as shown in table 6.6. These values are only approximate as the interfacial energies are not precisely known nor do they account for anisotropy of the ettringite crystals.

Second assumption, spherical pores with pressure $\Delta P = \gamma_{cl} \left(\frac{2}{r_c} \right)$

Figure 6.14b shows the crystallization pressure ΔP as a function of the pore radius for the different systems calculated according to equation 2.24 where R_c is assumed to be much higher than r_c and gives equation 2.25. The assumption on the pore shape, interfacial free energy and thickness of the film of solution around the crystal are the same as before. Here, the threshold pore radius of MIP is not taken into account. Below the minimum pore radius indicated by the vertical lines there is no pressure generation. Above this value, determined by the saturation index of ettringite, the pressure decreases with the pore entry radius. This assumption seems to be more accurate when using the MIP data as input because it is generally agreed that MIP measures pore entry radii rather than pore sizes. This corresponds to the second assumption.

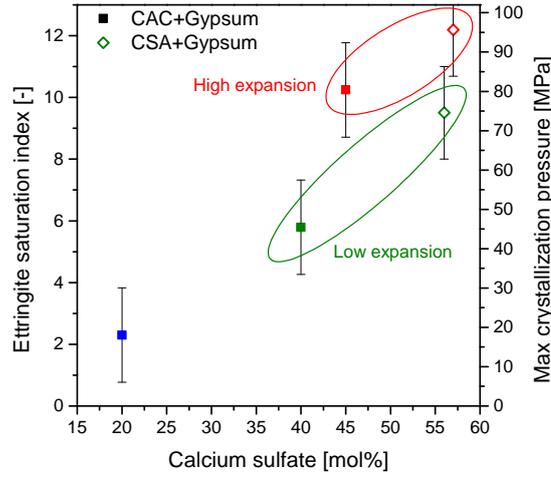


Figure 6.13: Ettringite saturation index as a function of gypsum content at 7 days.

Mechanical effects

As discussed by Scherer [58] a crystal growing in a single pore will not produce expansion. The crystallization pressure should be developed over regions many μm in size for overall expansion of the sample to be observed. The fraction of percolated porosity in which ettringite growth can generate pressure (“confined ettringite”) is relevant in these cases [60]. The difficulty in these systems is that it is impossible to measure directly the confined ettringite as all the porous matrix is composed mainly of this phase. Therefore, the volume of confined ettringite can only be estimated.

The average hydrostatic tensile stress generated is given by equation 6.1 [60].

$$\sigma = P \cdot g(\varphi) \quad (6.1)$$

Where P is the crystallization pressure and φ is the volume fraction of confined ettringite. $g(\varphi)$ is a geometric factor that depends on the shape of the pore. For a cylindrical pore:

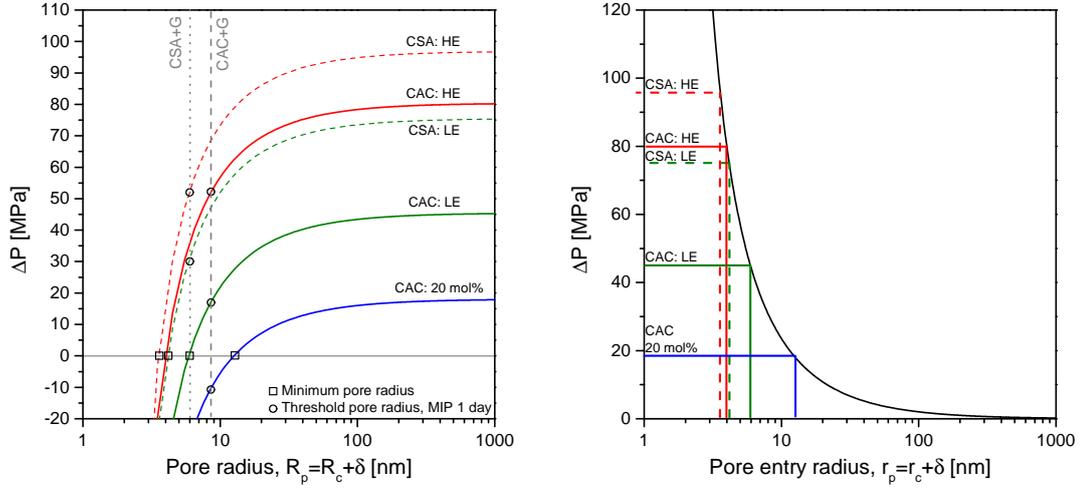
$$g(\varphi_{cyl}) = \frac{2}{3} \left(\frac{\varphi_{cyl}}{1 - \varphi_{cyl}} \right) \quad (6.2)$$

And for a filled large spherical pore with small entries:

$$g(\varphi_{sph}) = \left(\frac{\varphi_{sph}}{1 - \varphi_{sph}} \right) \quad (6.3)$$

These equations are based on spherical and cylindrical pores and so only approximate the situation in cement paste where the pores are irregular in shape and ettringite is highly anisotropic. Thus, equation 6.1 can be used to estimate the amount of confined ettringite needed to overcome the tensile strength of the cement paste which could potentially lead to cracking of the sample.

6.4. Understanding expansion: effect of calcium sulfate



(a) First assumption. SI of ettringite defines $r_{min} = r_p$ and MIP defines R_p . (b) Second assumption. SI of ettringite defines r_{min} , MIP defines r_p and $R_p \gg r_p$.

Figure 6.14: Crystallization pressure as a function of the pore radius for the first assumption (a) and the second assumption (b). Based on saturation indexes at 7 days of hydration, assuming $\delta = 1.5 \text{ nm}$. CAC systems: plain lines, CSA systems: dotted lines.

Table 6.6: For each system are presented the threshold pore radius (r_{thr}) measured with MIP, the minimum pore radius (r_{min}) calculated from pore solution analyses and the volume fraction of percolated porosity in which ettringite growth gives expansion pressure (φ_{ep}). A1 are the values calculated from the first assumption while A2 the values from the second assumption. The values necessary for the calculation of the volume fraction of confined ettringite in cylindrical (φ_{cyl}) and spherical (φ_{sph}) pores (equation 6.1) are the tensile strength (σ_t) and the crystallization pressure averaged over the pore size range ΔP_{mean} .

	CAC systems		CSA systems	
	LE	HE	LE	HE
r_{thr} [nm]	8	9	6	6
r_{min} [nm]	5.9	4.0	4.2	3.6
σ_t [MPa]	3.9±0.2		2.5±0.4	
First assumption				
φ_{ep} [vol%]	4.0%	12.0%	5.5%	9.0%
ΔP_{mean} [MPa]	7.1	30.8	15.0	26.8
φ_{cyl} [vol%]	45%	16%	20%	12%
φ_{sph} [vol%]	36%	11%	14%	9%
Second assumption				
φ_{ep} [vol%]	8.7%	16.5%	9.2%	13.1%
ΔP_{mean} [MPa]	11.7	21.2	25.3	31.5
φ_{cyl} [vol%]	33%	22%	13%	11%
φ_{sph} [vol%]	25%	16%	9%	7%

It is reasonable to take as average hydrostatic tensile stress the tensile strength of the cement paste estimated as 50% of the measured flexural strength [153], and as crystallization pressure the averaged pressure over the pore size range (ΔP_{mean}) corresponding to the percolated porosity measured with MIP above the minimum pore radius. All the values for the calculation and the resulting amounts of confined ettringite needed to overcome the tensile strength of the cement paste are shown in table 6.6. The results of these calculations are compared to the amount of percolated porosity in which ettringite can grow, discussed in section 6.4.1 in figure 6.14.

Figure 6.15 shows that the range of volume fraction of confined ettringite needed for cracking (φ_{sph} : lower limit and φ_{cyl} : upper limit, calculated with equation 6.1) is much higher than the amount of percolated porosity in which ettringite growth can occur in the case of both low expansive CAC and CSA systems (given by the volume of porosity above the minimum pore radius measured with MIP). However, in both high expansion systems the volume of confined ettringite needed for cracking is very similar to the volume of percolated porosity in which ettringite can grow. The total volume of porosity measured with MIP is also presented to show the maximum volume of porosity that could be filled by ettringite generating pressure, the values are always above the measured percolated porosity. These calculations are only approximate and contain many estimations. In addition to the assumptions of the surface energy for ettringite and the shape of the pores already discussed, it should also be mentioned that the flexural strength is obtained in a conventional test taking a few minutes as opposed to the expansion which takes place over a few days, this would allow deformation at lower stress due to creep effects. The two assumptions show the same trends.

Despite these approximations, the analysis indicates that as the supersaturation rises, the volume of percolated porosity in which ettringite can grow increases. This specific volume increases until a threshold is reached above which the confined volume of ettringite generating crystallization pressure is sufficient to cause cracking and unstable expansion.

A similar argument emerges from the analysis of ettringite formation after elevated temperature curing (DEF) by Chanvillard and Barbarulo [154]. They used poromechanics [155, 156, 157] to analyse a poroelastic skeleton (porous matrix) subject to deformations due to crystallization pressure. The cement paste or concrete is brittle so it cannot store elastic energy beyond a critical threshold [154]. When this threshold is reached, there is irreversible damage (expansion) which releases the stored elastic energy. This threshold is reached when the strain generates stresses above the critical tensile strength of the porous material. With these assumptions damage is considered.

The differences in behaviour between low and high expansive systems can be attributed to reaching a critical threshold, with the onset of extensive cracking. Figure 6.4 shows two domains, low expansive below the critical sulfate threshold and high expansive above this threshold. For low gypsum contents, the expansion increases gradually as the supersaturation of ettringite, the crystallization pressure and the volume of porosity containing confined

6.4. Understanding expansion: effect of calcium sulfate

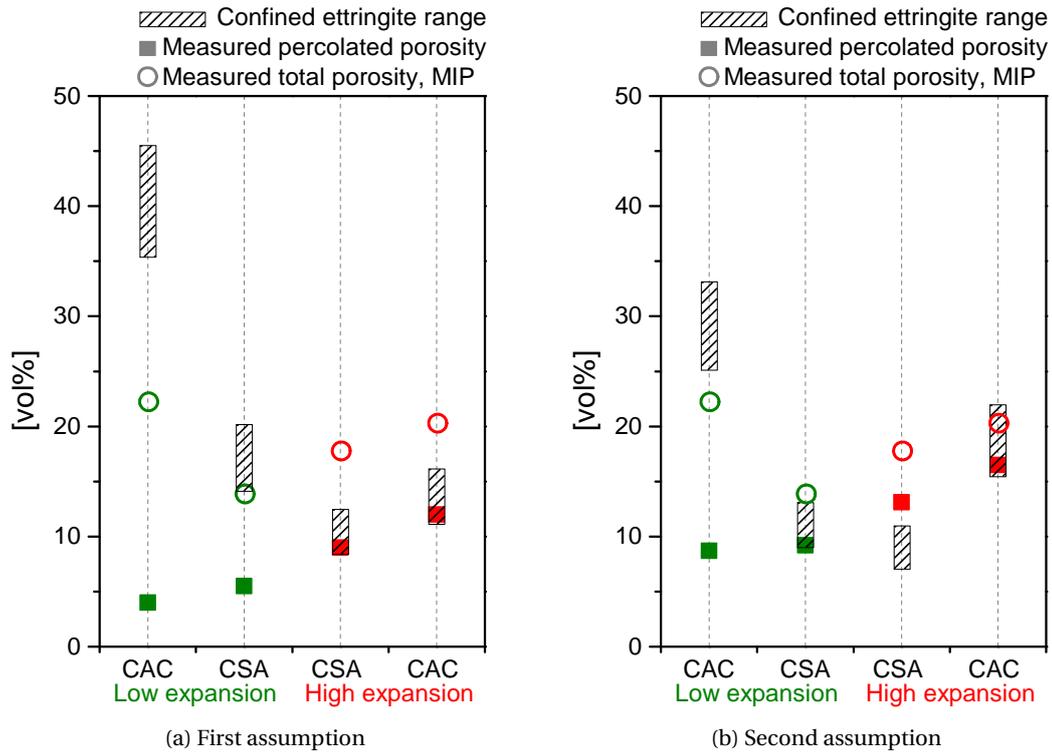


Figure 6.15: Volume of measured percolated porosity and confined ettringite range needed to cause cracking for the first assumption (a) and the second assumption (b). The total porosity measured with MIP is also presented.

ettringite increase. At around 45 mol% of gypsum (in the CAC systems) and 55 mol% (in the CSA systems) the slope of the curve becomes considerably steeper indicating cracking above the critical threshold of elastic deformation.

6.4.2 Summary on the effect of calcium sulfate

Systems of calcium aluminate cement and calcium sulfo aluminate cement, both with added gypsum, show unstable expansion when gypsum is added above a given threshold (around 45 mol% of gypsum for CAC and around 57 mol% for CSA systems or 50 mol% when sulfate from ye'elimite is not taken into account). Below this threshold there is a gradual increase in the amount of expansion at 28 days. The expansion occurs as a fairly rapid swelling within a few days of immersion of the samples in water, after which the sample dimensions remain stable and the samples stay intact over long periods of time (at least 65 days). Above this threshold the samples continue to expand gradually after the initial swelling and eventually fail. There is a marked difference in the strain to failure between the two systems (about 2.3% for the CAC-gypsum systems and 0.5% for the CSA-gypsum systems). The measured expansion represents high strains for a brittle material like cement paste. As the deformations and therefore the stresses develop slowly, there will be a certain amount of creep helping to dissipate the mechanical energy generated by the expansive phase.

In both cases ettringite and poorly crystalline aluminium hydroxide are the only hydrates formed. The intermixing of these different hydrates was much finer in the CSA-gypsum samples. A detailed microstructural investigation was made of systems above and below the threshold for unstable expansion. These studies showed no obvious difference between the systems:

- Comparable total amount of ettringite.
- Comparable pore size distributions.
- Comparable microstructures in the SEM.

On the other hand there was a distinct change in the pore solutions compositions at the threshold, with a drop in the concentration of aluminate ions, a strong increase in the concentration of calcium ions and small increase of sulfate ions. The solid phases present are the same, both gypsum and anhydrous phases (monocalcium aluminate or ye'elimite) are always in excess. However, thermodynamic modelling indicated that by increasing the gypsum content there is a sudden change when the gypsum is in excess. This indicates that even if solid gypsum is present in the low expansive system, it remains isolated from the pore solution by the hydrates. Despite the strong changes in the composition of the pore solutions, the supersaturation with respect to ettringite increases fairly uniformly with the gypsum content.

6.4. Understanding expansion: effect of calcium sulfate

Therefore we conclude that the onset on unstable expansion is a threshold effect, which can be explained by the combination of 2 mechanisms:

- The supersaturation of ettringite determines the range of pore sizes where it can precipitate and the magnitude of pressure. It is related to the ability of ettringite growth to penetrate an interconnected pore network - below the critical sulfate threshold ettringite can only exert pressure in a small number of isolated pores, above the critical sulfate threshold ettringite can form in a bigger fraction of porosity leading to a higher total volume of ettringite generating pressure and subsequent onset of unstable expansion.
- The formation of confined ettringite exerts pressure on the system. In the unstable high expansion systems, this pressure exceeds the tensile strength of the system leading to important deformations and unstable expansion.

The macroscopic expansion is thus strongly related to both the supersaturation of ettringite and the distribution and confinement of ettringite crystals in pores as illustrated in figure 6.16.

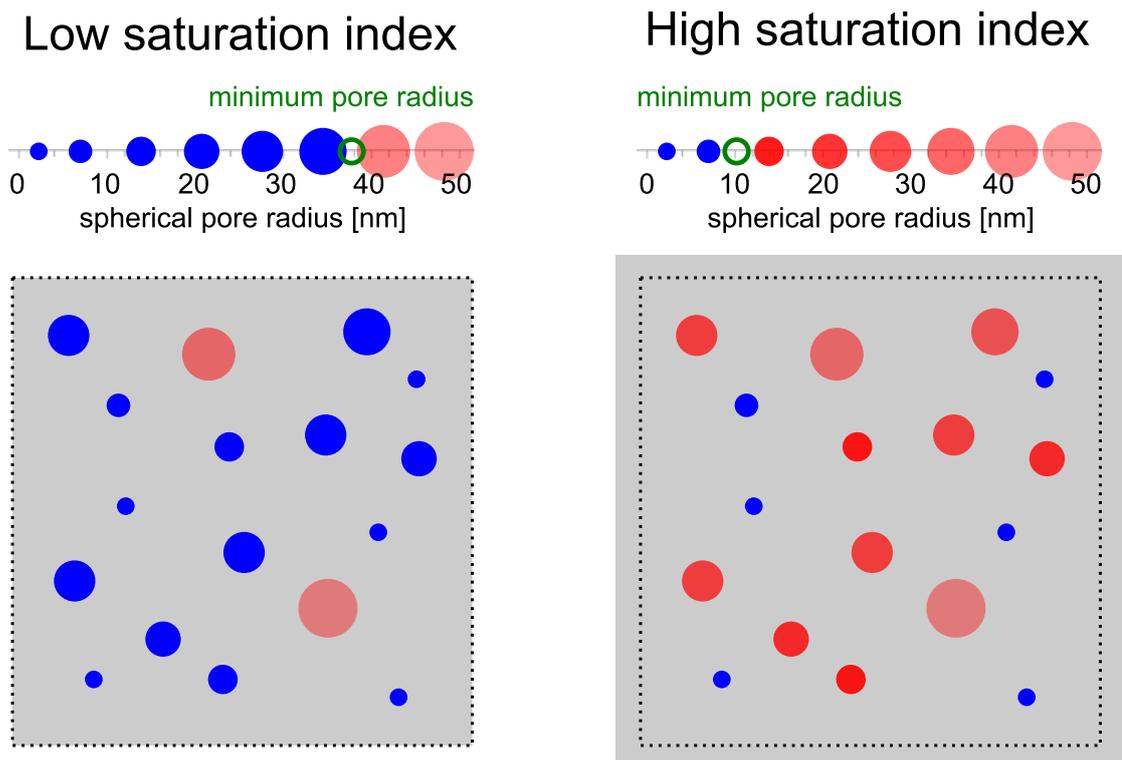


Figure 6.16: Effect of supersaturation on the pore size access. In blue are the undersaturated pores filled with pore solution. In red the supersaturated pores where ettringite grows and generates pressure. The red intensity increases with pressure, which is inversely related to the pore size.

6.5 Modelling of expansion: an elastic approach

6.5.1 Introduction of the model

A finite element model was developed on the basis of the second assumption described in the previous section 6.4 and on the pore models 1 and 2 presented in section 2.4.3. The minimum pore radius r_{min} is defined by the supersaturation of ettringite. Below r_{min} there is no pressure generation and above the pressure decreases with the pore radius. This model aims at showing the effect of the supersaturation of ettringite on the expansion of a sample of a given pore entry size distribution obtained from MIP measurements. It is a simplified two dimensional model. In isotropic materials the assumptions made in three dimensions are valid also for two dimensions. Moreover, no kinetics are taken into account.

Input parameters and main hypotheses

The pore models 1 and 2 represent the cylindrical and spherical pore shapes, respectively. They are used as the upper and lower boundaries to link the pore entry radius to the crystallization pressure $\Delta P(r)$ as shown in figure 6.17. The minimum pore radius where ettringite can grow is defined by the supersaturation of ettringite as described by equation 2.31. The supersaturation defines also the maximum crystallization pressure $\Delta P(r_{min})$ according to equation 2.30. The pressure in each pore is assumed to be a function of the pore size. This means that crystals in each pore have different supersaturations given by the size of the pore entrances. This is just an assumption and further calculations with homogeneous pressure determined by the measured saturation index of ettringite will be done.

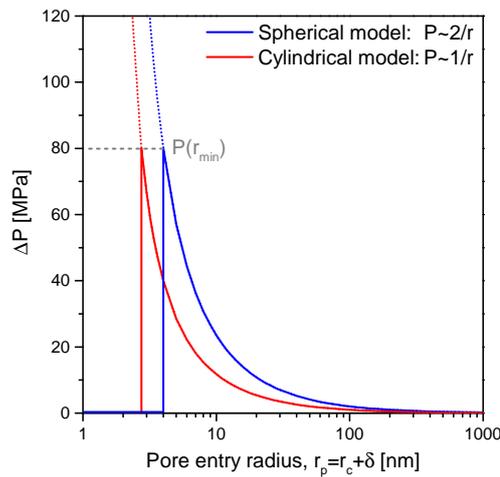


Figure 6.17: Crystallization pressure as a function of the pore entry radius for the spherical and cylindrical pore models.

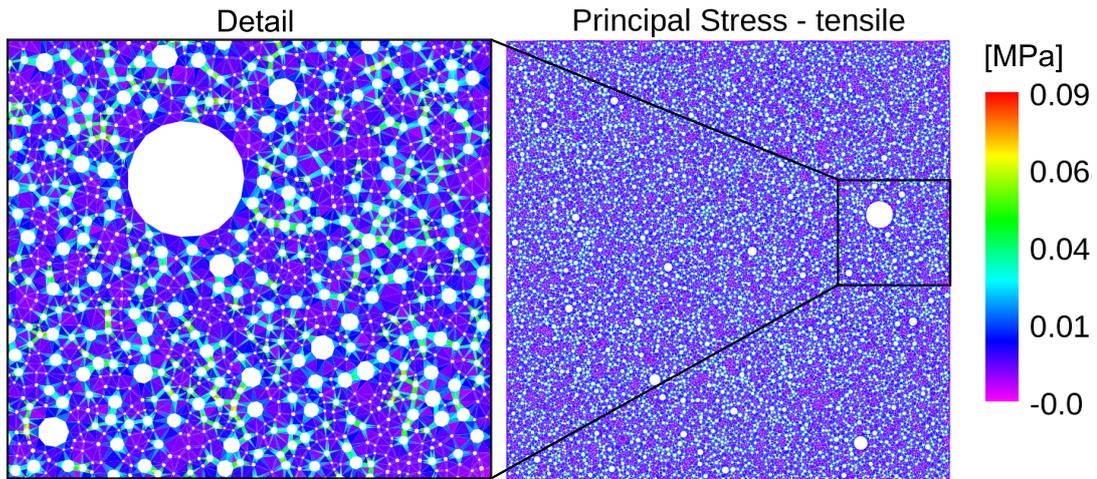


Figure 6.18: Model microstructure generated from MIP measurement with stress fields. Solid homogeneous matrix in colours and pores in white.

The input parameters are the MIP curve of the sample and the saturation index of ettringite at 1 day of hydration. The sample is composed of an homogeneous solid matrix and of pores where pressure is generated around all the pore surface. The properties of the solid matrix are assumed to be represented by the elastic properties of ettringite, $E=22.4$ GPa and $\nu=0.25$ [158, 159].

A microstructure with homogeneous solid material in which there are pores in amount and size according to MIP is generated. Note that here the pore entry size r_p given by MIP is represented in the model as a circular pore. These “pores” represented in white in figure 6.18 are representative of the expansive sites in the material and the pressure generated in these sites is related to the radius r_p . Only the pores larger than the minimum pore radius are under pressure. From a computational point of view it is quite challenging to generate a mesh containing objects (pores) going from 1 to 150 nm (2 orders of magnitude).

The main hypotheses are listed here:

- Mercury intrusion porosimetry gives effectively the pore entry size distribution.
- The pressure generated in each pore is determined from the pore entry radius with equations 2.23 and 2.25.
- The deformations in the model are purely elastic. Neither cracking nor creep are taken into account. With this hypothesis a lower bound of possible deformations is obtained as creep could result in 4-6 times higher deformations. In concrete it is usually assumed that creep leads to 2 to 3 times higher deformations according to the norm EN 1992-1-1, therefore in a pure cement paste this amount is even larger.

6.5.2 Sensitivity analysis

The main parameters of the model are varied to assess their influence on the expansion using the spherical pore model with small pore entries. Firstly, the thickness of the film of solution surrounding the crystal is varied. Figure 6.19 shows the expansion as a function of the saturation index of ettringite. The expansion follows a sigmoidal curve and increases with the supersaturation of ettringite. The thickness of the film of solution has almost no impact on the expansion. Therefore, the value of $\delta=1.5$ nm used in the previous sections is maintained for the following calculations.

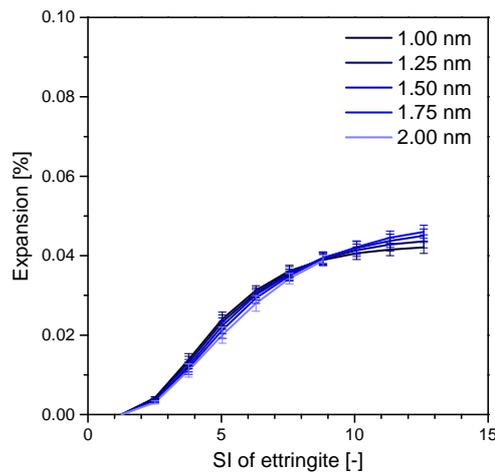


Figure 6.19: Modelling of expansion as a function of ettringite SI: effect of thin layer of solution around ettringite crystals. Spherical pore model.

The porous structure is simulated using different log-normal distributions representing similar curves to those obtained by MIP as in figure 6.20b. Figure 6.20a shows the influence of the median pore size on the expansion with a total porosity fixed at 20%. The smallest pores at 2.5 nm give the lower expansion as the lower pore radius generated by the code approaches this value, therefore a certain fraction of pores are missing in the calculations. At high SI, where all the pore sizes are accessible by ettringite, the expansion increases from 2.5 to 5.5 nm and decreases between 5.5 to 8.5 nm. Figure 6.17 shows that the pressure between 10 to 20 nm is quite low. Consequently, the expansion measured in the 6.5 and 8.5 nm pores size distributions is lower as a considerable part of the porosity is above 10 to 20 nm. At lower SI, where only a certain fraction of porosity is accessible by ettringite, the expansion increases with the median pore size.

6.5. Modelling of expansion: an elastic approach

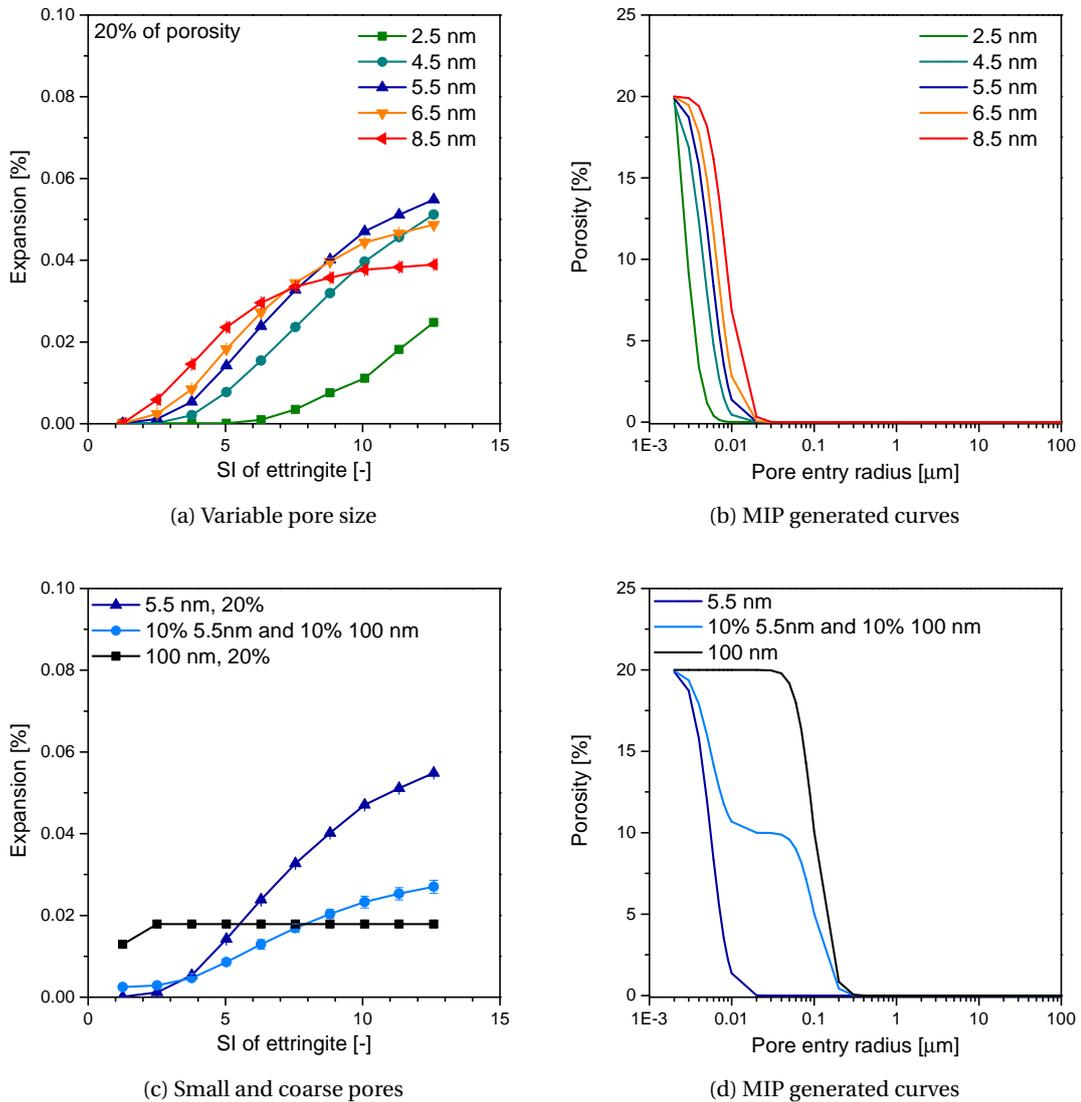


Figure 6.20: Modelling of expansion as a function of ettringite SI and MIP generated curves: effect of the pore size. Spherical pore model.

Two orders of magnitude larger pore sizes, 100 nm, give a constant expansion as a function of the SI of ettringite as shown in figure 6.20c because the minimum pore radius is always below this pore distribution (figure 6.20d). The expansion profile changes between a pore size distribution centered on 5.5 nm sized pores and a dual pore size distribution with 10% of 5.5 nm pores and 10% of 100 nm pores. It seems that the coarse pores do not have an influence and that the expansion is just reduced as there is only 10% of porosity. The smaller pores determine the expansion profile and the big pores have almost no influence in this model.

Chapter 6. Mechanisms leading to expansion

The influence of the total porosity is shown in figure 6.21a, where the expansion increases with the total porosity. This also confirms what observed previously, the expansion profile for 10% porosity is similar to the bimodal profile of figure 6.20c.

The equations obtained in the cylindrical pore model 1 (equation 2.23) and in the spherical pore model 2 (equation 2.25) linking the pore pressure to the pore radius $\Delta P(r)$ are compared in figure 6.21b. At low SI (<5) of ettringite the cylindrical pore model gives higher expansion values compared to the spherical pore model whereas at high SI (>7) the opposite is observed. The expansion is always higher using the cylindrical pore model in the 2.5 nm pore sizes. This clearly shows that the cylindrical pore model do not give a lower bound of expansion as it could be assumed from figure 6.17 because the minimum pore radius is reduced. The general trend observed from the modelling is that for low SI the cylindrical pore model gives the upper bound whereas for high SI is the spherical pore model that gives the upper bound. For the following calculations only the spherical pore model is used.

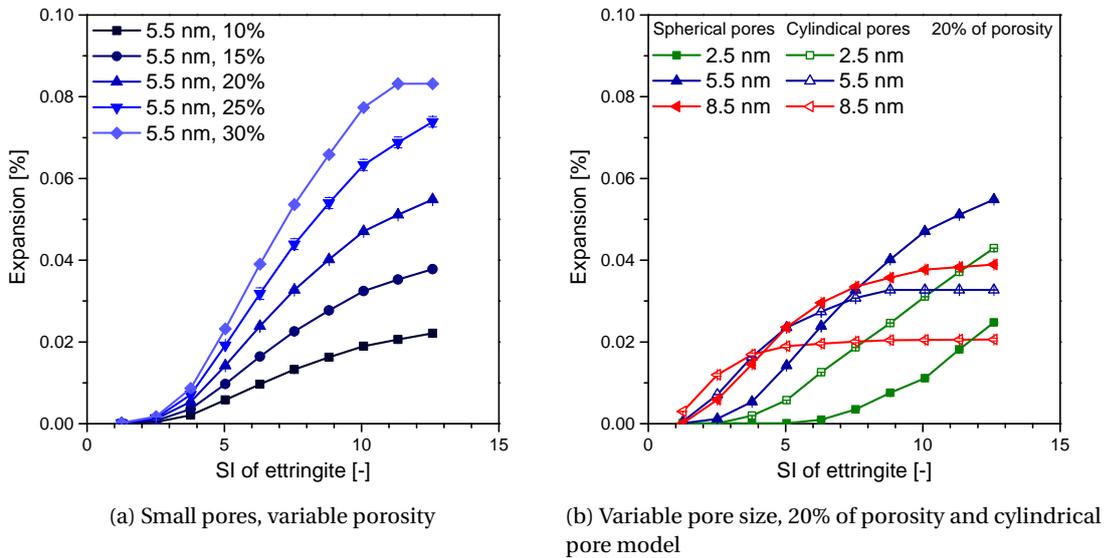


Figure 6.21: Modelling of expansion as a function of ettringite SI and MIP generated curves: effect of the porosity and pore model (spherical *vs* cylindrical)

6.5.3 Comparison between the model and the experiments

The measured expansion and saturation indexes of the samples studied in section 6.4 are compared to those from the model in figure 6.22. There is not much difference between the simulated 60CA-40G and 55CA-45G samples as the MIP curves are similar (figures 6.9a and 6.9c). The expansion increases with the saturation index of ettringite as expected for both the experiments and the model. The calculated values (right axis) are smaller than the measured values (left axis) using the elastic approach. When creep is emulated in the model by multiplying the calculated values by 5, as explained previously, there is good agreement between the experiments and the model. This is only an assumption and it may not be fully correct, moreover the accuracy of the elastic properties of the solid matrix could be improved, for example by measuring the elastic properties of the samples or by nanoindentation techniques. The saturation index of ettringite is strongly linked to the amount of calcium sulfate. This is confirmed by the behaviour of the model curves which is comparable to the shape of the expansion as a function of calcium sulfate amount as in figure 6.4. For low amounts of calcium sulfate and for low saturation indexes of ettringite, there is low expansion, whereas increasing calcium sulfate or supersaturation to the threshold level leads to higher expansion. In the next section, the model is used to understand the influence of the water to binder ratio and of the substitution with SCM on the expansion.

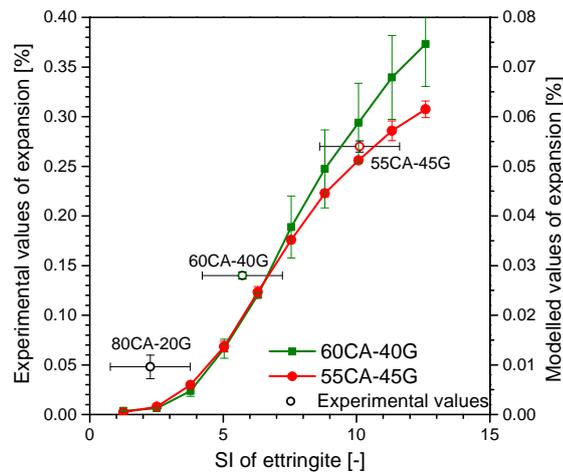


Figure 6.22: Modelling of expansion as a function of ettringite SI: comparison between experiments and modelling. Note that there is a factor of 5 between the experiments and the modelling.

6.6 Other factors influencing the expansion

The expansion is not only affected by the calcium sulfate amount in the system but also by other factors such as the porosity, the temperature and the alkalis. The effect of porosity on expansion was studied for variable water to binder ratios and variable substitution levels of limestone; therefore the same compositions as the ones used in the hydration study based on Ternal RG and hemihydrate were taken (see section 4.2). For the study of the other factors, systems composed of Secar 51 and gypsum were used as in the first part of this chapter.

6.6.1 Effect of porosity: water to binder ratio

The kinetics are affected by changes in the water to binder ratio as shown in figure 4.17 and in other studies on pure CAC hydration [118]. The calorimetric peak positions and the acceleration periods are unchanged whereas the deceleration periods are influenced by the water content or the available space for the reaction as described in section 4.5.1. The expansion of the 55CA-45HH system decreases with the water to binder ratio as shown in figure 6.23a. The total porosity and the threshold pore radius increase with the water to binder ratio (figure 6.23b). This suggests that ettringite is less confined when the water to binder ratio increases and therefore the expansion should decrease. Another parameter linked to the expansion is the saturation index of ettringite. The saturation index of ettringite of low and high expansion systems at 1 and 7 days as a function of the water to binder ratio is shown in figure 6.23c. The supersaturation is always negative for the low expansion systems whereas it is high, around 10, for the high expansion systems with a water to binder ratio of 0.4 and 0.5 at 1 day of hydration. The system with 0.67 w/b ratio has a low supersaturation. After 7 days, the supersaturation drops for the 0.5 w/b ratio system indicating that the ions in solution are consumed faster in systems with larger pores and higher porosity. At equilibrium conditions, the ettringite crystals tend to grow in big pores without exerting pressure and consuming the ions in solution [60]. The faster ions consumption causes a drop in supersaturation. This is linked to the faster consumption of anhydrous phases (CA and gypsum) and formation of more ettringite as observed with XRD analyses in figure 6.24. XRD analyses indicate that more anhydrous phases are consumed before the formation of a solid hydrated matrix, which causes a reduction of the potential ettringite forming in the solid hydrated matrix in confined conditions. This also shows that the expansion is not directly linked to the amount of ettringite as it is often mentioned in the literature. After 7 days where the ettringite amount is quite stable or decreases leading to the formation of monosulfoaluminate, the expansion is stationary.

6.6. Other factors influencing the expansion

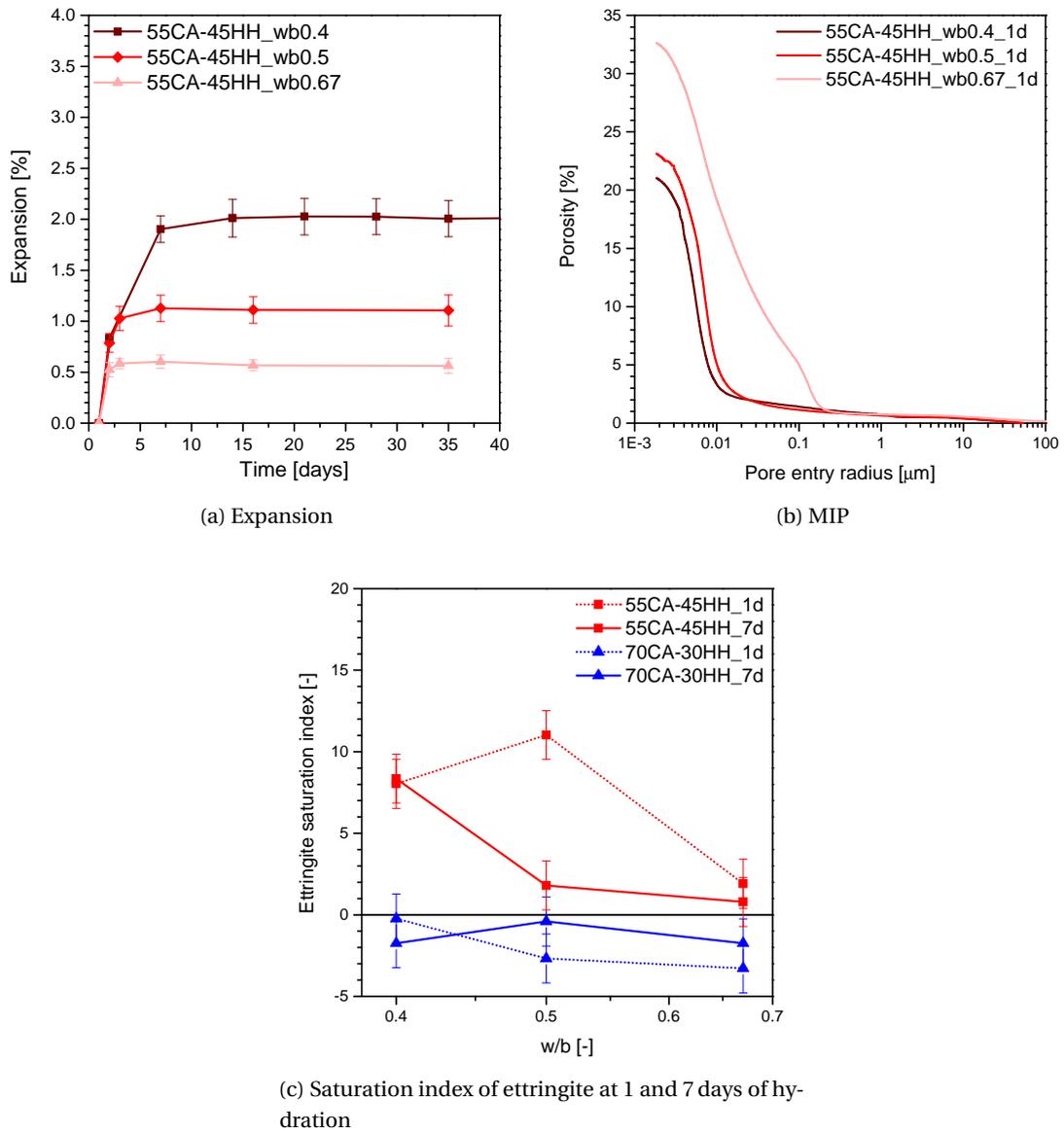


Figure 6.23: Expansion, MIP and ettringite SI of different calcium sulfate systems with variable water to binder ratios.

Chapter 6. Mechanisms leading to expansion

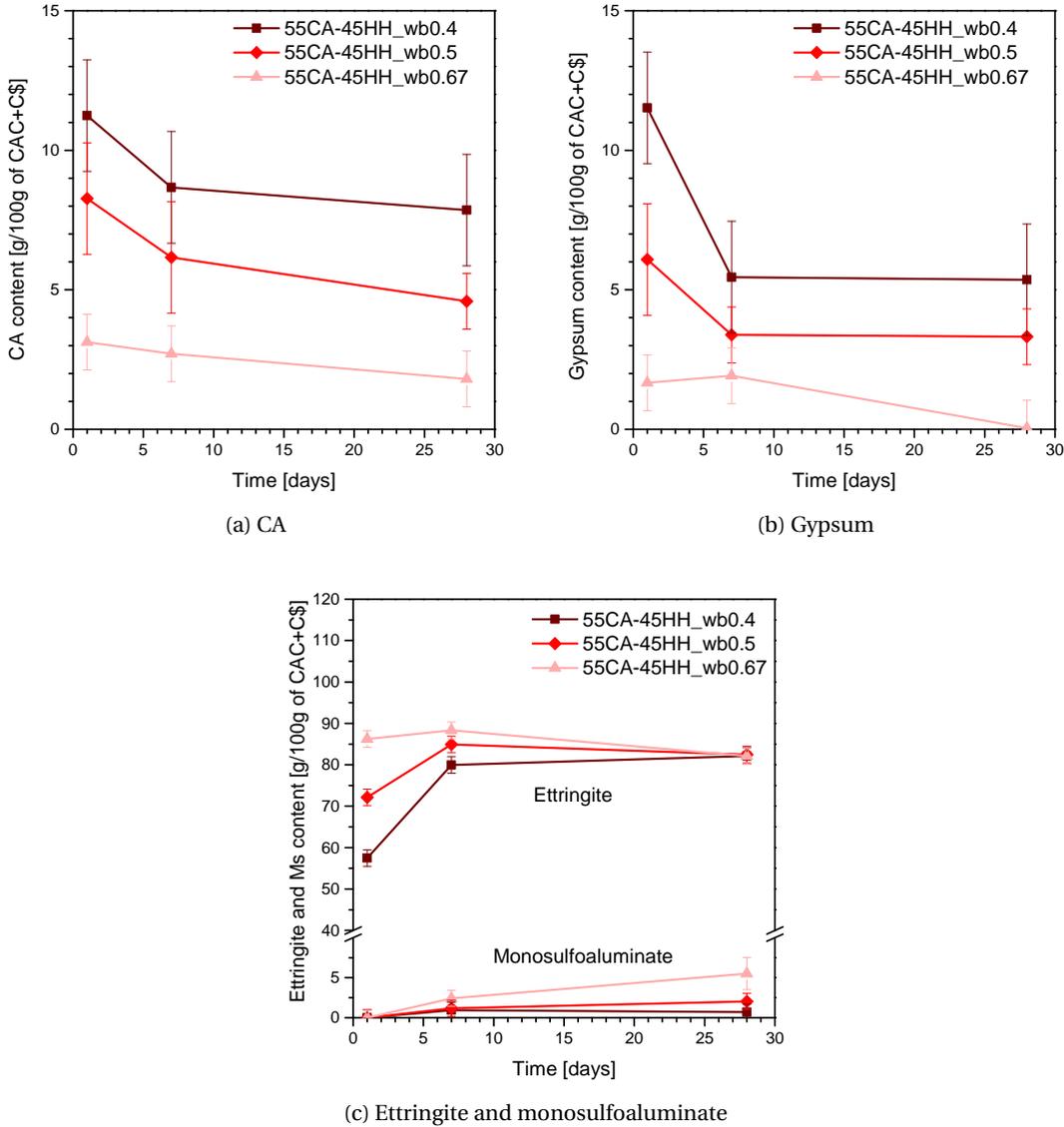


Figure 6.24: XRD quantification of the main phases for high expansive systems with variable water to binder ratios.

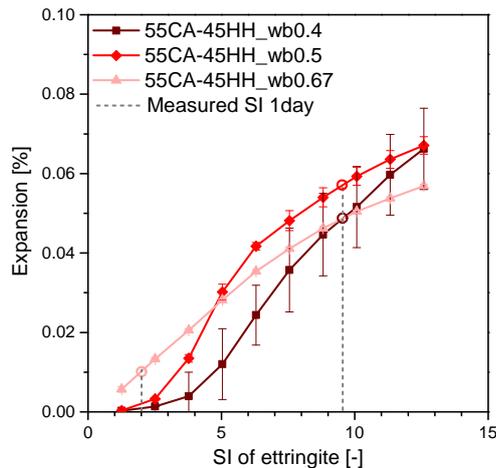


Figure 6.25: Modelling of expansion as a function of ettringite SI: effect of the water to binder ratio.

The modelled expansion shown in figure 6.25 represents the conditions at 1 day of hydration. It shows similar expansion values for the 0.4 and 0.5 w/b ratio and lower expansion for the 0.67 w/b ratio. This agrees quite well with the measured expansion after one day under water, even if the absolute values differ. When the hydration proceeds, the expansion increases up to 7 days of hydration and the supersaturation decreases for the 0.5 w/b system. This leads to a considerable reduction of the expansion. The different total porosity measured by MIP and used to generate the porous structure does not affect much the modelling results. This indicates that the main effect of the water to binder ratio on the expansion is due to faster drop in supersaturation. Expansion continues as long as ettringite is supersaturated.

6.6.2 Effect of porosity: substitution effect

The addition of SCM to the CAC-C \bar{s} system has various effects as shown in chapter 4. The filler effect leads to an effective increase of water to CAC+calcium sulfate ratio and to an acceleration of the kinetics at early age. SCM have a physical and chemical effect, here only the first days of hydration are analysed when the SCM are supposed to act as fillers.

The expansion as a function of time for the systems with variable amounts of calcium sulfate and with 20 wt.% limestone or without substitution is presented in figure 6.26a. This amount of substitution corresponds to a water to CAC+calcium sulfate ratio of 0.5. The expansion generally increases during the first 7 days of hydration, followed by a plateau. The expansion increases with the calcium sulfate content and decreases strongly for the substituted systems. The effect is similar to the 0.4 and 0.5 water to binder ratio systems presented in the previous section. The porosity and the threshold pore radius increase with the substitution and decrease with the calcium sulfate level as shown in figure 6.26b. The saturation index of ettringite during the first 16 hours of hydration is not modified by the substitution level as shown in figure 6.26c.

Chapter 6. Mechanisms leading to expansion

Probably there is a faster drop in supersaturation for substituted systems or higher water to binder ratios at later ages as observed in the previous section. The XRD analyses (figure 6.27) during the first 28 days seem to confirm this hypothesis as the anhydrous phases are more rapidly consumed in substituted systems and more ettringite is formed during the first day of hydration. The modelling based on the pore entry size distribution measured with MIP predicts higher expansion in the system with limestone because the total porosity is higher (figure 6.28). In real conditions, the supersaturation drops faster in the systems with higher porosity leading to lower magnitudes of expansion. The influence of limestone on expansion seems to be due only to the filler effect and not to a chemical effect. The modelling shows the same behaviour than the one observed for the systems with a water to binder ratio of 0.4 and 0.5, i.e. the expansion curve increases when the total porosity increases but the threshold pore radius is not too much affected.

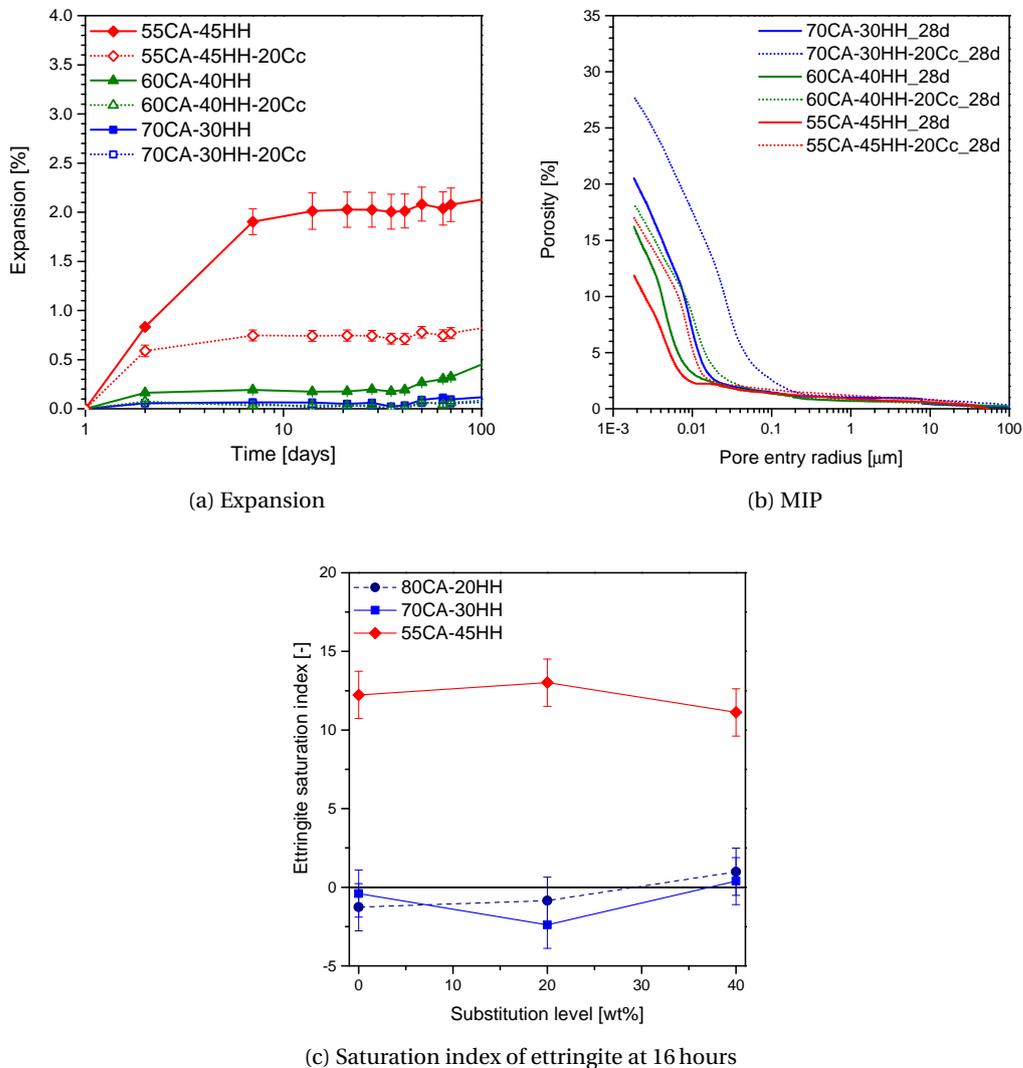


Figure 6.26: Expansion, MIP and ettringite SI of different calcium sulfate systems without and with substitution.

6.6. Other factors influencing the expansion

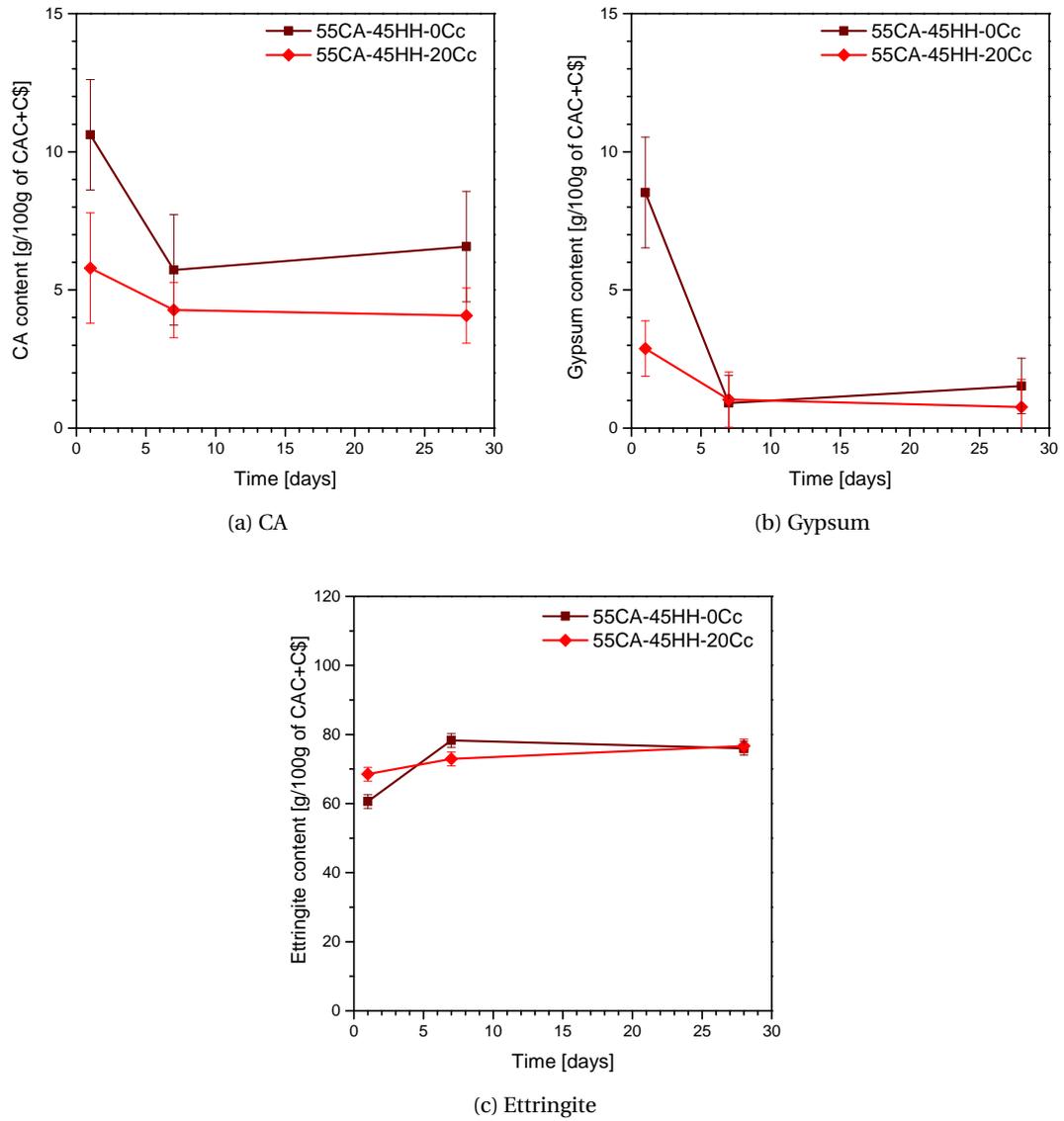


Figure 6.27: XRD quantification of the main phases for high expansive systems without and with 20 wt.% of limestone.

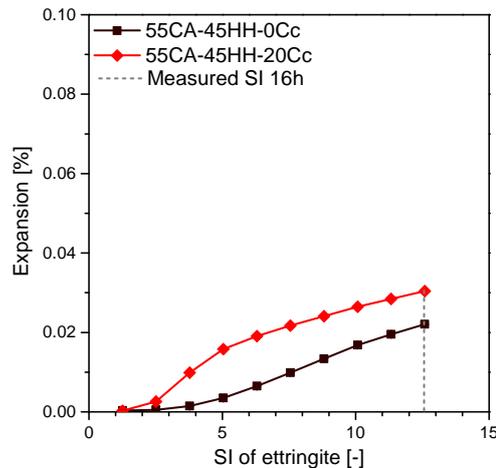


Figure 6.28: Modelling of expansion as a function of ettringite SI: effect of the substitution.

6.6.3 Summary on the effect of porosity: insights from the modelling

The modelling of expansion presented in section 6.5 shows good predictions of expansion for systems with comparable MIP curves and hydration kinetics. In the first part of the study, only the effect of calcium sulfate and therefore of ettringite saturation index is studied. This is well represented by the model. The part on the effect of porosity showed that the water to binder ratio or the substitution causing a dilution effect have both an effect on the porosity and kinetics. The porosity increases with the water content or substitution level and the anhydrous phases are consumed faster after one day of hydration. Both reduce the measured expansion as ettringite crystals grow probably in bigger pores, generating less pressures. Moreover, the ions in solution are consumed faster, leading to a drop of supersaturation. The model helps to understand the influence of the porosity on the expansion even if it does not take into account the kinetics and therefore is not able to predict the expansion for systems with variable pore size distributions where the supersaturation of ettringite decreases faster. This could be due in part to the limited accuracy of MIP in representing the pore size distribution. A comparison between MIP and proton NMR shows in figure 6.29 that the pore entry size distribution measured with MIP is close to the pore size distribution measured with NMR for systems with a narrow pore size distribution. This is probably the reason why the model works well for these systems. No measures were done for systems with variable pore size distributions by NMR. Probably for these systems the MIP is not representative anymore of the pore size distribution but remains representative of the pore entry size distribution. Despite the simplifications and assumptions done in the model, it helps to understand and distinguish the effects of the porosity and of the saturation index of ettringite (or minimum accessible pore size).

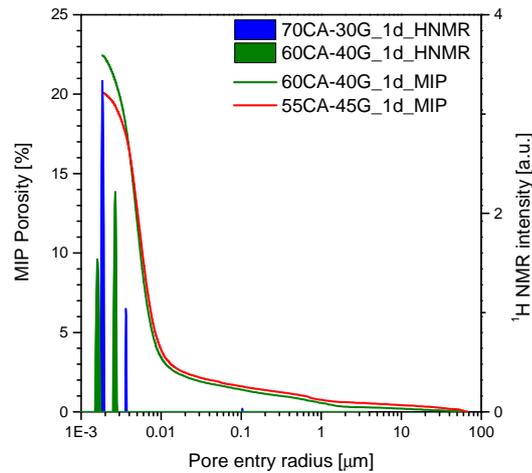


Figure 6.29: Comparison between MIP and H NMR measurements.

6.6.4 Effect of ettringite solubility and kinetics: temperature effect

The temperature is known to have effects on the kinetics [19] and on the solubility of ettringite as discussed in appendix A.1.1. Higher temperatures accelerate the reactions. The expansion of systems containing different amounts of calcium sulfate for 20 and 38°C is shown in figure 6.30. The expansion increases with the temperature for all the three systems as already observed by Chen on similar systems [83]. The solubility of ettringite increases with the temperature as shown in figure 6.31a. From 20 to 38°C the solubility increases by two orders of magnitude and therefore the saturation index of ettringite decreases by the same amount. According to figure 6.31b, the decrease of two orders of magnitude of SI causes a drop of crystallization pressure of less than 20 MPa and an increase of the minimum pore radius from 4 to 4.65 nm. For high expansive systems usually having crystallization pressures around 80-100 MPa it does not seem that the drop of pressure caused by the change in ettringite solubility is high enough to affect the expansion. From the results presented here it seems that the effect of the temperature on the expansion is through its impact on the kinetics. According to other studies [85], temperature accelerates the kinetics of ettringite formation causing more expansion. The expansion generated by confined ettringite is higher when the solid porous matrix is formed more rapidly. There is a competition between the consumption of ionic species in the solution causing a drop in supersaturation and the formation of a solid porous matrix. Expansion occurs if the supersaturation remains elevated after the formation of a solid skeleton. More investigations are needed on this topic to really understand the effect of the temperature on the expansion.

Chapter 6. Mechanisms leading to expansion

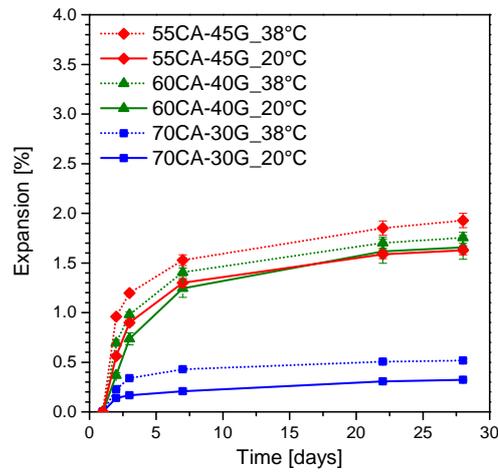
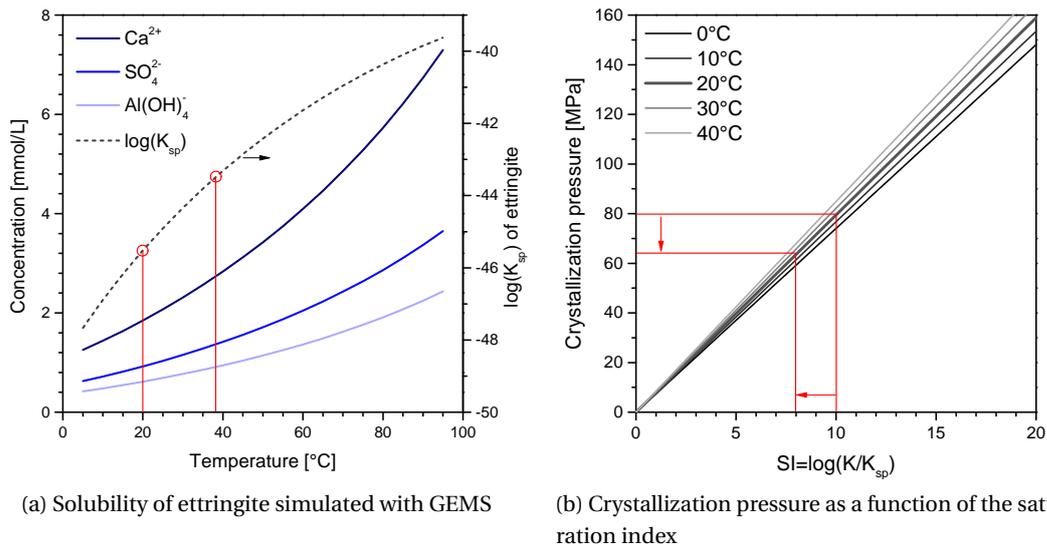


Figure 6.30: Expansion of variable calcium sulfate systems at 20 and 38°C.



(a) Solubility of ettringite simulated with GEMS

(b) Crystallization pressure as a function of the saturation index

Figure 6.31: Effect of the temperature on the solubility of ettringite and on the crystallization pressure.

6.6.5 Effect of alkalis

The effect of alkalis was studied by adding NaOH to the mixing water. The alkalis affect the kinetics as shown in figure 6.32a. There is a strong acceleration with 0.5 and 1M of NaOH and even stronger with 3.7M NaOH. The expansion measurements (figure 6.32b) do not show a clear effect on the expansion up to 1M of NaOH, but show a destructive behaviour for the system with 3.7M NaOH where the sample expanded considerably and was destroyed after one day under water. As explained in appendix A.1.1, the effect of alkalis and pH on the solubility of ettringite is not clear in the literature. Thermodynamic simulations of the solubility of ettringite confirmed a constant solubility product of ettringite with variable pH (or variable NaOH) as previously described by [160] in appendix A.1.1. Thermodynamic prediction shown in figure 6.33a of the phase assemblage indicates that the amount of ettringite should decrease as the NaOH concentration increases while the amount of monosulfoaluminate increases with the amount of thenardite (Na_2SO_4). Experimental XRD analyses (figure 6.33b) after one day of hydration show an increase of ettringite amount up to 1M NaOH followed by a decrease of it at 3.7M NaOH. The amount of anhydrous CA is not really affected whereas the amount of gypsum decreases when NaOH concentration increases leading to the formation of thenardite. No monosulfoaluminate is observed experimentally, maybe because of its poor crystallinity. The kinetics and the phase assemblage are modified by alkalis but probably not enough to have a significant effect on the expansion. Only with the higher alkali level of 3.7M NaOH the expansion is affected but at these high levels of alkalis the mechanisms of expansion are probably linked to thenardite formation instead of ettringite growth.

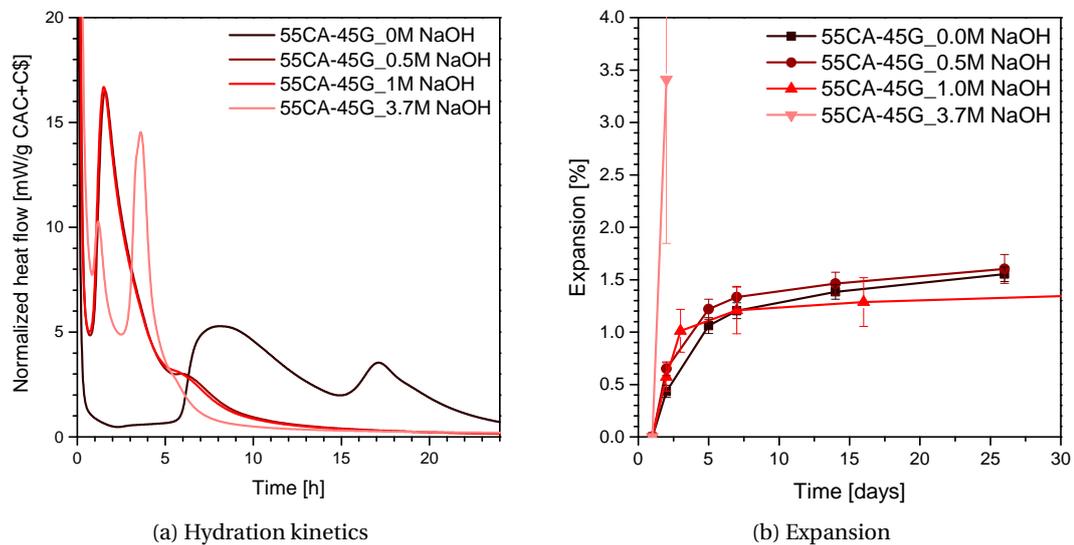


Figure 6.32: Hydration kinetics and expansion of the high calcium sulfate systems with variable NaOH concentrations.

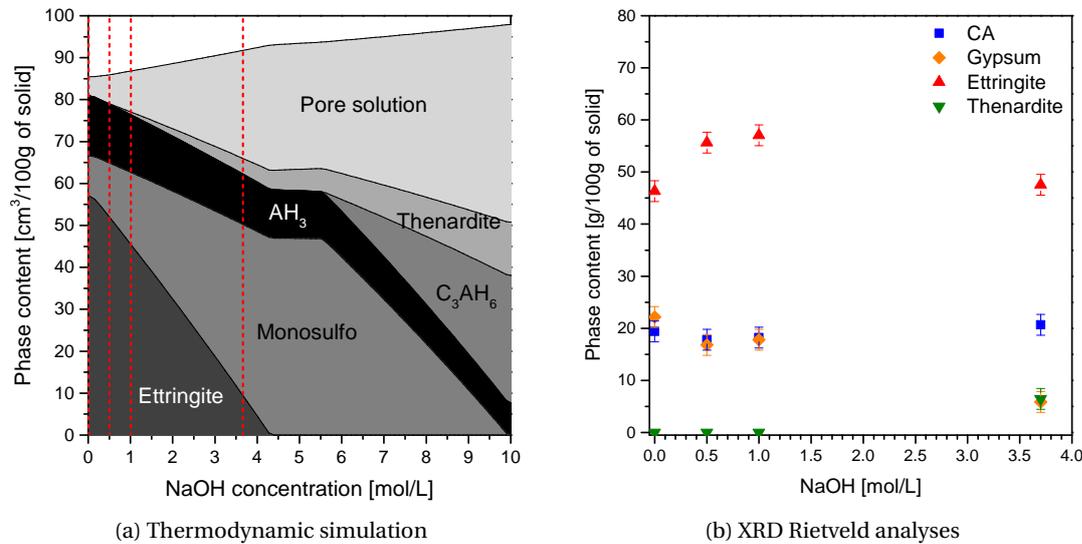
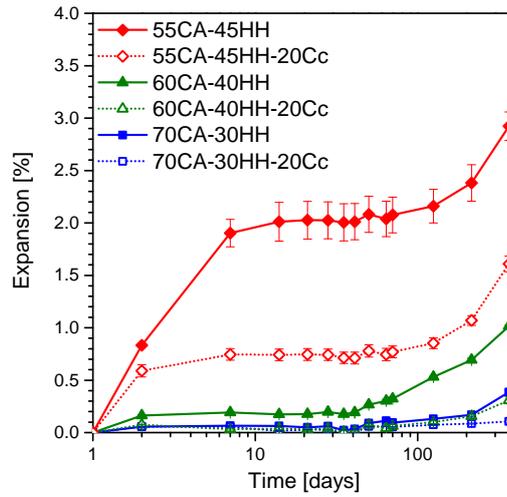


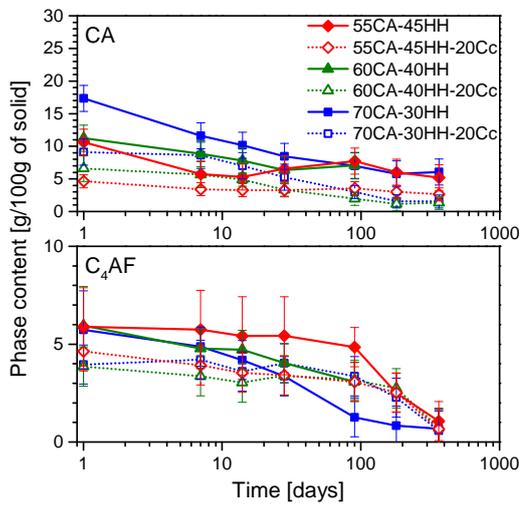
Figure 6.33: Comparison between the phase assemblage predicted by thermodynamic simulation and measures with XRD on alkaline compositions.

6.7 Long term expansion

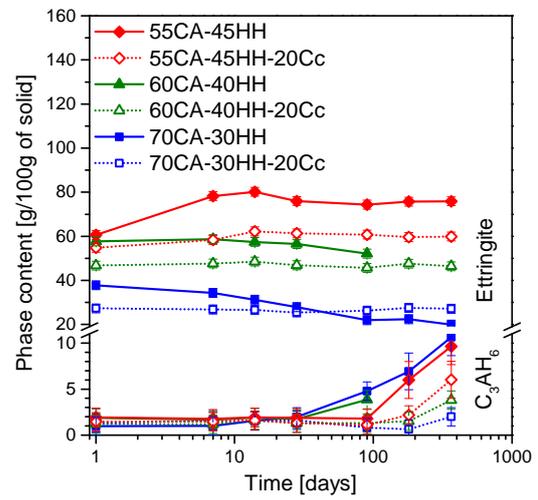
Figure 6.34a shows the expansion of cement paste prisms (described in section 3.2.3) as a function of the time during one year under water. The expansion increases during the first 7 days of hydration, followed by a plateau until 100 days and it increases again after 100 to 200 days of hydration. Pore solution analyses on samples after one year were not available but XRD quantitative analyses of limestone systems presented in figures 5.6 and 5.7 indicated the formation of hydrogarnet C_3AH_6 after 100 days of hydration. Figure 6.34b shows the evolution of the anhydrous CA and C_4AF phases and figure 6.34c shows the evolution of ettringite and hydrogarnet over time. Ettringite is stable or is consumed in low calcium sulfate systems without limestone but there is a clear formation of hydrogarnet at later ages, probably due to the consumption of CA and mainly C_4AF . This could be linked to the expansion observed after 100 days even if there are no previous studies showing this behaviour. Nevertheless, early expansion was observed in plain CAC systems as a result of the conversion of metastable CAH_{10} and C_2AH_8 to stable C_3AH_6 at 38°C [161] but the mechanism leading to that expansion was not reported. It should be possible that a supersaturated solution with respect to hydrogarnet at later ages in confined conditions leads to expansion. More investigations on expansion potentially generated by the hydrogarnet growth are needed to draw clear conclusions.



(a) Expansion



(b) CA and C₄AF quantification



(c) Etringite and hydrogarnet quantification

Figure 6.34: Comparison between the expansion and the phase evolution for variable calcium sulfate systems without and with 20 wt.% limestone substitution.

7 Conclusions

Contents

7.1 Conclusions	139
7.1.1 Hydration with and without SCM: effect of calcium sulfate	139
7.1.2 Mechanisms leading to expansion	141
7.2 Perspectives	144

7.1 Conclusions

This thesis was developed along two main axes: the study of the hydration of CAC-calcium sulfate systems, from the first hours to two years; and the study of the mechanisms of expansion.

7.1.1 Hydration with and without SCM: effect of calcium sulfate

The study of the **early age hydration** (<24 hours) indicated the origin of each calorimetric peak (figure 7.1). During the first peak hemihydrate dissolves while gypsum forms and during the second peak the reaction between CA and gypsum leads to the formation of ettringite and microcrystalline aluminium hydroxide. The third peak appears only when calcium sulfate is consumed. During this peak there is an accelerated reaction of CA with ettringite to form poorly crystalline monosulfoaluminate. This shows that the amount of calcium sulfate influences the phase assemblage.

Addition of supplementary cementitious materials (SCM) such as limestone or slag has a physical effect at early age called the “filler effect”. This consists of a nucleation effect and of a dilution effect. The filler leads to more surface for the heterogeneous nucleation of the hydrates and their growth. The dilution effect is the availability of more space for this growth as more water is available for the CAC-calcium sulfate component. Both effects accelerate the consumption of the anhydrous phases and lead to more hydrate formation as illustrated in figure 7.2.

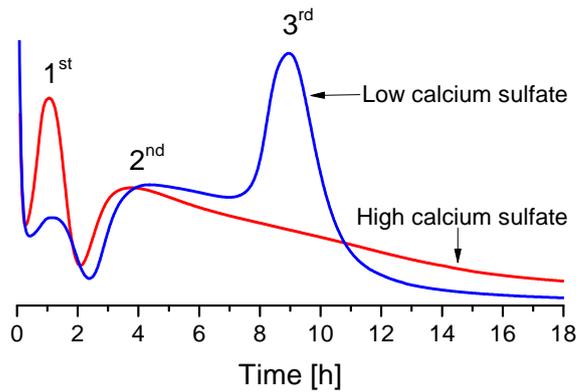


Figure 7.1: Comparison between the hydration kinetics of low and high calcium sulfate systems.

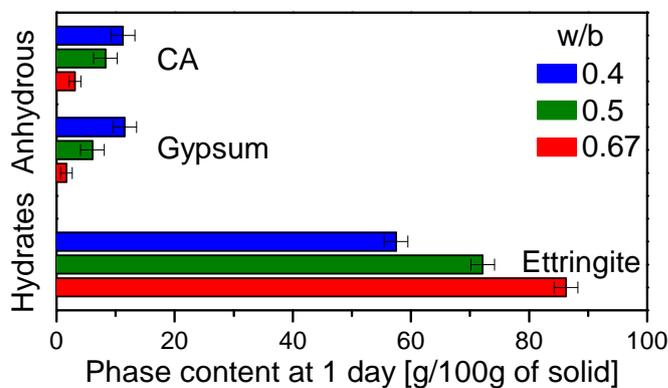


Figure 7.2: Phase content at 1 day of hydration for variable water to binder ratios of the system 55CA-45HH.

Limestone and slag react with the binder after the first day **up to 2 years of hydration**. This was observed initially by comparison of compressive strength of systems substituted with inert quartz or SCM. The study of the phase assemblage showed that SCM start to react with the system after the first day of hydration by forming hydrates such as hemicarboaluminate and monocarboaluminate for limestone and strätlingite for slag additions. The reaction of SCM is influenced by the relative amounts of calcium sulfate and calcium aluminate. Thermodynamic simulations with GEMS helped to understand the impact of calcium sulfate on the SCM reaction and give a consistent prediction of the phase assemblage. CAC reacts with calcium sulfate as long as it is present and, after its depletion, SCM start to react with calcium aluminate. Increasing amounts of calcium sulfate cause a reduction of the reaction of limestone and slag. The systems with excess of calcium sulfate have a pore solution of low pH, about 10.5, whereas when sulfate is depleted the pH increases up to 12. Probably the combination of excess of calcium sulfate and low pH, which slows down slag dissolution, causes low slag reaction.

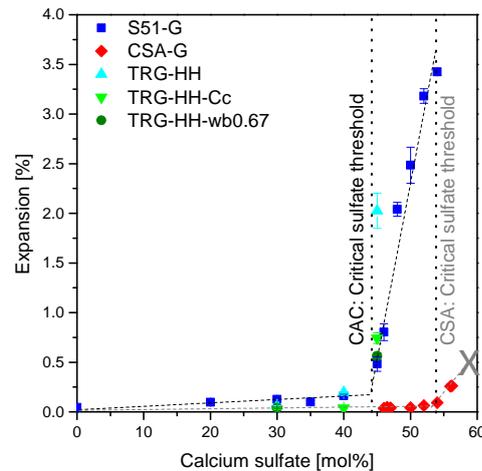


Figure 7.3: Expansion as a function of calcium sulfate at 28 days of hydration: comparison of different cements (Secar 51 *vs* Ternal RG), calcium sulfates (gypsum *vs* hemihydrate), with and without 20 wt.% limestone (Cc) substitution and with higher water to binder ratio of 0.67.

The increase of calcium sulfate affects the phase assemblage, reduces the amount of reacted SCM and can also lead to uncontrolled expansion whose mechanisms are discussed below.

7.1.2 Mechanisms leading to expansion

The long-term expansion of calcium aluminate cement or calcium sulfoaluminate cement in presence of added calcium sulfate was studied for samples under water. **Expansion increases with calcium sulfate** and shows a critical sulfate threshold around 45 to 55 mol.% of calcium sulfate with respect to calcium aluminate (figure 7.3).

Microstructural investigations showed that two systems with similar amounts of calcium sulfate immediately above and below the critical sulfate threshold have comparable microstructure, phase assemblage and porosity; the main difference being the supersaturation of ettringite. The solution changes around the threshold; the calcium and sulfate concentration increases and the aluminium concentration drops. The supersaturation with respect to ettringite increases with the calcium sulfate content, even if solid gypsum is observed above and below the threshold, and probably isolated from the pore solution by the hydrates. The rise of supersaturation results in an increase of the crystallization pressure but is not sufficient to explain the observed threshold.

This study shows that the supersaturation of ettringite determines the minimum pore radius where a crystal can grow, therefore with higher supersaturation a larger pore volume is accessible to growing ettringite crystals exerting pressure in the porous matrix. The supersaturation is related to the ability of ettringite growth throughout the interconnected pore network (figure 7.4): below the critical sulfate threshold (low saturation index) ettringite can only exert

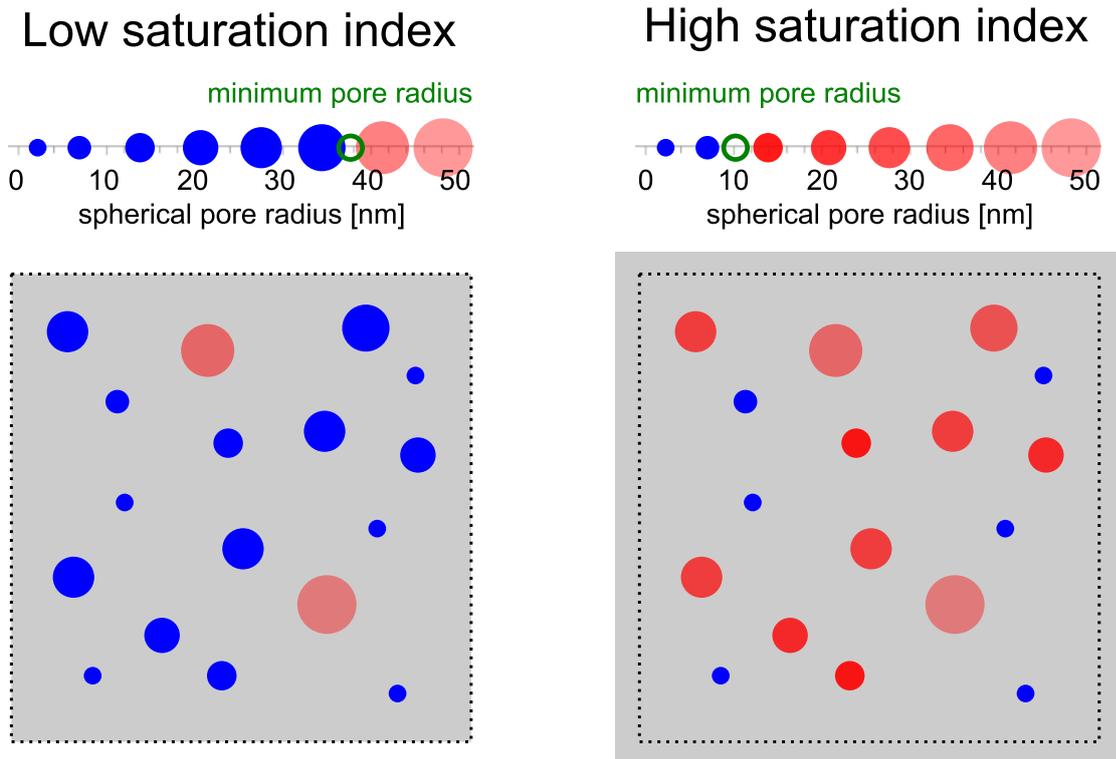


Figure 7.4: Effect of supersaturation on the pore size access. In blue are the undersaturated pores filled with pore solution. In red the supersaturated pores where ettringite grows and generates pressure. The red intensity increases with pressure, which is inversely related to the pore size.

pressure in a small number of pores; above the critical sulfate threshold (high saturation index) ettringite can form in a larger fraction of porosity leading to a higher total volume of ettringite generating pressure. This correlates to the onset of unstable expansion.

The critical sulfate threshold was then explained using the pore size distribution from MIP and the supersaturation of ettringite. As a **first approach** it was supposed that to have high and uncontrolled expansion, the pressure generated throughout the porosity should be larger than the tensile strength of the cement paste. The calculations showed that the pressure generated in the system above the critical sulfate threshold were above the tensile strength of the cement paste. Indicating that important deformations could develop and unstable expansion could occur.

This mechanism of expansion shows the links between the supersaturation of ettringite and the confinement provided by the porous structure. In a **second approach**, the mechanism of expansion illustrated in figure 7.4 was implemented in a finite element code to compute the relationship between expansion, saturation index and pore size distribution. In this model the damage is not considered and only elastic deformations are calculated. The deformations due to pressure in small pores show clearly a threshold effect between low and high supersat-

urations. Despite the simplifications, the same trends as the ones observed in figure 7.3 are seen.

The **effect of the porosity** was further studied by changing the water to binder ratio and by adding SCM in the system. Both studies showed a decrease of the expansion for the same level of calcium sulfate. Experimental observations confirmed that the porosity increases with the water or substitution level and that the expansion decreases. Quantitative XRD showed higher degree of hydration of CAC during the first day resulting in higher volumes of hydrates formed. Moreover, pore solution analyses showed that the ions in the solution were consumed faster causing a drop in supersaturation in the diluted systems. This is due to more space and water available for the reaction to proceed. In the literature, expansion is often linked to the amount of ettringite but it is shown here that this relationship is not direct; highly expansive systems showed a decrease of the expansion and an increase of ettringite content when the water to binder ratio or the substitution was increased. The decrease of expansion is linked to the drop of supersaturation rather than to the amount of ettringite. Further, the finite element model showed a reduction of the expansion when the porosity increases at a fixed saturation index of ettringite. This model does not take into account the kinetics, therefore the faster drop of supersaturation is not computed. Two comparable systems, one with only fine pores and another with fine and coarse pores, having similar supersaturation of ettringite, both will start to expand similarly during the first hours of hydration, nevertheless, the system with coarse pores will have a faster drop of supersaturation causing it to expand less at later ages. This is due to the preferential growth of crystals in larger pores at equilibrium conditions. Furthermore, the formation of ettringite in small pores is controlled by the diffusion of ions in the solution and depends on the connectivity of the porosity.

The **effect of the temperature** between 20 to 38°C and of alkalis was also investigated. The solubility of ettringite and the hydration kinetics are affected by the temperature. A preliminary study showed that the effect of temperature on the kinetics seems to be dominant compared to the increase of solubility (corresponding to a decrease in supersaturation, in crystallization pressure, and in the volume of ettringite generating pressure), resulting in higher expansion. This is probably due to the faster formation of a solid porous matrix providing confinement for ettringite growth. Consequently, the crystallization pressure builds up earlier and generates more expansion. The effect of alkalis (up to 1M NaOH) could not be established as no clear effect on the expansion was observed. Alkalis are known to affect the kinetics but do not affect the solubility of ettringite. Faster kinetics should lead to higher expansion as observed with higher temperatures. It was not possible during this thesis to make further investigations on these effects.

7.2 Perspectives

The **early hydration study** of calcium aluminate with calcium sulfate indicated that calcium sulfate affects the reaction of CA, however further investigations on synthesized CA with calcium sulfate could give more information on the mechanisms controlling the hydration. Usually, dry mix mortars are blended with additives such as accelerators, retarders, superplasticizers and defoamers. These components modify the early hydration and they can even affect the degree of reaction of SCM by increasing or reducing their dissolution. An extended study on these additives on the hydration and on the expansion would be interesting.

The **long term hydration study** showed that SCM do not react much in these systems and that their reaction decreases with calcium sulfate. Moreover, SCM increase the total porosity of these cementitious systems and this may have detrimental effects on the durability due to an easier ingress of aggressive agents from the environment, but keeping the minimum substitution level should not affect much the porosity and the durability. It was found that the maximum amount of limestone and slag that can react is about 5% and 15% of the binder, respectively. Consequently, high levels of substitutions are not useful but low to moderate levels could be interesting.

The most important aspect to retain from the **study on the expansion** is that the driving force for expansion to occur is the supersaturation of the crystal, in this case ettringite, which determines the crystallization pressure and also the minimum pore radius where the crystals can grow. The confinement required for high pressures generation is found when the supersaturation is high enough to form crystals in pores below about 20 nm. The finite element code used to calculate the expansion could be extended by introducing the kinetics. A first step would be to input in the model the evolution of the pore size distribution and of the saturation index of ettringite over time. Further investigations on the effect of the temperature and the alkalis are needed as their impact on the dimensional stability is not clear yet. Furthermore, expansion was measured always under water, but in applied conditions the material is in contact with the atmosphere at variable relative humidity. For example a relative humidity of 90% empties the pores above 10 nm, probably affecting the expansion. The study of the mechanism of expansion could be extended to ternary systems composed of CAC-C₅-PC to understand the influence of PC and its hydrates.

A Appendix

A.1 Properties of the main hydrates

The main hydrates formed in the studied systems are presented in table A.1 and a detailed description of their structure and properties is presented in the next sections.

Table A.1: Main hydrates chemical formula, density [79] and phase structure [13].

Phase name	Formula	Composition [wt.%]		Density [g/cm ³]	Phase structure
Sulfate phases		C\bar{s}	H₂O		
Ettringite	C ₃ A.3C \bar{s} .H ₃₂	32.5	45.9	1.78	AFt, trigonal or hexagonal
Monosulfoaluminate	C ₃ A.C \bar{s} .H ₁₂	21.9	34.7	2.01	AFm, hexagonal
Gypsum	C \bar{s} H ₂	79.1	20.9	2.31	monoclinic
Hemihydrate	C \bar{s} H _{0.5}	93.8	6.2	2.73	monoclinic
Carbonate phases		C\bar{c}	H₂O		
Hemicarboaluminate	C ₃ A.C \bar{c} _{0.5} .H ₁₂	8.9	36.7	1.98	AFm, hexagonal
Monocarboaluminate	C ₃ A.C \bar{c} .H ₁₁	17.6	34.9	2.17	AFm, trigonal
Silicate phases		SiO₂	H₂O		
Strätlingite	C ₂ ASH ₈	14.4	34.5	1.94	AFm, hexagonal
Other phases		-	Water		
Gibbsite	AH ₃	-	34.6	2.42	monoclinic
Hydrogarnet	C ₃ AH ₆	-	28.6	2.53	cubic

A.1.1 AFt phases: Ettringite

Ettringite is part of a family of hydrated calcium aluminate phases called AFt (Al₂O₃-Fe₂O₃-tri) characterized by the general formula $[Ca_3(Al, Fe)(OH)_6 \cdot 12H_2O]_2 \cdot X_3 \cdot yH_2O$ where X can be replaced by a doubly charged anion such as SO₄²⁻ or CO₃²⁻. The term "tri" is related to the triple X anion. Ettringite contains aluminium and sulfate ions; its molecular formula is

Appendix A. Appendix

$[Ca_3(Al)(OH)_6 \cdot 12H_2O]_2 \cdot (SO_4)_3 \cdot 2H_2O$ and using the cement shorthand notation it becomes $C_3A.3C\bar{s}.H_{32}$. It has an hexagonal crystal structure as shown in figure A.2 and is composed of four positively charged columns ($[Ca_3Al(OH)_6 \cdot 12H_2O]^{3+}$) parallel to the c-axis. The aluminium atoms are octahedrally coordinated to hydroxyl groups and are intercalated between planes with three calcium atoms, each one being coordinated to four hydroxyl groups of aluminium and to four water molecules as shown in figure A.2b. The positive charges of the columns are balanced by negative charged sulfate ions located in the channels between the columns (figure A.2a). Each channel contains four sites, three occupied by sulfate and one by two water molecules [162, 163, 13, 164]. Water molecules transfer the charge from the calcium aluminate to the negative sulfate ions giving cohesion to the crystal [165]. To summarize, there are 24 water molecules in the column coordinated to the Ca^{2+} ions and two water molecules in the channel (also called zeolitic water). The other H atoms are in the six hydroxyl groups surrounding aluminium. The morphology of ettringite crystals is highly affected by the pore solution composition [166] and is characterized by hexagonal needles as in figure A.3. It crystallizes as long needle-like crystals under low supersaturation conditions and as short needles or prisms with hexagonal structure [167, 27].

Ettringite is stable in the $CaO-Al_2O_3-SO_3-H_2O$ at temperatures below $114^\circ C$ and at $25^\circ C$ it is stable in alkaline solutions with pH comprised between 10.43 to 12.52 [16]. Its solubility increases with temperature as shown in figure A.1a. The effect of the pH on ettringite solubility is not clear in the literature. Some authors showed that its solubility increases with pH [168] whereas other authors indicate that pH has no effect as in figure A.1b. Thermodynamic simulations with GEMS show that the solubility decreases until pH of 12.7 and then increases (see section 6.6.5).

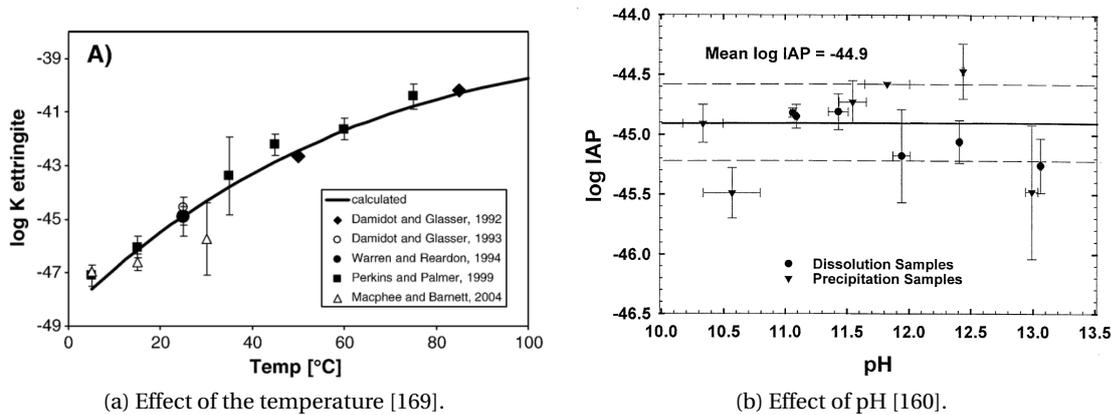


Figure A.1: Influence of the temperature and of the pH on ettringite solubility.

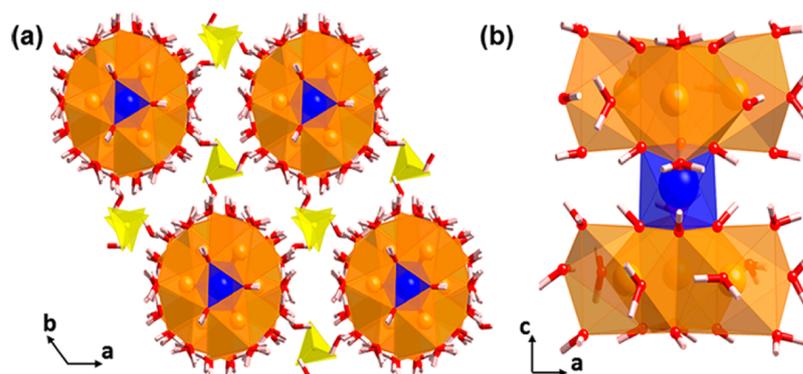
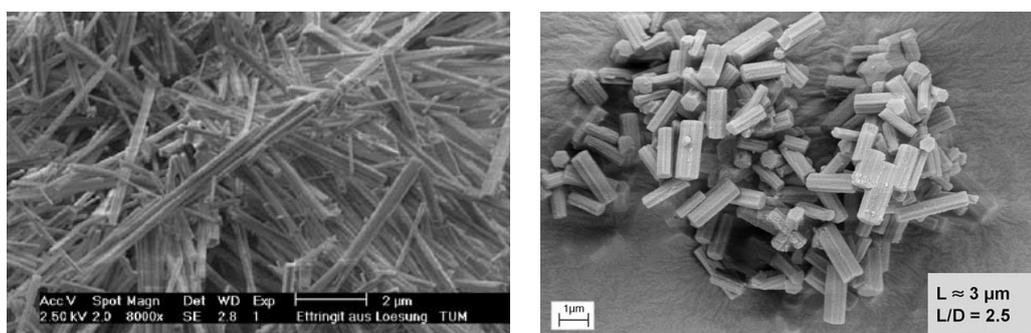


Figure A.2: Crystal structure of ettringite viewed along the c axis direction (a). Aluminate ions ($\text{Al}(\text{OH})_4^-$) are shown as blue octahedra, sulfate ions (SO_4^{2-}) are shown as yellow tetrahedra and calcium ions are inside orange polyhedra. Water and hydroxyl groups are denoted with red and with sticks for O and H atoms, respectively. Detail of a calcium aluminate column (b). [164]

Ettringite contains a lot of water molecules which are susceptible to drying and high temperatures, especially the zeolitic water. Ettringite loses up to 20 molecules of water in 50 days below 1% of relative humidity* at ambient temperature as shown in figure A.4a. The effect of the temperature for a fixed relative humidity is shown in figure A.4b where ettringite starts to lose water at 75°C and 9.8% RH. The amount of lost water decreases with the temperature and ettringite is stable for relative humidities between 100 down to 5% at ambient temperatures [170]. This suggests that the effect of vacuum drying on ettringite used to stop the hydration described in section 3.2.5 is negligible.



(a) Needle-like crystals [171]

(b) Hexagonal prismatic crystals [172]

Figure A.3: Example of synthesized ettringite crystals.

* Comparable to the conditions in a desiccator during hydration stopping.

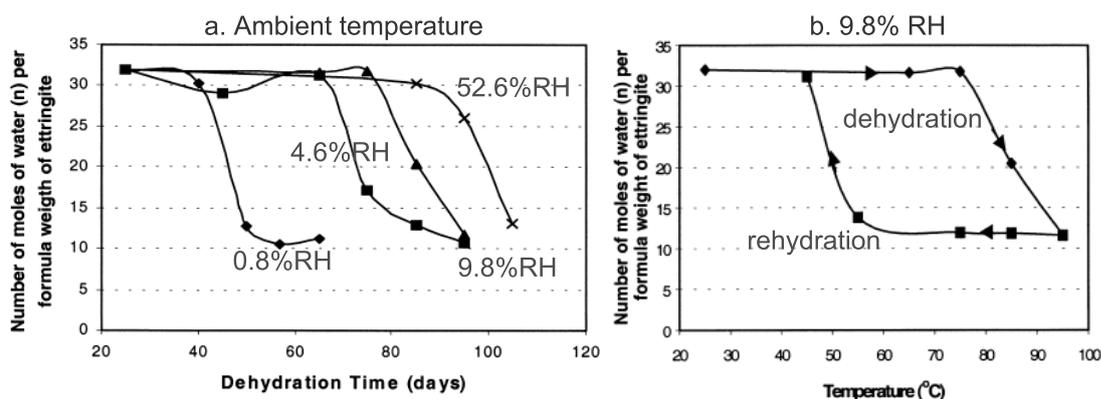


Figure A.4: Effect of relative humidity (a) and temperature (b) on the dehydration of ettringite [95].

A.1.2 AFm phases

AFm phase ($\text{Al}_2\text{O}_3\text{-Fe}_2\text{O}_3\text{-mono}$) refers to a family of hydrated calcium aluminate phases based on the hydrocalumite structure. The general formula is $[\text{Ca}_2(\text{Al}, \text{Fe})(\text{OH})_6] \cdot X \cdot y \text{H}_2\text{O}$ where X is an exchangeable charged anion (one formula unit of a singly charged anion: OH^- , Cl^- , $[\text{AlSi}(\text{OH})_8]^-$, or half a formula unit of a doubly charged anion: SO_4^{2-} , CO_3^{2-}). Using the cement shorthand notation the formula becomes $\text{C}_3(\text{A}, \text{F}) \cdot \text{CX}_2 \cdot y\text{H}$ and the term “mono” is related to the single formula unit of CX_2 . Other tripositive cations such as Fe^{3+} or Cr^{3+} may substitute aluminium. AFm crystals are formed by hexagonal platelets as shown in figure A.5 and the hexagonal or trigonal crystal structure of an ideal AFm phase is shown in figure A.6. The main layer is formed by $[\text{Ca}_2(\text{Al}, \text{Fe})(\text{OH})_6 \cdot 2\text{H}_2\text{O}]^+$ whereas the interlayers contain water molecules and the X anions which balance the charges. Different AFm may form in a cementitious system depending on the chemical composition and on the exposure conditions. These phases are difficult to study because of their low crystallinity and formation of solid solutions, which modify the position and intensities of the main reflections in the diffraction pattern. An example is given in figure A.7 for the solid solution between hydroxy-AFm (C_4AH_x , where the exchangeable ion is OH^-) and monosulfoaluminate ($\text{C}_3\text{A.C}\bar{5}. \text{H}_{12}$). The maximum replacement of hydroxyl ions is 50% at 25 °C and it decreases with temperature [13, 173].

The most stable AFm related to the studied systems are hemicarboaluminate, monocarboaluminate and strätlingite as shown in table A.8. Monosulfoaluminate is metastable with respect to ettringite and C_3AH_6 at temperatures around 25 °C and becomes stable above 40 °C as shown in the solubility diagram presented in figure 2.3. Monosulfoaluminate becomes increasingly stable at the expenses of ettringite when the temperature increases.

The relative humidity can have strong influences on the water content of AFm phases. The most susceptible phase to loose water is monosulfoaluminate as shown in figure A.9. Monosulfoaluminate has 12 bound water molecules between 30 to 99% relative humidity (RH), but can loose up to 3 water molecules during drying. This changes in water content can

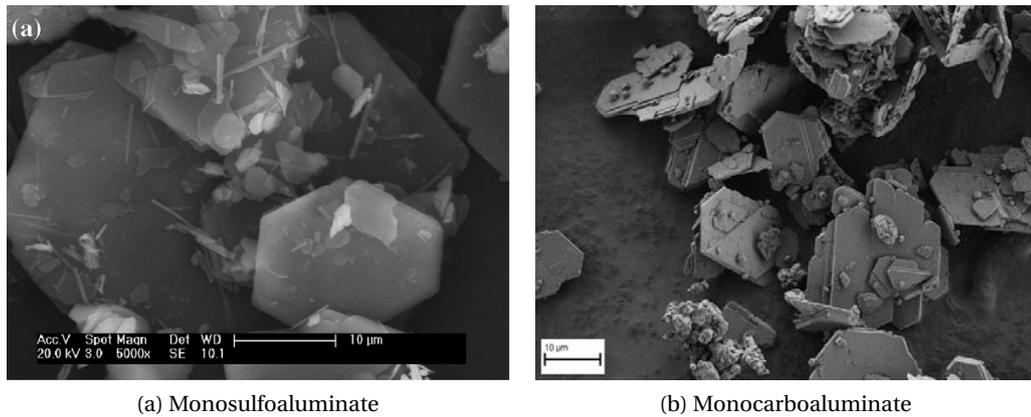


Figure A.5: Secondary electron images of AFm hexagonal platelets: monosulfoaluminate [173] and monocarboaluminate [174].

influence strongly the dimensional stability of the system as the phase changes in volume. Monocarboaluminate is stable for all the ranges of relative humidities [170]. According to the chemical composition of the system and of the activities of the different ions in solution, different AFm phases can coexist at the same time.

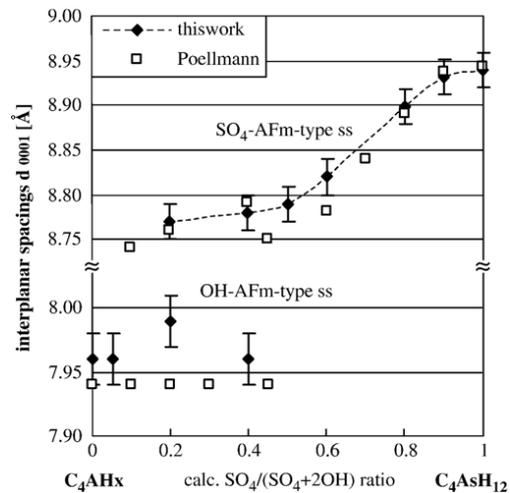


Figure A.7: Interplanar distances d_{0001} of monosulfoaluminate type solid solution and hydroxy-AFm type solid solution [173].

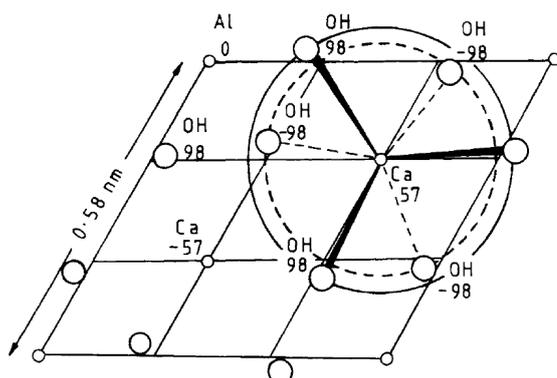


Figure A.6: Structure of a single principal layer of composition $[Ca_2Al(OH)_6]^+$ in an AFm phase, in *ab*-projection. Distances of calcium, aluminium and oxygen atoms above or below the central plane of the layer are in pm. Hydrogen atoms are not shown. Large circles illustrate the distortion of the CaO_6 octahedra, which allows the coordination of each calcium atom to rise to 7 through the addition of a water molecule (not shown) directly above or below it in this projection [13].

Distinctive anion	Formulae	Designation	Stability at 25 °C and 1 bar
OH^- , hydroxyl	$C_3A \cdot Ca(OH)_2 \cdot xH_2O$	Hydroxy-AFm	Unstable — decomposes to hydrogamet C_3AH_6 , and portlandite
OH^- ; CO_3^{2-}	$C_3A \cdot Ca[(OH)(CO_3)_{0.5}] \cdot xH_2O$	Hemicarboaluminate	Stable — but not many thermodynamic data available
CO_3^{2-}	$C_3A \cdot CaCO_3 \cdot xH_2O$	Monocarboaluminate	Stable
SO_4^{2-}	$C_3A \cdot CaSO_4 \cdot xH_2O$	Monosulfoaluminate	Calculated to be stable but only above 40 °C — at lower temperatures decomposition to AFt, C_3AH_6 and gibbsite possible
$[AlSi(OH)_8]^-$	C_2ASH_8	Gehlenite hydrate, strätlingite	Stable
Cl^-	$C_3A \cdot CaCl_2 \cdot xH_2O$	Friedel' salt	Stable, but not described in this paper. Mainly occurs as an alteration product of cement paste in saline environments

Figure A.8: Thermodynamic stabilities of selected AFm phases at 25 °C [173].

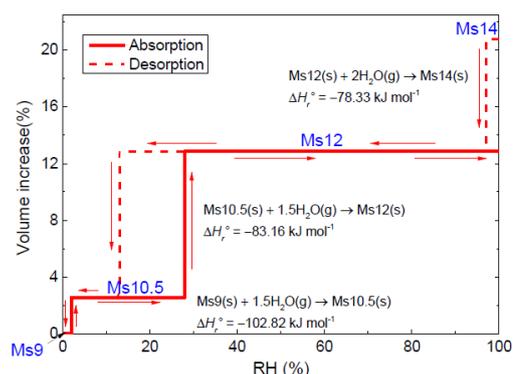


Figure A.9: Volume changes of monosulfoaluminate with respect to changes in RH at 25 °C [170].

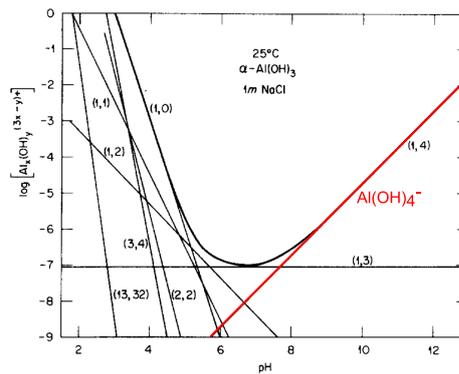


Figure A.10: Solubility of gibbsite as a function of pH. The straight lines represent the concentrations of individual species (x,y), indicating the stoichiometries of species of the type $Al_x(OH)_y^{3x-y}$. The red curve highlights the specie found in alkaline environments and the bold curve shows the total concentration of all aqueous aluminium species in equilibrium with gibbsite at 25 °C. Adapted from [175].

A.1.3 Hydrogarnet

Hydrogarnet (C_3AH_6) has a similar cubic structure to the one of garnets (C_3AS_3) where the calcium is in distorted cubic coordination, aluminium is in octahedral coordination and silicon in tetrahedral coordination. There are two oxygen atoms bonded to calcium, one to aluminium and one to silicon. In the hydrogarnet, the tetrahedral sites of Si are empty or partially empty and the charge is balanced by replacing each of the oxygen atoms bonded to it with hydroxyl ions. Aluminium (Al^{3+}) can be substituted by iron (Fe^{3+}) leading to solid solutions of C_3AH_6 and C_3FH_6 . As silicon can be also in the crystalline structure, solid solution of the two hydrated forms can coexist with C_3AS_3 and C_3AF_3 . Katoite is generally referred to as an hydrogarnet with a S/A molar ratio below 1.5 [13].

A.1.4 Aluminium hydroxide

Aluminium hydroxide (AH_3) exists with different degrees of crystallinity. The crystalline polymorphs are gibbsite, bayerite and nordstrandite and are characterized by variable $Al(OH)_3$ layer structures. The structure and exact composition of amorphous or microcrystalline aluminium hydroxide is not well known, nevertheless it is a gel-like phase and its formation is strongly related to the temperature. It has probably a crystal structure close to gibbsite but on a short range order making this phase X-Ray amorphous. Gibbsite forms only above ambient temperatures in cementitious systems. The amorphous gel has a specific surface area of $285 \text{ m}^2/\text{g}$ whereas the crystalline gibbsite has a surface area of $20 \text{ m}^2/\text{g}$ (BET) [176]. It is highly probable that the gel has a cohesion role in the cementitious matrix due to its higher specific surface. This can be compared to the main phase in Portland cement where the binding phase is amorphous C-S-H, which has a similar specific surface area. Figure A.10 shows the concentrations of aluminium hydroxyl species in equilibrium with gibbsite. Its

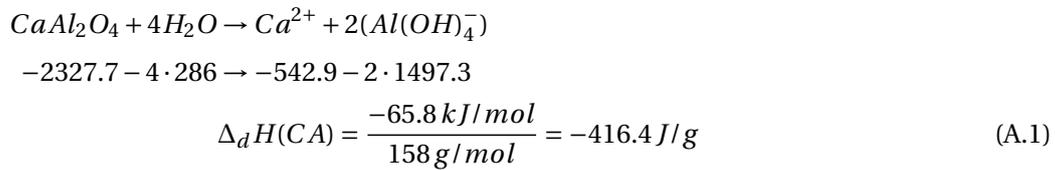
solubility is really low for pH between 5 to 8 and the dissolved specie in alkaline solutions is $Al(OH)_4^-$.

A.2 Calculation of enthalpies

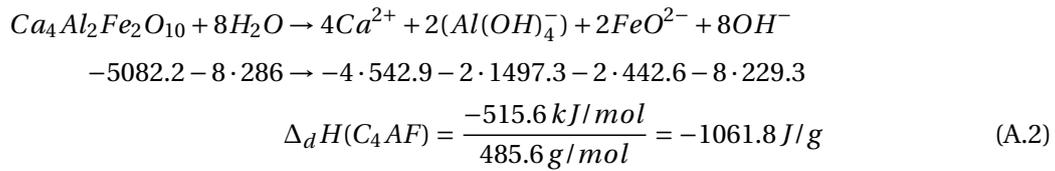
A.2.1 Enthalpies of dissolution

The enthalpies of dissolution of the main phases are described here. The enthalpy of formation of each phase and each specie at 20°C are found in the CEMDATA14 database [78].

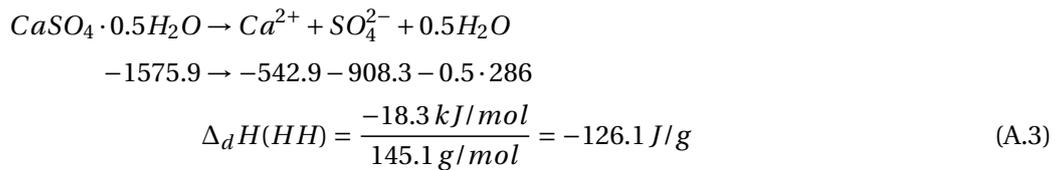
CA dissolution:



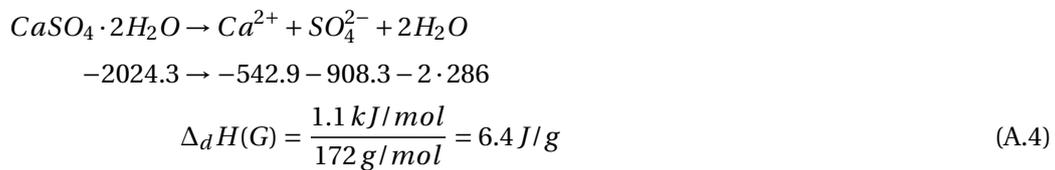
C₄AF dissolution:



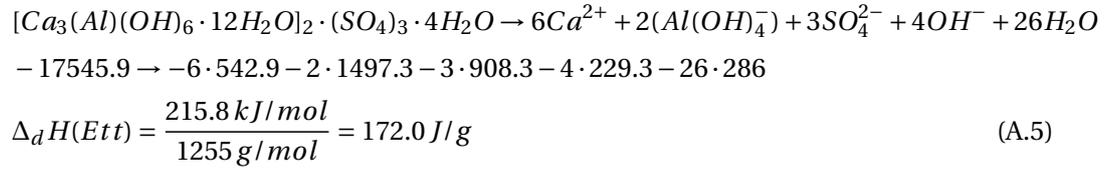
Hemihydrate dissolution:



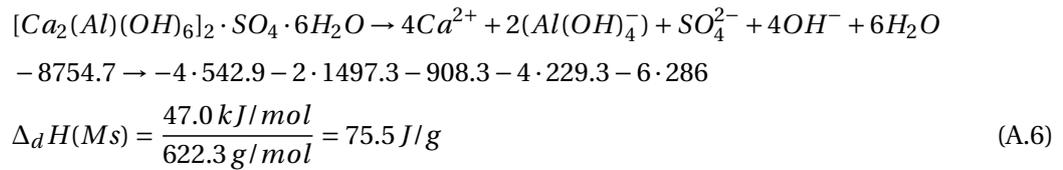
Gypsum dissolution:



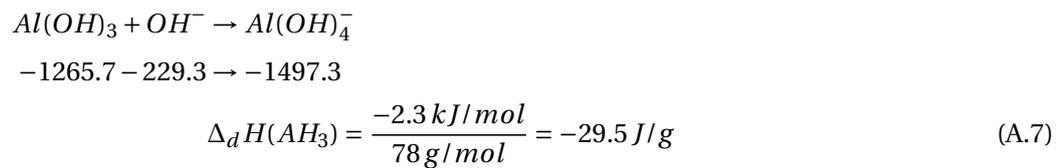
Ettringite dissolution:



Monosulfoaluminate dissolution:



AH₃ dissolution:



A.2.2 Calculation of the enthalpy of reaction of calcite

The case of monocarboaluminate



knowing the enthalpy of formation ($\Delta_f H^\circ$) of each phase and water in kJ/mol

$$3(-2327) + (-1207) + 17(-286) \rightarrow (-8250) + 2(-2530) \quad (A.9)$$

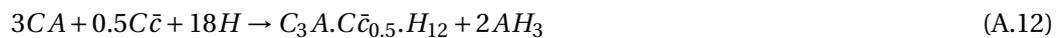
the enthalpy of reaction of calcite ($\Delta_r H(C\bar{c})$) is obtained (molar mass of calcite 100 g/mol)

$$\Delta_r H(C\bar{c}) = -260 \text{ kJ/mol} = -2600 \text{ J/g} \quad (A.10)$$

In chapter 5.3 the heat generated by the reaction of 0.8 g of calcite is given by

$$\text{Heat} = \frac{0.8 \text{ g} \cdot 2600 \text{ J/g}}{80 \text{ g of } CAC + C\bar{s}} = 26 \text{ J/g of } CAC + C\bar{s} \quad (A.11)$$

The case of hemicarboaluminate



Appendix A. Appendix

knowing the enthalpy of formation ($\Delta_f H^\circ$) of each phase in kJ/mol and water

$$3(-2327) + 0.5(-1207) + 18(-286) \rightarrow (-8270) + 2(-2530) \quad (\text{A.13})$$

the enthalpy of reaction of calcite ($\Delta_r H(C\bar{c})$) is obtained

$$\Delta_r H(C\bar{c}) = -597.5 \text{ kJ/mol} = -5975 \text{ J/g} \quad (\text{A.14})$$

The reaction of 0.8 g of calcite is given by

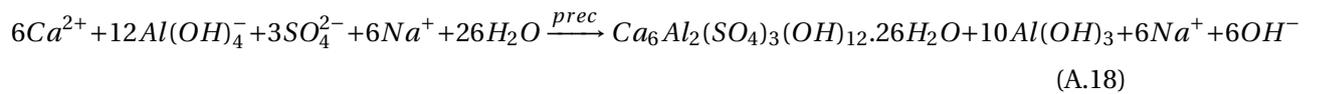
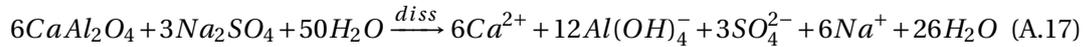
$$\text{Heat} = \frac{0.8 \text{ g} \cdot 5975 \text{ J/g}}{80 \text{ g of } CAC + C\bar{s}} = 59.75 \text{ J/g of } CAC + C\bar{s} \quad (\text{A.15})$$

A.3 How does Na_2SO_4 lead to alkaline solution?

Calcium aluminate cement and Na_2SO_4 in water react and lead to an alkaline solution according to the following reaction (just as an example, it works with different reactions and aluminates):



This can be demonstrated by showing the dissolution-precipitation reaction and using the conventional chemistry notation:



this clearly shows that OH^- are in solution to balance the charges with sodium ions. An alkaline solution promoting slag dissolution is obtained after this reaction.

A.4 Study on ternary systems based on PC-CAC-C \bar{s}

In the main part of the thesis are presented only the chapters on the study of CAC based systems but the "traditional" ternary products used as dry mix mortars based on PC-CAC-C \bar{s} have also been studied. The main part of this study was presented in a paper for the International Conference on Calcium Aluminates, Avignon, May 2014. This paper is presented in the next pages. (Note that here the term OPC , ordinary Portland cement, is used to describe plain Portland cement. This term is no longer applicable and in the thesis the correct term PC is used.)

HYDRATION AND MICROSTRUCTURE OF RAPID-STRENGTH BINDERS BASED ON OPC ACCELERATED BY EARLY ETTRINGITE FORMATION

J. BIZZOZERO and K. L. SCRIVENER

Laboratory of Construction Materials, Swiss Federal Institute of Technology (EPFL), Lausanne 1015, Switzerland
julien.bizzozero@epfl.ch

SUMMARY: The aim of this study is to compare the hydration kinetics and the microstructure development of binders based on ordinary Portland cement accelerated by early ettringite formation brought by mixed calcium aluminate cement and calcium sulfate (CAC+CS̄) or calcium sulfoaluminate cement and calcium sulfate (CSA+CS̄). The ratio between OPC and rapid cement addition has been adjusted to evaluate its impact on chemical and physical properties. Binders containing 70% and 5% of OPC have been compared, hydration being quicker for lower percentage of OPC, i.e. higher ettringite content. The phase assemblage has been followed over time by XRD-Rietveld, TGA and SEM-EDX analyses. Microstructure has been studied by SEM-BSE images. These systems are complex in terms of phase development; there are crystalline phases (ettringite, calcium monosulfoaluminate, hemicarboaluminate, monocarboaluminate and Portlandite) and amorphous phases (C-S-H and AH3). Due to their strong intermixing, complementary techniques are essential for the understanding of the microstructural development.

Keywords: AFm, AFt, blended cements, building chemistry, hydration.

INTRODUCTION

Rapid-strength binders based on ordinary Portland cement (OPC) accelerated by early ettringite formation are used for special applications where rapid setting, rapid hardening and rapid drying are required. These binders are mainly used in the building chemistry industry for rapid repair applications and for flooring installations with self-levelling compounds. Size variation control is crucial for the latter application, where a high surface is exposed to the environment causing a rapid drying of the binder. Shrinkage compensation is then important in order to minimize crack formation. Shrinkage compensating concrete is also used for applications where the permeability must be minimized, for example for underground constructions and bridge decks ^[1]. Rapid setting and strength development binders are capable of reaching more than 30 MPa in 3 hours of hydration. These properties are achieved by the acceleration of OPC

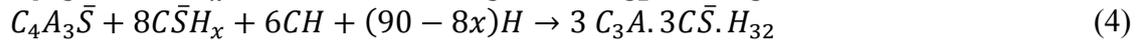
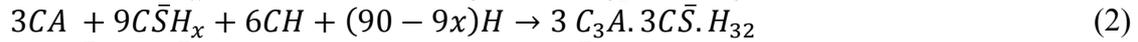
with the addition of type M or type K cements. Type M cements are composed of calcium aluminate cement (CAC, main phase is CA) with calcium sulfate ($C\bar{S}$) and Type K cements are composed of calcium sulfoaluminate cement (CSA, main phase is ye'elimite $C_4A_3\bar{S}$) and $C\bar{S}$. The early ettringite formation gives high early strength and the OPC hydration gives later age strength.

The hydration steps of ternary systems composed of OPC, CAC or CSA and $C\bar{S}$ are complex and a single component can have a big influence on the hydration and properties development. The main reactions occurring in each component are described below (adapted from ^[2,3]).

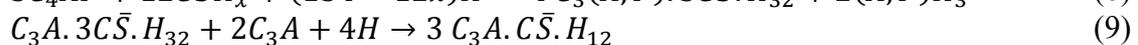
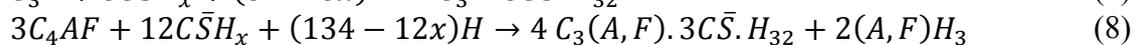
The binary systems composed of CAC- $C\bar{S}$ and CSA- $C\bar{S}$ lead to the same hydrates formation even if the main anhydrous phases are different. In both cases the main hydrates formed are ettringite and aluminium hydroxide (reactions (1) and (3)). In CSA systems the ye'elimite phase and calcium sulfate are rapidly consumed during the first hours of hydration to form ettringite and amorphous aluminium hydroxide, no gypsum is precipitated from the dissolution of anhydrite. Ettringite stops to form at around 28 days and if belite is present there is formation of strätlingite (C_2ASH_8) (similar to reaction (13)) ^[4]. It has been reported that the maximum amount of ettringite in ternary systems OPC-CSA- $C\bar{S}$ is attained at 1 day of hydration ^[3].

When lime or calcium hydroxide are present, the hydration of the aluminate phases with calcium sulfate leads to the formation of ettringite according to reactions (2) and (4). This is the case when these binary systems are blended with OPC. Mehta, Collepardi and Turriziani reported that the hydration rate of $C_4A_3\bar{S}$ and CA is reduced by the presence of pure CH. The effect is less intense when there is CH coming from the hydration of OPC ^[5,6].

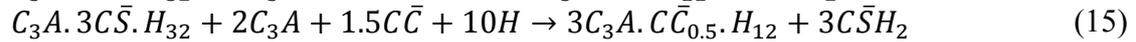
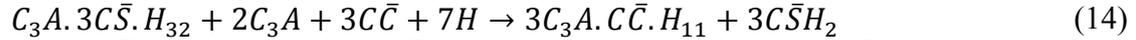
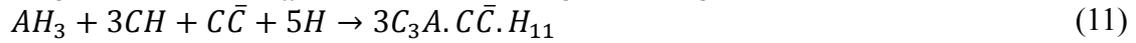
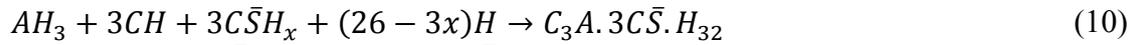
When calcium sulfate is depleted, the reaction between CA or $C_4A_3\bar{S}$ and ettringite forms monosulfoaluminate as described by a similar reaction (9) with C_3A .



The reactions of the main phases of plain OPC lead to the formation of C-S-H and CH (reactions (5) and (6)). Minor phases form ettringite from the dissolution of the aluminates and sulfates (reactions (7) and (8)). Reaction (9) describes the dissolution of ettringite when the calcium sulfates are depleted and there are still aluminates available for the formation of monosulfoaluminate. These reactions may be affected by the presence of other binders such as CAC, CSA and added $C\bar{S}$. Usually in ternary systems the OPC can be considered as a filler for the first 7 days of hydration, except free CaO and alkalis, but it influences the late properties of the binder ^[3].



Other coupled reactions between hydrates and anhydrous phases coming from the different cements are also relevant. AH_3 and CH cannot coexist thermodynamically and therefore they dissolve and form different products depending on the phases present in the system. Ettringite can be formed if there is calcium sulfate (reaction (10)), monocarboaluminate if there is calcium carbonate ($CC\bar{}$) (reaction (11)) and hydrogarnet (C_3AH_6) if no other phases are participating in the reaction (12). Alite (C_3S) from OPC can react with AH_3 arising from the hydration of the $CAC-C\bar{S}$ or $CSA-C\bar{S}$ system to form strätlingite (C_2ASH_8) and CH (reaction (13)). When calcium carbonate is present in the system with calcium aluminate phases (CA or C_3A) there can be consumption of ettringite and precipitation of monocarboaluminate (reaction (14)) or hemicarboaluminate (reaction (15)). Atmospheric carbonation can also be a source of calcium carbonate by the reaction of C or CH with gaseous CO_2 .



The involved reactions in the real systems are quite complex and kinetics of dissolution of the anhydrous phases will determine which phase will be formed at a given age. Experimental studies are necessary to understand the hydration path of the different systems.

The objectives of this study are:

- Follow the hydration and quantify the hydration of each component over time.
- Study the microstructure.

MATERIALS AND METHODS

The composition of the different studied binders is given in Table 1.

Table 1. Composition of different systems.

Name	OPC [wt%]	CAC-C \bar{S} [wt%]	CSA [wt%]	w/s [-]	Admixtures [wt% of solid]
CAC-C \bar{S} - 70%OPC	70	30	-	0.35	0.35
CSA1- 70%OPC	70	-	30	0.40	0.10
CSA2	-	-	100	0.40	0.10

The composition (by XRD Rietveld analysis) of the different materials is given in Table 2. The CSA 2 is a ready mixed product, the presence of 3.3% C_3S indicates that there may be a component of OPC around 5% in the mixture.

Table 2. Main phase composition of different binders (wt%, accuracy: $\pm 2\%$).

	OPC	CAC-C \bar{S}	CSA1	CSA2
C ₃ S	49	-	-	3
β -C ₂ S	16	3	6	40
CA	-	45	-	-
C ₃ A	6	1	3	2
C ₄ AF	9	-	3	3
C ₄ A ₃ \bar{S}	-	-	37	27
C \bar{S}	-	30	22	11
C \bar{S} H _{0.5}	5	-	3	3
C \bar{S} H ₂	1	-	-	-
C \bar{C}	7	-	2	2

All the experiments were carried out at 20°C and the analyses were done on cement pastes. All the mixes were prepared under the same conditions. Water was added to the dry powder and mixed for 2 minutes using a paddle mixer (1600rpm).

The hydration kinetics were followed by isothermal calorimetry with a TAM Air (3114/3236) from Thermometric. The mixing was done ex situ.

For XRD, TGA and SEM analyses, the samples were cast in polystyrene cylinders of 35 mm diameter and 50 mm height. After 24 hours the samples were demoulded and placed in cylindrical recipients of 37 mm of diameter containing around 8 g of demineralized water for 95 g of sample mass to minimize leaching. For each age of curing (1, 7, 14, 28, 90 and 180 days) two slices were cut from the cylinders and then introduced into isopropanol to stop hydration.

XRD analyses were done with a PANalytical X'Pert Pro MPD diffractometer in a (CuK α , $\lambda=1.54 \text{ \AA}$) working in Bragg-Brentano geometry with a 2 θ -range of 5°-65°. The samples were finely ground and backloaded into the sample holders to minimize preferred orientation. The Rietveld refinements were done using the X'Pert High Score Plus software from PANalytical using an external rutile standard (Kronos 2300 Titanium dioxide) to have an absolute quantification of the crystalline phases.

TGA was carried out using a Mettler Toledo TGA/SDTA851e. Around 50 mg of ground cement paste were placed in alumina crucibles covered by aluminium lids to reduce the carbonation before the analysis. The temperature ranged from 30 to 950 °C with a heating rate of 10 °C/min under N₂ atmosphere to prevent carbonation.

SEM was done using a FEI Quanta 200 with an electric beam generated by a tungsten filament operating at an accelerating voltage of 15 kV. The chemical analyses were measured by energy dispersive X-ray spectroscopy (EDS) using a Bruker AXS Microanalysis XFlash 4030 Silicon drift detector. The cement paste samples were impregnated with epoxy resin under vacuum conditions in order to fill the open porosity with the resin and after were polished and coated with carbon.

RESULTS AND DISCUSSION

The hydration kinetics differ between CAC based systems and CSA based systems (Fig. 1, left), CSA having a faster hydration during the first hours. In CSA systems the first peak marks the initial dissolution of anhydrous phases followed by the induction period

and the second peak at around 1.5 hours corresponds to the main reaction of $C_4A_3\bar{S}$ and $C\bar{S}$ that lead to the formation of ettringite and amorphous aluminium hydroxide. The CAC based system shows 3 peaks during the first 4 hours of hydration. The first is similar to that of CSA systems, the nature of the second one is still unknown and the third peak at around 2.5 hours corresponds to the reaction of CA and $C\bar{S}$ followed by the precipitation of ettringite and amorphous aluminium hydroxide. Fig. 1 (right) shows the cumulative heat of hydration for the first 3 days of hydration. The CAC based system has reactions happening after 30 and 60 hours of hydration. These increases of cumulative heat are due mainly to the dissolution of alite (OPC phase) as confirmed by XRD. The CSA1-70%OPC shows a late dissolution at around 55 hours related to the hydration of alite. CSA2 shows only an initial big dissolution during the first 2 hours followed by a plateau. In this system the C_3S does not seem to react during the first 3 days.

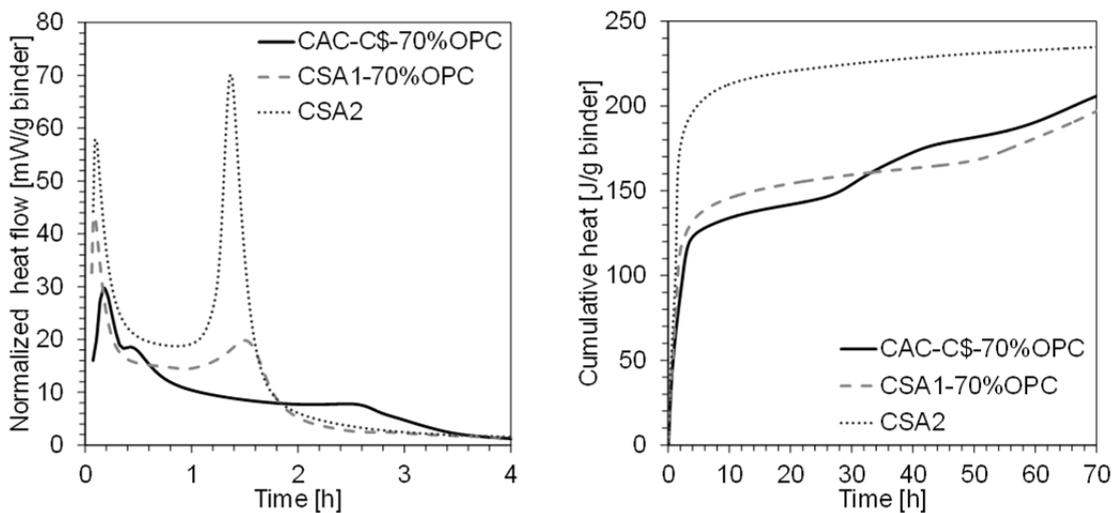


Fig. 1: Heat flow (left) and cumulative heat (right) as a function of time.

The Fig. 2, Fig. 3 and Fig. 4 show XRD Rietveld analyses of the different systems for anhydrous and hydrated phases. On the time axis, 0.1 day corresponds to the anhydrous composition. XRD on CAC based system show that CA and $C\bar{S}$ are depleted during the first day of hydration and that C_3S is mainly consumed, but not depleted, between 1 and 14 days of hydration (Fig. 2). C_2S starts to dissolve after 28 days. Calcium carbonate ($C\bar{C}$) dissolution is difficult to evaluate due to its low content below the error of the measurement, but it is participating to the formation of hemicarboaluminate and monocarboaluminate. The ettringite forms during the first day of hydration and after is consumed with time to form monosulfoaluminate (Ms), hemicarboaluminate (Hc) and monocarboaluminate (Mc). According to the stoichiometric reactions (1) and (7) and taking the composition of the anhydrous blend, the maximum amount of ettringite should be 37.3%. The Rietveld analyses give 30.9% of ettringite at 1 day, which is lower than the maximum expected amount. This can be due to the fact that ettringite is already partly consumed at 1 day or that the ettringite is affected by the isopropanol and vacuum during hydration stopping^[7,8]. Another source of error is that from the measure: $\pm 2\%$. There is also formation of a small amount ($<2\%$) of Portlandite and hydrogarnet (C_3AH_6). C-S-H and amorphous aluminium hydroxide (AH_3) are XRD amorphous,

therefore they are not quantified. These two and the other unrefined phases are measured as a single “amorphous” phase.

The XRD Rietveld analyses of the CSA1-70%OPC system show a similar phase evolution to the CAC-C \bar{S} -70%OPC system (Fig. 3), particularly concerning C₃S and ettringite, therefore the same considerations are done on these phases. C₄A₃ \bar{S} and C \bar{S} are depleted between 1 and 7 days of hydration. C₂S starts to react after 14 days. The maximum amount of ettringite calculated according to reactions (3) and (7) is 26.7%. The Rietveld analyses give 29.3%, this value is in contrast with what is observed in the previous system where the ettringite is underestimated by XRD analysis due probably to sample preparation. The Portlandite content is higher in this system than in the CAC based system.

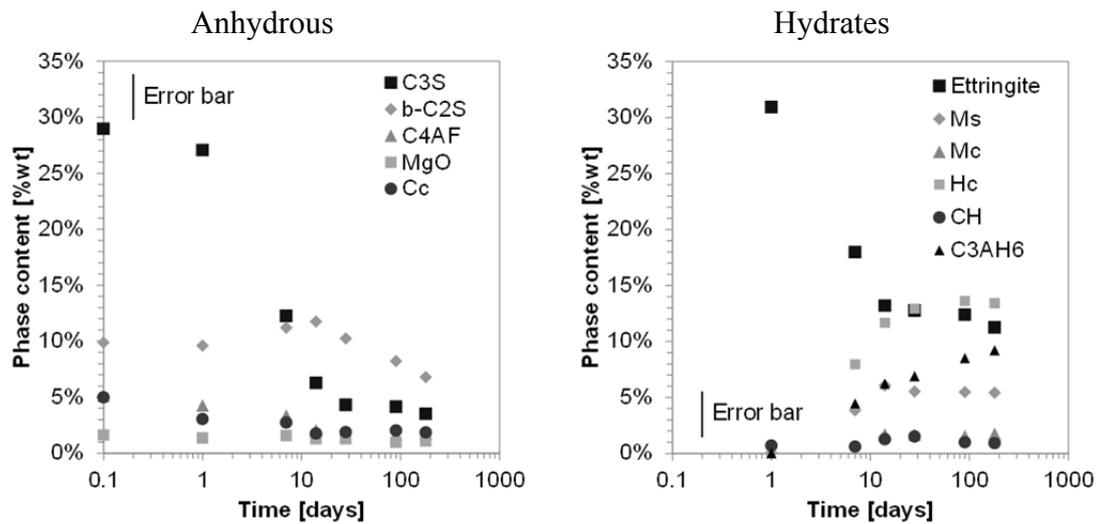


Fig. 2: XRD Rietveld analyses of CAC-C \bar{S} -70%OPC.

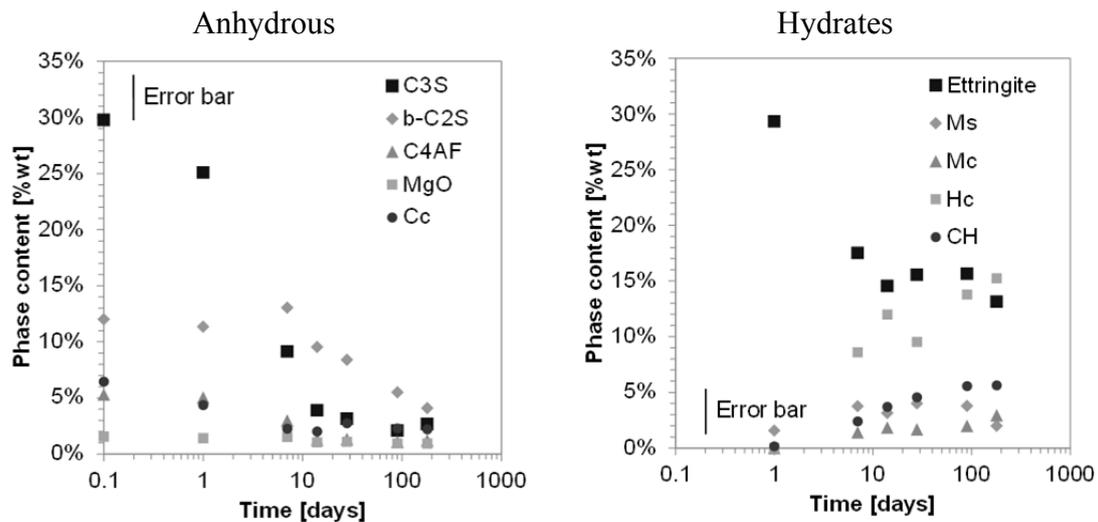


Fig. 3: XRD Rietveld analyses of CSA1-70%OPC.

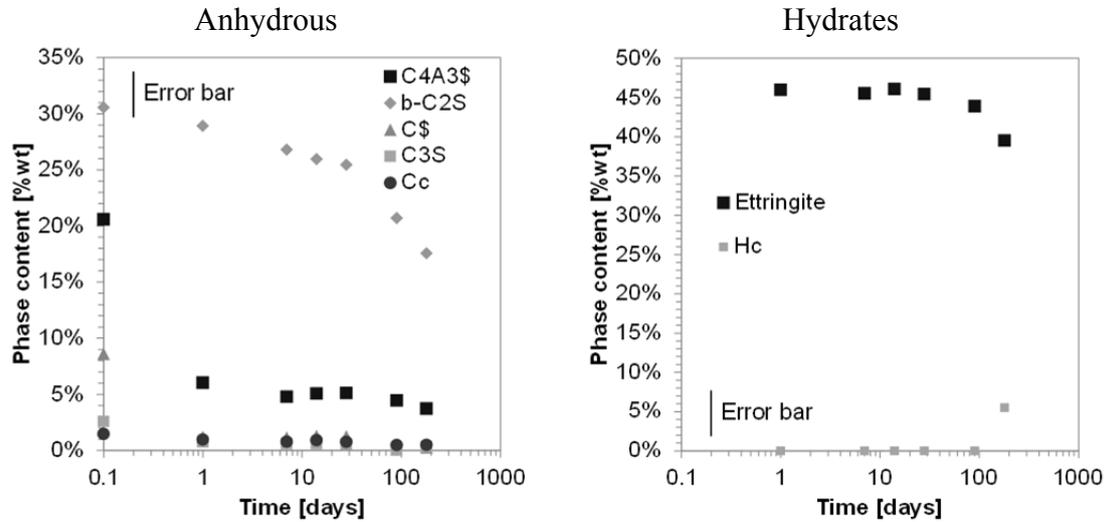


Fig. 4: XRD Rietveld analyses of CSA2.

The CSA2 system (Fig. 4) is different from the previous two systems, mainly because it is CSA dominated. Anhydrite is depleted and ye'elite is mainly consumed before the first day of hydration. C_2S is slowly consumed until 28 days of hydration after which its reaction seems to increase. Ettringite forms rapidly during the first day and is stable until 90 days, when it starts to dissolve and hemicarboaluminate forms. No Portlandite is detected in this system and the aluminium hydroxide is not observed by XRD. The maximum amount of ettringite calculated according to reactions (3) and (7) is 47.6%; compared to 46.0% of ettringite measured by the Rietveld analysis at 1 day.

Fig. 5 shows the degree of hydration (DH) of the different systems. The degree of hydration is calculated according to equation (16):

$$DH (\%) = 1 - \frac{W_{anhydrous}(t)}{W_{anhydrous}(t=0)(1 - W_{H_2O,TGA})} \quad (16)$$

$W_{anhydrous}(t)$ is the weight fraction of the phases of the given cement (OPC, CAC or CSA) at time t , $W_{H_2O,TGA}$ is the water mass loss measured by TGA from 30 to 600°C. For the systems with 70%OPC there are three degrees of hydration:

1. DH CAC- $C\bar{S}$ or CSA- $C\bar{S}$ taking as phases $W_{anhydrous}(t)$ the main phases of the CAC or CSA with $C\bar{S}$.
2. DH OPC calculated from the consumption of C_3S and other minor phases except C_2S because it is present in both CAC- $C\bar{S}$ and CSA binder.
3. DH TOT taking all the anhydrous phases into account.

The degrees of hydration show that CAC- $C\bar{S}$ or CSA are reacting mainly during the first 7 days of hydration and that OPC is reacting mainly from 1 to 28 days. The contribution of C_2S is observed in the DH TOT after 28 days of hydration, mostly in the CSA2 system.

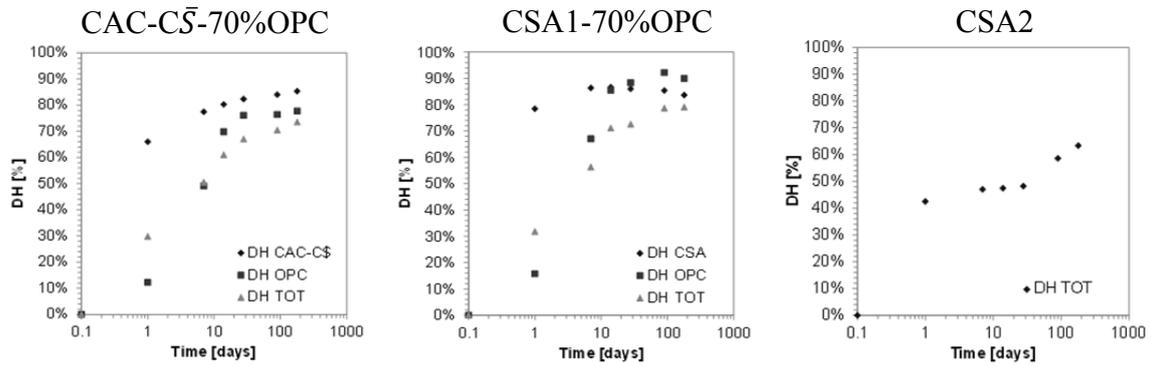


Fig. 5: Degree of hydration calculated from XRD Rietveld analyses.

Thermogravimetric analyses are complementary to XRD analyses as they show the presence of some X-Ray amorphous phases like AH_3 and C-S-H (difficult to identify). Moreover it is easier to notice the precipitation of small amounts of CH.

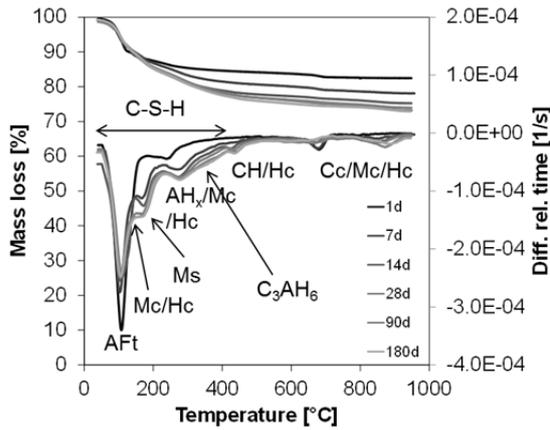


Fig. 6: TGA of CAC-CS-70%OPC.

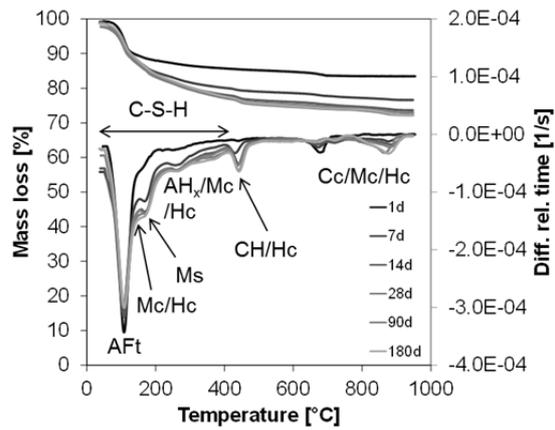


Fig. 7: TGA of CSA1-70%OPC.

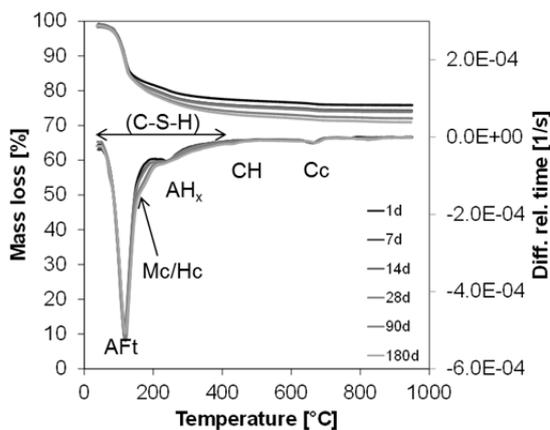


Fig. 8: TGA of CSA2.

Fig. 6 and Fig. 7 show that ettringite is consumed over time and Ms, Hc and Mc are formed. Calcium carbonate is partially consumed for the formation of Hc and Mc.

As observed before by XRD analyses, the CSA2 system differs from the systems with 70% of OPC. Fig. 8 shows that the main fraction of ettringite is formed during the first day of hydration and after it remains constant, this is in contrast with what has been observed by XRD Rietveld analyses where ettringite is probably dissolved after 90 days and hemicarboaluminate precipitates. Nevertheless the formation of Hc is observed also by TGA. AH_3 is identified in this system but C-S-H is difficult to observe because its temperature range of water loss is overlapping with other major phases.

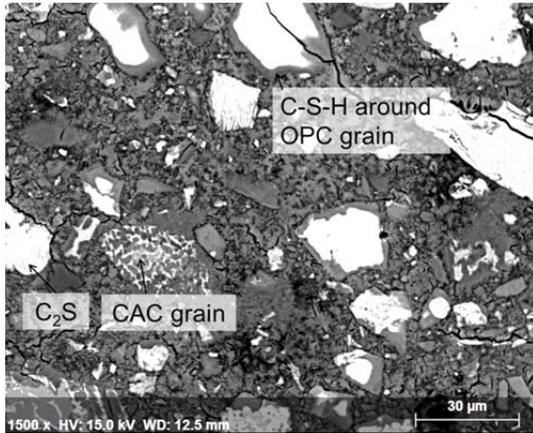


Fig. 9: CAC-CS-70%OPC at 28 days.

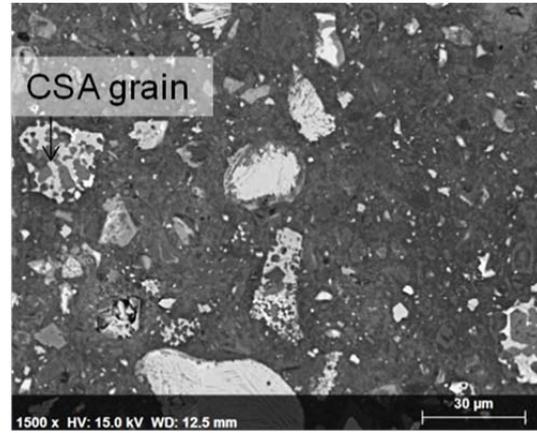


Fig. 10: CSA1-70%OPC at 28 days.

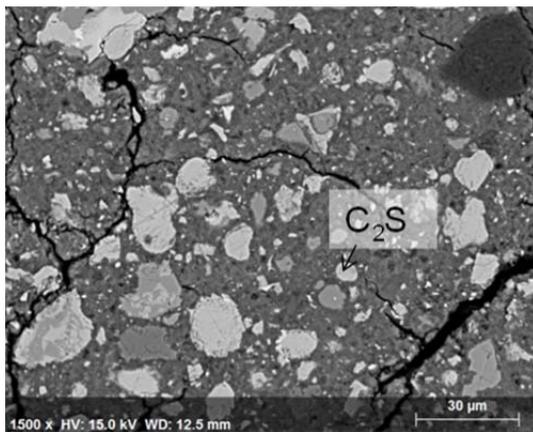


Fig. 11: CSA2 at 28 days.

Microstructural investigations at 28 days of hydration show the differential dissolution between OPC phases and CAC or CSA phases. The complete dissolution of the main phase CA in the CAC grain is shown in Fig. 9 and the ye'elinite phase dissolution in the CSA grain is observed in Fig. 10. Some hydrates are formed inside the CAC or CSA grain. Only the phases reacting slower like C_2AS , ferrites and perovskites are remaining.

Fig. 9 shows well the C-S-H forming around a C_3S grain and an unaffected C_2S grain. The analyses of microstructures at different ages for both systems with 70%OPC show a densification of the hydrated matrix over time.

Fig. 11 depicts the CSA2 system at 28 days showing that the C_2S has not reacted. Partly dissolved grains similar to what has been observed in the previous figures are not detected in this system. There is no noticeable evolution in the densification of the hydrated matrix of this system. There are a lot of cracks present in the micrographs; this is probably due to the high vacuum causing shrinkage and cracking of ettringite. For all the systems it is difficult to distinguish the hydrates because of the high intermixing. With localized chemical analyses (EDS) it is possible to characterize the main hydrated phases of the binders.

EDS point analyses on the different systems are shown in Fig. 12. The best element ratios are represented on the axis for each system in order to highlight the presence of the main hydrates. For the systems with 70%OPC, the presence of C-S-H

intermixed with other main hydrates as ettringite (AFt), monosulfoaluminate (Ms), hemicarboaluminate (Hc) and monocarboaluminate (Mc) is observed. The C-S-H composition in Portland cement pastes has usually a Ca/Si ratio between 1.2 and 2.1 [9]. From EDS analyses on ternary binders it seems that this ratio is between 1.7 and 2, the water content in this phase is not known and is not in the scope of this study. In the CSA2 system another element ratio is used to show the binary composition of the hydrates, namely ettringite and amorphous aluminium hydroxide. There is a strong intermixing between these two phases.

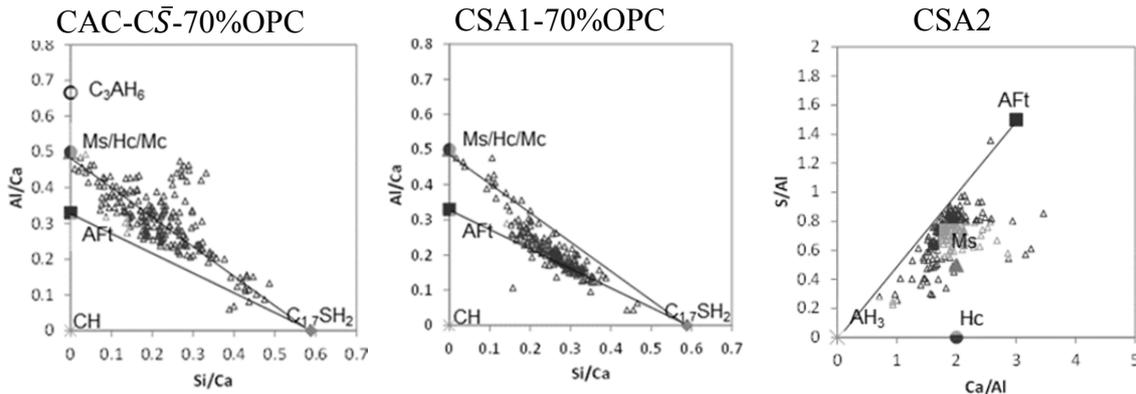


Fig. 12: SEM-EDS point analyses at 28 days.

CONCLUSIONS

The hydration of the two systems containing 70% OPC is as follows: quick formation of ettringite during the first hours leading to rapid hardening and slower hydration of OPC leading to long term strength. At 28 days the hydrates assemblage, presented in Table 3, is close to OPC with C-S-H resulting from C_3S hydration as the main hydrate. For the CSA2 system, there is massive formation of ettringite and amorphous aluminium hydroxide while no C-S-H seems to be formed.

Table 3. Summary of the main phases (-: absent, +/-: traces, +: low amount, ++: high amount).

At 28 days	AFt	Ms	Mc	Hc	CH	C_3AH_6	AH_3	C-S-H
CAC-C $\bar{5}$ -70%OPC	12.8	5.2	1.7	12.9	1.5	6.9	++	++
CSA1-70%OPC	15.6	4.0	1.7	9.5	4.6	+/-	+/-	++
CSA2	45.4	-	-	+/-	-	-	++	+/-

ACKNOWLEDGEMENTS

The authors appreciate the financial support from Kerneos France.

REFERENCES

- [1] Nocun-Wczelik W, Konik Z, Stok A. *Blended systems with calcium aluminate and calcium sulphate expansive additives*. Construction and Building Materials, 25 (2), 2011, pp 939-943.
- [2] Chen I. A, Hargis C. W and Juenger M. C. G. *Understanding expansion in calcium sulfoaluminate-belite cements*. Cement and Concrete Research, 42 (1), 2012, pp 51-60.
- [3] Pelletier L, Winnefeld F and Lothenbach B. *The ternary system Portland cement-calcium sulphoaluminate clinker-anhydrite: Hydration mechanism and mortar properties*. Cement and Concrete Composites, 32 (7), 2010, pp 497-507.
- [4] Winnefeld F, Lothenbach B. *Hydration of calcium sulfoaluminate cements - Experimental findings and thermodynamic modelling*. Cement and Concrete Research, 40 (8), 2010, pp 1239-1247.
- [5] Mehta P. K. *Effect of Lime on Hydration of Pastes Containing Gypsum and Calcium Aluminates or Calcium Sulfoaluminate*. Journal of the American Ceramic Society, 56 (6), 1973, pp 315-319.
- [6] Collepardi M, Turriziani R. *The paste hydration of $4CaO \cdot 3Al_2O_3 \cdot SO_3$ in presence of calcium sulphate, tricalcium silicate and dicalcium silicate*. Cement and Concrete Research, 2 (2), 1972, pp 213-223.
- [7] Zhou Q, Glasser F. P. *Thermal stability and decomposition mechanisms of ettringite at < 120 degrees C*. Cement and Concrete Research, 31 (9), 2001, pp 1333-1339.
- [8] Zhang L, Scherer G. W. *Comparison of methods for arresting hydration of cement*. Cement and Concrete Research, 41(10), 2011, pp 1024-1036.
- [9] Richardson I. G. *The nature of C-S-H in hardened cements*. Cement and Concrete Research, 29(8), 1999, pp 1131-1147.

A.5 Code used for the measurement of the degree of reaction of slag by SEM-IA

```

1  %written by Pawel Durdzinski and Julien Bizzozero 2014
2
3  %Please cite us if you use this code for results you will publish:
4  %"Code written by Pawel Durdzinski and Julien Bizzozero, LMC-EPFL,
5  %Switzerland, 2014" or cite this thesis.
6
7  %Variables to define:
8  hamNr = 22;% even number used for the Hamming or Hanning filter (22 is a good
   value)
9  Mg_gray=100;%grey level to select Mg grains (100 is a good value for 255 grey
   levels)
10
11 %Choose auto or manual mode for BSE grey levels of slag phase
12 auto_x=menu('Choose auto or manual mode for BSE grey levels selection of slag
   peak.', 'Manual', 'Automatic');
13 auto=auto_x-1;
14
15 fnames = dir('*Mg*.png');
16 bnames = dir('*BSE*.png');
17
18 areaFraction = zeros(length(fnames),1);
19
20 %plots the histograms of BSE images to select manually the correnct grey levels.
21 if auto==0
22
23     for verse =1:length(fnames)
24
25         bse = imread(bnames(verse).name);
26         bse = double(bse);
27         bse=bse(:,:,1);
28
29         clear smooth1
30         clear smooth2
31
32         %cutting of the bse so the size matches
33         bses = bse((hamNr/2)+1:end-(hamNr/2), (hamNr/2)+1:end-(hamNr/2));
34
35         %taking the adequate grey level areas from bse image
36         histogram=hist(double(bses(:)),255);
37
38         %filling the 0 values of the histogram
39         for j=1:length(histogram)
40             if (histogram(j)~=0)
41                 histogram_mod(j)=histogram(j);
42             else
43                 histogram_mod(j)=(histogram(j-1)+histogram(j+1))/2;
44             end
45         end
46
47         % collect data of all histograms to plot in 3D
48         %area(histogram_mod)
49         histogram_plot(verse,:)=histogram_mod;
50     end
51
52     figure (2); mesh(histogram_plot);
53     uiwait(2);

```

Appendix A. Appendix

```
54     prompt = {'Enter low value:', 'Enter high value:'};
55     dlg_title = 'Enter manually the values of grey levels around slag peak';
56     num_lines = 1;
57     def = {'160', '255'};
58     answer = inputdlg(prompt, dlg_title, num_lines, def);
59     man_low_g = str2num(answer{1});
60     man_high_g = str2num(answer{2});
61 end
62
63 for verse = 1:length(fnames)
64
65     Mgmap = imread(fnames(verse).name);
66     bse = imread(bnames(verse).name);
67
68     Mgmap = double(Mgmap);
69     bse = double(bse);
70     bse = bse(:,:,1);
71
72     clear smooth1
73     clear smooth2
74
75     %smoothing of the image with Hamming windows
76     for i=1:length(Mgmap(1,:))
77         smooth1(:,i) = conv(Mgmap(:,i), hamming(hamNr));
78     end
79
80     for i=1:length(smooth1(:,1))
81         smooth2(i,:) = conv(smooth1(i,:), hamming(hamNr));
82     end
83
84     smooth2 = smooth2(hamNr:end-hamNr, hamNr:end-hamNr);
85     smooth2 = smooth2./((sum(hamming(hamNr)))^2);
86
87     mgs = smooth2;
88
89     %cutting of the bse so the size matches
90     bses = bse((hamNr/2)+1:end-(hamNr/2), (hamNr/2)+1:end-(hamNr/2));
91
92     %taking the adequate grey level areas from bse image
93     histogram = hist(double(bses(:)), 255);
94
95     %taking areas with high Mg content from Mg map
96     maskMg = (mgs > Mg_gray);
97
98     % Find slag peak position
99     eroded_Mg = imerode(maskMg, strel('disk', 15));
100    bses_Mg = (bses.*eroded_Mg);
101    Slag_peak_position = sum(sum(bses_Mg))./sum(sum(bses_Mg ~= 0));
102
103    if auto == 0
104        mask = (man_low_g < bses & bses < man_high_g);
105    else
106        mask = (Slag_peak_position - 25 < bses & bses < 240); %the low_grey level and
107        %high_grey level are found from the peak position -20 and +40.
108    end
109
110    %% Erode and dilate option
111    %% Close holes
112    closedI = imfill(mask, 'holes');
```

A.5. Code used for the measurement of the degree of reaction of slag by SEM-IA

```
113 mask=closedI;
114 closedII = imfill(maskMg,'holes');
115 maskMg=closedII;
116
117 %merge both to get the result filter
118 result=(mask.*maskMg);
119
120 %calculate the area fraction
121 i=size(result);
122 areaFraction(verse) = sum(sum(result))/(i(1)*i(2))*100;
123
124 end
125
126 %Results
127 areaFractionAverage=mean(areaFraction);
128 error=std(areaFraction)/sqrt(verse);
129 values=[areaFractionAverage,error];
```

A.6 Code used for the modelling of the expansion

```
1 // Author: Cyrille Dunant <cyrille.dunant@gmail.com>, (C) 2014 //
2
3 #include "main.h"
4 #include "../utilities/samplingcriterion.h"
5 #include "../features/features.h"
6 #include "../physics/physics_base.h"
7 #include "../physics/fracturecriteria/mohrcoulomb.h"
8 #include "../physics/fracturecriteria/ruptureenergy.h"
9 #include "../physics/weibull_distributed_stiffness.h"
10 #include "../physics/stiffness.h"
11 #include "../physics/materials/gel_behaviour.h"
12 #include "../physics/materials/paste_behaviour.h"
13 #include "../physics/materials/aggregate_behaviour.h"
14 #include "../physics/stiffness_with_imposed_deformation.h"
15 #include "../physics/diffusion.h"
16 #include "../features/pore.h"
17 #include "../features/sample.h"
18 #include "../features/sample3d.h"
19 #include "../features/inclusion.h"
20 #include "../features/expansiveZone.h"
21 #include "../features/crack.h"
22 #include "../geometry/geometry_with_exclusion.h"
23 #include "../features/enrichmentInclusion.h"
24 #include "../mesher/delaunay_3d.h"
25 #include "../solvers/assembly.h"
26 #include "../utilities/itoa.h"
27 #include "../utilities/granulo.h"
28 #include "../utilities/placement.h"
29 #include "../utilities/random.h"
30 #include "../utilities/writer/triangle_writer.h"
31 #include "../utilities/writer/voxel_writer.h"
32
33 #include <fstream>
34
35 #include <cmath>
36 #include <typeinfo>
37 #include <limits>
38 #include <time.h>
39
40 using namespace Mu ;
41
42 int main(int argc, char *argv[])
43 {
44     std::fstream psdfile(argv[1]) ;
45     double thresholdRadius = 30. ;
46     if(argc > 3)
47         thresholdRadius = std::max(atof(argv[3]), 30.) ;
48     double maxRadius ;
49     double poreFraction ;
50     double waterLayerDepth = 1.5 ;
51     double factor = 1000. ;
52     double minRadius = waterLayerDepth*.25 ;
53     double shapeFactor = 200 ;
54
55     psdfile >> poreFraction >> maxRadius ;
56     while(!psdfile.eof())
57     {
58         double dummy ;
```

A.6. Code used for the modelling of the expansion

```
59     psdfile >> poreFraction >> dummy ;
60 }
61 poreFraction /= 100. ;
62 maxRadius = std::min(maxRadius*factor, thresholdRadius) ;
63
64 std::vector<Inclusion *> incs = PSDGenerator::get2DInclusions(maxRadius,
65     maxRadius*maxRadius*M_PI*40., new GranuloFromCumulativePSD(argv[1],
66     CUMULATIVE_ABSOLUTE_REVERSE, 1000., maxRadius, minRadius), PSDEndCriteria
67     (.1, 0., 50000) ) ;
68 double bulk = 13.9 ;
69 double shear = 8.75 ;
70 double E = (9.*bulk*shear)/(3.*bulk+shear) ;
71 double nu = (3.*bulk-2.*shear)/(2.*(3.*bulk+shear)) ;
72
73 std::cout << "maxr = " << maxRadius << ", porefrac = " << poreFraction <<
74 std::endl ;
75
76 std::vector<Feature *> pores ;
77 double poreArea = 0 ;
78 for(size_t i = 0 ; i < incs.size() ; i++)
79 {
80     pores.push_back(incs[i]);
81     incs[i]->setBehaviour(new VoidForm()) ;
82     poreArea += incs[i]->area() ;
83 }
84
85 double sampleSide = sqrt(poreArea/poreFraction) ;
86
87 Sample s(sampleSide, sampleSide, 0., 0.) ;
88 s.setBehaviour(new ElasticOnlyPasteBehaviour(E, nu, SPACE_TWO_DIMENSIONAL)
89 );
90
91 pores = placement2D(s.getPrimitive(), pores, waterLayerDepth*4., 0, 2000000)
92 ;
93
94 FeatureTree ft(&s) ;
95
96 for(size_t i = 0 ; i < pores.size() ; i++)
97     ft.addFeature(&s, pores[i]);
98
99     ft.addBoundaryCondition(new
100 BoundingBoxDefinedBoundaryCondition(SET_ALONG_XI, LEFT, 0.));
101     ft.addBoundaryCondition(new
102 BoundingBoxDefinedBoundaryCondition(SET_ALONG_ETA, BOTTOM, 0.));
103
104     std::vector<GeometryDefinedBoundaryCondition *> boundaryConditions ;
105     for(size_t i = 0 ; i < pores.size() ; i++)
106     {
107         boundaryConditions.push_back(new
108 GeometryDefinedBoundaryCondition(SET_NORMAL_STRESS, static_cast<Geometry
109 *>(pores[i]), 0)) ;
110         ft.addBoundaryCondition(boundaryConditions.back()) ;
111     }
112
113
114 ft.setOrder(LINEAR) ;
115 ft.setSamplingNumber(192) ;
116 std::fstream outfile(argv[2], std::ios::out | std::ios::app) ;
```

Appendix A. Appendix

```
117   outfile << "# psd = " << argv[1] << ", outfile = " << argv[2] << std::endl
118 ;
119   outfile << "# P0 R_crit Vol dx dy \n" << std::endl ;
120   outfile.close() ;
121   for(double p = 10 ; p < 110 ; p+=10)
122   {
123     std::fstream outfile(argv[2], std::ios::out | std::ios::app) ;
124     double criticalRadius = thresholdRadius ;
125     double poresUnderPressure = 0 ;
126     for(size_t i = 0 ; i < pores.size() ; i++)
127     {
128       double pressure = p-shapeFactor/(pores[i]->getRadius()-waterLayerDepth)
129 ;
130
131       if(pressure > 0 && pores[i]->getRadius() > waterLayerDepth)
132       {
133         pressure = std::min(shapeFactor/(pores[i]->getRadius()-
134 waterLayerDepth), p) ;
135         boundaryConditions[i]->setData(pressure*1e-3) ;
136         criticalRadius = std::min(pores[i]->getRadius(), criticalRadius) ;
137         poresUnderPressure += pores[i]->area() ;
138       }
139     }
140
141     ft.step() ;
142     std::vector<double> apparentStrain =
143 ft.getMacroscopicStrain(s.getPrimitive()) ;
144     outfile<< p << " " << criticalRadius << " " <<
145 poresUnderPressure/poreArea << " " << apparentStrain[0] << " " <<
146 apparentStrain[1] << std::endl ;
147     outfile.close() ;
148
149     MultiTriangleWriter writerm( "displacements_pores", "displacements_layer",
150 nullptr ) ;
151     writerm.reset( &ft ) ;
152     // writerm.getField( PRINCIPAL_STRAIN_FIELD ) ;
153     writerm.getField( PRINCIPAL_REAL_STRESS_FIELD ) ;
154     writerm.append() ;
155     writerm.writeSvg(50, true) ;
156
157   }
158
159   return 0 ;
160 }
```

Bibliography

- [1] U.S. Geological Survey, Mineral Commodity Summaries, February 2014.
URL <http://minerals.usgs.gov/minerals/pubs/commodity/cement/>
- [2] World Steel Association, World steel production 2013.
URL <http://www.worldsteel.org/statistics/statistics-archive/2013-steel-production.html>
- [3] E. Gartner, Industrially interesting approaches to "low-CO₂" cements, *Cement and Concrete Research* 34 (2004) 1489–1498.
- [4] S. Lamberet, Durability of ternary binders based on Portland cement, calcium aluminate cement and calcium sulfate, Ph.D. thesis, Ecole Polytechnique Fédérale de Lausanne EPFL (2005).
- [5] J. Kighelman, Hydration and Structure Development of Ternary Binder System as used in Self-Levelling Compounds, Ph.D. thesis, Ecole Polytechnique Fédérale de Lausanne EPFL (2007).
- [6] K. Onishi, T. A. Bier, Investigation into relations among technological properties, hydration kinetics and early age hydration of self-leveling underlayments, *Cement and Concrete Research* 40 (2010) 1034–1040.
- [7] A. J. Majumdar, B. Singh, R. N. Edmonds, A. Majumbar, Hydration of Mixtures of C12a7 and Granulated Blastfurnace Slag, *Cement and Concrete Research* 19 (1989) 848–856.
- [8] A. J. Majumdar, B. Singh, R. N. Edmonds, Hydration of Mixtures of Ciment-Fondu Aluminous Cement and Granulated Blast-Furnace Slag, *Cement and Concrete Research* 20 (1990) 197–208.
- [9] B. Singh, A. J. Majumdar, K. Quillin, Properties of BRECEM - Ten-year results, *Cement and Concrete Research* 29 (1999) 429–433.
- [10] G. Kakali, S. Tsivilis, E. Aggeli, M. Bati, Hydration products of C3A, C3S and Portland cement in the presence of CaCO₃, *Cement and Concrete Research* 30 (2000) 1073–1077.

Bibliography

- [11] J. P. Bayoux et al., Study of the hydration properties of aluminous cement and calcium sulfate mixes, in: R.J. Mangabhai (Ed.), *Calcium aluminate cements*, E & FN Spon, London, 1990, pp. 320-334., 1990.
- [12] K. L. Scrivener, A. Capmas, *Calcium Aluminate Cements*, in: P. C. Hewlett (Ed.), *Lea's Chemistry of Cement and Concrete (Fourth Edition)*, Butterworth-Heinemann, Oxford, 2003, Ch. 13, pp. 713–782.
- [13] H. F. W. Taylor, *Cement Chemistry*, Thomas Telford, 1997.
- [14] K. L. Scrivener, *Calcium Aluminate Cements*, in: J. Newman, B. S. Choo (Eds.), *Advanced Concrete Technology Vol 1*, Butterworth-Heinemann, Oxford, 2003, Ch. 2.
- [15] J. A. Ding, Y. Fu, J. J. Beaudoin, Study of hydration mechanisms in the high alumina cement - Sodium silicate system, *Cement and Concrete Research* 26 (1996) 799–804.
- [16] D. Damidot, F. Glasser, Thermodynamic investigation of the CaO-Al₂O₃-CaSO₄-H₂O system at 50 C and 85 C, *Cement and Concrete Research* 22 (1992) 1179–1191.
- [17] F. Winnefeld, B. Lothenbach, Hydration of calcium sulfoaluminate cements - Experimental findings and thermodynamic modelling, *Cement and Concrete Research* 40 (2010) 1239–1247.
- [18] F. Winnefeld, S. Barlag, Calorimetric and thermogravimetric study on the influence of calcium sulfate on the hydration of ye'elinite, *Journal of Thermal Analysis and Calorimetry* 101 (2010) 949–957.
- [19] A. Quennoz, Hydration of C3A with Calcium Sulfate Alone and in the Presence of Calcium Silicate, Ph.D. thesis, Ecole Polytechnique Fédérale de Lausanne EPFL (2011).
- [20] M. Collepardi, G. Baldini, M. Pauri, M. Corradi, Tricalcium aluminate hydration in the presence of lime, gypsum or sodium sulfate, *Cement and Concrete Research* 8 (1978) 571–580.
- [21] P. Meredith, A. M. Donald, N. Meller, C. Hall, Tricalcium aluminate hydration: Microstructural observations by in-situ electron microscopy, *Journal of Materials Science* 39 (2004) 997–1005.
- [22] H. Minard, S. Garrault, L. Regnaud, A. Nonat, Mechanisms and parameters controlling the tricalcium aluminate reactivity in the presence of gypsum, *Cement and Concrete Research* 37 (2007) 1418–1426.
- [23] C. Gosselin, E. Gallucci, K. Scrivener, Influence of self heating and Li₂SO₄ addition on the microstructural development of calcium aluminate cement, *Cement and Concrete Research* 40 (2010) 1555–1570.

- [24] P. W. P. Brown, L. O. Liberman, G. Frohnsdoref, Kinetics of the early hydration of tricalcium aluminate in solutions containing calcium sulfate, *Journal of the American Ceramic Society* 67 (1984) 793–795.
- [25] W. Corstanje, H. Stein, J. Stevels, Hydration reactions in pastes $C_3S+C_3A+CaSO_4.2aq+H_2O$ at 25°C.I, *Cement and Concrete Research* 3 (1973) 791–806.
- [26] R. Feldman, V. Ramachandran, The influence of $CaSO_4.2H_2O$ upon the hydration character of $3CaO.Al_2O_3$, *Magazine of Concrete research* 18 (1966) 185–196.
- [27] K. L. Scrivener, P. L. Pratt, Microstructural studies of the hydration of C_3A and C_4AF independently and in cement paste., in: *Proceedings of the British Ceramic Society*, 1984, pp. 207–219.
- [28] J. Skalny, M. E. Tadros, Retardation of Tricalcium Aluminate Hydration by Sulfates, *Journal of the American Ceramic Society* 60 (1977) 174–175.
- [29] P. Lawrence, M. Cyr, E. Ringot, Mineral admixtures in mortars: effect of inert materials on short-term hydration, *Cement and Concrete Research* 33 (2003) 1939–1947.
- [30] V. Kocaba, Development and Evaluation of Methods to Follow Microstructural Development of Cementitious Systems Including Slags, Ph.D. thesis, Ecole Polytechnique Fédérale de Lausanne EPFL (2009).
- [31] B. Lothenbach, K. Scrivener, R. Hooton, Supplementary cementitious materials, *Cement and Concrete Research* 41 (2011) 1244–1256.
- [32] S. Dittrich, J. Neubauer, F. Goetz-Neunhoeffler, The influence of fly ash on the hydration of OPC within the first 44h—A quantitative in situ XRD and heat flow calorimetry study, *Cement and Concrete Research* 56 (2014) 129–138.
- [33] W. A. Gutteridge, J. A. Dalziel, Filler cement: The effect of the secondary component on the hydration of Portland cement, *Cement and Concrete Research* 20 (1990) 853–861.
- [34] E. Berodier, K. L. Scrivener, Understanding the filler effect on the nucleation and growth of C-S-H, *Journal of the American Ceramic Society* (2014) DOI:10.1111/jace.13177.
- [35] A. Negro, A. Bachiorri, M. Murat, Interaction, in aqueous medium, between calcium carbonate and monocalcium aluminate at 5°C, 20°C and 40°C., *Bulletin de Mineralogie* 105 (1982) 284–290.
- [36] C. Fentiman, Hydration of carbo-aluminous cement at different temperatures, *Cement and Concrete Research* 15 (1985) 622–630.
- [37] L. Pelletier-Chaignat, F. Winnefeld, B. Lothenbach, C. J. Muller, Beneficial use of limestone filler with calcium sulphoaluminate cement, *Construction and Building Materials* 26 (2012) 619–627.

Bibliography

- [38] Y. Ohba, A. Nakamura, J. K. Lee, E. Sakai, M. Daimon, Influence of CaCO₃ on the hydration of various types of calcium aluminates with anhydrite, in: Proceedings of 10th International Congress on the Chemistry of Cement, Gothenburg, Sweden, 1997, p. 8.
- [39] T. Matschei, B. Lothenbach, F. P. Glasser, The role of calcium carbonate in cement hydration, *Cement and Concrete Research* 37 (2007) 551–558.
- [40] K. D. Ingram, K. E. Daugherty, A review of limestone additions to Portland cement and concrete, *Cement and Concrete Composites* 13 (1991) 165–170.
- [41] B. Lothenbach, G. Le Saout, E. Gallucci, K. Scrivener, Influence of limestone on the hydration of Portland cements, *Cement and Concrete Research* 38 (2008) 848–860.
- [42] M. Zajac, A. Rossberg, G. Le Saout, B. Lothenbach, Influence of limestone and anhydrite on the hydration of Portland cements, *Cement and Concrete Composites* 46 (2014) 99–108.
- [43] B. Lothenbach, G. Le Saout, E. Gallucci, K. L. Scrivener, Influence of limestone on the hydration of Portland cements, *Cement and Concrete Research* 38 (2008) 848–860.
- [44] A. Gruskovnjak, B. Lothenbach, F. Winnefeld, R. Figi, S. C. Ko, M. Adler, U. Mäder, Hydration mechanisms of super sulphated slag cement, *Cement and Concrete Research* 38 (2008) 983–992.
- [45] R. N. Edmonds, A. J. Majumdar, The hydration of mixtures of monocalcium aluminate and blastfurnace slag, *Cement and Concrete Research* 19 (1989) 779–782.
- [46] B. R. Bickmore, K. L. Nagy, A. K. Gray, A. R. Brinkerhoff, The effect of Al(OH)₃ on the dissolution rate of quartz, *Geochimica et Cosmochimica Acta* 70 (2006) 290–305.
- [47] E. Douglas, J. Brandstet, A preliminary study on the alkali activation of ground granulated blast-furnace slag, *Cement and concrete research* 20 (1990) 746–756.
- [48] T. Chappex, K. L. Scrivener, The influence of aluminium on the dissolution of amorphous silica and its relation to alkali silica reaction, *Cement and Concrete Research* 42 (2012) 1645–1649.
- [49] R. Snellings, Solution-Controlled Dissolution of Supplementary Cementitious Material Glasses at pH 13: The Effect of Solution Composition on Glass Dissolution Rates, *Journal of the American Ceramic Society* 96 (2013) 2467–2475.
- [50] X. Q. Wu, W. M. Jiang, D. M. Roy, Early Activation and Properties of Slag Cement, *Cement and Concrete Research* 20 (1990) 961–974.
- [51] L. Fernandez-Carrasco, E. Vazquez, Reactions of fly ash with calcium aluminate cement and calcium sulphate, *Fuel* 88 (2009) 1533–1538.

- [52] C. D. Lawrence, The Production of Low-Energy Cements, in: P. C. Hewlett (Ed.), *Lea's Chemistry of Cement and Concrete (Fourth Edition)*, Butterworth-Heinemann, Oxford, 2003, Ch. 9, pp. 421–470.
- [53] P. Lura, O. M. Jensen, K. van Breugel, Autogenous shrinkage in high-performance cement paste: An evaluation of basic mechanisms, *Cement and Concrete Research* 33 (2003) 223–232.
- [54] Y. Fu, P. Gu, P. Xie, J. J. Beaudoin, Effect of chemical admixtures on the expansion of shrinkage-compensating cement containing a pre-hydrated high alumina cement—based expansive additive, *Cement and Concrete Research* 25 (1995) 29–38.
- [55] M. Cohen, Modeling of expansive cements, *Cement and Concrete Research* 13 (1983) 809–818.
- [56] M. Cohen, Theories of expansion in sulfoaluminate-type expansive cements: schools of thought, *Cement and Concrete Research* 13 (1983) 809–818.
- [57] P. K. Mehta, Mechanism of expansion associated with ettringite formation, *Cement and Concrete Research* 3 (1973) 1–6.
- [58] G. W. Scherer, Crystallization in pores, *Cement and Concrete Research* 29 (1999) 1347–1358.
- [59] G. W. Scherer, Stress from crystallization of salt, *Cement and Concrete Research* 34 (2004) 1613–1624.
- [60] R. J. Flatt, G. W. Scherer, Thermodynamics of crystallization stresses in DEF, *Cement and Concrete Research* 38 (2008) 325–336.
- [61] P. W. Brown, H. F. W. Taylor, The role of ettringite in external sulfate attack, *The American Ceramic Society* (1999) 73–98.
- [62] M. Polivka, Factors influencing expansion of expansive cement concretes, *ACI SP-38* (1973) 239–250.
- [63] H. Taylor, C. Famy, K. Scrivener, Delayed ettringite formation, *Cement and Concrete Research* 31 (2001) 683–693.
- [64] Y. Yamazaki, T. Monji, K. Sugiura, Early age expanding behavior of mortars and concretes using expansive additives of CaO-CaSO₄-4CaO•3Al₂O₃•SO₃ system, in: *The VI International Congress on the Chemistry of Cement*, Moscow, 1974.
- [65] V. Alunno Rossetti, G. Chiochio, A. Paolini, Expansive properties of the mixture C₄A₃H₁₂ - 2Cs I. An hypothesis on the expansion mechanism, *Cement and Concrete Research* 12 (1982) 577–585.

Bibliography

- [66] I. Odler, M. Gasser, Mechanism of Sulfate Expansion in Hydrated Portland Cement, *Journal of the American Ceramic Society* 71 (1988) 1015–1020.
- [67] K. Ogawa, D. Roy, C4A3s hydration, ettringite formation, and its expansion mechanism: III. Effect of CaO, NaOH and NaCl-Conclusions, *Cement and Concrete Research* 12 (1982) 247–256.
- [68] J. Lavalle, "Recherches sur la formation lente des cristaux a la temperature ordinaire" (Research on the slow formation of crystals at ordinary temperatures), *Compte Rend. Acad. Sci. (Paris)* 36 (1853) 493–495.
- [69] S. Taber, The growth of crystals under external pressure, *American Journal of Science* 41 (1916) 532–556.
- [70] J. Thomson, On crystallization and liquefaction as influenced by stresses, tending to change of form in the crystals, *Dublin Phil. Mag. J. Sci.* 24 (1862) 395–401.
- [71] L. A. Rijniers, Salt crystallization in porous materials : an NMR study, Ph.D. thesis, Eindhoven University of Technology (2004).
- [72] C. W. Correns, W. Steinborn, Experimente zur Messung und Erklärung der sogenannten Kristallisationskraft, *Z. Krist. A* 101 (1939) 117–133.
- [73] C. W. Correns, Growth and Dissolution of Crystals under Linear Pressure, *Discussions of the Faraday Society* (5) (1949) 267–271.
- [74] D. H. Everett, The thermodynamics of frost damage to porous solids, *Transactions of the Faraday Society* 57 (1961) 1541–1551.
- [75] H. Freundlich, *Colloid & Capillary Chemistry*, Methuen, London, 1926, pp. 154–157.
- [76] R. J. Flatt, Salt damage in porous materials: how high supersaturations are generated, *Journal of Crystal Growth* 242 (2002) 435–454.
- [77] M. Steiger, Crystal growth in porous materials-II: Influence of crystal size on the crystallization pressure, *Journal of Crystal Growth* 282 (2005) 470–481.
- [78] Available at www.empa.ch/cemdata, Version cemdata14, release date 07.05.2014 during the 4th GEMS Workshop, EMPA, Switzerland.
- [79] M. Balonis, F. Glasser, The density of cement phases, *Cement and Concrete Research* 39 (2009) 733–739.
- [80] D. Torr ns-Mart n, L. Fern ndez-Carrasco, Effect of sulfate content on cement mixtures, *Construction and Building Materials* 48 (2013) 144–150.
- [81] J. Bizzozero, C. Gosselin, K. L. Scrivener, Expansion mechanisms in calcium aluminate and sulfoaluminate systems with calcium sulfate, *Cement and Concrete Research* 56 (2014) 190–202.

- [82] I. Odler, J. Colan-Subauste, Investigations on cement expansion associated with ettringite formation, *Cement and Concrete Research* 29 (1999) 731–735.
- [83] I. A. Chen, C. W. Hargis, M. C. G. Juenger, Understanding expansion in calcium sulfoaluminate-belite cements, *Cement and Concrete Research* 42 (2012) 51–60.
- [84] J. Beretka, M. Marroccoli, N. Sherman, G. Valenti, The influence of C4A3s content and ratio on the performance of calcium sulfoaluminate-based cements, *Cement and Concrete Research* 26 (1996) 1673–1681.
- [85] K. Ogawa, D. Roy, C4A3s hydration ettringite formation, and its expansion mechanism: I. expansion; Ettringite stability, *Cement and Concrete Research* 11 (1981) 741–750.
- [86] D. Min, T. Mingshu, Formation and expansion of ettringite crystals, *Cement and Concrete Research* 24 (1994) 119–126.
- [87] C. Famy, K. L. Scrivener, A. Atkinson, A. R. Brough, Influence of the storage conditions on the dimensional changes of heat-cured mortars, *Cement and Concrete Research* 31 (2001) 795–803.
- [88] H. Chen, Autogenous and Thermal Deformations and their Interaction in Early Age Cementitious Materials, Ph.D. thesis, Ecole Polytechnique Fédérale de Lausanne EPFL (2013).
- [89] S. Diamond, Mercury porosimetry: An inappropriate method for the measurement of pore size distributions in cement-based materials, *Cement and Concrete Research* 30 (2000) 1517–1525.
- [90] R. Vočka, C. Gallé, M. Dubois, P. Lovera, Mercury intrusion porosimetry and hierarchical structure of cement pastes: Theory and experiment, *Cement and concrete research* 30 (2000) 521–527.
- [91] S. Irico, D. Gastaldi, F. Canonico, G. Magnacca, Investigation of the microstructural evolution of calcium sulfoaluminate cements by thermoporometry, *Cement and Concrete Research* 53 (2013) 239–247.
- [92] Z. Sun, G. W. Scherer, Pore size and shape in mortar by thermoporometry, *Cement and Concrete Research* 40 (2010) 740–751.
- [93] D. C. Creagh, J. H. Hubbell, X-ray absorption (or attenuation) coefficients, in: E. Prince (Ed.), *International Tables for Crystallography Volume C: Mathematical, physical and chemical tables*, 6th Edition, International Union of Crystallography, 2006, pp. 220–229.
- [94] D. A. Porter, K. E. Easterling, *Phase Transformations in Metals and Alloys*, Third Edition (Revised Reprint), CRC Press, 1992.
- [95] Q. Zhou, F. P. Glasser, Thermal stability and decomposition mechanisms of ettringite at < 120 degrees C, *Cement and Concrete Research* 31 (2001) 1333–1339.

Bibliography

- [96] L. Zhang, G. W. Scherer, Comparison of methods for arresting hydration of cement, *Cement and Concrete Research* 41 (2011) 1024–1036.
- [97] A. Ipavec, R. Gabrovšek, T. Vuk, V. Kaučič, J. Maček, A. Meden, Carboaluminate Phases Formation During the Hydration of Calcite Containing Portland Cement, *Journal of the American Ceramic Society* 94 (2011) 1238–1242.
- [98] K. K. Aligizaki, *Pore Structure of Cement-Based Materials: Testing, Interpretation and Requirements*, CRC Press, 2005.
- [99] D. Jansen, F. Goetz-Neunhoeffler, B. Lothenbach, J. Neubauer, The early hydration of Ordinary Portland Cement (OPC): An approach comparing measured heat flow with calculated heat flow from QXRD, *Cement and Concrete Research* 42 (2012) 134–138.
- [100] B. H. O'Connor, M. D. Raven, Application of the Rietveld Refinement Procedure in Assaying Powdered Mixtures, *Powder Diffraction* 3 (1988) 2–6.
- [101] W. Hörkner, H. Müller-Buschbaum, Zur kristallstruktur von CaAl_2O_4 , *Journal of Inorganic and Nuclear Chemistry* 38 (1976) 983–984.
- [102] P. Ballirano, A. Maras, S. Meloni, R. Caminiti, The monoclinic I2 structure of bassanite, calcium sulphate hemihydrate ($\text{CaSO}_4 \cdot 0.5 \text{H}_2\text{O}$), *European Journal of Mineralogy* 13 (2001) 985–993.
- [103] A. A. Colville, S. Geller, Crystal structures of CaFeAlO and CaFeAlO_2 1.43 0.57 5 2 1.28 0.72 5, *Acta Crystallogr. B* 28 (1972) 3196–3200.
- [104] F. Goetz-Neunhoeffler, J. Neubauer, Refined ettringite ($\text{Ca}_6\text{Al}_2(\text{SO}_4)_3(\text{OH})_{12} \cdot 26\text{H}_2\text{O}$) structure for quantitative X-ray diffraction analysis, *Powder diffraction* 21 (2006) 4–11.
- [105] W. G. Mumme, R. J. Hill, G. Bushnell-Wye, E. R. Segnit, Rietveld crystal structure refinements, crystal chemistry and calculated powder diffraction data for the polymorphs of dicalcium silicate and related phases, *Neues Jahrb. Mineral. Abh* 169 (1995) 35–68.
- [106] R. Allmann, Refinement of the hybrid layer structure $[\text{Ca}_2\text{Al}(\text{OH})_6]^{+*}[1/2\text{SO}_4 \cdot 3\text{H}_2\text{O}]$, *Neues Jahrbuch für Mineralogie, Monatshefte* (1977) 136–144.
- [107] K. Leinenweber, K. Parise, High-pressure synthesis and crystal structure of $\text{CaFeTi}_2\text{O}_6$, a new perovskite structure type, *Journal of Solid State Chemistry* 114 (1995) 277–281.
- [108] H. Saalfeld, M. Wedde, Refinement of the crystal structure of gibbsite, $\text{Al}(\text{OH})_3$, *Zeitschrift für Kristallographie* 139 (1974) 129–135.
- [109] I. P. Swainson, M. T. Dove, W. W. Schmahl, A. Putnis, Neutron powder diffraction study of the åkermanite-gehlenite solid solution series, *Physics and Chemistry of Minerals* 19 (1992) 185–195.

- [110] M. Francois, G. Renaudin, O. Evrard, A cementitious compound with composition $3\text{CaO} \cdot \text{Al}_2\text{O}_3 \cdot \text{CaCO}_3 \cdot 11\text{H}_2\text{O}$, *Acta Crystallographica Section C: Crystal Structure Communications* 54 (1998) 1214–1217.
- [111] N. Nakagiri, M. H. Manghnani, L. C. Ming, S. Kimura, Crystal structure of magnetite under pressure, *Physics and Chemistry of Minerals* 13 (1986) 238–244.
- [112] T. Runčevski, R. E. Dinnebier, O. V. Magdysyuk, H. Pöllmann, Crystal structures of calcium hemicarboaluminate and carbonated calcium hemicarboaluminate from synchrotron powder diffraction data, *Acta Crystallographica Section B* 68 (2012) 493–500.
- [113] E. N. Maslen, V. A. Streltsov, N. R. Streltsova, X-ray study of the electron density in calcite, CaCO_3 , *Acta Crystallographica Section B: Structural Science* 49 (1993) 636–641.
- [114] C. Cohen-Addad, P. Ducros, A. Durif, E. F. Bertaut, A. Delapalme, Détermination de la position des atomes d'hydrogène dans l'hydrogrinat $\text{Al}_2\text{O}_3 \cdot 3\text{CaO} \cdot 6\text{H}_2\text{O}$ par résonance magnétique nucléaire et diffraction neutronique, *Journal de Physique* 25 (1964) 478–483.
- [115] A. G. De la Torre, M.-G. López-Olmo, C. Álvarez Rúa, S. García-Granda, M. A. G. Aranda, Structure and microstructure of gypsum and its relevance to Rietveld quantitative phase analyses, *Powder diffraction* 19 (2004) 240–246.
- [116] R. Rinaldi, M. Sacerdoti, E. Passaglia, Stratlingite: crystal structure, chemistry, and a reexamination of its polytype vertumnite, *European Journal of Mineralogy* 2 (1990) 841–849.
- [117] V. Kocaba, E. Gallucci, K. L. Scrivener, Methods for determination of degree of reaction of slag in blended cement pastes, *Cement and Concrete Research* 42 (2012) 511–525.
- [118] C. Gosselin, Microstructural Development of Calcium Aluminate Cement Based Systems with and without Supplementary Cementitious Materials, Ph.D. thesis, Ecole Polytechnique Fédérale de Lausanne EPFL (2009).
- [119] S. Mindess, J. F. Young, D. Darwin, *Concrete*, Prentice Hall; 2 edition, 2002.
- [120] E. W. Washburn, The Dynamics of Capillary Flow, *Physical Review* 17 (3) (1921) 273–283.
- [121] A. B. Abell, K. L. Willis, D. A. Lange, Mercury intrusion porosimetry and image analysis of cement-based materials, *Journal of Colloid and Interface Science* 211 (1999) 39–44.
- [122] D. N. Winslow, S. Diamond, A Mercury Porosimetry Study of the Evolution of Porosity in Portland Cement, *Journal of Materials* 5 (1970) 564–585.
- [123] R. A. Cook, K. C. Hover, Experiments on the contact angle between mercury and hardened cement paste, *Cement and Concrete Research* 21 (1991) 1165–1175.
- [124] F. Moro, H. Böhni, Ink-bottle effect in mercury intrusion porosimetry of cement-based materials, *Journal of colloid and interface science* 246 (2002) 135–49.

Bibliography

- [125] R. A. Cook, K. C. Hover, Mercury porosimetry of hardened cement pastes, *Cement and Concrete Research* 29 (1999) 933–943.
- [126] H. Midgley, J. Illston, Some comments on the microstructure of hardened cement pastes, *Cement and Concrete Research* 13 (1983) 197–206.
- [127] D. N. Winslow, M. D. Cohen, D. P. Bentz, K. A. Snyder, E. J. Garboczi, Percolation and pore structure in mortars and concrete, *Cement and Concrete Research* 24 (1) (1994) 25–37.
- [128] A. C. A. Muller, K. L. Scrivener, A. M. Gajewicz, P. J. McDonald, Densification of C–S–H Measured by ^1H NMR Relaxometry, *The Journal of Physical Chemistry C* 117 (2013) 403–412.
- [129] P. Longuet, L. Burglen, A. Zelwer, La phase liquide du ciment hydraté (The liquid phase of hydrated cement), *Rev. Matér Constr. Trav. Publics Cim. Bétons* 676 (1973) 35–41.
- [130] R. Barneyback, S. Diamond, Expression and analysis of pore fluids from hardened cement pastes and mortars, *Cement and Concrete Research* 11 (1981) 279–285.
- [131] M. Bérubé, C. Tremblay, Chemistry of pore solution expressed under high pressure: influence of various parameters and comparison with the hot water extraction method, in: *Proceedings of the 12th International Conference on Alkali-Aggregate Reaction in Concrete*, Beijing, 2004, pp. 833–842.
- [132] B. Lothenbach, Thermodynamic equilibrium calculations in cementitious systems, *Materials and Structures* 43 (2010) 1413–1433.
- [133] Available at <http://gems.web.psi.ch/>, retrieved 15.06.2014.
- [134] D. A. Kulik, T. Wagner, S. V. Dmytrieva, G. Kosakowski, F. F. Hingerl, K. V. Chudnenko, U. R. Berner, GEM-Selektor geochemical modeling package: revised algorithm and GEMS3K numerical kernel for coupled simulation codes, *Computational Geosciences* 17 (2013) 1–24.
- [135] W. Hummel, U. Berner, E. Curti, F. J. Pearson, T. Thoenen, Nagra/PSI chemical thermodynamic data base 01/01, *Radiochimica Acta* 90 (2002) 805–813.
- [136] T. Matschei, B. Lothenbach, F. P. Glasser, Thermodynamic properties of Portland cement hydrates in the system $\text{CaO-Al}_2\text{O}_3\text{-SiO}_2\text{-CaSO}_4\text{-CaCO}_3\text{-H}_2\text{O}$, *Cement and Concrete Research* 37 (2007) 1379–1410.
- [137] C. Dunant, Experimental and Modelling Study of the Alkali-Silica-Reaction in Concrete, Ph.D. thesis, Ecole Polytechnique Fédérale de Lausanne EPFL (2009).
- [138] P. P. Barret, D. Ménétrier, D. Bertrandie, Contribution to the study of the kinetic mechanism of aluminous cement setting I — Latent periods in heterogeneous and homogeneous milieus and the absence of heterogeneous nucleation, *Cement and Concrete Research* 4 (1974) 545–556.

- [139] W. B. Lou, B. H. Guan, Z. B. Wu, Calorimetric study of ternary binder of calcium aluminate cement, Portland-limestone cement and FGD gypsum, *Journal of Thermal Analysis and Calorimetry* 101 (2010) 119–127.
- [140] J. Bizzozero, K. Scrivener, Limestone reaction in calcium aluminate cement - calcium sulfate systems, *Cement and Concrete Research* (2014) submitted.
- [141] R. Féret, Compacité des mortiers hydrauliques, *Ann. Ponts Chaussées* 4.
- [142] M. Rossler, I. Odler, Investigations on the Relationship between Porosity, Structure and Strength of Hydrated Portland-Cement Pastes .1. Effect of Porosity, *Cement and Concrete Research* 15 (1985) 320–330.
- [143] D. L. Rayment, A. J. Majumdar, Microanalysis of High-Alumina Cement Clinker and Hydrated Hac Slag Mixtures, *Cement and Concrete Research* 24 (1994) 335–342.
- [144] L. Hench, D. Clark, Physical chemistry of glass surfaces, *Journal of Non-Crystalline Solids* 28 (1978) 83–105.
- [145] A. Roy, Sulfur speciation in granulated blast furnace slag: An X-ray absorption spectroscopic investigation, *Cement and Concrete Research* 39 (2009) 659–663.
- [146] F. P. Glasser, L. Zhang, High-performance cement matrices based on calcium sulfoaluminate-belite compositions, *Cement and Concrete Research* 31 (2001) 1881–1886.
- [147] T. Desbois, R. Le Roy, A. Pavoine, G. Platret, A. Feraille, A. Alaoui, Effect of gypsum content on sulfoaluminate mortars stability, *European Journal of Environmental and Civil Engineering* 14 (2010) 579–597.
- [148] W. Nocuń-Wczelik, Z. Konik, A. Stok, Blended systems with calcium aluminate and calcium sulphate expansive additives, *Construction and Building Materials* 25 (2011) 939–943.
- [149] C. Evju, S. Hansen, Expansive properties of ettringite in a mixture of calcium aluminate cement, Portland cement and β -calcium sulfate hemihydrate, *Cement and Concrete Research* 31 (2001) 257–261.
- [150] W. Hummel, U. Berner, E. Curti, F.J. Pearson, T. Thoenen, Nagra/PSI Chemical Thermodynamic Data Base 01/01, Universal Publishers, Parkland, Florida USA.
- [151] Available at <http://www.empa.ch/cemdata/>, Version cemdata07.2, release date 14.08.2008, retrieved 20.07.2013.
- [152] C. Yu, W. Sun, K. L. Scrivener, Mechanism of expansion of mortars immersed in sodium sulfate solutions, *Cement and Concrete Research* 43 (2013) 105–111.

Bibliography

- [153] S. Popovics, Strength and related properties of concrete: A quantitative approach (1998) p. 125.
- [154] G. Chanvillard, R. Barbarulo, Stress from Confined Crystallization Occurrence by Internal Phase Change: Application to the Case of Delayed Ettringite Formation in Hardened Cement Paste, in: "Proceedings of Mechanics and Physics of Porous Solids - A Tribute to Prof. Olivier Coussy", Ecole des Ponts ParisTech (2011) 285–302.
- [155] O. Coussy, Deformation and stress from in-pore drying-induced crystallization of salt, *Journal of the Mechanics and Physics of Solids* 54 (2006) 1517–1547.
- [156] O. Coussy, *Mechanics and Physics of porous solids*, Wiley, New York, 2010.
- [157] Z. Sun, G. W. Scherer, Effect of air voids on salt scaling and internal freezing, *Cement and Concrete Research* 40 (2010) 260–270.
- [158] C.-J. Haecker, E. Garboczi, J. Bullard, R. Bohn, Z. Sun, S. Shah, T. Voigt, Modeling the linear elastic properties of Portland cement paste, *Cement and Concrete Research* 35 (2005) 1948–1960.
- [159] B. Bary, N. Leterrier, E. Deville, P. Le Bescop, Coupled chemo-transport-mechanical modelling and numerical simulation of external sulfate attack in mortar, *Cement and Concrete Composites* 49 (2014) 70–83.
- [160] R. B. Perkins, C. D. Palmer, Solubility of ettringite ($\text{Ca}_6[\text{Al}(\text{OH})_6]_2(\text{SO}_4)_3 \cdot 26\text{H}_2\text{O}$) at 5–75°C, *Geochimica et Cosmochimica Acta* 63 (1999) 1969–1980.
- [161] J. H. Ideker, Early-Age Behavior of Calcium Aluminate Cement Systems, Ph.D. thesis, The University of Texas at Austin (2008).
- [162] N. Skoblinskaya, K. Krasilnikov, Changes in crystal structure of ettringite on dehydration. 1, *Cement and Concrete Research* 5 (1975) 381–393.
- [163] N. Skoblinskaya, K. Krasilnikov, L. Nikitina, V. Varlamov, Changes in crystal structure of ettringite on dehydration. 2, *Cement and Concrete Research* 5 (5) (1975) 419–431.
- [164] H. Manzano, A. Ayuela, A. Telesca, P. J. M. Monteiro, J. S. Dolado, Ettringite Strengthening at High Pressures Induced by the Densification of the Hydrogen Bond Network, *The Journal of Physical Chemistry C* 116 (2012) 16138–16143.
- [165] A. Moore, H. F. W. Taylor, Crystal Structure of Ettringite, *Nature* 218 (1968) 1048–1049.
- [166] A. M. Cody, H. Lee, R. D. Cody, P. G. Spry, The effects of chemical environment on the nucleation, growth, and stability of ettringite $[\text{Ca}_3\text{Al}(\text{OH})_6]_2(\text{SO}_4)_3 \cdot 26\text{H}_2\text{O}$, *Cement and Concrete Research* 34 (2004) 869–881.
- [167] P. K. Mehta, Morphology of Calcium Sulfoaluminate Hydrates, *Journal of the American Ceramic Society* 52 (1969) 521–522.

- [168] F. P. Glasser, The stability of ettringite, in: Int. RILEM TC 186-ISA Workshop on Internal Sulfate Attack and Delayed Ettringite Formation, 2002, pp. 43–64.
- [169] B. Lothenbach, T. Matschei, G. Möschner, F. P. Glasser, Thermodynamic modelling of the effect of temperature on the hydration and porosity of Portland cement, *Cement and Concrete Research* 38 (2008) 1–18.
- [170] L. Baquerizo, T. Matschei, K. Scrivener, VOLUME STABILITY OF CAC-CaSO₄-CaCO₃-H₂O SYSTEMS DURING DRYING, in: C. H. Fentiman, R. J. Mangabhai, K. L. Scrivener (Eds.), *Calcium Aluminates: Proceedings of the International Conference*, IHS BRE Press, Avignon, 2014, pp. 274–281.
- [171] J. Plank, C. Hirsch, Impact of zeta potential of early cement hydration phases on superplasticizer adsorption, *Cement and Concrete Research* 37 (2007) 537–542.
- [172] F. Goetz-Neunhoeffler, J. Neubauer, P. Schwesig, Mineralogical characteristics of Ettringites synthesized from solutions and suspensions, *Cement and Concrete Research* 36 (2006) 65–70.
- [173] T. Matschei, B. Lothenbach, F. P. Glasser, The AFm phase in Portland cement, *Cement and Concrete Research* 37 (2007) 118–130.
- [174] R. Gabrovsek, T. Vuk, V. Kaucic, The Preparation and Thermal Behavior of Calcium Monocarboaluminate, *Acta chimica slovenica* 55 (2008) 942–950.
- [175] B. Hitch, R. Mesmer, C. Baes, F. Sweeton, The solubility of (a-Al(OH)₃) in 1 molal NaCl as a function of pH and temperature., Oak Ridge National Laboratory Report ORNL-5623.
- [176] K. Kaiser, G. Guggenberger, Mineral surfaces and soil organic matter, *European Journal of Soil Science* 54 (2003) 219–236.

List of publications

Scientific journals

- J. Bizzozero, C. Gosselin and K. L. Scrivener. Expansion mechanisms in calcium aluminate and sulfoaluminate systems with calcium sulfate. *Cement and Concrete Research* 56 (2014): 190-202.
- J. Bizzozero and K. L. Scrivener. Limestone reaction in calcium aluminate cement-calcium sulfate systems. *Cement and Concrete Research* (2014) submitted.

Conference papers with talk

- J. Bizzozero and K. L. Scrivener. Hydration and microstructure of rapid-strength binders based on OPC accelerated by early ettringite formation. *International Conference on Calcium Aluminates*, Paper 26, Avignon, France, May 2014, ISBN 978-1-84806-316-7.
- J. Bizzozero and K. L. Scrivener. Hydration of calcium aluminate cement based systems with calcium sulfate and limestone. *International Conference on Calcium Aluminates*, Paper 23, Avignon, France, May 2014, ISBN 978-1-84806-316-7.
- J. Bizzozero, C. Gosselin and K. L. Scrivener. Expansion mechanisms in ettringite systems. *International Conference on Calcium Aluminates*, Paper 21, Avignon, France, May 2014, ISBN 978-1-84806-316-7.
- J. Bizzozero and K. L. Scrivener. Hydration and microstructure development of OPC blended with calcium aluminate and sulfoaluminate cements. *First International Conference on Sulphoaluminate Cement: Materials and Engineering Technology*, Paper 7, Wuhan, China, October 2013.
- J. Bizzozero, C. Gosselin and K. L. Scrivener. Dimensional stability of calcium aluminate and sulfoaluminate systems. *31st Cement and Concrete Science Conference*, Paper 27, Imperial College, London, UK, September 2011, ISBN: 978-0-9570152.

List of publications

Workshops with talk

- J. Bizzozero and K. L. Scrivener. Mechanisms and modelling of expansion in calcium aluminate based systems. Cemnet meeting, University of Bern, Bern, Switzerland, September 2014.
- J. Bizzozero and K. L. Scrivener. Modeling of CaO, Al₂O₃, CaSO₄ and CaCO₃ systems. 4rd GEMS Workshop on Thermodynamic Modeling of Cementitious Systems, EMPA, Dübendorf, Switzerland, May 2014.
- J. Bizzozero, C. Gosselin and K. L. Scrivener. Dimensional stability of calcium aluminate and sulfoaluminate systems. Expansive Reactions Workshop, OSU, Oregon, USA, July 2011.

Julien Bizzozero

Av. de Tivoli 70
CH - 1007 Lausanne
+41 79 624 30 05
julien.bizzozero@gmail.com

Professional experience

- 2010 – 2014 **Research Assistant** at Laboratory of Construction Materials (LMC), EPFL, Switzerland
- Supervised and trained visiting PhD students
 - Supervised master students during their semester projects
 - Taught practical works for civil engineering and material science students
- 2009 – 2010 **Laboratory Assistant** at EPFL
Sample preparation for different techniques (SEM, XRD, TGA) and mechanical testing.

Education and trainings

- 2010 – 2014 **PhD in Materials Science and Engineering**
Laboratory of Construction Materials (LMC), EPFL, Switzerland
Study of the hydration and dimensional stability of special binders composed of calcium aluminate cement, calcium sulfate and supplementary cementitious materials.
Analytical techniques: Isothermal calorimetry, X-Ray diffraction (XRD), thermogravimetric analysis (TGA), scanning electron microscopy (SEM), mercury intrusion porosimetry (MIP) and pore solution analysis.
- 2014 **GEMS3**, Thermodynamic Modelling of Cementitious Systems, EMPA, Switzerland (2 days)
- 2013 **Project management** (CRPM), Switzerland (4 days)
- 2005 – 2010 **Master and Bachelor in Materials Science and Engineering**
Ecole Polytechnique Fédérale de Lausanne (EPFL), Switzerland
Orientation: Structural materials for use in transport, energy and infrastructure
Specialization: Management of Technology and Entrepreneurship
- 2001 – 2005 **Federal Diploma** (specialization in physics and applied mathematics)
Secondary School of Lugano 2, Switzerland

Languages

French	Native language
Italian	Bilingual
English	Intermediate, Level B2/C1 (European Framework of Reference for Languages)
German	School knowledge, Level A2 (European Framework of Reference for Languages)

Others

IT Skills: Office suite, Origin, Matlab, GEMS, X'Pert High Score Plus (Rietveld analysis).

Other interests: Running, climbing, skiing and windsurfing.

